high fidelity readout of electron spins in silicon mos quantum dots

David Niegemann

THÈSE

Pour obtenir le grade de

DOCTEUR DE L'UNIVERSITÉ GRENOBLE ALPES

École doctorale : PHYS - Physique
Spécialité : Nanophysique
Unité de recherche : Institut Néel

Lecture haute fidélité des spins d'électrons dans les boîtes quantiques silicium mos

high fidelity readout of electron spins in silicon mos quantum dots

Présentée par :

David NIEGEMANN

Direction de thèse :

Franck BALESTRO PROFESSEUR DES UNIVERSITES, Université Grenoble Alpes	Directeur de thèse
Matias URDAMPILLETA CHARGE DE RECHERCHE, Université Grenoble Alpes	Co-encadrant de thèse

Rapporteurs :

MATTHIEU DELBECQ
Maître de conférences HDR, SORBONNE UNIVERSITE
DOMINIK ZUMBÜHL
Professeur, Universität Basel

Thèse soutenue publiquement le **6 décembre 2022**, devant le jury composé de :

MATTHIEU DELBECQ Maître de conférences HDR, SORBONNE UNIVERSITE	Rapporteur
NATALIA ARES Professeur assistant, University of Oxford	Examinatrice
DAVID FERRAND Professeur des Universités, UNIVERSITE GRENOBLE ALPES	Président
DOMINIK ZUMBÜHL Professeur, Universität Basel	Rapporteur

Invités :

TRISTAN MEUNIER
Directeur de recherche, CNRS DELEGATION ALPES

Résumé

La découverte et la démonstration d'algorithmes quantiques plus performants que tous les algorithmes classiques ont donné naissance au nouveau domaine de recherche qu'est la technologie de l'information quantique. Depuis l'invention du transistor et la commercialisation des microprocesseurs qui a suivi, le développement des ordinateurs a été guidé par la loi de Moore. Au cours des premières décennies, l'industrie a réussi à tenir ses promesses d'une puissance de calcul plus grande avec chaque nouvelle génération, il semble que la loi de Moore touche lentement à sa fin. La technologie de l'information quantique pourrait offrir une voie vers une croissance continue de la puissance de calcul, non pas par une augmentation du nombre de transistors, mais par un changement de la logique de calcul. Ce changement de paradigme nécessite d'énormes quantités de recherche pour rattraper la technologie moderne. La plupart des estimations donnent une limite inférieure d'un million de qubits physiques pour qu'un processeur quantique soit utile pour résoudre des problèmes du monde réel avec des algorithmes quantiques. Bien que les plus grands processeurs quantiques actuels se composent d'environ 100 qubits, ces derniers sont loin d'être parfaits. Souffrant de différentes erreurs, les processeurs quantiques actuels nécessitent de grandes équipes d'experts pour faire fonctionner. La construction d'un processeur quantique comportant des millions de qubits nécessite une technologie fiable et scalable. Dans ce contexte, les qubits de spin dans les boîtes quantiques semiconductrices constituent une plateforme de qubits intéressante qui pourrait bénéficier des techniques de fabrication à grande échelle de l'industrie moderne des semiconducteurs. La communauté s'accorde largement à dire que les qubits doivent satisfaire aux cinq critères de DiVincenzo pour être considérés pour des processeurs quantiques à grande échelle. La communauté des qubits de spin semiconducteur se concentrait jusqu'à présent sur la démonstration de deux de ces critères, notamment "des temps de décohérence longs et significatifs" et "un ensemble "universel" de portes quantiques". Les résultats exceptionnels ont conduit à recentrer maintenant l'effort sur les autres critères. Nous travaillons sur deux d'entre eux. Nous utilisons un dispositif fabriqué dans un processus FDSOI de 300 mm, promettant l'évolutivité requise par le premier critère de DiVincenzo : "Un système physique évolutif avec un qubit bien caractérisé". Le dispositif consiste en un nanofil de silicium qui relie deux réservoirs. Des grilles, patternées sur le dessus du nanofil, permettent l'accumulation de boîtes quantiques dans les coins du nanofil. Dans notre dispositif, nous créons un système de 2×2 boîtes quantiques dans le nanofil. Nous utilisons la réflectométrie rf comme capteur de charge, en utilisant l'un des QD comme capteur. Ensuite, nous utilisons ce dispositif pour réaliser un double boîte quantique. Nous mesurons le blocage de spin de Pauli en utilisant la lecture ST et la lecture de parité, ce qui nous permet de faire la distinction entre le singlet S et les trois états triplets T_0, T_- et T_+ ou entre les états de spin non polarisés S et T_0 et les états de spin polarisés T_- et T_+. Nous démontrons une haute fidélité pour les deux types de lecture. La fidélité de la lecture ST est $> 99\,\%$ à 50 kHz en raison d'une relaxation relativement rapide, la lecture de la parité dépasse $99.9\,\%$ ($99\,\%$) à 50 kHz (250 kHz). Ainsi, les deux lectures répondent à la cinquième condition de DiVincenzo : "une capacité de mesure spécifique au qubit". De plus, nous effectuons ces mesures à une température de 0.5 K, ce qui montre la robustesse en température de ce type de

lecture. En utilisant ce readout, nous caractérisons le système à deux spins en utilisant des expériences de Landau-Zener et de spin-funnel.

Mots clés: reflectomètrie, boîtes quantiques, spin, semiconducteur

Abstract

The discovery and demonstration of quantum algorithms that outperform all classical algorithms gave rise to the new research field of quantum information technology. Since the invention of the transistor and the following commercialisation of microprocessors, computation hardware development was driven by Moores law. While in the first decades the industry managed to deliver on the promise of more computing power with every new generation of hardware, it seems like Moores law slowly comes to an end. Quantum information technology might opens a path towards continued growth in computing power, not by an increase of transistor number, but by a change in computation logic. This paradigm shift that never occurred before in information science, requires vast amounts of research to catch up with the mature technology of modern computer hardware. Most estimates today give a lower bound of one million physical qubits for a quantum processor to be useful for solving real world problems with quantum algorithms. While the largest quantum processors today consist of around 100 qubits, these qubits are far from being perfect. Suffering from different errors, today's quantum processors require large teams of experts to make the hardware work like intended. Building a quantum processor with millions of qubits requires a reliable and scalable technology. In this context, spin qubits in semiconductor quantum dots (QDs) are an interesting qubit platform that might be able to harness the large-scale fabrication techniques of modern semiconductor industry.
The community widely agrees that qubits must fulfill the five DiVincenzo criteria to be considered for large scale quantum processors. While the Semiconductor spin qubit community focused so far on the demonstration of two of these criteria, namely "Long relevant decoherence times" and "A 'universal' set of quantum gates". The outstanding results lead to refocusing now the effort towards the other criteria. In this thesis, we work on two of these. First, we use a device made in a state-of-the-art 300 mm FDSOI process, promising scalability as required by the first DiVincenzo criteria "A scalable physical system with well-characterized qubit". The device consists of a silicon nanowire that connects two reservoirs. Gates, patterned on top of the nanowire, allow the accumulation of quantum dots in the nanowire corners. In our device, we form a 2×2 QD array in the nanowire. We use rf-reflectometry as a remote sensor to measure the charge state of this array, using one of the QDs as a sensor. Next, we use this device to form a double quantum dot and tune it to the two electron regime. We perform Pauli spin blockade measurements using ST- and parity-readout which allows us to distinguish either between singlet S and the three triplet states T_0, T_-, and T_+ or between the unpolarized spin states S, and T_0 and the polarized spin states T_-, and T_+. We demonstrate high fidelity for both readout types. While the ST-readout fidelity is $> 99\,\%$ at 50 kHz due to a relatively fast relaxation, the parity-readout exceeds $99.9\,\%$ ($> 99\,\%$) at 50 kHz (250 kHz). Thus, both readouts fulfill DiVincenzo's fifth requirement "A qubit-specific measurement capability". Moreover, we perform these measurements at a temperature of 0.5 K, showing the temperature robustness of this kind of readout. Using this readout, we characterize the two spin system using Landau-Zener and spin-funnel experiments.
The thesis is structured as follows. In chapter 1, we begin with an introduction to quantum information and motivate spins in semiconductor quantum dots as a qubit platform.

Chapter 2 discusses the physics of semiconductor quantum dots, followed by chapter 3, describing rf-reflectrometry as a readout technique for semiconductor quantum dots. Next, in chapter 4 we give an overview of the experimental techniques used in this thesis. In the fifth chapter, we present our results of charge sensing and control in a six gate device using a 2×2 subarray. After, chapter 6 discusses our results on spin readout of a double quantum dot, including preparation and readout fidelity. In the last chapter, we give an outlook on potential improvements of the presented work and general paths towards large scale qubit architectures based on semiconductor spin qubits.

Key words: Spin, Quantum dots, Semiconductor, Reflectometry

Contents

1 Motivation

> Those who can imagine anything, can create the impossible.
>
> Alan Turing

In this chapter we want to motivate the research presented in this thesis. Apart from doing research out of curiosity, placing the research of this thesis in a greater context might makes sense with an increased interest of industrial applications in this field of research. The ultimate goal of the research domain is building a universal quantum computer. During my PhD, we worked on the most basic element of such a quantum computer, namely a quantum bit or qubit. What such a qubit is and what one can do with it will be discussed in the following. The presented information is by far not complete and there exist excellent resources for a more complete treatment of these topics that will be mentioned throughout this chapter. We will try to limit ourself to the information to the fundamentals about qubits and the aspects that relate to the work presented in this thesis.

1.1 Fundamentals of quantum information processing

Quantum information processing corresponds to classical information processing using quantum bits instead of classical bits. A few decades ago, the first algorithms were invented, which exploit the properties of quantum bits distinguishing these from classical bits. These algorithms outperform all classical algorithms [Deu92]. To explain why quantum information processing can outperform classical information processing, we need to discuss the properties of quantum bits first. For a deeper dive into the topic of quantum information processing the reader is advised to consult the more complete resources [Asf20; Ihn10; Nie09].

1.1.1 From a classical to a quantum bit

In classical information processing, a bit is the smallest chunk of information. Information is here considered as the information

$$\Delta I = U_{\text{before}} - U_{\text{after}}, \tag{1.1}$$

one retrieves from the difference of the uncertainty before (after) the experiment U_{before} (U_{after}). Without loss of generality, we can assume that our experiment has p possible

outcomes with equal probability $\Omega = 1/p$. The uncertainty is then given by

$$U = k \cdot \log_2(1/p) = -k \cdot \log_2(p), \tag{1.2}$$

where k is a normalization factor. This definition results in $U_{\text{after}} = 0$ and if we imagine an experiment with just two outcomes, we find that the normalization factor should be set to $k = 1/\log_2(2)$. A two outcome experiment is the smallest unit of information we can get, and we call this smallest unit of information a bit. Generalizing this idea to an experiment with n different outcomes where the outcome i has probability $1/p_i$, we find

$$H(\{p_i\}) \equiv \frac{U}{N} = -\sum_{i=0}^{n-1} p_i \log_2(p_i) bit \tag{1.3}$$

which is known as the Shannon entropy. For a more elaborate discussion on this topic, we refer to Thomas Ihn's book [Ihn10] on which this paragraph is based.
We have seen that the only property of a bit is its state. We will refer to these two states as 0 and 1. To describe more complex information, one uses sequences of bits, increasing the amount of possible states to 2^N, where N is the number of bits in the sequence. Similar to the classical bit, measuring the state of a quantum bit yields as well either 0 or 1. So, what is the difference? Classical bits and quantum bits differ in what happens before the measurement. While a classical bit is always either in state 0 or in state 1, a qubit is in a superposition of the two possible states. Only the measurement yields to the so-called collapse of the wave function. Following the Copenhagen interpretation, the measurement forces the qubit to be in on of the two states. Which state the qubit is found in is probabilistic and can be calculated using the amplitude resulting from the projection of the qubit state on the measurement basis. This means, that a qubit is not really a bit in the sense that it carries just one bit of information. Rather the measurement process just gives one bit of information. We will see that there are actually two continuous parameters that define a qubit state. To build qubits, one uses quantum two-level systems.
In general, every quantum two-level system can be considered as a quantum bit or qubit as we can interpret each level as the respective bit state. The wave function $|\psi\rangle$ of a perfect two-level system can be written in terms of two orthogonal eigenvectors $|0\rangle$ and $|1\rangle$, where we used the Dirac notation, where $|0\rangle$ ($|1\rangle$) corresponds to the eigenvector of the ground (excited) state. These eigenvectors thus span the Hilbert space in which the quantum system lives.

$$|\psi\rangle = \alpha\,|0\rangle + \beta\,|1\rangle = \begin{pmatrix} \alpha \\ \beta \end{pmatrix} \tag{1.4}$$

where $\alpha, \beta \in \mathbb{C}$ and

$$|\alpha|^2 + |\beta|^2 = 1. \tag{1.5}$$

The normalization condition 1.5 reduces the four possible qubit parameters (real and imaginary part of α and β) to three. As the absolute phase of the quantum states is

arbitrary, we can set it to zero, making α a real number. It follows that we can express the two numbers as

$$\alpha = \cos(\theta/2) \qquad \beta = e^{i\varphi}\sin(\theta/2) \tag{1.6}$$

where θ parametrizes the probabilities of the two qubit states ($p_0 = \cos^2(\theta/2)$ and $p_1 = \sin^2(\theta/2)$). A system of N qubits can then be described as a superposition of the 2^N basis states of the Hilbert space. For a two qubit system, these would be $|00\rangle, |01\rangle, |10\rangle, |11\rangle$ with $|ij\rangle = |i\rangle_A \otimes |j\rangle_B$. Dealing with a quantum system, the state of the qubit, namely the values of α and β, change according to the Hamiltonian $\hat{H}$ describing the qubit system. Interestingly, as soon as one deals with more than one qubit, the absolute phase becomes important. One must take the relative phase of the qubits to each other into account and therefore, the number of parameters increases by four for each additional qubit (2 absolute values and 2 phases per qubit). The importance of the relative phase becomes clear with the concept of entanglement. One can consider for example the state

$$|\psi\rangle = \frac{1}{\sqrt{2}}(|00\rangle + |11\rangle) \tag{1.7}$$

which one can not describe as a product of two independent qubits $|i\rangle$ and $|j\rangle$ as the two qubit states are correlated or so-called entangled. Entanglement is an important property as it allows performing conditional operations on an ensemble of two or more qubits. This conditional operations are known as multi-qubit gates. Gates are the operations performed to change the qubit states. Entangled qubits are as well a pure quantum property of qubits and allow the realization of quantum algorithms (the sequence of quantum and classical gates on a set of qubits), which can outperform classical algorithms (sequence of classical gates on a set of qubits or bits). Before we go into more details of quantum information, we want to introduce a few very helpful concepts widely used in the community.

1.1.2 Describing a qubit system - The Bloch sphere, Pauli matrices and Rabi oscillations

Common methods to describe a qubit system are the Bloch sphere and the Pauli matrices[1]. While the Bloch sphere is a tool to visualize the complex qubit state, Pauli matrices are used as a basis for the qubit Hamiltonian and facilitate the description of the evolution of the qubit state.
Using equation 1.6, the potential states of a qubit are a function of the two angles φ and

1 The Bloch sphere can only be used for single qubits. To describe multi qubit systems one uses density matrices. A short overview of density matrices can be found in the appendix.

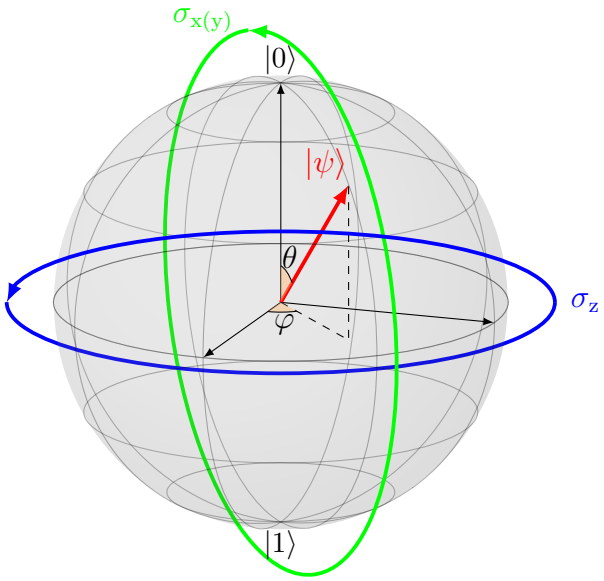

Figure 1.1: A Bloch sphere representing a qubit state $|\psi\rangle$. The state vector is fully defined by the azimuthal angle θ and polar angle φ. The σ_z components of the Hamiltonian rotate φ, while the $\sigma_{x(y)}$ components rotate θ[b].

b Note that θ in this figure is not rotating in the correct direction. However, most figures in textbooks and research articles depict the Bloch sphere like that, and we will stick to this convention.

θ. These define the direction of the so-called polarization vector $\mathbf{P} = (P_x, P_y, P_z)$, with

$$P_x = \sin\theta\cos\varphi \tag{1.8}$$
$$P_y = \sin\theta\sin\varphi \tag{1.9}$$
$$P_z = \cos\theta. \tag{1.10}$$

This describes the surface of a sphere of radius one as the quantum state has the norm 1 or 100 % probability. The polar angle is described by θ and the azimuthal angle by φ. This sphere is known as the Bloch sphere and depicted in figure **1.1**. The visualization allows a 3D representation of the complex 2D quantum state [2]. By convention, the two qubit states are located at the poles (e.g. $|0\rangle$ at the North Pole and $|1\rangle$ at the South Pole or vice versa). Any qubit state $|\phi\rangle$ can then be described as a point on the sphere. We will see that this picture is in particular intuitive for spins[3].
As the state of a qubit is considered a position on the Bloch sphere, the change of the qubit state is considered moving on the Bloch sphere. To move on the Bloch sphere, one needs

2 Mathematically, we map from $SU(2)$ to $SO(3)$.
3 We want to issue a warning here to imagine the polarization vector to represent the spin state. A spin qubit state is defined by the z-component of the spin and the xy-components are of no interest. The Bloch sphere is only representing the z-component state of a spin state and ignores the xy-components.

to control the angles φ and θ. In other words, qubit control requires two independent controls. One to rotate the qubit state latitudinal, given by θ and one to rotate the polar angle ϕ of the qubit state. The angle θ rotates between the two poles that are representing the two qubit eigenstates. A typical way to demonstrate qubit control is to perform a Rabi experiment that shows controlled rotations between the poles. We will discuss the Rabi experiment in the following. As we describe the qubit state as a vector, we remember that vector rotations can be performed by rotation operators. In quantum mechanics the use of the Pauli matrices has proven to be a useful way to understand the rotation in complex 2D space.
The Pauli matrices

$$\sigma_{\mathrm{x}} = \begin{pmatrix} 0 & 1 \\ 1 & 0 \end{pmatrix} \tag{1.11}$$

$$\sigma_{\mathrm{y}} = \begin{pmatrix} 0 & -i \\ i & 0 \end{pmatrix} \tag{1.12}$$

$$\sigma_{\mathrm{z}} = \begin{pmatrix} 1 & 0 \\ 0 & -1 \end{pmatrix} \tag{1.13}$$

$$\tag{1.14}$$

form a basis for complex 2×2 Hermitian[4] and unitary[5] matrices and as will become clear in the following, it is very useful to express a qubit Hamiltonian in terms of Pauli matrices. They span the group SU(2) which is isomorphic to SO(3). In other words, there is a reversible mapping between the SU(2) and SO(3) groups. As SO(3) can be interpreted as rotations in 3D, SU(2) is exactly what we need to describe rotation of a qubit state (complex 2D) on the Bloch sphere (3D real). We can always describe the Hamiltonian of a qubit using Pauli matrices and the identity I as a basis. The reason one uses Pauli matrices for qubit Hamiltonians is that it makes it easy to identify which components of the Hamiltonian are driving rotations around the different axes (e.g. the σ_{z} component drives the φ rotation). For a more complete treatment of Pauli matrices, the reader is advised to textbooks like [Sak93].
Using the Pauli matrices to describe a two-level system, it becomes evident that no rotations between the two eigenstates occur. In the eigenbasis the off-diagonal elements of the Hamiltonian are zero and thus the σ_{x} and σ_{y} terms are zero. In this situation, the qubit state rotates around the z-axis of the Bloch sphere. The solution to rotate between qubit states is to add $\sigma_{\mathrm{x}}(\sigma_{\mathrm{y}})$ components to the Hamiltonian. Such a change of Hamiltonian can be achieved with a driving force that mixes the two eigenstates and is known as Rabi experiment. To perform so-called Rabi oscillations, rotating latitudinal on the Bloch

4 A Hermitian matrix is a complex square matrix that is equal to its own conjugate transpose, often indicated with a †.

5 Determinant equals 1, indicating that these matrices do not change volumes in hyperspace of the matrices. A property of matrices describing rotations.

sphere, we can use a driving force

$$\hat{H}' = \hbar\gamma \begin{pmatrix} 0 & \exp(-i\omega t/2) \\ \exp(-i\omega t/2) & 0 \end{pmatrix}, \tag{1.15}$$

where γ can be interpreted as the strength of the drive (e.g. power of a microwave tone) and ω as the frequency of the drive. As is evident from the off-diagonal elements, this Hamiltonian allows transitions between the two eigenstates. Starting in state $|\psi(0)\rangle = |0\rangle$, the probability for finding the state in one of the two states after time t is then given by the Rabi formula

$$|c_2(t)|^2 = \frac{\gamma^2}{\gamma^2 + (\omega - \omega_0)^2/4} \sin^2 \sqrt{\gamma^2 + \frac{(\omega - \omega_0)^2}{4}} t \tag{1.16}$$

$$|c_1(t)|^2 = 1 - |c_2(t)|^2. \tag{1.17}$$

At resonance where the driving photons $\hbar\omega$ match the separation energy of the two states $\hbar\omega_0$, the drive allows rotating completely between the two states at frequency γ/π. At driving frequencies slightly off-resonance, we find rotations of frequency $\Omega = \sqrt{\gamma^2 + \frac{(\omega-\omega_0)^2}{4}}$, faster than at resonance [Sak93]. However, off-resonance the oscillations do not cycle fully between the two states and therefore, only the on-resonance drive is relevant for qubit applications. For driving the qubit faster, one can increase the driving power γ. To sum it up, for a full qubit control we need an oscillating drive with σ_x and/or σ_y component at the resonance frequency of the qubit. With this drive, we can then move freely on the Bloch sphere, applying no drive when we want to rotate φ and applying the drive when rotations of θ are required. It is important to mention here that the described Hamiltonian is often not static and fully known, due to environmental perturbations or imperfect manipulation. This leads to so-called decoherence, meaning that one loses information about the angles θ and φ. The θ decoherence can be interpreted as relaxation (excitation) and is measured using the relaxation time T_1. The φ decoherence is the loss of quantum phase information and is driven by perturbations on the diagonal elements of the Hamiltonian. For a spin qubit this can be for instance fluctuations of the local magnetic field due to nuclear spins. The time of decoherence of a qubit is given by the decoherence time T_2 when measured using a Ramsey experiment or T_2^* using a Hahn echo experiment[6]. Now that we have the tools to move on the Bloch sphere, we want to introduce the concept of quantum gates in the next section.

1.1.3 From classical gates to qubit operations

A qubit would be useless if we were not able to perform operations on it. A single qubit operation is the controlled change from one qubit state to another. Modern computers work with so-called logical gates, build out of electrical circuits, that perform a boolean

6 For a description of these experiments the reader is advised to consult the original work by Hahn[Hah50] or a more hands-on explanation by the IBM Qiskit team[Asf22].

function. For instance one of the simplest gates is the NOT gate that inverts the bit state from 0 to 1 or vice versa. While one could think about an infinite number of gates, classical computers use a limited number of primitive gates and build more complex operations out of these. Going now from classical gates to quantum gates, a few things change. While classical gates are not necessarily reversible, quantum gates are unitary transformations, thus always reversible. Moreover, we have seen that qubits can be in a superposition of states. Therefore, we can think of gates that yield an output that is not only 0 or 1, but any possible quantum state. Last but not least, qubits can be entangled. This causes counterintuitive effects as the operation on one of the qubits, changes as well the state of the other qubit [Asf20]. We will start with the physical description of a qubit's time evolution.
The time evolution of a quantum state ψ is described by the Schrödinger equation

$$\hat{H}\left|\psi\right\rangle = -\frac{i}{\hbar}\frac{d}{dt}\left|\psi\right\rangle \tag{1.18}$$

, where the Hamiltonian $\hat{H}$ is a time-independent unitary operator. For a quantum two-level system this Hamiltonian can be represented as a 2×2 matrix. Solving the Schrödinger equation yields

$$\left|\psi(t_\mathrm{f})\right\rangle = \hat{U}\left|\psi(t_0)\right\rangle = \exp\left(\frac{-i\hat{H}t}{\hbar}\right)\left|\psi(t_0)\right\rangle \tag{1.19}$$

for the time evolution from $t = t_0$ to $t = t_\mathrm{f}$, where $\hat{U} = \exp\left(\frac{-i\hat{H}t}{\hbar}\right)$ is the time evolution operator.
An arbitrary rotation of the state of a two-level quantum system (or qubit for our purposes) on the Bloch sphere can be expressed by the operator

$$\begin{aligned} R(\phi) &= \exp(-i\phi\boldsymbol{a}\cdot\boldsymbol{\sigma}/2) = \exp(-i\phi(a_\mathrm{x}\sigma_\mathrm{x} + a_\mathrm{y}\sigma_\mathrm{y} + a_\mathrm{z}\sigma_\mathrm{z})) \\ &= \exp(-i\phi a_\mathrm{x}\sigma_\mathrm{x})\exp(-i\phi a_\mathrm{y}\sigma_\mathrm{y})\exp(-i\phi a_\mathrm{z}\sigma_\mathrm{z}) = R_\mathrm{x}(\phi)R_\mathrm{y}(\phi)R_\mathrm{z}(\phi), \end{aligned} \tag{1.20}$$

where ϕ is the rotation angle, $\boldsymbol{a}$ the rotation axis, and $\boldsymbol{\sigma} = (\sigma_\mathrm{x}, \sigma_\mathrm{y}, \sigma_\mathrm{z})^T$ the vector of Pauli matrices. Comparing equation 1.19 with equation 1.20, it becomes clear that we can write $Ht/\hbar = \phi\boldsymbol{a}\cdot\boldsymbol{\sigma}$. Writing the rotation like this, allows to split the rotation around an arbitrary axis $\boldsymbol{a}$ into the three Cartesian axes x, y and z.
If we want to exploit a two-level quantum system as a qubit, we need to control the Hamiltonian in order to change deterministically the qubit state. The goal for an experimentalist is to conceive a quantum system such that the desired parameters of the Hamiltonian can be controlled in a way to move freely on the Bloch sphere. Additionally, the qubit should not be vulnerable to uncontrollable contributions from the environment (e.g. electrical noise).

Let's assume that we have a two-level system with the general Hamiltonian

$$\hat{H}_0 = \frac{\hbar\omega_0}{2}\sigma_z, \tag{1.21}$$

where the two levels are energetically separated by $\hbar\omega_0$. The time evolution of a state $|\psi\rangle$ is given by

$$|\psi(t)\rangle = \exp\left(\frac{-i\hat{H}t}{\hbar}\right)|\psi(0)\rangle = \begin{pmatrix}\exp(-i\omega_0 t/2) & 0\\ 0 & -\exp(-i\omega_0 t/2)\end{pmatrix}|\psi(0)\rangle \tag{1.22}$$

and thus the state rotates in the xy-plane. We have seen in the previous section **1.1.2** that we can use a Rabi type driving force to rotate around the x(y)-axis. The controlled application of the Rabi drive allows moving to concrete positions on the Bloch sphere with respect to the initial state. A set of these concrete rotations on the Bloch sphere that allows to perform all required operations for quantum algorithms is called a universal gate set. One can think of this gate set as the basis vectors that span the space of quantum gates. There are different universal gate sets for quantum computing. As quantum gates often involve more than a single qubit, multi qubit gates exist. To understand how one can implement such multi qubit gates it makes sense to consider the unitary rotations on the Bloch sphere using rotation operators $R_x(\phi) = e^{i\frac{\phi}{2}\sigma_x}$ and $R_z(\theta) = e^{i\frac{\theta}{2}\sigma_z}$. If we want to rotate multiple qubits at the same time, we can do this by using the external product of these operations $R_1 \otimes R_2$, where R_i stands for a rotation operation on qubit i. This allows to build unitaries that act on the complete quantum system. In practice, it is often very difficult to perform operations on multiple qubits at the same time and nowadays, most qubit processors just offer the application of single qubit gates and one two-qubit gate (e.g. a CNOT gate)[7] which is sufficient to build a universal gate set. Even though this makes the algorithms a bit longer in terms of how many gates must be applied, the physical implementation is for most systems much easier. A compact way to describe the requirements for building a quantum computer are given by the DiVincenzo criteria [DiV00b].

1.2 The DiVincenzo criteria - A how-to guide for building a quantum computer

In 2000 David P. DiVincenzo proposed five criteria which must be fulfilled in order to build a quantum computer[DiV00b]. Following this proposal, we want to motivate the particular interest of spin qubits in semiconductor quantum dots. In the following, we will go through every criterion and discuss in how far spin qubits fulfill these requirements.

7 X- and Z- rotation of single qubits and a CNOT build a universal set of quantum gates and are thus sufficient to perform any quantum algorithm[DiV00b].

1.2.1 A scalable physical system with well characterized qubits

This criterion has two components. First, we need a well characterized qubit system. For this, there are many proposals and as described in [Los98; Van19], spin qubits are such a system. Second, the system must be scalable. This is a very strong requirement, as it is nowadays the greatest challenge to overcome. One can argue that this is the striking argument for semiconductor quantum dots. As silicon is the favored material for spin qubits in semiconductor quantum dots and the fabrication might be performed in an industrial CMOS fabrication process. In other words, the fabrication of semiconductor quantum dot architectures could use the most scalable technology which exists nowadays. There are other challenges than just a scalable fabrication process, and we will discuss this in section **1.3**.

1.2.2 Initializing qubits to a simple fiducial state

A known initial state of the system is fundamental to perform any operation on it and have trustable results. Moreover, quantum error correction requires a continuous supply with low-entropy states (e.g. the ground state). One of the most common ways to initialize a qubit system is to let it decay into the ground state by waiting much longer than T_1. While one can perform this relaxation approach in quantum dots, it is often much faster and therefore preferred to unload the electron from the quantum dot and subsequently pulse the control gates to allow only tunneling from the reservoir to the ground state, but not the excited state, of the quantum dot. Resulting in tunneling of an electron in the ground state.

1.2.3 Long relevant decoherence times

Decoherence is a quantum concept that is unknown in the classical world. As we have seen in section **1.1.2**, the quantum state of a two-level system is defined by the angles θ and φ. These angles could in principle be deterministically predicted using the time evolution operator. However, in real systems the time evolution operator is perturbed by the environment. To achieve high fidelity operations the perturbations must be small compared to the control drive and for known perturbations, correcting control elements can be added. Decoherence times are the major reason why the focus from well understood GaAs/AlGaAs heterostructure quantum dots is shifting to silicon quantum dots. As DiVincenzo explains, the decoherence time of the qubit must be $10^4 - 10^5$ the "clock time" of the quantum computer, which corresponds to the time for the application of an individual quantum gate. As spin qubits in silicon have a coherence time of a few 100 µs [Vel15], this would require quantum gates in the order of a few ns. The coherence times can be further enhanced using enriched ^{28}Si as this would provide a nuclear spin free environment [Abr17; Wit10].

1.2.4 A "universal" set of quantum gates

Qubit evolution is governed by unitary operators, characterized by the Hamiltonian describing the system. The ability to "turn on" some Hamiltonian for a given time t and by that carry out a specific operation on the qubit is fundamental to quantum computation and error correction. It can be difficult to apply arbitrary rotations of a qubit on its Bloch sphere. In 1997 Alexei Kitaev found a solution for this problem which is now known as the Solovay-Kitaev theorem[Kit97]. It requires a set of quantum gates S which is dense in $SU(2^n)$, which is the group of unitary matrices with determinant 1 operating on n qubits. Such a set of quantum gates is known as universal[Aha03]. Kitaev showed that universal quantum gates can approximate any arbitrary rotation using the universal quantum gates in sequential order[Nie09].

1.2.5 A qubit-specific measurement capability

It is unfortunate that the qubit-specific measurement capability comes as one of the last requirements, as it would actually make sense to put it in the beginning. Considering that before one can think about any manipulation of quantum states, one needs to ensure the capability to distinguish the different states, makes it obvious that this requirement stands in the beginning of every qubit implementation. The qubit readout is often benchmarked in terms of fidelity[8], but there are a few other properties of a readout scheme one should consider. Coming back to the first requirement, the readout scheme should be scalable. This means that the footprint as well as additional device components should be as small as possible. We will see that the readout technique used in the presented experiments is well suited to fulfill these requirements. The presented work focuses mainly on this DiVincenzo criterion, and we will come back to it in the following chapters.

1.3 The case for silicon quantum dot spin qubits

In DiVincenzo's study, he concludes that at the time of writing it is still not clear which system is best suited to be used for a quantum computer. Nowadays, the probably most advanced technology is based on superconducting circuits. In terms of number of qubits the so-called transmon qubits, based on Josephson junctions, present the largest arrays of up to ~ 100 qubits[Ibm]. Such a qubit chip made by Google demonstrated the potential of such an intermediate size qubit array to outperform classical computers using quantum algorithms[Aru19] and their capabilities of simulating quantum systems that are not easily controlled as real systems[Mi21]. Being devil's advocate here, these qubit arrays are still far from an error corrected universal quantum computer which will probably require $10^6 - 10^8$ qubits[Met13; Wec14]. The fact that the qubits are not perfectly isolated, but cross-talk couples all qubits with each other is probably a problem that will be of increasing importance for large scale architectures.
Another interesting technology are ion traps that trap individual ions in a chain using

8 We will discuss fidelity and visibility in detail in the results chapter **6**.

lasers. Each ion is used as a qubit, and they are coupled through phononic excitations of the chain. While the properties of these qubits are outstanding and each qubit is, thanks to its atomic nature, indistinguishable (except in terms of position in the chain), the scaling has been very challenging so far and the largest arrays consist of $\sim 10 - 20$ qubits[Ega21; Fri18]. Not only is the control of the ion chain increasingly difficult with an increasing number of ions, but ion trap qubits are operated in the kHz range, which would make a quantum computer based on ion traps rather slow. In terms of physical footprint, a single superconducting qubit is in the order of $100 \times 100\,\mu m^2$, corresponding to $10\,m^2$ for 10^6 qubits and the spacing between ions in ion traps is as large as 1 mm. Hence, it is unlikely that one can build a quantum computer chip using a 2D architecture with these platforms.
Apart from superconducting qubit platforms, spins in semiconductors offer another interesting solid state qubit platform. Spin qubits can be trapped by donor potentials or in semiconductor quantum dots which form potential traps that can host single electrons or holes. The spin degree of freedom of these charge carriers can be used as a qubit in different ways. Spin qubits can in principle fulfill the DiVincenzo criteria and the footprint of a qubit would be smaller than $100 \times 100\,nm^2$. In terms of physical size, putting billions of qubits on a standard chip of a few cm^2 would be possible. As the spin only directly couples to magnetic fields (indirectly to electric fields through spin-orbit coupling), spins in a nuclear spin free environment like isotopically enriched ^{28}Si already demonstrated coherence times of a few hundred µs [Kaw16]. These long coherence times allow performing single qubit gates that surpass 99.9 % fidelity at a speed of a few 10 GHz [Yan19; Yon17]. Moreover, two-qubit gates with fidelities above 99 % were recently demonstrated in three different device types [Mąd22; Noi22; Xue22]. Even though the fidelity decreases with increasing temperature, spin qubits can be operated at temperatures $> 1\,K$ [Cam22; Yan20]. The best spin readout fidelities surpass the 99 % threshold [Bor21; Nie22; Zhe19]. Other challenges come up when scaling up, for instance the number of input-output connections (IO's) to the qubit chip need to be considered[Van17] and cooling power can be a limiting factor. So far, spin qubits are not strongly affected by these limitations, but the community is already working on the optimization of thermal load and cryo-CMOS[Pau21; Xue21].
Before presenting the technology used for the devices used during this work, we want to give a brief overview of the landmark results of the semiconductor spin qubit.

1.3.1 Evolution of spin qubits

Semiconductor spin qubits have shown a rapid evolution in the last decades and the pace of improvement is seemingly just increasing, making the state-of-the-art view presented in the following probably outdated at the time of reading. The story of spin qubits in semiconductors started with the use of nanofabrication to form and measure quantum dots almost 30 years ago[Han07]. After, the theory for such systems improved and more sophisticated experiments involving magnetic fields were performed[Kou97; Sas98]. Around the 2000s, different proposals for spin qubits were published[DiV00a; Lev02; Mei03]. Shortly after, the first single-shot spin readout in quantum dots was measured[Elz04]. A year after in

2005, the first singlet-triplet qubit was demonstrated [Pet05a]. In 2006, Koppens et al. published the first work on a single-spin qubit using electron spin resonance (ESR)[Kop06] and in 2008 the Tarucha group used electron dipole spin resonance (EDSR) to control a single spin[PL08]. These first qubit demonstrations used GaAs/AlGaAs as a host material and the decoherence due to the nuclear spin bath already foreshadowed the limited fidelity spin qubits in GaAs/AlGaAs could achieve. At the same time of these first qubit experiments, Si was considered as a possible alternative host material for donor based [Hil05; Kan98; Sou04] and quantum dot based spin qubits [Fri03]. The additional challenges that Si poses for quantum dots (e.g. larger electron mass) and the head start GaAs/AlGaAs had, resulted in a delayed demonstration of the superior properties of Si. The first results of Si quantum dots in the single electron/hole regime were published in 2007 (Si/SiGe)[Sim07] and 2009 (Si MOS)[Lim09; Zwa09]. First single shot spin measurements were done by Morello et al. in 2010 [Mor10]. Similar to Hanson et al. in GaAs/AlGaAs in 2005, Maune et al. performed 7 years later singlet-triplet oscillations in Si QDs [Mau12]. In the same year, a single-atom electron spin was controlled using ESR[Pla12] in the same way Koppens did six years earlier in GaAs/AlGaAs. In 2014, the Dzurak group at UNSW published the first article about high fidelity qubit control in Si QDs, a result demonstrating that Si spin qubits can overcome the fault-tolerant threshold for error correction codes[Vel14]. Only a year later another crucial experiment for a every qubit platform was performed by the same group, namely performing a two-qubit logic gate[Vel15]. Shortly after, the first Si QD qubit was demonstrated in a device made in an industrial 300 mm Si process[Mau16]. After, Yoneda et al. showed unprecedented gate fidelities $> 99.9\,\%$ in Si/SiGe QDs. The first two-qubit processor was made by the Vandersypen group in 2018 [Wat18]. More recently the Tarucha group measured a three-qubit state[Tak21] and in 2022, three groups demonstrated high fidelity single- and two-qubit gates [Mąd22; Noi22; Xue22]. Now that single- and two-qubit gates surpassed the surface code threshold, one could jump to the conclusion that it is only a question of scale, but this ignores important DiVincenzo criteria. It is not only the gate fidelity that determines the quality of a qubit, but the product of initialization fidelity, gate fidelity and readout fidelity. So far, no device demonstrated high fidelity operation using this more rigorous definition[Sta22]. Spin readout fidelities $> 99\,\%$ were demonstrated using Pauli spin blockade (PSB)[Bor21; Zhe19] and a few protocols to improve the readout signal[Die21]. Moreover, the demonstration of such high fidelities is still outstanding for devices made in an industry compatible process, which would be required to keep the promiss of scalability.
Nowadays, different quantum dot platforms exist, and we want to give an overview of the most prominent architectures in the following.

1.3.2 Semiconductor spin qubit platforms

Today, one can distinguish broadly three classes of platforms. The heterostructure based quantum dots, MOS quantum dots and donor based platforms. The latter one is based on the control of a single donor electron and many techniques for this technology are similar, we don't want to discuss the details of this platform and the reader is referred to reviews like [Bur21; Sch14; Zwa13]. We will start our discussion with the heterostructure type.

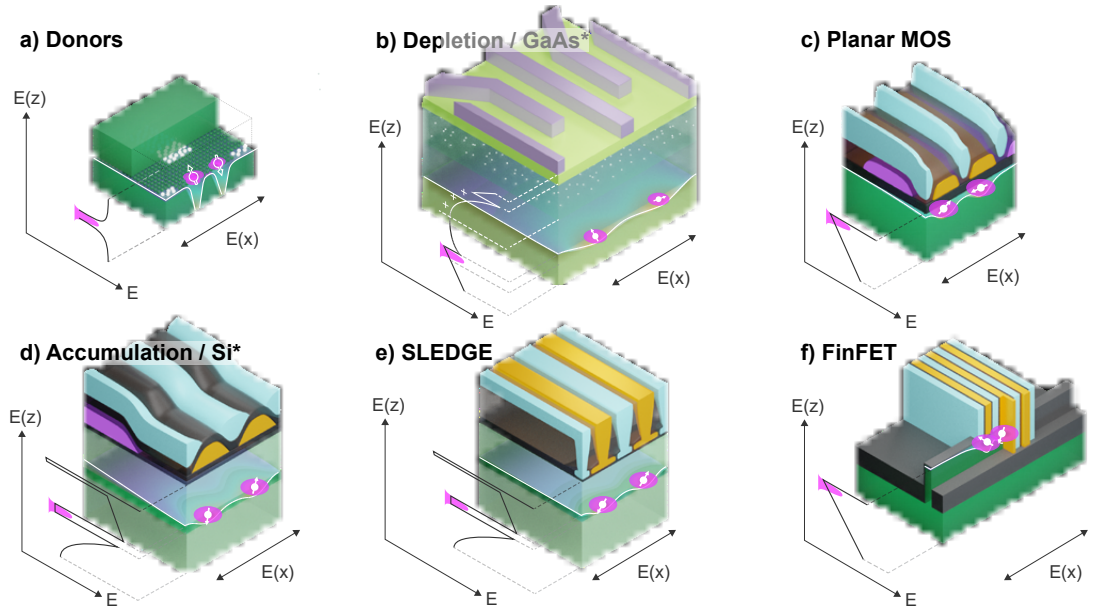

Figure 1.2: A selection of popular device architectures to confine electron spins. The confinement along the z-direction is indicated with a sketch of the band structure on the side of each architecture. **a)** Is an illustration of a donor based confinement where a donor is implanted in a substrate, and it's potential traps an electron. Control of the electron is achieved using gates on the surface of the substrate. **b)** Depletion gate device using a heterostructure like GaAs/AlGaAs. The quantum dots are formed using a 2-dimensional electron gas formed through band gap engineering at an interface of the heterostructure and confinement in the plane using depletion gates on the surface of the heterostructure. **c)** Planar MOS architecture that uses overlapping gates to accumulate and control electrons at the Si-SiO_2 interface. **d)** Accumulation/Si heterostructure where the electrons are confined in the z-direction by a buried quantum well (typically Si in SiGe). Gates on the surface of the heterostructure confine the electrons in the plane. **e)** SLEDGE (single layer etch-defined gate electrodes) device using a Si/SiGe heterostructure where the defining gates are connected to vias that allows easier fan out of the gate connections. **f)** FinFET device using gates on top of a nanowire to trap electrons in the corners of the nanowire. Figure taken from [Bur21].

Heterostructure based semiconductor quantum dots

Heterostructure QDs use a substrate that consists of layers of different materials. These materials have different band gaps and electrochemical potentials. The controlled growth and doping of these materials allows so-called band gap engineering. The engineered band structure of the substrate results in a so-called 2-dimensional electron gas (2DEG) at an interface of two materials. The most popular material where this was demonstrated is a heterostructure made of AlGaAs/GaAs. Nowadays, Si heterostructures made of Si/SiGe exist and allow to transfer some experience from AlGaAs/GaAs to Si/SiGe. The 2DEG confines the electrons along the growth direction of the substrate. To form quantum dots in the plane, electrical gates are epitaxially grown on top of the substrate. Different gate architectures are used while the most common is the accumulation gate architecture as it is

illustrated in figure **1.2d)** and used in [Mil22; Noi22; Xue22]. A rather recent development is the SLEDGE (single layer etch-defined gate electrodes) architecture, depicted in figure **1.2e)**, that uses vias to connect to the accumulation gates, facilitating fan out of the gate connections [Ha21], demonstrated by a team at HRL Laboratories, LLC. The electric fields of the gates allow accumulating electrons (form quantum dots) or to control the coupling between individual quantum dots. The qubits that are based on these structures have shown some of the best fidelities of any quantum dot based qubit and many research groups are already working on small arrays of such quantum dots [Mil22; Noi22; Xue22]. While the number of qubits is so far in the small single digits and being restricted to a 2DEG makes it hard to conceive a scalable architecture, the SLEDGE architecture might offer a solution to the fan-out challenge.
A technology closer to modern-day microprocessor fabrication are MOS based quantum dots that we want to present in the next section.

MOS based quantum dots

Metal-oxide-semiconductor (MOS) structures can also be used to form quantum dots. MOS structures are nowadays used in almost every microprocessor and the technology has matured to the most scalable, humankind has ever invented[9]. Despite the experience using this technology and in particular using it with silicon as a substrate, the research for quantum dots using this technology is still in its infancies. Different ways to form quantum dots have been explored, ranging from pure electrostatic confinement to partial geometric confinement. We will start with a very popular platform that does not require advanced semiconductor fabrication techniques, but can be made in an academic clean room. The substrate is silicon (Si) covered by a silicon-oxide (SiO_2) layer of a few nm. On top of this, metallic gates are epitaxially grown, resulting in a structure like it is depicted in figure **1.2c)**. The challenge of this architecture is that it is not sufficient to have a simple single layer of gates. Instead, one grows multiple layers with different purposes (accumulation, reservoirs, qubit control). The art of fabrication of these devices is the accurate positioning of the gates and the right amount of isolation between the gates using atomic layer deposition (ALD) to form an oxide between them. Accumulation of electrons at the interface Si-SiO_2 allows forming quantum dots. Even though two qubit gates and even a unit cell were demonstrated in such devices[Hua19; Yan20], it remains to be seen if an architecture can scale up remaining on a planar surface which requires a large gate overhead. During this thesis, the devices used were based on a FinFET (Fin-field effect transistor) geometry, an architecture often used for modern transistors[Kam22].

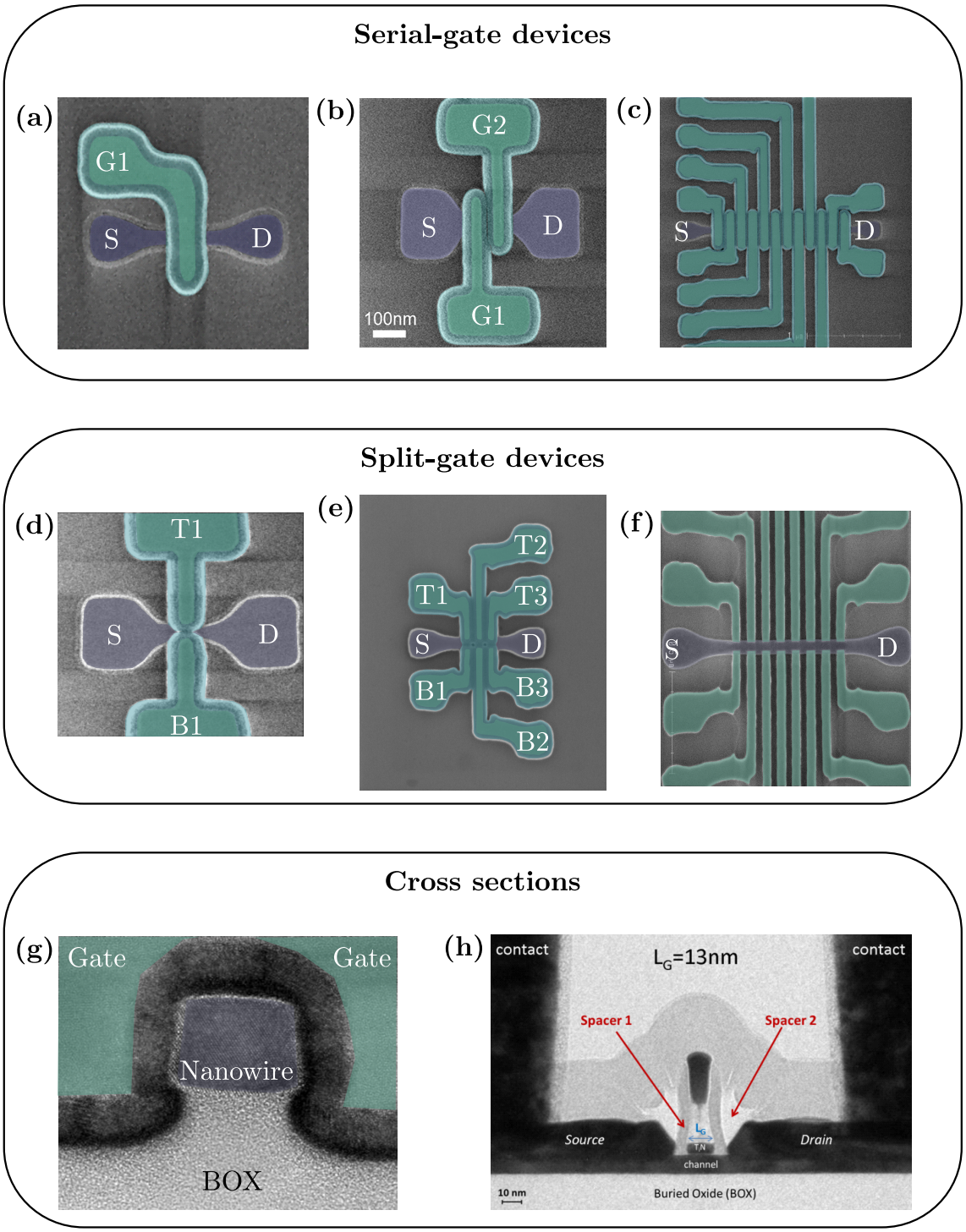

Figure 1.3: Scanning electron microscope micrograph of a device with a single wrap around gate **(a)**, two wrap around gates **(b)** and a device with twelve wrap around gates (c). Micrographs of split-gate type devices with a single pair of split-gates **(d)**, three pairs of split-gates **(e)** and eight pairs of split-gates **(f)**. A cross-section transmission electron microscope (TEM) micrograph perpendicular to the nanowire **(g)** and along the nanowire **(h)**.

1.3.3 FDSOI transistors for silicon spin qubits - Moore's law 2.0

The economic potential of universal quantum computers [Coo22] motivated large industrial players in the semiconductor industry to enter the race for building the first economically viable universal quantum computer[Boh22; Moh21; Vin16; Zwe22]. In terms of technology, this is a great paradigm shift in the business of computing, not pursuing Moore's law to build computer chips with more and faster transistors, but to take a step back and use a different kind of computing logic (quantum algorithms) to be more efficient with less. Even though a quantum computer is considered better than a classical computer to solve some problems, a powerful universal quantum computer will probably still require millions of qubits [Fow12; Met13; Wec14][10]. This is why the semiconductor industry sees a competitive edge in pursuing this R&D effort. At the day of writing, no large scale quantum device based on semiconductor quantum dots exists. The challenge the community is facing, is to find the right architecture and fabrication recipe for a scalable high fidelity qubit unit cell. We will discuss in section **7.2** how such a unit cell could look like and how a large scale quantum processor could be build from that. The large scale fabrication techniques used by semiconductor companies are not compatible with academic clean room facilities. The latter are designed for maximal flexibility at the cost of specificity. The devices presented in this thesis were therefore made by an industrial partner, namely the CEA Leti, using a state-of-the-art industrial 300 mm Si process.
The idea that lead to the device architecture was to build a device that resembles as much as possible a classical transistor as it is fabricated for classical electronics. Such a design would make it likely that one can harness the reproducibility and scalability of modern CMOS technology that is second to none. The CMOS technology used for the devices *fully depleted silicon-on-insulator* (FDSOI) Fin-*field-effect transistors* (FinFETs). For these devices, one uses a silicon wafer as a base. The silicon is covered with a thin layer of buried silicon oxide (BOX), acting as an insulator. A thin film of silicon is deposited on the BOX. After, a silicon nanowire is patterned by etching the Si on the BOX. The nanowire connects the reservoirs source (S) and drain (D), that are grown afterwards. The reservoirs can be either p- (holes) or n-doped (electrons). The devices made by CEA-LETI can be grouped in two different gate architectures. The so-called pump devices have a chain of wrap around gates. False-color scanning electron microscope (SEM) micrographs are depicted in figure **1.3(a)**, **(b)** and **(c)** with one, two and twelve gates respectively. The gates are highlighted in green, spacers blue and the source/drain reservoirs in violet. The second device type are split-gate devices which gates are split in the center of the nanowire forming gate pairs that wrap just around one side of the nanowire. This results in two symmetric gate chains along the nanowire, and we label the i-th gate either Ti or Bi for top or bottom respectively. False-color scanning electron microscope (SEM) micrographs

9 Complementary Metal-oxide-semiconductor (CMOS) is actually better known for state-of-the-art technology, but the manufacturing process is the same and as we don't use holes and electrons in the same device, calling these structures MOS is more accurate.

10 This is not to say that a quantum computer with less qubits is useless, but it would not be able to use quantum algorithms to outperform classical computers in all tasks where the quantum algorithm is in principle better than the classical one.

of split-gate devices are depicted in figure **1.3(d)**, **(e)** and **(f)** with one, three and eight pairs of split-gates respectively. A cross-section perpendicular to the nanowire is depicted in figure **1.3(g)** showing the nanowire on the BOX with gates on the side, which are separated from the nanowire by an oxide. A cross-section of a single gate device along the nanowire is depicted in figure **1.3(h)**. The exact gate stack as well as fabrication process are described in the experimental section **3.2**. The electrical potential of the gates traps the electrons in the corners of the nanowire (see section 5.2) and the sharp potential allows to form quantum dots. Thanks to this architecture less gates are needed to form quantum dots compared to planar MOS architectures. Using this architecture, the first spin qubit in an industrially fabricated device was demonstrated [Mau16]. After, high fidelity spin readout was demonstrated using this platform [Urd19] and recently enhanced spin coherence could be measured by using isotopically enriched ^{28}Si [Pio22].

1.3.4 Spin readout in quantum dots

With the demonstration of high fidelity quantum gates in three different spin qubit platforms [Mil22; Noi22; Xue22], high fidelity spin qubits are no longer an exception. In case that this high fidelity can be achieved in larger spin qubit arrays, it would be a big step towards an error-correction capable quantum processor. Additional to high fidelity gates, a high fidelity qubit readout is indispensable [Fow12].
Spin qubit readout is typically achieved through a spin-to-charge conversion and a subsequent charge measurement using a sensitive electrometer like a single electron transistor (SET) or quantum point contact (QPC). Examples of the integration of these charge sensors in quantum dot devices can be seen in figures **1.4(a)** and **(b)**. Figure **1.5(c)** illustrates this two step readout process and highlights the possible path that can result in the final binary signal labeled $|1\rangle$ and $|0\rangle$. The scheme shows that the fidelity of spin qubit

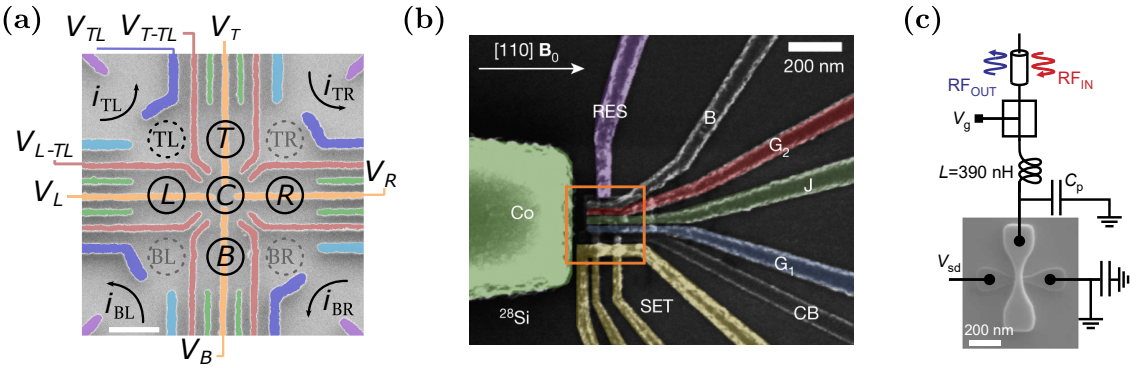

Figure 1.4: Device examples, each using a different charge sensor used for quantum dot charge sensing. **(a)** depicts a device that uses four quantum point contacts located in the four corners. The sensing currents are labeled i_{TL}, i_{TR}, i_{BL}, and i_{BR}. The device presented in **(b)** uses a single electron transistor (SET) highlighted in yellow. **(c)** A device using gate-based rf-reflectometry. The reflectometry setup is connected to a gate that is used to accumulate quantum dots in the device. The figures are reprints from [Mor20], [Yan20], and [GZ15] respectively.

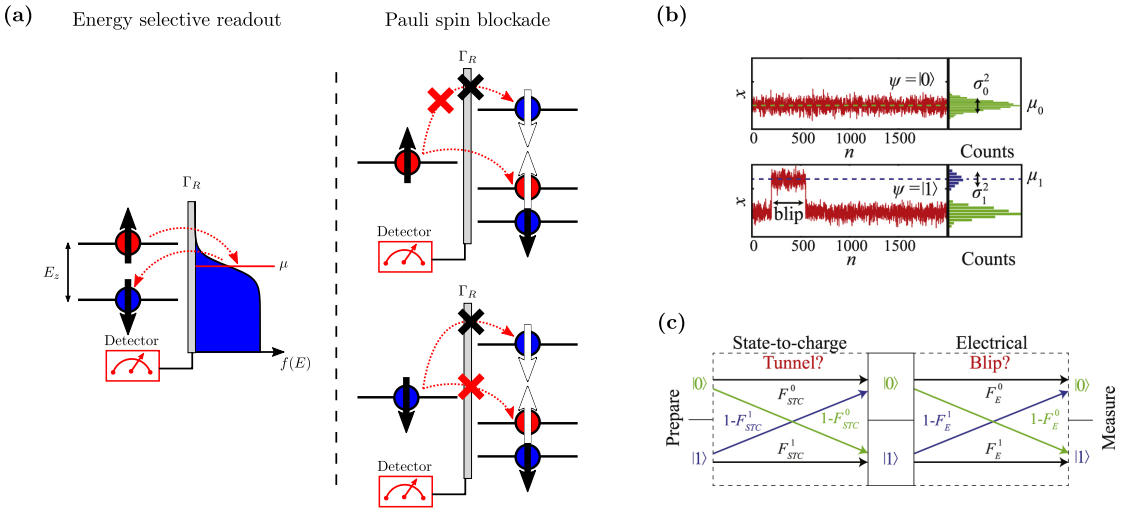

Figure 1.5: Single-shot spin readout techniques. **(a)** Schematic of energy selective readout (left) and Pauli spin blockade readout (right). For the energy selective readout the two spin states ↑ and ↓ are energetically separated by the Zeeman energy E_z and the electrochemical potential μ of the reservoir nearby is aligned in between the two qubit levels such that an electron in the higher energy state can tunnel from the QD to the reservoir. A dectector senses the charge state of the QD. The Pauli spin blockade allows tunneling of a spin in the lowest energy level if the spin state allows forming a singlet state with the spin which is already occupying the second quantum dot. The higher energy levels are energetically inaccessible (black cross) and if no singlet state can be formed tunneling is blocked by Pauli spin blockade (red cross). **(b)** Examples for two different current measurements. The upper (lower) panel shows a signal trace without (with) a tunneling event. When an electron tunnels out of the QD, the signal strength changes until after some time an electron tunnels back in the QD and the signal strength returns to the former level. **(c)** depicts the possible path of the spin measurement that can result in the two measurement outcomes $|1\rangle$ and $|0\rangle$. The first step is State-to-charge (we use spin-to-charge) where the state information is transformed into charge information. The second step is the electrical readout where the charge information is transformed into electrical information. Adapted from [Kei19].

readout depends on the fidelity of the spin-to-charge conversion and the signal-to-noise ratio (SNR) of the charge sensor [Kei19]. We will discuss the spin-to-charge conversion mechanisms in detail in section **2.3**. The first single-shot spin readout was done by Elzerman et al. [Elz04], establishing energy selective spin readout as it is depicted in figure **1.5(a)** and **(b)**. Later, tunnel selective readout showed to be an alternative for single shot readout [Han05]. Both of these readouts use a reservoir and are destructive, meaning that the quantum information is lost after the readout. The first single shot readout in a silicon device used energy selective readout [Mor10]. Even though many devices today still use such a destructive readout [Xue22; Yon17], the readout fidelity does not reach $> 99\,\%$.
In contrast, Pauli spin blockade (PSB), depicted in figure **1.5(a)**, achieved high fidelity readout in different spin qubit architectures[Bor21; Bro17; Zhe19]. In contrast to the other spin-to-charge conversion techniques, PSB does not use a reservoir as a reference, but another electron spin, hosted in another QD [Ono02]. As PSB requires a two-spin

system, it is the natural readout choice for singlet-triplet systems [Mau12; Pet05a]. However, it can also be used to readout the state of a single spin, using the second spin only as an ancillar reference spin[Fog18]. Additionally, for non-single shot measurements, the rectifying current due to PSB in a double quantum dot system is often used to demonstrate spin control [Cam22; Mau16]. Apart from high fidelity readout, Pauli spin blockade is relatively temperature robust thanks to the discrete energy levels of the QDs and all high temperature operation of spin qubits was demonstrated using PSB for spin-to-charge conversion [Cam22; Yan19]. Using architectures with multiple QDs allows as well to perform quantum non-demolition measurements [Nak19; Xue20; Yon20]. A back-action free measurement that allows to conserve the qubit information facilitates the implementation of error-correction protocols [Fow12; Nak19]. Additionally, non-demolition measurements allow to increase the fidelity with repeated measurements that might me required in large arrays where a high SNR can not be guaranteed [Xue20].
The most popular charge sensors for spin qubit devices are single electron transistors (SETs) or quantum point contacts (QPCs) (see figure **1.4(a)** and **(b)**). These highly sensitive devices can be operated in DC- and AC-mode, while the latter one achieved the highest charge sensitivities of $\sim 1\ \mu e/\sqrt{\text{Hz}}$ [Aas01; Bre06; Mas10]. While these charge sensors require at least three electrodes, the still relatively small size of quantum dot arrays allowed to integrate these in the device design. Even in the largest quantum dot arrays that exist today, such sensors are located at the edges and are used for charge sensing [Bor22; Mor20]. However, these devices showed that the charge sensitivity to the inner QDs of the arrays is very low and foreshadowes that either spin shuttling or local sensors will be required. A promising technique for local charge sensing with a minimal footprint is gate-based charge sensing [GZ15], depicted in figure **1.4(c)**. Gate-reflectometry uses a single gate electrode, such that it minimizes the footprint of the sensor on the device level. Moreover, gate-based dispersive readout does not require a reservoir and therefore, would be easier to integrate in large scale architectures. Achieving a high SNR using gate-based dispersive readout has so far only been achieved by operating at GHz frequencies using high-Q superconducting cavities [Bor21; Zhe19]. For devices that are not integrated in a superconducting cavity, standard SMD inductors or on-chip inductors can be used. The readout signal with these inductors is too small to be used for high fidelity readout [Pak18; Wes19] and instead of dispersive readout, the rf-probed QD can be used as a local charge sensor[Urd19].
In this thesis we have tried to explore the problem of measuing spin states in foundry-fabricated devices where we have tried to tackle the above mentioned challenges. In the next chapter we give an overview of the physics of semiconductor quantum dots. Next, we present our experimental setup. After, chapter **4** gives an in-depth discussion of rf-reflectometry. In chapter **5** we present charge sensing in a foundry-fabricated device and in chapter **6** we discuss our spin sensing results. We conclude with an outlook for the future of QDs for quantum computing in chapter **7**.

2 Theoretical background

> One shouldnt work on
> semiconductors, that is a filthy mess;
> who knows whether any
> semiconductors exist.
>
> Wolfgang Pauli

2.1 Physics of semiconductor quantum dots

The research of this thesis focused on the physics of semiconductor quantum dots (QDs). These systems experienced an increased interest from the research community of mesoscopic systems in the last few decades thanks to their versatility as a test bed for solid state quantum systems. While there is a vast range of different uses of quantum dot systems e.g. in photonics [Mic00], the work presented here used QDs as hosts for single electrons. Moreover, in contrast to many other quantum dot systems, the presented quantum dots are no self-assembled quantum dots, resulting from lattice mismatch and the formation of islands[Ter96], but by electrical confinement using metallic gates. In the following, we want to give an overview of the most important properties of these quantum dots which will enable us to interpret the experiments that were performed during this thesis.

2.1.1 Gate defined semiconductor quantum dots - Artificial atoms in semiconductors

Semiconductor quantum dots (QDs) are potential traps of the scale of tens of nanometers in a semiconductor host material. The spatial confinement in the order of the de Broglie wavelength yields discretization of the eigenenergies of electron charge states in such systems. Connecting quantum dots to an electron reservoir through tunnel barriers allows exchange of electrons between reservoir and quantum dot. The electrostatic potential of quantum dots is controlled via metallic electrodes. By changing the potential of these electrodes with respect to the reservoir electrochemical potential, one can control the charge state of the QDs. Historically, the preferred material for the realization of semiconductor quantum dots was a heterostructure of GaAs-$Al_xGa_{1-x}As$[1]. These heterostructures can be grown in a way that the resulting band structure has a two-dimensional electron gas (2DEG) at an interface. This 2DEG can be further confined in the xy-plane by metal electrodes on top of the substrate. However, even though the material is well studied and

1 x denotes the relative amount of Al in the $Al_xGa_{1-x}As$

is still used as a test bed for quantum dot experiments, the properties are not favorable for the realization of spin qubits, compared to host materials like silicon.
Nowadays, more and more work is done using silicon as the host material. Silicon has a natural abundance of 98 % of ^{28}Si which has nuclear spin 0. As a result, Si QDs experience a very small hyperfine interaction and hence, allows longer coherence times than e.g. GaAs-$Al_xGa_{1-x}As$[Zwa13]. Additionally, silicon can be isotopically enriched to 99.999 % ^{28}Si [Abr17], yielding negligible hyperfine interaction. Another important advantage is the compatibility with industrial CMOS fabrication techniques, making silicon the most scalable host material. While still much work is done with academically fabricated devices, we will focus here on devices which were fabricated by an industrial partner in a 300 mm silicon process. We will present the devices in detail in section **1.3.3**.
Before diving into the device specific properties, we will discuss the physics of semiconductor quantum dots that apply to all existing platforms.

2.1.2 Quantum dot states - A particle in a box problem

We will start our discussion of semiconductor quantum dots with a simple model every physics students knows, the particle in a box problem. Semiconductor quantum dots can be considered as charge islands of nanometer scale where the size is in the order of the de Broglie wavelength. The charge island is occupied with N electrons and thus has the charge $Q = eN$. The electrostatic energy can then be written as

$$E_{\mathrm{C}} = \frac{Q^2}{C} = \frac{e^2N^2}{C}, \tag{2.1}$$

where we have introduced the quantum dot capacitance C. We will see that it is useful to describe QDs using classical capacitances in the following.
Besides the purely classical electrostatic energy that arises from the repulsion of charges, there is also a quantum effect that contributes to the energy spectrum of QDs. We know from the "particle in a box system" that in such a system the density of states becomes discrete for a 3D confinement and this is exactly what can be found experimentally in QDs [Ash96; Mac93]. The quantization of states results in an additional energy that must be paid when charge carriers are loaded in the QD. In other words, not all electrons can occupy the ground state, but every energy level of the quantum dot can only be occupied by two electrons (spin degeneracy). The additional energy cost one has to pay to put an electron in the next higher energy level can be estimated as

$$\Delta E \approx \frac{h^2}{m_{\mathrm{eff}}L^2}, \tag{2.2}$$

where m_{eff} is the effective electron mass and L is the size of the confinement potential[1][Zwa13]. A simple model that builds on these two energies is the constant interaction

1 This assumes a harmonic potential and a spherical symmetry of the quantum dot, which is usually not the case. It is therefor just an estimate for the order of magnitude of the energy spacing.

model.

2.1.3 The constant interaction model

Treating a system of gate defined quantum dots as an electronic circuit is often useful for conceiving an experiment. To make an estimation of some properties of a quantum dot system, one often uses the so-called *constant interaction model*. The model assumes that we can model the electrostatics of the electrodes and a quantum dot by a single constant capacitance C_1. For a simple quantum dot connected to two reservoirs (source and drain) and controlled by one gate (G), the capacitance is $C_1 = C_\mathrm{S} + C_\mathrm{D} + C_\mathrm{G}$, where C_i with $i \in \{S,D,G\}$ is the capacitance between dot and source, drain, and gate respectively. A cartoon of such a circuit is depicted in figure **2.1(a)**. With this capacitance, we can then calculate the charge on the quantum dot as

$$Q = \sum_\mathrm{i} C_\mathrm{i}(V_\mathrm{QD} - V_\mathrm{i}) = C_\mathrm{S}(V_\mathrm{QD} - V_\mathrm{S}) + C_\mathrm{D}(V_\mathrm{QD} - V_\mathrm{D}) + C_\mathrm{G}(V_\mathrm{QD} - V_\mathrm{G}), \tag{2.3}$$

where V_i with $i \in \{QD,S,D,G\}$ is the potential of the quantum dot, source, drain, and gate respectively. The energy of a quantum dot occupied by N electrons is then given by

$$U(N) = \frac{[-|e|(N - N_0) + \sum_\mathrm{i} C_\mathrm{i}V_\mathrm{i}]^2}{2C} + \sum_{\mathrm{n}=1}^{N} E_\mathrm{n}, \tag{2.4}$$

where N_0 is the equilibrium charging number which compensates for background charges, $C = \sum_\mathrm{i} C_\mathrm{i}$ is the total capacitance and E_n is the energy of the single-particle energy level which depends on the specificity of the QD potential. A sketch of the QD energy as a function of gate voltage for different charge states is depicted in figure **2.1(b)**. The plot shows the clear minimal energy for a specific charge state at a given gate voltage. The first term in equation 2.4 accounts for the electrostatics between the different elements of the circuit (e.g. reservoir-QD, QD-gate, QD-QD). The second term describes the discrete single-particle energy levels of a particular quantum dot, assuming these are unaffected by any change of the control voltages. Even though the single-particle energy levels as well as the capacitive coupling are not constant in reality, the error made by using these assumptions is often negligible in a small voltage range. Experimental results proved the usefulness of the model to explain the charging phenomena of semiconductor quantum dots[Jeh06]. The electrochemical potential $\mu(N)$ of the QD is given by the potential between two subsequent charging states. We can therefore write

$$\mu(N) \equiv U(N) - U(N-1) = (N - N_0 - \frac{1}{2})E_\mathrm{C} - \frac{E_\mathrm{C}}{|e|}(\sum_\mathrm{i} C_\mathrm{i}V_\mathrm{i}) + E_\mathrm{N}, \tag{2.5}$$

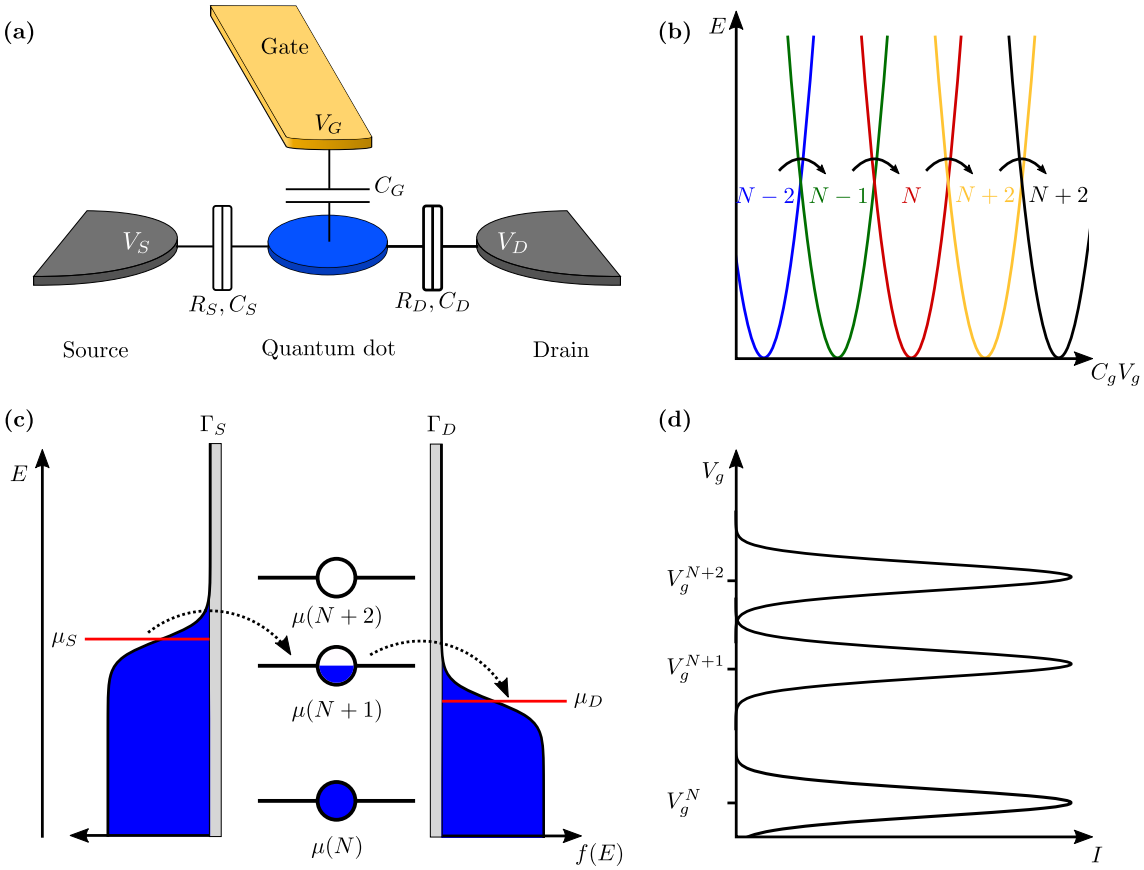

Figure 2.1: **(a)** Model of a single quantum dot connected to source and drain reservoir through tunnel junctions. **(b)** Electrostatic energy of different charging states of the quantum dot as a function of gate voltage V_g. **(c)** Schematic of tunneling through a quantum dot with discrete energy levels and a bias between the two electrochemical potentials of the reservoirs. **(d)** Coulomb blockade oscillations as a function of gate voltage V_g at small bias, resulting in single energy level tunneling. Adapted from [Wie02].

where $E_C = e^2/C$ is the charging energy. One often writes the electrostatic term as

$$\frac{E_C}{|e|}\left(\sum_i C_i V_i\right) = |e| \sum_i \alpha_i V_i \tag{2.6}$$

$$\alpha_i = \frac{C_i}{C}, \tag{2.7}$$

where α is the gate lever arm, converting the gate potential to the electrochemical potential of the QD. Using the definition in equation 2.5, we can further define the energy necessary to add an additional electron, the so-called addition energy,

$$E_{add}(N) = \mu(N+1) - \mu(N) = E_C + \Delta E, \tag{2.8}$$

where $\Delta E = E_N - E_{N-1}$ denotes the energy spacing between the energy levels of the quantum dot. For every second electron, the energy spacing ΔE is zero due to the spin degeneracy of each orbital. However, a magnetic field can lift the spin degeneracy and the two opposite spin states for the same orbital are separated by the Zeeman energy $E_z = g\mu_B B_z$. For quantum dots with significant orbital spacing, this yields to an even-odd pattern in the energy levels. Moreover, the addition energy can be used to determine the energy level physics, which is of particular interest for silicon quantum dots as their energy levels can be either similar to atomic orbitals or originating from valley states[Leo20]. Orbital states resemble atomic orbitals (for instance s- or p- orbitals). Valley states which are only seen in host materials with a conduction band minimum that is not located at the Γ point, such as Si, fill the valleys before occupying the next orbital state. We will discuss this feature in the next section.

2.1.4 Orbital- and valley-states in silicon quantum dots

The silicon lattice has diamond crystal structure. As a result, silicon is an indirect semiconductor with the minimum of the conduction band close to the X-point (see figure **2.2(a)**). This yields to a total of six degenerate conduction band minima, so-called valleys, highlighted in the inset in figure **2.2(a)** that shows the Brillouin zone with the 6 valleys. These valleys give distinct properties to Si that are not observed in materials like GaAs with a direct band gap. The valley degeneracy is typically not observed in experiments as the strong z-confinement lifts the degeneracy between k_x, k_y, and k_z valleys, illustrated in figure **2.2(b)**. The lowest valleys are the k_z valleys, split-off from the

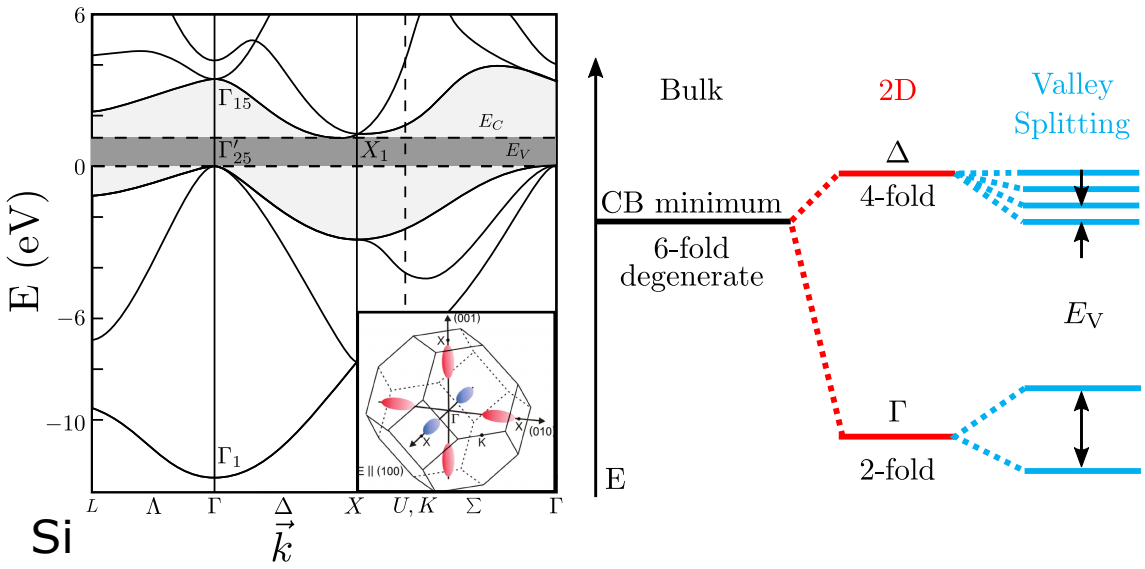

(a) Silicon bandstructure **(b)** Valley splitting

Figure 2.2: Silicon band structure with the first Brillouin zone as an inset. The ellipsoids in the first Brillouin zone indicate the valley position in reciprocal space. **(b)** Valley splitting due to quantum dot asymmetry and local strain. Adapted from [Che74; Isb12; Zwa13].

other valleys by a few µeV to a few meV. The sharpness of the electrical potential at the Si interface results in a lifting of the degeneracy between the $+k_z$ and $-k_z$ valleys. The valley splitting sensitivity to the confinement potential results in tunability of the valley splitting by the gate voltage applied to the quantum dot [Bou18; Ibb18; Sar09]. In experiments this tunability is rather difficult to exploit as the gate potential is mainly used to control the charge state of the quantum dot. The valleys offer another degree of freedom and thus play a role similar to orbital levels of the quantum dots. In the case that the valley splitting is much smaller (larger) than the orbital splitting ($E_V \ll (\gg) E_O$), we can simply replace the orbital(valley) energy in the addition energy ΔE with the valley (orbital) energy. If orbital and valley energy spacings become comparable, they hybridize to valley-orbital states[Fri10]. We will discuss the valley splitting in our devices when it comes to lifting of spin blockade in section **6.2.4**.
Compared to GaAs/AlGaAs quantum dots, silicon quantum dots are much smaller ($\sim$ 10 nm for Si and $\sim$ 100 nm for GaAs/AlGaAs). This size difference originates from the difference in effective mass for Si and GaAs/AlGaAs. The effective mass for GaAs/AlGaAs is $m^*_{\mathrm{GaAs}} = 0.067 m_0$ and thus much smaller than for Si $m^*_{\mathrm{l}} = 0.98 m_0$ and $m^*_{\mathrm{t}} = 0.19 m_0$ [Had03; Ihn10]. Hence, we see from $\Delta E = h^2/m^* L^2$ that a Si quantum dot needs to be smaller than a GaAs quantum dot to achieve the same level spacing.

2.1.5 Electronic transport through quantum dots

While we have already seen in **2.1.3** how to describe the electrostatic coupling between quantum dots, we want to introduce here the concepts for electron exchange between quantum dots or quantum dots and reservoirs. We will describe the coupling between systems as tunneling capacitances which are electrically equivalent to a capacitor with a resistor in parallel. The resistance must be large to allow storing charges in a quantum dot. It turns out that the lower limit for the tunneling resistance is the resistance quantum h/e^2 [Ihn10]. If the resistance is smaller, the charge state is fluctuating and control of the charge state down to the single electron level is not possible. To describe what happens when electrons are exchanged through tunnel barriers, we will start with a quick overview of the Landauer-Büttiker formalism. After, we will discuss resonant and non-resonant tunneling.

Coulomb blockade oscillations

In this section we will discuss the physics of transport through quantum dots. The physics of quantum transport is very rich and out of the scope of this thesis, and we will therefore restrict this section to the results that are relevant for us. For a more complete treatment of this topic we recomment [Bee91; Hou92; Kou97].
A cartoon of transport through a single quantum dot is depicted in **2.1(c)**. The cartoon depicts transport through a single energy level at low temperature compared to the charging energy. Moving the energy levels of the QD through the bias window results in Coulomb blockade oscillations of the current as they are illustrated in the plot in **2.1(d)**. When no energy level is in the bias window, the current goes to zero, whereas when an

energy level passes through the bias window, the current rises rapidly. We will limit our discussion to the case of classical Coulomb blockade ($\Delta E \ll k_\mathrm{B}T \ll e^2/C$ and quantum Coulomb blockade ($k_\mathrm{B}T \ll \Delta E < e^2/C$), where only one or a few energy levels of the QD contribute to transport, and we can ignore thermal excitations. Assuming that the reservoirs are filled according to the Fermi-Dirac statistic $f(E-\mu) = [1+\exp((E-\mu)/k_\mathrm{B}T)]^{-1}$, the electrostatic energy of the QD is

$$U(N) = \frac{N^2e^2}{2C} - Ne\phi_\mathrm{ext}, \tag{2.9}$$

where ϕ_ext is the potential from compensating charges nearby the quantum dot. These compensating charges can either be intrinsic in the device (e.g. charge traps, ionized donors, etc.) or induced by electrical voltages V_g from nearby gates. We therefore write for a QD, that is controlled by a single gate, $\phi_\mathrm{ext} = \phi_\mathrm{D} + \alpha V_\mathrm{g}$, with α the lever arm of the gate.

Classical Coulomb blockade

For the classical Coulomb blockade, thermal excitation to higher orbitals is possible as $\Delta E \ll k_\mathrm{B}T$ and thus, many energy levels can contribute to the conductance. In this case, the line shape of an individual conductance peak is given by

$$G = G_\infty \frac{\delta/k_\mathrm{B}T}{2\sinh(\delta/k_\mathrm{B}T)} \approx G_\infty \frac{1}{2}\cosh^{-2}\left(\frac{\delta}{2.5k_\mathrm{B}T}\right), \tag{2.10}$$

with $1/G_\infty = 1/G_\mathrm{l} + 1/G_\mathrm{r}$ the Ohmic sum of the two barriers and δ the energetic distance from the center of the peak [Kou97].

Quantum Coulomb blockade

For the quantum Coulomb conductance we want to distinguish two regimes. First, the weak tunnel coupling regime $k_\mathrm{B}T \ll h\Gamma$ and second, the regime of strong tunnel coupling $h\Gamma \gg k_\mathrm{B}T$. While the strong coupling regime is treated using the Landauer-Büttiker formalism, the weak tunnel coupling regime allows to ignore the finite width of the transmission resonances of the tunneling.
In the case of weak tunnel coupling, $h\Gamma \ll k_\mathrm{B}T$, the conductance through a quantum dot is generally given by

$$G = \frac{e^2}{k_\mathrm{B}T}\sum_{\mathrm{p}=1}^{\infty}\sum_{\mathrm{N}=1}^{\infty}\frac{\Gamma_\mathrm{p}^l\Gamma_\mathrm{p}^r}{\Gamma_\mathrm{p}^l+\Gamma_\mathrm{p}^r}P_\mathrm{eq}(N)F_\mathrm{eq}(E_\mathrm{p}|N)[1-f(E_\mathrm{p}+U(N)-U(N-1)-\mu)], \tag{2.11}$$

where $\Gamma_\mathrm{p}^{l,(r)}$ is the tunneling rate between left (right) reservoir and quantum dot, $P_\mathrm{eq}(N)$ is the probability that N electrons occupy the quantum dot in equilibrium, $F_\mathrm{eq}(E_\mathrm{p}|N)$ is the free energy of the internal degrees of freedom with respect to the initial energy E_p and N electrons in the quantum dot, that can be approximated by the Fermi-Dirac statistic if

$k_\mathrm{B}T \gg \Delta E$ and the spectrum can be assumed to be continuous. A full derivation of this formula is given in [Bee91]. With our assumptions that $k_\mathrm{B}T \ll \Delta E < e^2/C$, one finds the conductance

$$G = G_\infty \frac{\Delta E}{4k_\mathrm{B}T} \cosh^{-2}\left(\frac{\delta}{2k_\mathrm{B}T}\right). \tag{2.12}$$

For strong coupling, $k_\mathrm{B}T \leq h\Gamma \ll \Delta E$, the conductance can be approximated using the Breit-Wigner formula

$$G_\mathrm{BW} = \frac{2e^2}{h} \frac{(h\Gamma)^2}{(h\Gamma)^2 + \delta^2}. \tag{2.13}$$

We see that in the case of strong coupling the conductance is not temperature dependent anymore and the line shape follows a Lorentzian.

Cotunneling

While we discussed so far only first order tunneling effect, we want to briefly outline a second order process that can cause unintended effects in quantum dot systems. The so-called cotunneling process involves the tunneling through an excited (or occupied) state that would classically be energetically forbidden. While the electron requires more energy to tunnel in the excited state (out of the occupied), total energy is conserved as the electron gives back this excess energy when the second tunneling process takes place where the electron tunnels to a state of lower energy. Cotunneling occurs if the tunnel coupling is sufficiently strong that second-order effects become non-negligible to describe the full tunneling dynamics. For us, this is of particular importance for arrays of quantum dots, where some quantum dots are very weakly coupled to the reservoir, but the tunnel coupling

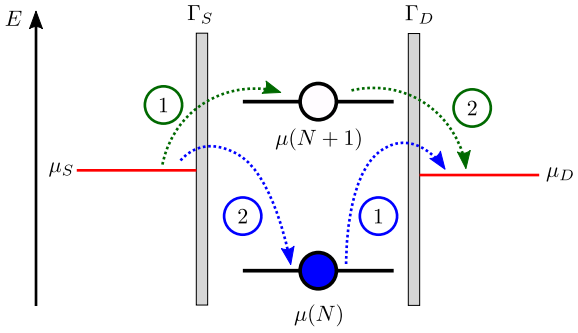

Figure 2.3: Scheme of two different cotunneling processes of a single quantum dot system coupled to source and drain reservoirs. In the first process (blue), a quantum dot state below μ is emptied first towards the drain reservoir and subsequently refilled by an electron from the source reservoir. In the second process (green), an electron tunnels from the source reservoir to an excited state above μ of the source reservoir. Next, the electron tunnels from the excited state to the drain reservoir, giving back the excess energy that was required to tunnel to the excited state. Adapted from [Ihn10].

in a chain of quantum dots is strong. In such a configuration cotunneling between QDs is more effective than direct tunneling between QD and reservoir. A cartoon of two different cotunneling processes is depicted in figure **2.3**. The figure shows two processes of electron cotunneling through a single dot. It involves an energy level that would be filled (blue arrows) in thermal equilibrium or an excited energy level that would be empty (green arrows). In the first case, the electron tunnels out of the QD into the drain reservoir, followed by repopulation of the QD reservoir with an electron from the source reservoir. In the second case, an electron tunnels from the source reservoir to the drain reservoir through the excited QD reservoir. The two mechanisms depicted result in the cotunneling rate

$$t_{\tau \mathrm{l}} = \frac{t^*_{\mathrm{ld}} t_{\tau \mathrm{d}}}{\varepsilon_\tau - \mu_{\mathrm{N}}} + \frac{t^*_{\mathrm{ld}'} t_{\tau \mathrm{d}'}}{\mu_{\mathrm{N+1}} - \varepsilon_{\mathrm{l}}}, \tag{2.14}$$

where the subscript l labels a state in the source reservoir, τ a state in the drain reservoir and d, d' the states referring to μ_{N}, $\mu_{\mathrm{N+1}}$ respectively.

2.1.6 Coupled quantum dots

The model we used so far consisted of a single quantum dot, tunnel coupled to reservoirs. Next, we want to extend our model to the physics of a double quantum dot system. Two things will obviously change. First, both sides of the system now have a discrete energy spectrum. Second, the electrostatics of one quantum dot will affect the other quantum dot. We will describe the tunnel coupling between the two quantum dots with the interdot capacitance C_{m}. In this discussion, we will assume that the quantum dots are in series, as depicted in figure **2.4 (a)**, leaving both quantum dots tunnel coupled to a reservoir. We will see that while the single quantum dot resembled an atom, a double quantum dot resembles a two-atomic molecule where the coupling between the two can range from weak coupling (ion like) to strong coupling (covalent like). Using the constant interaction model, we can describe the electrochemical potential for QD 1 as

$$\begin{aligned}\mu_1(N_1,N_2) &= U(N_1,N_2) - U(N_1-1,N_2) \\ &= (N_1 - \frac{1}{2})E_{\mathrm{C},1} + N_2 E_{\mathrm{C_m}} - \frac{E_{\mathrm{C},1}}{|e|}(C_{\mathrm{S}}V_{\mathrm{S}} + C_{\mathrm{G},11}V_{\mathrm{G},1} + C_{\mathrm{G},12}V_{\mathrm{G},2}) \\ &\quad + \frac{E_{\mathrm{C_m}}}{|e|}(C_{\mathrm{D}}V_{\mathrm{D}} + C_{\mathrm{G},22}V_{\mathrm{G},2} + C_{\mathrm{G},21}V_{\mathrm{G},1}),\end{aligned} \tag{2.15}$$

where $C_{\mathrm{G,ij}}$ describes the capacitance between QD i and gate j, and C_{S} (C_{D}) is the capacitance between QD 1 (2) and the source (drain) reservoir [Han07]. Interchanging the QD index 1 with 2, gives the electrochemical potential of QD 2. The effect of the capacitance C_{m} is depicted in the tilting of the transition lines in figure **2.4(d)**. Charge transition crossings split up into two so-called triple points, where the distance depends on the capacitive coupling C_{m} between the QDs. As can be seen in figure **2.4(e)**, between the two triple points is a transition where electrons are only exchanged between the two quantum dots, without any exchange with a reservoir. These transitions are called interdot

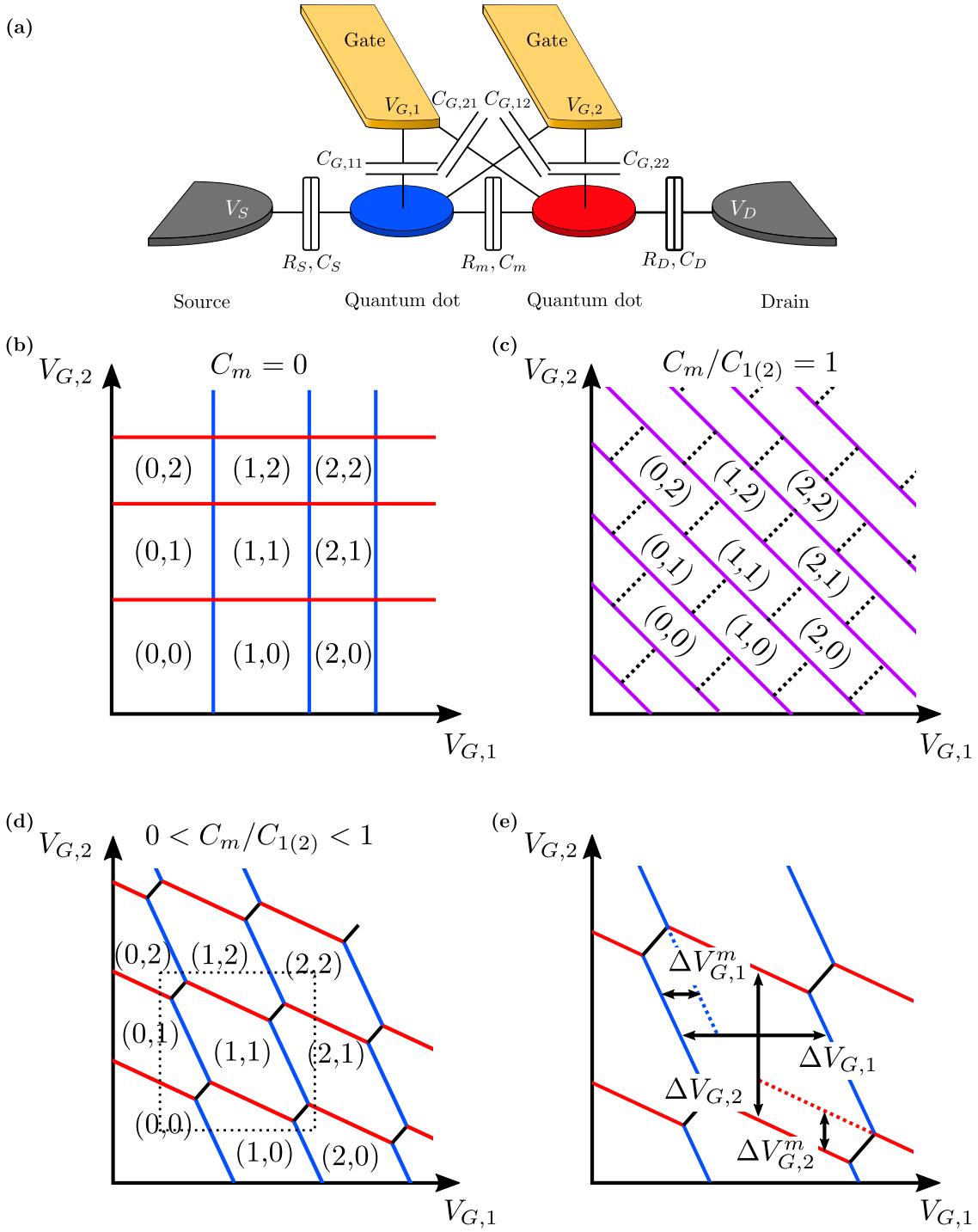

Figure 2.4: Schematic of a linear double quantum dot system **(a)** and stability diagrams of different coupling regimes **(b)-(e)**. The stability diagram **(b)** is representative for a completely decoupled quantum dot, whereas **(c)** is representative for a double quantum dot where the quantum dots form a single large quantum dot.In the intermediate regime depicted in figure **(d)**, the stability diagram shows a honeycomb pattern. **(e)** shows a single cell of the honeycomb pattern as in the dotted square in **(d)**. The different voltages indicated in **(e)** are defined in the main text. Adapted from [Wie02].

transitions. For sufficiently strong tunnel coupling, delocalization of the electrons results in an effective occupation of both quantum dots at the same time. In this case we do not consider the system a double quantum dot anymore, but rather one big single quantum dot. The intermediate regime with two coupled quantum dots is of particular interest for us as it allows to study the dynamics between spins. We can further understand the triple points using figure **2.4 (e)**. The hexagon shape results from the capacitances between gate and quantum dot and between quantum dots. The voltage spacings in figure **2.4 (e)** are given by

$$\Delta V_{\mathrm{G},1} = \frac{|e|}{C_{\mathrm{G},1}}(1 + \frac{\Delta E}{E_{\mathrm{C}1}}) \tag{2.16}$$

$$\Delta V_{\mathrm{G},2} = \frac{|e|}{C_{\mathrm{G},2}}(1 + \frac{\Delta E}{E_{\mathrm{C}2}}) \tag{2.17}$$

$$\Delta V^m_{\mathrm{G},1} = \frac{|e|C_{\mathrm{m}}}{C_{\mathrm{G},1}C_2} = \Delta V_{\mathrm{G},1}\frac{C_{\mathrm{m}}}{C_2}(1 + \frac{\Delta E}{E_{\mathrm{Cm}}}) \tag{2.18}$$

$$\Delta V^m_{\mathrm{G},2} = \frac{|e|C_{\mathrm{m}}}{C_{\mathrm{G},2}C_1} = \Delta V_{\mathrm{G},2}\frac{C_{\mathrm{m}}}{C_1}(1 + \frac{\Delta E}{E_{\mathrm{Cm}}}), \tag{2.19}$$

with $C_{1(2)} = C_{\mathrm{L(R)}} + C_{\mathrm{G},1(2)} + C_{\mathrm{m}}$ and $\Delta E = E_{\mathrm{m}} - E_{\mathrm{n}}$ the energy between two consecutive energy levels which can be zero due to spin degeneracy [Wie02]. The double quantum dot system allows to implement the so-called charge qubit.

2.1.7 Charge qubits in double quantum dots

A qubit implementation that can be implemented without using the spin of an electron is using its location in a double quantum dot (DQD) system. The Hamiltonian describing the system of a single electron in a DQD is given by

$$\hat{H}(t) = \begin{pmatrix} 0 & \Delta \\ \Delta & \varepsilon(t) \end{pmatrix}, \tag{2.20}$$

where Δ is the tunnel coupling energy and $\varepsilon(t)$ is the detuning between the dots that can be controlled through the gates. For $|\varepsilon| \gg \Delta$ the two states of the system are $|0\rangle = |L\rangle = (1|0)$ and $|1\rangle = |R\rangle = (0|1)$, where the first (second) state refers to the state where the electron is located in the left (right) dot. These are the qubit states of the system. To manipulate the qubit system, one can reduce the detuning, resulting in hybridization of the states. At zero detuning, the eigenstates of the Hamiltonian hybridize to

$$|S\rangle = \frac{1}{\sqrt{2}}(|L\rangle + |R\rangle) \tag{2.21}$$

$$|A\rangle = \frac{1}{\sqrt{2}}(|L\rangle - |R\rangle). \tag{2.22}$$

Initializing in $|L\rangle$ and pulsing to the zero detuning position gives

$$|L\rangle = \frac{1}{\sqrt{2}}(|S\rangle + |A\rangle) \tag{2.23}$$

and the tunneling coupling drives oscillation between the two states

$$|\psi(t)\rangle = \cos\frac{\Delta t}{2\hbar}|L\rangle + i\sin\frac{\Delta t}{2\hbar}|R\rangle \tag{2.24}$$

Even though the implementation of such a qubit is relatively straight forward, the coherence time is in the same order of magnitude as the time to operate the qubit ($\sim$ ns) and therefore the fidelity very low[Hay03; Ihn10]. Much more promising qubit implementations use the spin of one or multiple electrons[1].

2.2 Spin states in single and double quantum dots

The spin state of an electron is probably the poster child of a two-level quantum system. The reason is probably that spin is a uniquely quantum property and the math necessary to describe the system is rather simple. While the energy splitting can be controlled by an external magnetic field, the states can be flipped by emitting or absorbing a photon. However, the physics of spins in quantum dots is much richer than the single electron model. For instance, entangling two electrons with each other allows control of the spin states even without a photon. In this section we will first focus on spin states in a single quantum dot and after, extend the discussion to double quantum dot systems.

2.2.1 A single electron spin in a quantum dot

As discussed in section 1.3, single electron spins are one of the most promising quantum systems for quantum information processing. The control of single electrons in quantum dots provides a platform to explore the dynamics of single electron spins. Moreover, spins are less sensitive to undesired perturbations as they interact with magnetic fields rather than electric fields. Even though electric fields can affect spins through spin-orbit coupling, this second order coupling is much weaker than direct coupling and results in long coherence times compared to charge qubits. Control of single spins in quantum dots therefore requires control of the magnetic environment of the spins. The two spin states can be separated using an external magnetic field B_z, giving rise to a Zeeman term

$$E_\mathrm{z} = S_\mathrm{z} g \mu_\mathrm{B} B_\mathrm{z}, \tag{2.25}$$

where $S_\mathrm{z} \in \{-1/2, +1/2\}$ is the spin component along the z-axis of the electron, g the gyromagnetic factor ($\approx +2$ in silicon), and $\mu_\mathrm{B} = \frac{e\hbar}{2m_\mathrm{e}} \approx 58\,\mu\mathrm{eV\,T^{-1}}$ the Bohr magneton.

1 In general one can use the spin of electrons or holes. As we worked with electron devices, we will mostly refer to electron spins.

For silicon spin qubits the spin down state is the ground state and the spin up state is the excited state. This degeneracy lifting results in a change of the addition energy, for $\Delta E_\mathrm{z} < \Delta E = E_\mathrm{N} - E_\mathrm{N\text{-}1}$ the addition energy for subsequent electrons, assuming the system is in its ground state, shifts by $\pm\Delta E_\mathrm{z}$ with + for even to odd and − for odd to even electron charging. The Hamiltonian to describe a single spin is then

$$H = -\left(\frac{e}{m_\mathrm{e}}\right)\boldsymbol{S}\cdot\boldsymbol{B} = -\left(\frac{eB}{m_\mathrm{e}}\right)S_\mathrm{z} = -\left(\frac{eB}{2m_\mathrm{e}}\right)\hbar\sigma_\mathrm{z} = \frac{\hbar\omega_0}{2}\sigma_\mathrm{z}. \tag{2.26}$$

with the Larmor frequency $\omega_0 = g\mu_\mathrm{B}B_\mathrm{z}/\hbar$. Knowing the Hamiltonian, we can come back to the Bloch sphere picture to understand how to use the system as a qubit. The spin direction can be considered as the position on the Bloch sphere, where the spin up state corresponds to the North Pole and the spin down state to the South Pole. We see in the Hamiltonian that there is a σ_z component that allows to rotate around the z-axis with frequency ω_0. However, there are no off-diagonal elements to the Hamiltonian or in other words, there is no σ_x or σ_y component and hence, no rotation between the two states can be performed in this system. We have already seen that we need to transform the Hamiltonian to the Hamiltonian of the Rabi problem (see section 1.1.2). For a single spin, we can transform the Hamiltonian by adding a time-dependent perpendicular magnetic field $B_\mathrm{ac} = B_0(\cos(\omega t)\sigma_\mathrm{x} + \sin(\omega t)\sigma_\mathrm{y})$ that drives Rabi oscillations. The resulting Hamiltonian is then

$$\hat{H} = \frac{\hbar\omega_0}{2}\sigma_\mathrm{z} + \hbar\Omega\cos(\omega t + \phi_0)\sigma_\mathrm{x}, \tag{2.27}$$

where ω is the frequency of the oscillating magnetic field and ϕ_0 is the phase of the drive at $t = 0$. There are indeed different experimental realizations of this Rabi drive ranging from microwave antenna near the QD [Vel15; Yon21; Zha19] to micro-magnets [Kaw16; PL08; Tak16] or intrinsic strong spin-orbit coupling [Hen20; Mau16]. A drawback of microwave or micro-magnets is the required integration of these which can be challenging, especially when building a compact qubit unit cell for large scale qubit arrays. Moreover, driving only one qubit instead of all qubits near the driving force can be challenging when having multiple qubits near the microwave antenna or micro-magnet. To avoid this cross-talk effect, the g-factor of the electron spin can be used to control the resonance frequency and might be a way to tune the qubit in and out of resonance[Vah21]. The g-factor depends on the spin-orbit coupling and varies between dots due to differences in the quantum wave functions. Here again, the electrostatic tuning of quantum dots, enables some control of the g-factor. So far g-factor tuning was mostly performed for hole spins [Lil21; Voi15] or donors[Lau15], showing promising tuning ranges of up to 500 %.

2.2.2 Two-spin systems

A way to avoid the requirements for an external magnetic drive for the spin qubit and to get to a electronically controlled qubit is the use of the singlet-triplet qubit. The singlet-triplet qubit consists of two coupled spins. Typically, one uses two electrons in a double quantum dot (DQD) system to implement such a qubit. We will first discuss the spin

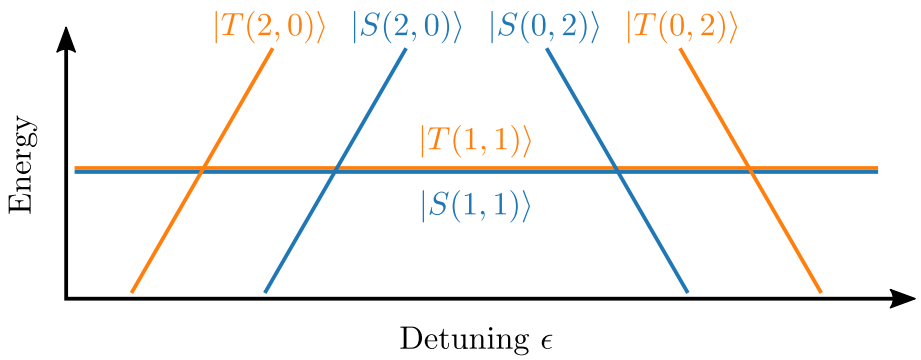

(a) $t_c = 0$, $B_z = 0$

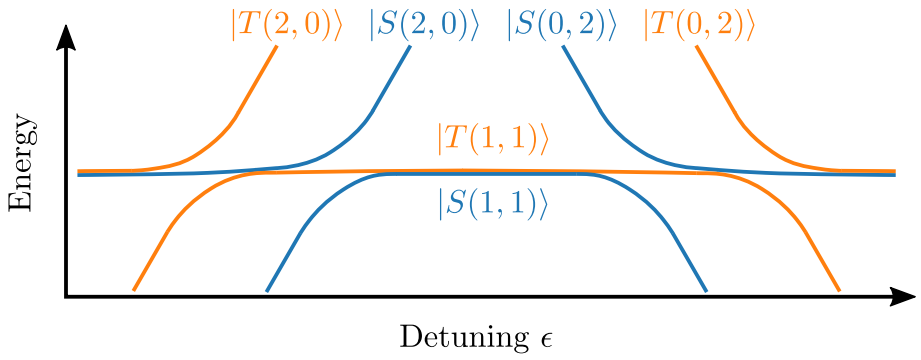

(b) $t_c \neq 0$, $B_z = 0$

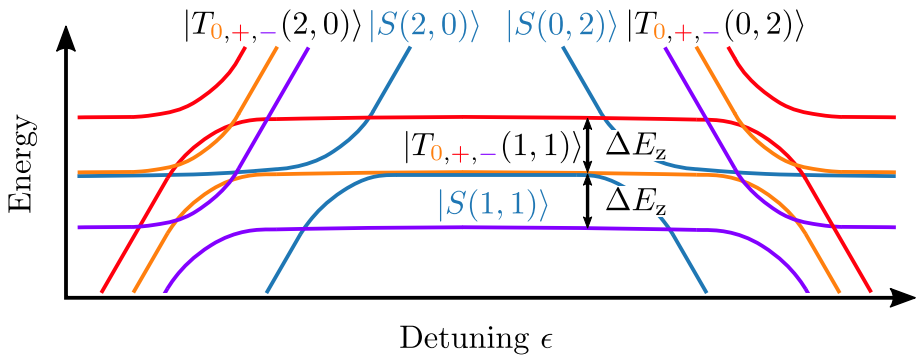

(c) $t_c \neq 0$, $B_z \neq 0$

Figure 2.5: Energy diagram of the singlet and triplet states for different interdot tunneling t_c and magnetic fields B_z. Adapted from [Ber15].

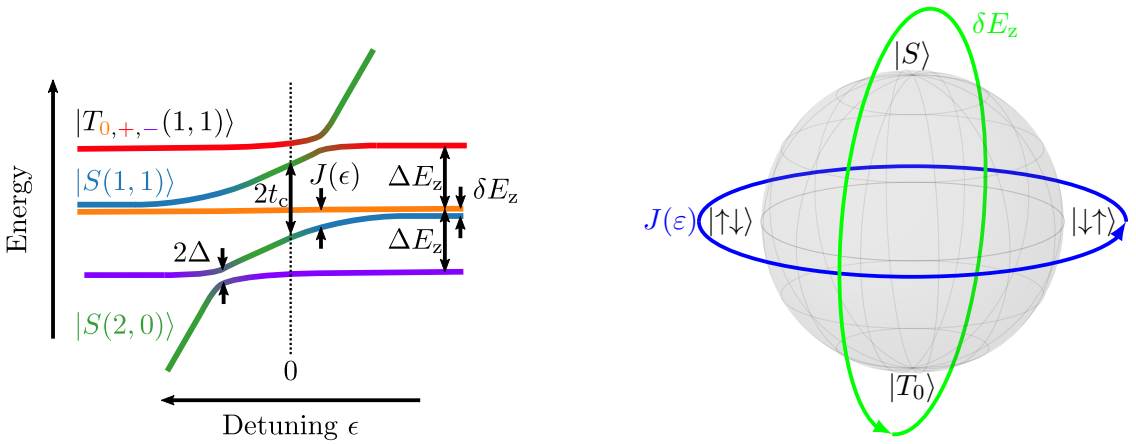

(a) Singlet-triplet energy diagram

(b) Bloch sphere of the singlet-triplet qubit

Figure 2.6: (a) Energy diagram of the singlet and triplet states around the interdot transition. **(b)** Bloch sphere of the singlet-triplet qubit. Adapted from [Fog18].

states of such a two spin system and then go through the implementation of a qubit in such a system.

The singlet-triplet basis of a two-spin system

Charging a single quantum dot with two electrons, the electrons can either have opposite spins and occupy the same orbital or occupy different orbitals (e.g. ground state and first excited state) which allows arbitrary spin configurations. To be more concrete here, as Fermions, the total wave function of an ensemble of electrons must be antisymmetric under permutation. This means that either the orbital wave function is symmetric and the spin wave function antisymmetric or vice versa. For two spins, the four lowest energy states are

$$|S\rangle = |gg\rangle \otimes \frac{1}{\sqrt{2}}(|\uparrow\downarrow\rangle - |\downarrow\uparrow\rangle) \tag{2.28}$$

$$|T_0\rangle = \frac{1}{\sqrt{2}}(|ge\rangle - |eg\rangle) \otimes \frac{1}{\sqrt{2}}(|\uparrow\downarrow\rangle + |\downarrow\uparrow\rangle) \tag{2.29}$$

$$|T_-\rangle = \frac{1}{\sqrt{2}}(|ge\rangle - |eg\rangle) \otimes |\downarrow\downarrow\rangle \tag{2.30}$$

$$|T_+\rangle = \frac{1}{\sqrt{2}}(|ge\rangle - |eg\rangle) \otimes |\uparrow\uparrow\rangle\,, \tag{2.31}$$

where $g(e)$ denotes ground (excited) state. The singlet state $|S\rangle$ has symmetric orbital wave function and total spin $S = 0$. It is always the ground state for $\mathbf{B} = 0$. The three triplet states $|T_-\rangle\,, |T_0\rangle\,,$ and $|T_+\rangle$ have antisymmetric orbital wave function and are spin degenerate for $\mathbf{B} = 0$ with total spin $S = 1$ and $m_s = -1{,}0{,}1$, respectively. We want to mention here that the difference in energy between singlet and triplet state is not simply the difference between ground and excited orbital state. While this is the main

contribution, electrons in the triplet states experience a smaller Coulomb interaction due to the smaller orbital overlap as well as reduced kinetic energy. To understand the latter one, we need to take into account the Heisenberg uncertainty principle. As the location uncertainty Δx of the electrons is greater in the triplet states, the momentum uncertainty Δp of the triplet state is smaller, yielding to a smaller kinetic energy [Rei15]. We will take these effects into account by defining the energy splitting between singlet and triplet states for $\mathbf{B} = 0$ as

$$E_{\mathrm{ST}} \equiv \Delta E_{\mathrm{orb}} - E_{\mathrm{K}}, \tag{2.32}$$

where E_{K} is the sum of Coulomb energy and kinetic energy difference.
The single-particle energies of the different states can then be written as

$$\begin{aligned}
U_{\mathrm{S}} &= E_{\uparrow,0} + E_{\downarrow,0} + E_{\mathrm{C}} \\
&= 2E_{\downarrow,0} + \Delta E_{\mathrm{z}} + E_{\mathrm{C}} && (2.33)\\
U_{\mathrm{T}_-} &= E_{\downarrow,0} + E_{\downarrow,1} - E_{\mathrm{K}} - E_{\mathrm{C}} = 2E_{\downarrow,0} + \Delta E_{\mathrm{orb}} - E_{\mathrm{K}} + E_{\mathrm{C}} \\
&= 2E_{\downarrow,0} + E_{\mathrm{ST}} + E_{\mathrm{C}} && (2.34)\\
U_{\mathrm{T}_0} &= E_{\downarrow,0} + E_{\uparrow,0} - E_{\mathrm{ST}} + E_{\mathrm{C}} = 2E_{\downarrow,0} + \Delta E_{\mathrm{orb}} - E_{\mathrm{K}} + \Delta E_{\mathrm{z}} + E_{\mathrm{C}} \\
&= 2E_{\downarrow,0} + E_{\mathrm{ST}} + E_{\mathrm{C}} + \Delta E_{\mathrm{z}} && (2.35)\\
U_{\mathrm{T}_+} &= 2E_{\uparrow,0} + E_{\mathrm{ST}} + E_{\mathrm{C}} = 2E_{\downarrow,0} + \Delta E_{\mathrm{orb}} - E_{\mathrm{K}} + 2\Delta E_{\mathrm{z}} + E_{\mathrm{C}} \\
&= 2E_{\downarrow,0} + E_{\mathrm{ST}} + 2\Delta E_{\mathrm{z}} + E_{\mathrm{C}}, && (2.36)
\end{aligned}$$

where $E_{\downarrow(\uparrow),0(1)}$ is the orbital energy of spin down (up) state for the ground (excited) orbital, E_{C} is the Coulomb energy and E_{ST} is the energy difference between singlet and triplet state. While the discussion so far dealt with the singlet-triplet states in a single QD, we want to discuss now the particularities of a DQD system that allows us to control the strength of the interaction between the electrons.

A singlet-triplet system in a double quantum dot

The energy diagram for a double quantum dot system with two electrons for detuning ranging from the (2|0) over the (1|1) regime to the (0|2) regime with/without tunnel coupling t_{c} and with/without magnetic field B_{z} is depicted in figure **2.5**. For us, the interdot transitions are of particular interest and an energy diagram for detuning ε around the interdot transition $(2|0) - (1|1)$ is depicted in figure **2.6(a)**. At the interdot transition, the triplet ground states remain (1|1) and the triplet (2|0) states are energetically inaccessible. In contrast, the singlet state hybridizes to $|S_{\mathrm{H}}\rangle = \cos(\theta/2)\,|(1|1)S\rangle + \sin(\theta/2)\,|(2|0)S\rangle$ with $\theta = -\arctan(2t_{\mathrm{c}}/\varepsilon)$, where t_{c} is the tunnel coupling and ε the detuning with respect to the interdot position. For large enough negative detuning (deep in (1|1)) the S and T_0 states become degenerate and the singlet-triplet basis stops being the eigenbasis for the system. Instead, the spins evolve independently according to their local environment [Pet05a]. Close to the interdot transition, the tunnel coupling yields an exchange energy $J(\varepsilon)$ between the S_{H} and T_0 state. Splitting off the T_+ and T_- states by the Zeeman

energy ΔE_z results in an avoided crossing of the hybridized singlet $|S_H\rangle$ and the triplet $|T_-(1|1)\rangle$ ($|T_+(1|1)\rangle$). This avoided crossing is a result of magnetic fields perpendicular to the external magnetic field B_z, spin-orbit coupling and residual nuclear spins. We summarize all these effects in a spin-flip term $\Delta(\theta)$. Important to mention is that in real DQD systems the QDs are not identical which gives rise to different g-factors and possibly different local magnetic field, resulting in a differential Zeeman term $\delta E_z \cos(\theta)$ with $\delta E_z = g_2 \mu_B B_z^{(2)} - g_1 \mu_B B_z^{(1)}$ that separates the $|S(1|1)\rangle$ and $|T_0(1|1)\rangle$ states. In the (1|1) regime, it is this term rather than the different orbital energy between singlet and triplet that separates the two spin states and the eigenstates become $|\uparrow\downarrow\rangle$ and $|\downarrow\uparrow\rangle$ rather than $|S\rangle$ and $|T_0\rangle$. The Hamiltonian of the system at the interdot transition in the basis $\{|T_+\rangle, |T_0\rangle, |T_-\rangle, |S_H\rangle\}$ is [Fog18]

$$\hat{H} = \begin{pmatrix} \Delta E_z - \varepsilon/2 & 0 & 0 & \Delta(\theta) \\ 0 & -\varepsilon/2 & 0 & \delta E_z \cos\theta \\ 0 & 0 & -\Delta E_z - \varepsilon/2 & -\Delta(\theta) \\ \Delta^*(\theta) & \delta E_z \cos\theta & -\Delta^*(\theta) & \varepsilon/2 - J(\varepsilon) \end{pmatrix}. \tag{2.37}$$

Even though we are dealing here with a four level system, we can use the S_H and T_0 states as a subsystem to build a qubit. The sub-system $S_H - T_0$ can be described by the Hamiltonian

$$\hat{H}_{ST} = \begin{pmatrix} -\varepsilon/2 & \delta E_z \cos\theta \\ \delta E_z \cos\theta & \varepsilon/2 - J(\varepsilon) \end{pmatrix}. \tag{2.38}$$

We see that the Hamiltonian has the form of the Rabi problem and the detuning allows us to control the strength of the terms. We can look at this situation as a shift of basis which can be controlled by detuning and corresponds to a rotation of the Bloch sphere. The Bloch sphere of the ST-qubit is depicted in figure **2.6(b)**. While close to the interdot, where the exchange energy $J(\varepsilon)$ is large compared to δE_z, the eigenstates are $|S_H\rangle$ and $|T_0\rangle$. For very negative detuning (deep in (1|1)) $J(\varepsilon)$ becomes negligible, and the new basis states become the two spin states $|\uparrow\downarrow\rangle$ and $|\downarrow\uparrow\rangle$. These states are separated by δE_z. At the interdot transition these states have been on the equator of the Bloch sphere. Thus, the control of the qubit is achieved by detuning ε control between the two regimes, firstly demonstrated by Petta et al. [Pet05a]. This full electronic control of the qubit comes at a cost, as mentioned before, it requires two quantum dots. Additionally, the qubit driving frequency depends on the strength of the exchange energy which is not as easy to control as an external magnetic field. Moreover, detuning is prone to electronic noise and thus the ST-qubit is more easily perturbed by this noise source than the single spin qubit. Last but not least, the T_- and T_+ states can interact with the qubit states and cause state leakage. This state leakage can be understood using the Landau-Zener theory of transfers through avoided level crossings. We want to discuss the main result of this theory in the following.

Landau-Zener transitions

When crossing an anticrossing between for instance the $|T_-\rangle$ and $|S_\mathrm{H}\rangle$ state, state leakage can become non-negligible. It turns out that to avoid leakage when passing this anticrossing we need to change the energy of our state non-adiabatically. The theory that describes the probability of transitioning adiabatically or non-adiabatically is provided by the theory of Landau-Zener (LZ) transitions [She10]. The probability to cross an avoided level crossing without changing the state is given by

$$P_+ = \exp\left(-2\mathrm{Im}\int_0^{t_0}[E_+(t') - E_-(t')]dt'\right) \tag{2.39}$$

$$= \exp\left(-2\pi\frac{\Delta^2}{4\nu}\right), \tag{2.40}$$

where t_0 is the time is takes to pass the anticrossing, $E_+ - E_-$ is the energy separation between the two states $\pm t_0 = \pm i\Delta/\nu$ is the imaginary time of the LZ integral where Δ is the energy separation of the two states and ν the driving velocity. We will see that this theory allows us to measure the avoided crossing Δ of the $S - T_-$ anticrossing.
Now that we have seen that spins offer different ways to realize qubits, we want to discuss the ways how to measure such a small magnetic moment.

2.3 Spin-to-charge conversion

The spin of an electron has a magnetic momentum of $\mu_\mathrm{B} \approx 9.27\times10^{-24}\,\mathrm{J\,T^{-1}}$. This value is so small that even the most sensitive magnetometers that achieve $\sim \mathrm{fT}/\sqrt{\mathrm{Hz}}$ sensitivities [Buc18] would not be able to measure it without averaging over such a long time that the spin state probably changed during the measurement. This is the reason why one typically uses an indirect spin measurement that relies on the conversion of the spin information into charge information. Charge sensors are sensitive enough to sense a fraction of the elementary charge and thus can rapidly retrieve the information in a single-shot fashion. We want to present here three of the most popular spin-to-charge conversion techniques.

2.3.1 Energy selective readout

One way to realize spin-to-charge conversion relies on energy selective tunneling. In a magnetic field $B_\mathrm{z} \neq 0$ the two spin states of an orbital state in a QD ($|\mathrm{GS}\rangle$ and $|\mathrm{ES}\rangle$) are energetically separated by the Zeeman energy $E_\mathrm{z} = g\mu_\mathrm{B}B_\mathrm{z}$. We will refer to their energies as E_GS and E_ES respectively. In contrast, the effect of the magnetic field on the energy states in a reservoir are negligible and the electrochemical potential μ can be considered constant. If μ is aligned between the two states $|\mathrm{GS}\rangle$ and $|\mathrm{ES}\rangle$, an electron in $|\mathrm{ES}\rangle$ would tunnel to the reservoir whereas one in $|\mathrm{GS}\rangle$ would remain in the QD. The tunneling out of $|\mathrm{ES}\rangle$ would be subsequently followed by an electron tunneling from the reservoir into $|\mathrm{GS}\rangle$. An experimental sequence to perform such a measurement is depicted in figure **2.7 (a)**, **(b)** and **(c)**, where **(a)** shows the pulse sequence applied to the QD to shift the energy

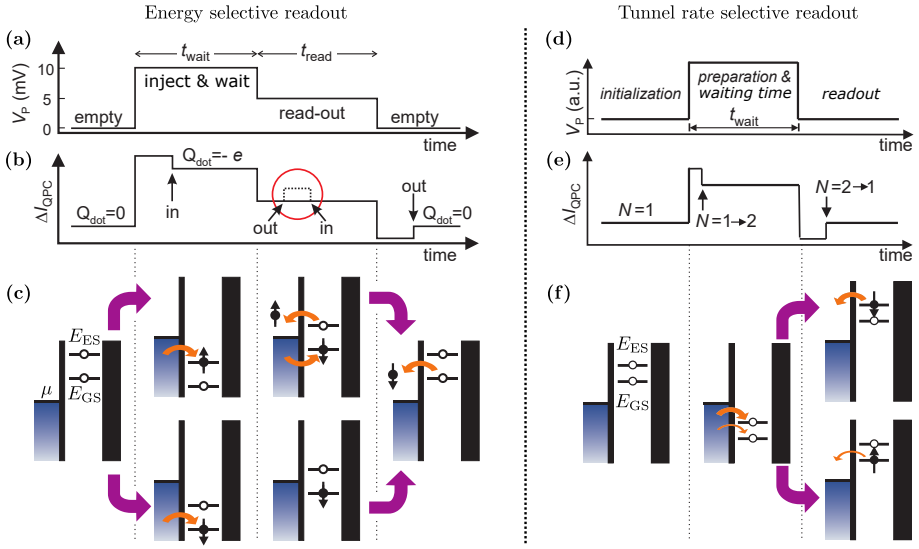

Figure 2.7: Schemes of energy selective readout (left) and tunnel rate selective readout (right). The plot **(a)** (**(d)**) depicts the pulse sequence for the energy (tunnel rate) selective readout applied to the quantum dot to load and unload charges. The plot in **(b)** (**(e)**) depicts the corresponding signal a nearby charge sensor would measure. The cartoon in **(c)** (**(f)**) describes the two processes that allow to distinguish the spin states. Adapted from [Elz04] (left) and [Han05] (right).

levels, **(b)** is a corresponding idealized charge measurement during the pulse sequence and **(c)** is a cartoon that shows the different system states during the pulse sequence. A QD is first emptied and then loaded with a single electron of a random spin state. In the following the QD is aligned such that μ falls in between the two energy levels and an electron in $|\mathrm{ES}\rangle$ would tunnel out of the QD, whereas an electron in $|\mathrm{GS}\rangle$ would remain in the QD. If an electron tunneled out of the QD, an electron from the reservoir will tunnel into the lower energy level of the QD. Finally, the QD can be emptied again, and the measurement can be repeated. This type of measurement was first done by Elzerman et al. [Elz04] and is therefore also known as Elzerman readout.

Even though energy selective readout is widely used nowadays, there are many challenges to deal with using this spin-to-charge conversion technique. First, it requires that $E_z \gg k_B T$ to avoid broadening of the population statistics around μ, making it often necessary to work at high magnetic fields B_z while working at as low temperature as possible. Additionally, the pulse to the tunneling position must be very precise and if there is a small shift of μ, the pulse sequence must be recalibrated. Photon assisted tunneling can also cause tunneling of $|\mathrm{GS}\rangle$, resulting in false positives. Finally, depending on the tunneling rate, the readout speed must be much higher than the tunneling rate which can be challenging for tunneling rates approaching MHz.

2.3.2 Tunnel rate selective readout

A technique that tries to overcome the challenges, the formerly presented energy selective readout is facing, is tunnel rate selective readout [Han05]. For this readout, one exploits the different tunnel rates Γ between reservoir and quantum dot for different states. We consider again a spin ground state $|\mathrm{GS}\rangle$ and a spin excited state $|\mathrm{ES}\rangle$. When both states are above μ, the states will have a tunneling rate to the reservoir of $\Gamma_\downarrow$ and $\Gamma_\uparrow$ respectively. In the case where $\Gamma_{\mathrm{ES}} \gg \Gamma_{\mathrm{GS}}$, one can exploit this tunneling rate difference to read out the spin state. The experimental sequence is depicted in figure 2.7 **(d)**. Corresponding to the experiment, an idealized charge measurement is depicted in figure 2.7 **(e)** and a cartoon of the system during the different steps of the experiment is sketched in figure 2.7 **(f)**. One starts with one electron in the QD and loads a second by pulsing both states $|\mathrm{GS}\rangle$ and $|\mathrm{ES}\rangle$ below μ. For small magnetic fields such that $E_\mathrm{z} < E_{\mathrm{ST}}$ with E_{ST} the splitting between singlet and triplet states, the excited state $|\mathrm{ES}\rangle$ is a triplet state and the ground state $|\mathrm{GS}\rangle$ the singlet state. The triplet states are forming more p-like orbitals whereas the singlet state forms more s-like orbitals. The different orbital shape results in different overlap of the wave functions with the reservoir and hence different tunnel rates. Raising both states well above μ for a time τ with $\Gamma_{\mathrm{GS}}^{-1} \ll \tau \ll \Gamma_{\mathrm{ES}}^{-1}$ results in tunneling of an electron in $|\mathrm{ES}\rangle$, while an electron in $|\mathrm{GS}\rangle$ has a much greater probability to remain in the QD. Thus, measuring if the charge on the QD changes during τ allows to distinguish the two spin states.
The greatest challenge for high fidelity tunnel rate selective readout is to fulfill the requirement $\Gamma_\downarrow^{-1} \ll \tau \ll \Gamma_\uparrow^{-1}$. As an electron in both states can tunnel out of the QD, the achievable fidelity is limited to $1-\alpha-\beta$ with the error rates $\alpha = 1 - e^{-\Gamma_\uparrow \cdot \tau}$ and $\beta = \frac{(1/T_1)e^{-\Gamma_\uparrow \cdot \tau} + (\Gamma_\downarrow - \Gamma_\uparrow)e^{-(\Gamma_\downarrow + 1/T_1)\cdot\tau}}{\Gamma_\downarrow + 1/T_1 - \Gamma_\uparrow}$, where T_1 is the relaxation rate from $|\downarrow\rangle$ to $|\uparrow\rangle$. In particular if one performs this measurement using just a single instead of two electrons in the QD, the $|\mathrm{ES}\rangle$ and $|\mathrm{GS}\rangle$ orbitals are identical, and the tunnel rate is very similar. We will see in section **6.2.4** that the different orbital shapes can have significant effects in other experiments as well.

2.3.3 Pauli spin blockade

A mechanism that does not rely on the splitting of the two spin states is Pauli spin blockade[Ono02]. This technique exploits the Pauli principle, namely not allowing two electrons with the same spin state occupy the same orbital state. The required device architecture is different in this case as it does not consist of a single quantum dot, but a double quantum dot. We consider a system of two electrons with either two electrons in one QD (2|0) or one electron in each QD (1|1). Starting from the (1|1) state, transferring one electron from one QD to the other requires that the electrons have antiparallel spin to obey the Pauli principle when they occupy the same orbital. This effect was first observed in quantum dots using current measurements [Joh05a; Ono02] and later as well using remote sensing [Joh05b; Pet05b]. To be more exact, the two electrons must form a singlet state, which is the ground state in the (2|0) configuration, to allow tunneling between

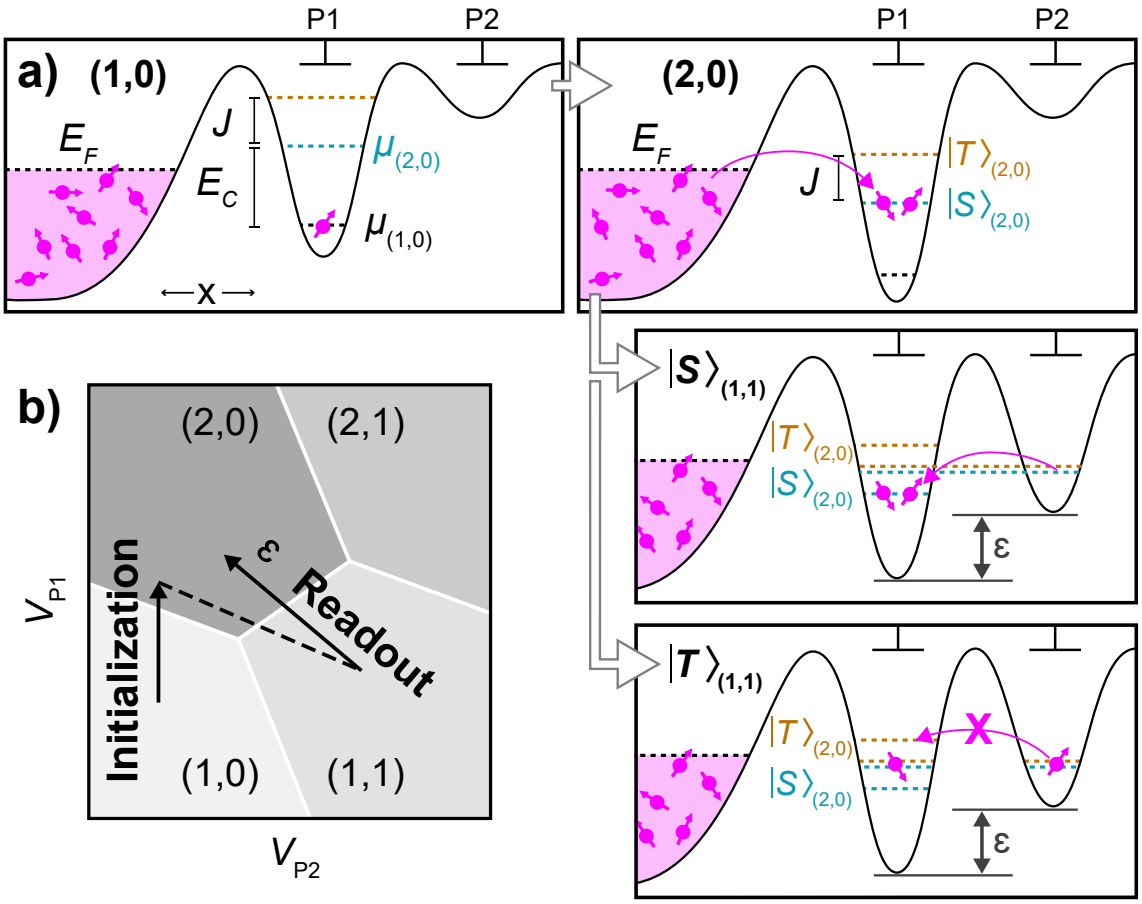

Figure 2.8: **a)** Scheme of a Pauli spin blockade (PSB) measurement from initialization to preparation to manipulation to measurement. The first frame depicts the initialization of a single electron in a quantum dot near a reservoir by pulsing the gates in the (1,0) regime. The next frame shows the preparation of a singlet state. Loading of an electron by pulsing the gates to the (2,0) regime results in a preparation of the singlet ground state. By pulsing in the (1,1) regime, either a singlet or a triplet state can be prepared (not shown). The final measurement in (2,0) (last two frames) show the either non-blocked transfer of singlet (upper frame) or blocked transfer of triplet (lower frame). **b)** indicates a pulse scheme for the experiment described in **a)** at a (2,0)-(1,1) interdot transition. Reprint from [Bur21].

the two quantum dots. To better understand this effect, we can use the energy diagram depicted in figure **2.5(b)** ($B_z = 0$) and in figure **2.5(c)** $B_z \neq 0$. The energy diagrams show that the singlet state hybridization between (1|1) and (2|0) occurs at different detuning compared to the hybridization of the triplet states. The detuning difference corresponds to the energetic splitting between singlet and triplet states. If we operate the double quantum dot only in the detuning window where the singlet can transition between the two charge states and the triplet remains in the (1|1) state, this spin selective tunneling can be exploited to determine the spin state with high fidelity. Even though this scheme might seems to be more complicated than tunnel rate selective and energy selective readout, PSB has a few advantages. First, there is actually no need of a reservoir if one has another way to initialize the states in the desired state. Second, one has different ways to use this readout. One can use it to distinguish singlet and triplet states, but one could also consider one of the electrons as a reference spin that is always in the ground state and the other spin is treated as a single spin qubit and the PSB allows to measure the single spin. In fact, using device architectures with ancillary quantum dots can be used to further improve the readout. So far, the only non-demolition measurements of spin qubits used ancillar spins in nearby quantum dots[Nak19; Yon20]. We will discuss the experimental implementation of PSB in our devices in detail in chapter **6**.

3 Experimental techniques for semiconductor quantum dots

> That which is not measurable is not science.
>
> Ernest Rutherford

In this chapter we will discuss the techniques used to perform the presented experiments. As the experimental techniques span from cryogenics, to nanofabrication, over microwave engineering to low-noise measurements, we will first discuss in this chapter cryogenics. After, we will present the low-noise electronics used to perform these sensitive experiments and last but not least the nanofabrication of devices and high impedance inductors. We will start with the literally biggest part of the experimental setup: the cryostat.

3.1 Cryogenics

In order to perform experiments using electrons confined in semiconductor quantum dots, the thermal energy[1] must be lower than the energies separating the quantum states. Working with electron spins in silicon quantum dots, this energy is usually given by the Zeeman energy, which is for typical magnetic fields of 300 mT approximately 0.04 meV $\sim$ 10 GHz $\sim$ 0.48 K. Considering that this is even below the temperature of the thermal radiation from space ($\approx$ 3 K), one can imagine that to reach such low temperatures, not only an endothermic process which works as such low temperatures is needed, but a sophisticated isolation from heat sources as well. We will first focus on the basic working principle of a dilution fridge and afterwards discuss the different techniques used to thermally isolate the system.

3.1.1 Principles of dilution cryostats

Dilution cryostats or dilution fridges are a well established tool to perform low-temperature experiments in solid state physics. If simple ^{4}He-cryostats do not reach sufficiently low temperatures, a dilution fridge is often the cryostat of choice. A typical dilution fridge consists of several temperature stages and two separate cooling cycles. The primary cycle, a closed cycle circulating a mixture of ^{3}He and ^{4}He and an open cycle, the secondary cycle, circulating ^{4}He. A scheme of a table-top dilution fridge, as it was used for most of the experiments shown here, is depicted in figure **3.1**.
To cool down from room temperature to 4 K which is often referred to as precooling, liquid

1 We are mostly interested in the thermal energy of electrons at this point, as the thermal energy of the phonon bath is usually lower.

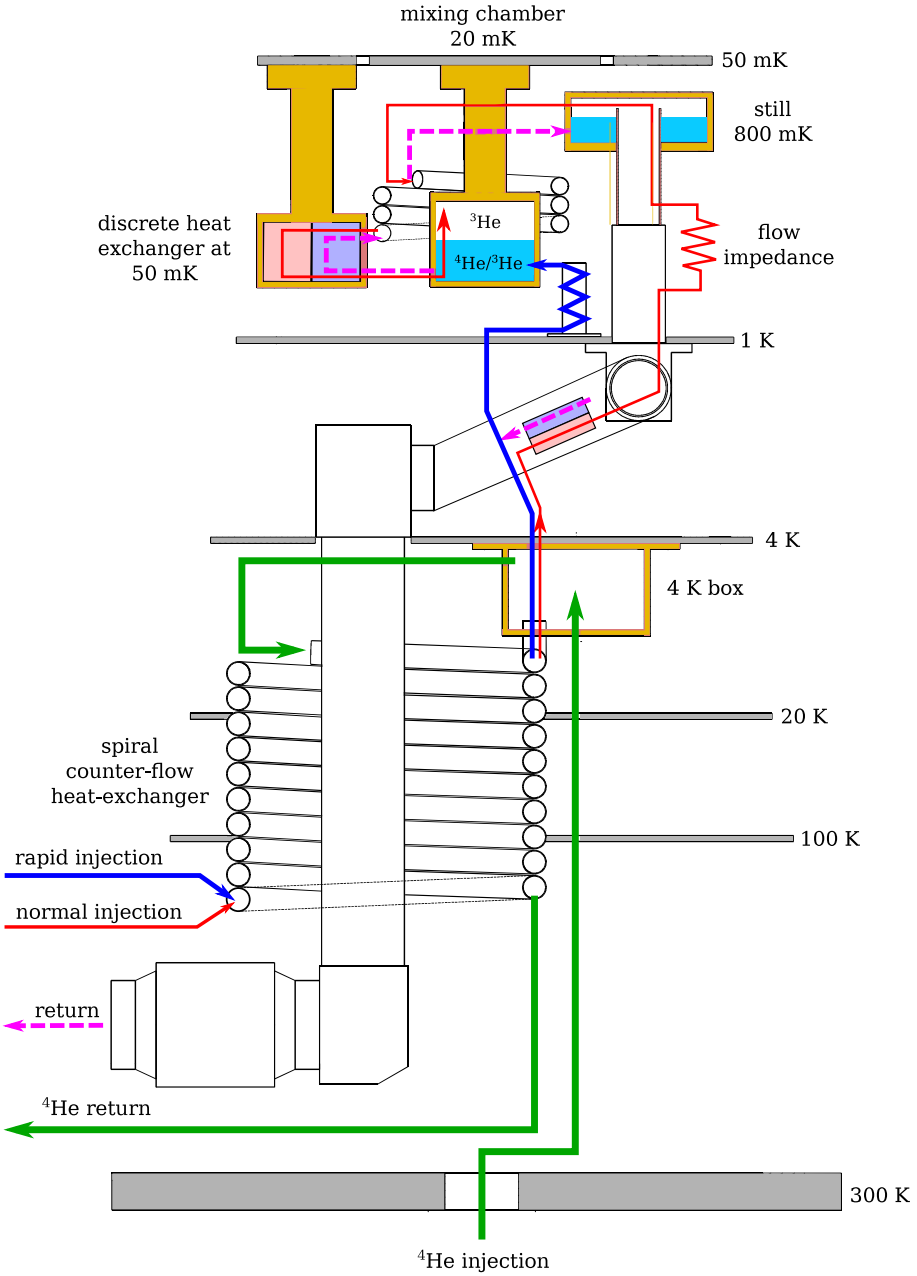

Figure 3.1: Schematic of a table-top dilution fridge of type Sionludi. A combination of two helium circuits allow cooling down to temperatures of $\approx 20\,\mathrm{mK}$. The secondary cooling circuit (green) is used to precool the helium in the first circuit down to liquid helium temperature (4 K). The primary circuit circulates a mixture of ^{3}He and ^{4}He. This mixture is separated in a ^{3}He rich and a ^{3}He poor phase in the mixing chamber. Extracting ^{3}He from the ^{3}He poor phase and reinjecting it in the ^{3}He rich phase allows cooling down to temperatures of $\approx 20\,\mathrm{mK}$. Adapted from [Thi14].

^{4}He is injected from a dewar underneath the dilution fridge in the secondary cycle at a relatively high rate of $\sim 4\,\mathrm{L\,h^{-1}}$. As depicted in green in figure **3.1**, the injected ^{4}He fills the so-called 4 K box, which is mounted at the 4 K stage. The evaporated cold helium gas from the 4 K box is evacuated through a spiral counter-flow heat-exchanger. This heat-exchanger allows cooling down the injection of the primary cycle as well as cooling down the 20 K and 100 K stages on which it is mounted.
In order to precool the stages, part of the mixture of ^{3}He and ^{4}He is injected into the primary cycle. The primary cycle allows to cycle the mixture via two different paths. The so-called fast injection is used for precooling and is traced in blue in the diagram. The so-called slow injection (red in the diagram) is made for a continuous cycle. Both of these enter into the dilution fridge through the counter-flow heat-exchanger, where the mixture is thermalized to 4.2 K by the secondary cycle. From the 4 K stage, the fast injection goes directly to the 1 K stage from where it enters into the mixing chamber. From the mixing chamber, the mixture leaves the dilution fridge through the discrete heat exchanger and the still. Bypassing elements of the slow injection path between the 4 K stage and the mixing chamber with connections of large cross-section reduce the flow impedance. This results in a higher circulation rate and with it a higher cooling power.
When all stages of the dilution fridge are thermalized, the condensation of the mixture is initiated by switching to the slow injection. A compressor pressurizes the mixture to 4 bar before injecting it through two heat exchangers (the one thermalized by the secondary cycle and another one between the 4 K and 1 K stages, thermalized by the reflow of the mixture from the still). The second heat exchanger is terminated by a flow impedance at the 1 K stage. Passing through the flow impedance implies a pressure gradient, which causes the gas, thermalized to 4 K, drop in temperature down to ~ 2 K. The mixture is then transferred through the still and several heat exchangers, before it is injected into the mixing chamber. The mixing chamber is constantly evacuated to 0.1 mbar by external pumps, reducing the temperature further due to adiabatic expansion. This further cooling results in the condensation of the gas. Evaporating gas is evacuated through the reverse direction of the heat-exchangers previously passed, cooling down the incoming mixture. This yields to even more condensed mixture within the mixing chamber, filling it up to the point where the liquid mixture reaches the still. The crucial property of a mixture of ^{3}He and ^{4}He comes now into play. When the mixture reaches a temperature below ~ 800 mK, the mixture separates into two phases. The ^{3}He rich phase is lighter and thus floats on top of the ^{4}He rich phase . As a consequence, the ^{4}He rich phase stays at the bottom of the mixing chamber, connected with the still, while incoming helium enters into the ^{3}He rich phase. Despite the high ^{4}He concentration of the mixture within the still, the higher vapor pressure of ^{3}He yields to an evaporation of mainly ^{3}He ($\sim 97\,\%$) within the still. After being pumped from the still, the gas is reinjected into the ^{3}He rich phase, establishing a closed cycle.
The endothermic process occurs when ^{3}He diffuses from the ^{3}He rich phase into the ^{4}He rich phase. As the enthalpy H of ^{3}He, in the ^{3}He rich phase, is higher than for ^{3}He, in

the ^{4}He rich phase, the achieved cooling power is given by

$$\dot{Q} = \dot{n}_3 \Delta H = \dot{n}_3(\gamma_\mathrm{d} T_\mathrm{mc}^2 - \gamma_\mathrm{c} T_\mathrm{i}^2) \simeq 84 \dot{n}_3 T_\mathrm{mc}^2, \tag{3.1}$$

where $\dot{n}_3$ is the rate of ^{3}He circulation times, ΔH the enthalpy difference, γ_d (γ_c) the enthalpy coefficient of ^{3}He in the dilute (concentrated) phase, and T_mc (T_i) the temperature of the mixing chamber (inlet temperature) [Zu22]. The lowest temperature achievable is then given by the equilibrium between heating through heat leaks, power dissipation by the experiment, etc., and is usually in the range of a few tens of mK.

3.1.2 Low temperature electronics

The dilution cryostat allows us to reach temperatures as low as a few tens of mK. The limiting factor for the temperature of the cryostat is the heat load that must be compensated. The cooling power of a dilution fridge is given by equation **3.1**. Thus, the cooling power increases quadratically with increasing temperature. The heat load to be compensated has different sources. First, the radiative heating from outside is mostly shielded through a cascade of radiative shields. While the last shield is thermalized at 4 K, the device is additionally shielded at the cold plate level. Another heat load is the conductive heat from the supporting structure of the cryostat and the electrical wires. The supporting structure is separated in stages at different temperatures as depicted in figure 3.1 and these stages thermally decoupled. The electrical wiring cannot be thermally decoupled and therefore typically made out of material with low thermal conductivity. Thermal anchoring at each temperature stage allows to reduce the heat load at the lowest temperature stage where the cooling power is low. During operation, the main heat source is the heat dissipation of the electronics. The low-temperature low-noise amplifier (LNA) is installed at the 4 K stage and has a power consumption of 120 mW. The DC-operation of the device is typically at such low currents that one can neglect the power dissipation here. A variable heat source is the application of pulses using an AWG as these pulses are typically attenuated at low-temperature stages to use the full voltage range of the AWG. However, for typical experiments the duty cycle (time of pulse × power dissipation / time of experimental cycle) is relatively low and no heating occurs. As a result, the cryostat typically operates around 100 mK.
At such a temperature, the thermalization between electrons and phonon bath is not efficient enough to keep them in equilibrium, meaning that the electron temperature is typically a bit higher than the measured temperature (phonons) of 100 mK. For our experiments the electron temperature is of interest as it defines the noise in our system according to the Johnson-Nyquist noise

$$P = k_\mathrm{B} T \Delta f, \tag{3.2}$$

where k_B is the Boltzmann constant, T is the temperature and Δf is the frequency bandwidth. Additionally, electromagnetic radiation can travel through wires, making the direct connection of a 300 K instrument with the device at 100 mK impossible. The solution for DC wires is the use of filtering cables or filtering elements in addition of thermal anchor-

ing. The DC wires used in this thesis used π-filters with a cut-off frequency of $\sim 1\,\mathrm{MHz}$ at cryogenic temperatures. For frequencies above $\sim 1\,\mathrm{GHz}$ filtering with discrete elements becomes difficult as the stray capacitances render the filter more and more inefficient [Fre95]. Different techniques exist to filter at these higher frequencies ranging from fine-grain metal powder filters to adapted cable types like microcoax or Thermocoax [Gla97; Man11; Zor95]. In our setup, superconducting NbTi wires with an Eccosorb covering in a constantan matrix were used. Eccosorb absorbs microwaves very efficiently and is nowadays commonly used in cryogenic setups. For a more detailed description of the wiring, we refer to the thesis of Stefan Thiele [Thi14].
For sending high-frequency signals between a few tens of MHz and a few GHz another approach is necessary. The goal is to send AC-signals through large bandwidth cables without introducing a lot of noise. This can be achieved by using thermally anchored coaxial cables in combination with broadband attenuators. The input signal will be attenuated in the same way as the noise and therefore, must have a sufficiently high SNR when sending the signal from room temperature through the attenuated coaxial cables. The attenuation is typically done with at least $20\,\mathrm{dB}$ at $4\,\mathrm{K}$ and $20\,\mathrm{dB}$ at $100\,\mathrm{mK}$. The attenuation allows to efficiently thermalize the inner conductor of the coaxial cable. In our experiment, we had four coaxial cables where three were used as input lines and one was used as output. We used cryogenic attenuators from XMA corporation®.

3.1.3 Control electronics and data acquisition

The experimental setup required different instruments to send and receive signals. We will start with the control instruments and then describe the data acquisition. We can again distinguish between DC- and AC-electronics. The DC signals are controlled with a digital-to-analog (DAC) converter. The DAC used in our experiments was developed at the Néel institute. The DAC has 16 channels with a 16-bit resolution and a fast slew rate $\mathrm{SR} \simeq 2.5\,\mathrm{V\,\mu s^{-1}}$ at a noise level of $25\,\mathrm{nV}/\sqrt{\mathrm{Hz}}$. With a voltage range of $\pm 5\,\mathrm{V}$ the 16-bit translate into a resolution of $153\,\mu\mathrm{V}$. The control of the DAC is done using a sbRIO-9602 National Instruments® field-programable gate array (FPGA). Appart from the communication with the DAC, the FPGA provides as well trigger outputs that allow to trigger other instruments in the experiment sequence. The experimental sequence for the triggers and DAC are sent to the FPGA from a local computer using a python/labview software interface. The experimental sequence that consists of a sequence of DAC, trigger and wait commands allows to synchronize the different instruments and the short time per instruction of $16\,\mu\mathrm{s}$ allows fast control.
The triggers allow controlling AC instruments like radio-frequency sources and arbitrary waveform generators (AWGs). While the commands for these instruments are sent directly from a PC, the triggers allow to synchronize all instruments. To ensure that the signals indeed arrive at the right time, we recommend control the signals using an oscilloscope.
For the data acquisition, we used a NI USB-6229 16-bit analog-to-digital converter (ADC). The ADC has a $250\,\mathrm{kHz}$ bandwidth for a single channel and is split if two channels are used. Triggering the ADC allows to control the time of acquisition.

3.2 Fabrication workflow for FDSOI quantum dot devices

The devices used in this thesis were fabricated in an industrial 300 mm Si process. Such processes require state-of-the-art equipment which is often not compatible with the flexibility demands of an academic clean room, but deliver on the other hand highly reproducible results on a large scale. The fabrication was therefore done by the CEA-LETI, a semi-industrial research institute with adequate clean room facilities and experience. In the following, we want to outline the fabrication process.

The devices are fabricated on a 300 mm wafer. The wafer surface is covered by a 145 nm buried oxide layer. On this oxide, a 11 nm Si layer is deposited. In our case, this layer consisted of ^{28}Si enriched Si. The devices are patterned in this thin layer on the oxide and such fabrication technology is also known as Silicon-On-Insulator (SOI). The silicon nanowire that builds the first element of our devices is mesa patterned using electron-beam lithography and etching. While the default design was set to nanowire width between 80 nm and 100 nm, in this thesis we worked with trimmed devices where the nanowire was etched to a width of $\sim$ 40 nm. In the next step, the gate stack is grown on top of the nanowire. The interface nanowire-gate consists of 6 nm thermally grown SiO_2. Next, 5 nm of TiN, deposited using atomic layer deposition (ALD). A 50 nm Poly-Si layer is grown on top and finally topped with a bilayer hard mask of 30 nm SiN and 25 nm SiO_2. A hybrid deep-UV-electron-beam gate-patterning scheme is used to transfer the gate structure into the hard mask, alternating lithography and etch steps. A final etch step is used to split the gates along the nanowire by 40 nm into 6 gates (2×3). The gate width for the devices used in this thesis ranged from 40 nm to 60 nm and most of the presented results used the 40 nm type. Finally, n-doping of the source (S) and drain (D) reservoirs is done using ion implantation followed by a N_2 spike anneal. To protect the device, it is encapsulated, and the gates are connected to Al bond pads using vias to metal layers.

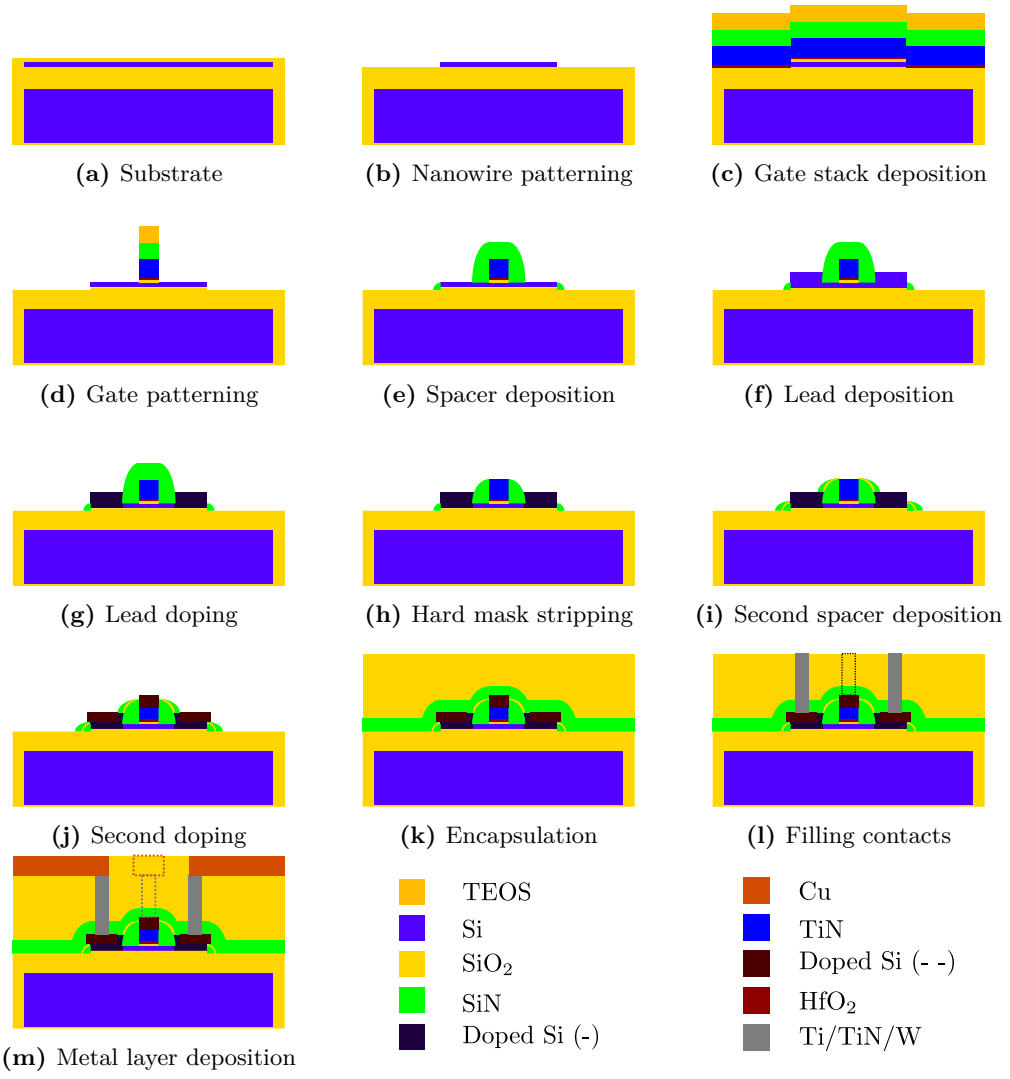

Figure 3.2: Fabrication steps for a device as it was used in this project. Initially, a Si nanowire is patterned from an SOI substrate, depicted in figures **(a)-(b)**. After, the gates are deposited and patterned, illustrated in figures **(c)-(e)**. Next, source and drain contacts are formed, shown in figures **(f)-(j)**. Finally, the device is encapsulated **(k)** and contacted to metal layers which will form bond pads **(l)-(m)**. Adapted from [Nie19]

3.3 Fabrication of high impedance inductors for rf-reflectometry

In the course of this thesis, we developed a fabrication recipe for high impedance Nb inductors for rf-reflectometry measurements. Compared to SMD inductors, on-chip Nb inductors have four advantages for our experiments. First, completely free design, only limited by the lithographic resolution. Second, smaller parasitic capacitance as bond pads are smaller and in general, less metal is used. Third, no resistive losses as the Nb is superconducting. Fourth, smaller footprint.
We will see in section **4.1** that a main goal of designing rf-circuits is matching the load to the 50 Ω lines. In this regard, the small parasitic capacitance and the well controlled inductance allow fine-tuning of the matching circuit. A challenge remains however the test of the circuit as the critical temperatures of our inductors was between 4 K and 5 K. Thus, even cryogenic probe stations with base temperatures just above 5 K were not sufficiently cold to test the inductors. We finally tested a few inductors using a dilution cryostat which didn't allow us to measure statistically significant numbers of inductors to optimize all parameters. We are hopeful that with access to powerful microwave simulation software like Sonnet®, the circuits can be further improved. Nevertheless, we found after a few tries an inductance that was compatible with our rf-circuit and improved it considerably compared to circuits using SMD inductors.

3.3.1 Fabrication

The fabrication recipe for the inductors was developed with the help of the Nanofab team of the Néel Institute and special thanks goes to Latifa Abbassi and Bruno Fernandez who helped me with finding the right lithography parameters.
The complete fabrication is illustrated in figure **3.3**. We start with a 3 inch wafer of intrinsic silicon. We pursue the following steps to get from a whole wafer to a final die with a single Nb inductor.

1. Clean wafer in aceton and isopropyl alcohol (IPA) using an ultrasound bath followed by a 5 minute O2 plasma cleaning at 20 W in a reactive ion etching machine.
2. Deposition of 60 nm Nb on wafer using a UHV electron beam deposition.
3. Spin coat wafer with 1818 resist for protection
4. Baking of resist on hotplate at 115 °C for 1 min.
5. Cutting wafer in 1 cm^2 squares
6. Cleaning die using 3 min of aceton ultrasound bath followed by 1 min of IPA ultrasound bath to remove resist and dust particles
7. Prebake die on hot-plate for 1 min at 115 °C to remove any condensed water from the surface
8. Spin coat wafer with 1805 resist for 30 s at 6000 rpm and an initial acceleration of 6000 rpm s^{-1} resulting in a resist thickness of 380 nm
9. Baking of resist on hotplate at 115 °C for 1 min.

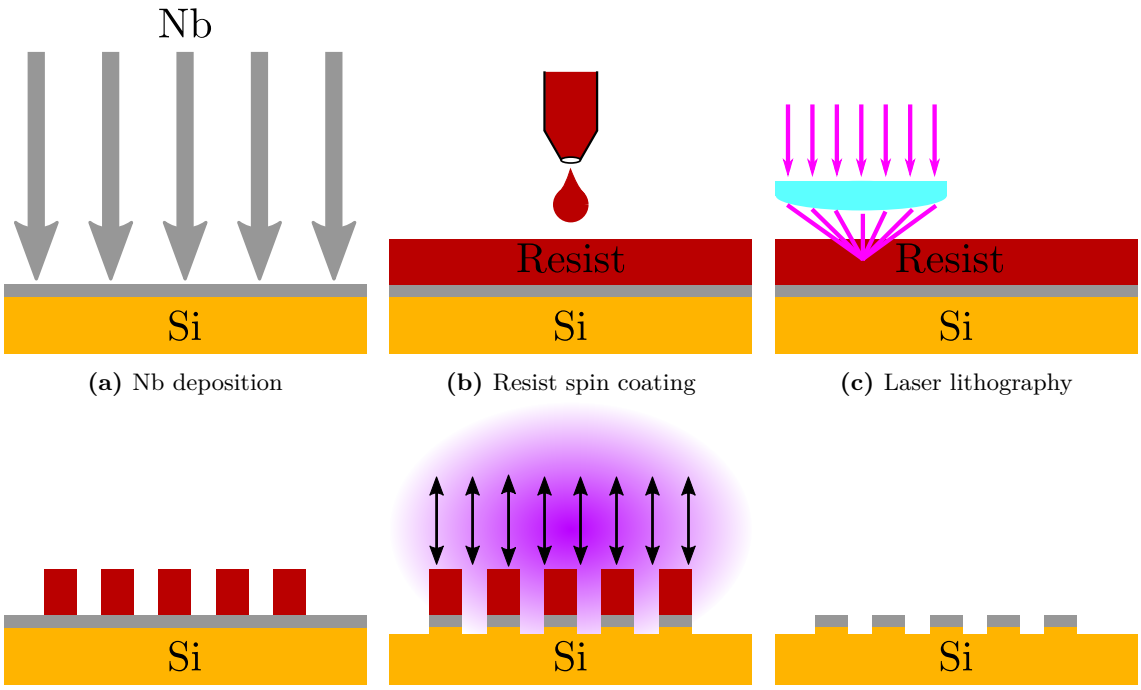

(a) Nb deposition **(b)** Resist spin coating **(c)** Laser lithography

(d) Development **(e)** Reactive ion etching **(f)** Remove resist

Figure 3.3: Fabrication process of high impedance inductors.

10. Laser lithography using an inverted mask of the desired pattern with a dose of 30.
11. Development of lithography using a solution of deionized water and Microdev in a ratio 1 : 1 for 30 s with an additional 10 s if the development was not sufficient after 30 s.
12. Reactive ion etching using an Sf6 plasma at 20 W for 2 min and 30 s, allowing to use the 1805 resist as a mask while the Nb is etched.
13. Cleaning die using 3 min of aceton ultrasound bath followed by 1 min of IPA ultrasound bath to remove resist.
14. Spin coat wafer with 1818 resist for protection.
15. Baking of resist on hotplate at 115 °C for 1 min.
16. Cutting die in smaller dies with a single inductor.

Between each non-repeatable step (e.g. lithography), the die was checked under a microscope for any dust that could prohibit a clean process. If dust or any other non-desirable defect was detected, the die was cleaned using aceton and IPA. The yield of this process is very high and was finally above 90 % if one worked carefully and cleaned any dust particles after every step. A few examples of fabrication issues are depicted in figure **3.5**. If plastic particles e.g. from the plastic pipettes contaminate the resist, the diffraction of the laser light can cause circular spots of overexposure of the resist as can be seen in figure **3.4(a)**. An example of a dust particle on an inductor is depicted in figure **3.4(b)**. In case

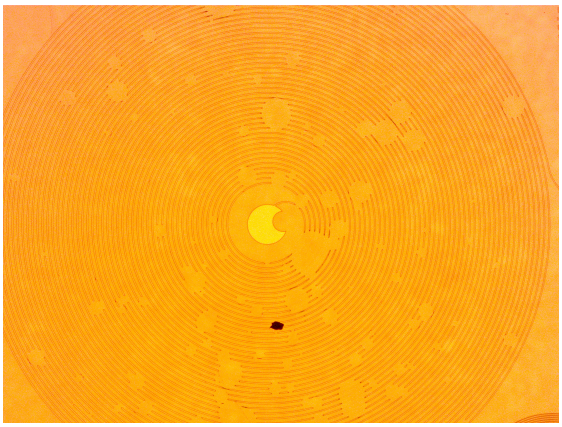

(a) Resist contamination

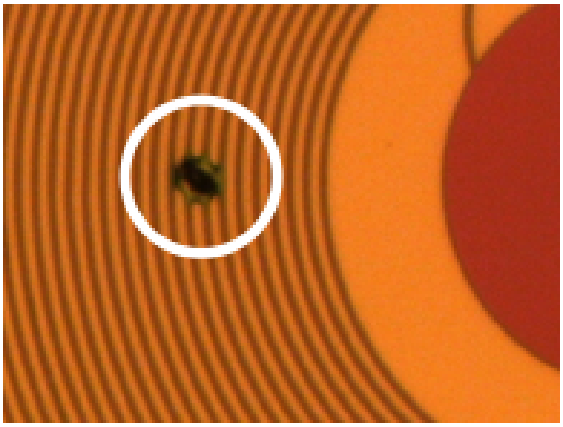

(b) Dust particle

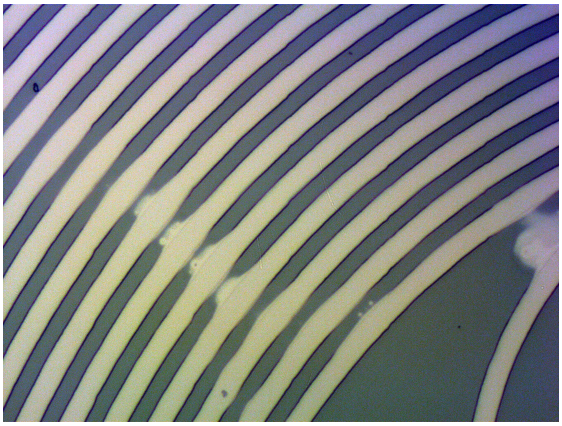

(c) Insufficient etching

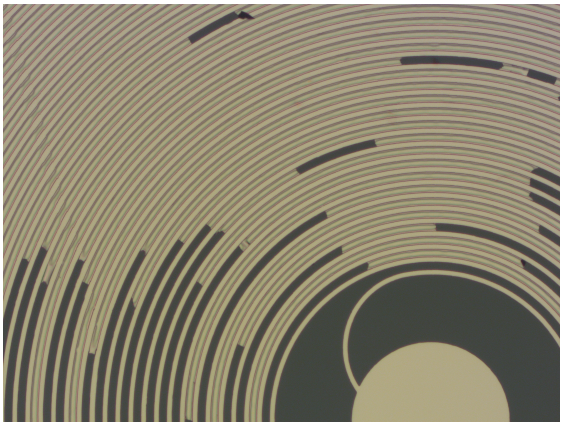

(d) Insufficient development

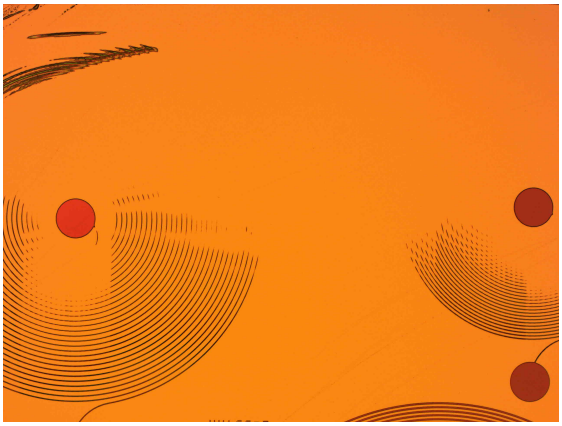

(a) Overexposure

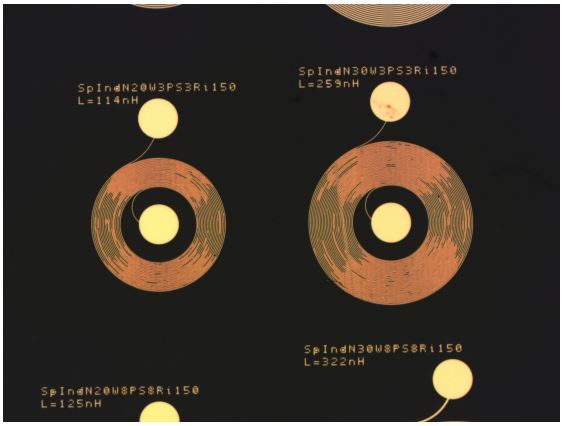

(b) Insufficient development

Figure 3.5: Fabrication defects

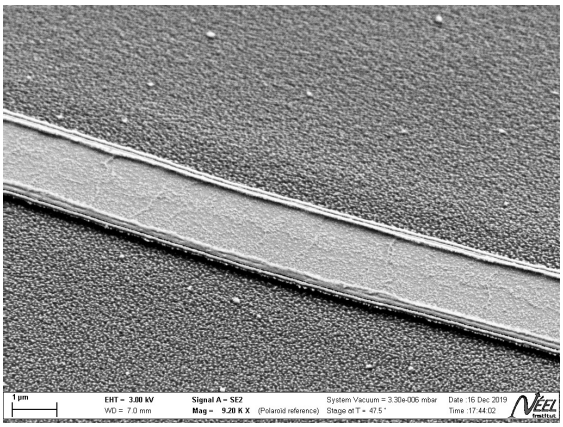

(a) Nb track

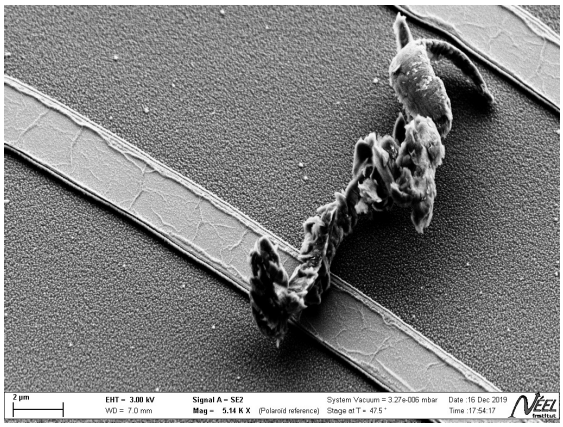

(b) Dust particle

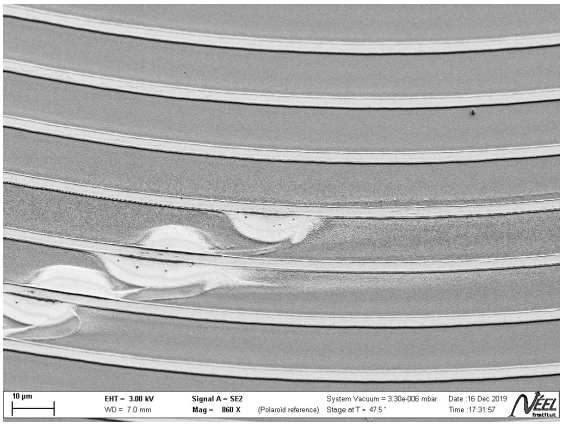

(c) Insufficient etching

Figure 3.6: Scanning electron micrographs of Nb inductors on silicon.

of insufficient etching, some Nb residue can remain between the Nb tracks as depicted in figure **3.4(c)** and figure **3.6(c)**. A non-problematic issue can be insufficient development that can be corrected by visual inspection of the chip after development and follow up with another development step. Examples of insufficient development are given in figure **3.4(d)** and figure **3.5(b)**. If the development of the resist is unsuccessful, one should consider renewing the developer as it might degraded with time or if one has already developed several dies, the developer might lost its reactivity. As the inductors are made by a top-down approach instead of the in academia more common bottom-up approach, the lithography uses an inverted mask (exposing all that has to be removed). For such lithography a lower dose is necessary than for a standard mask and overexposure is a common problem. A typical result of overexposure in our design are very thin Nb tracks and sometimes vanishing features as can be seen in figure **3.5(a)**. Another error source is overexposure at the edges of the die. The laser tends to refocus in the beginning and overexposes one of the edges. It is advisable to reject the edges and only use a square of $0.9\,\mathrm{cm} \times 0.9\,\mathrm{cm}$ for the pattern.

In figure **3.6(a)** a scanning electron microscope micrograph of a single track of an inductor is shown. The micrograph reveals that the Nb is well etched and there is considerable additional etching into the Si substrate. This etching into the Si substrate helps to reduce the capacitance due to the reduction of dielectric between tracks. The substrate etching has to be taken into account if one wants to simulate the properties of the inductor. An additional feature are sidewalls on the track. These are redepositions during the etching process and can result in small capacitive contributions. Even though this effect is small, in order to optimize the capacitance, one should try to reduce this effect as much as possible by optimizing the etching rf-power.

3.3.2 Characterization

For the lithography mask, we used the free software KLayout that allows to view and edit GDS files that are used by the lithography machine as a mask. While KLayout provides some macro-features that can be used to parametrize paths, we used the python package *gdspy* to create inductors that we subsequently edited in KLayout. An example of a final mask for the laser lithography is depicted in figure **3.7**. We used the formula

$$L = \frac{\mu n^2 d_{\text{avg}} c_1}{2} (\ln(c_2/\rho) + c_3\rho + c_4\rho^2), \tag{3.3}$$

where $\mu = 4\pi \cdot 10^{-7}$, n the number of turns, $d_{\text{avg}} = 0.5(d_{\text{out}} + d_{\text{in}})$ the average diameter of the spiral, $\rho = (d_{\text{out}} - d_{\text{in}})/(d_{\text{out}} + d_{\text{in}})$ the fill ratio of the inductor and $c_1 = 1.00$,

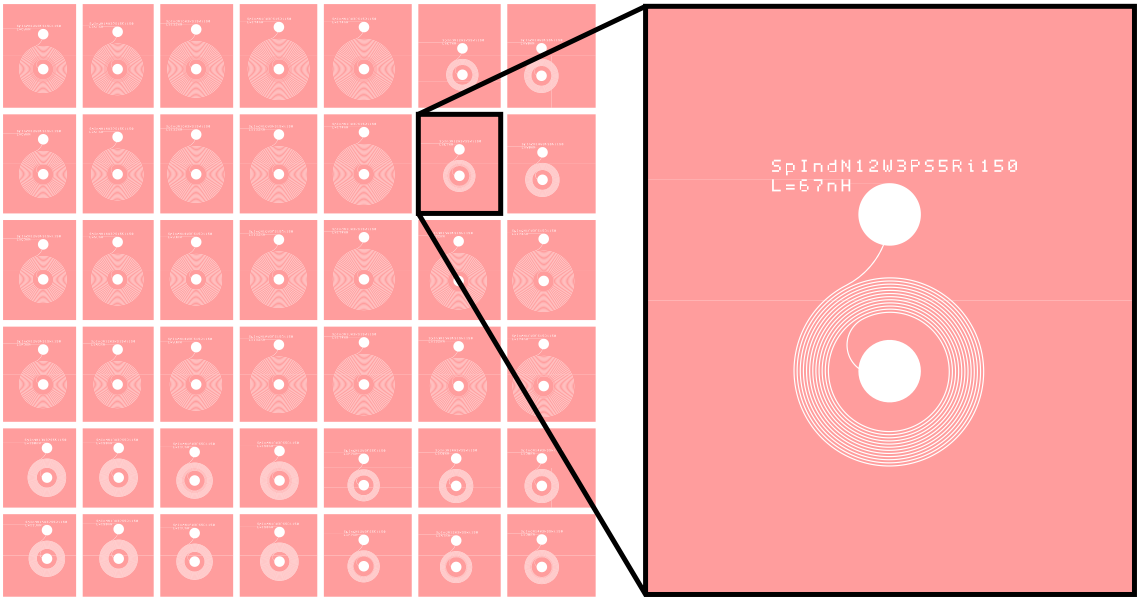

Figure 3.7: Laser lithography mask for an array of spiral inductors. The inductors are generated using gdspy and tracks separating the inductors are used as marks for subsequent cutting. Each inductor has an ID that allows extracting all necessary parameters to reproduce it as well as the expected inductance.

$c_2 = 2.46$, $c_3 = 0.00$ and $c_3 = 0.20$ geometry dependent parameters [Moh99].
To find the right parameters for the geometry of the inductors, we parametrized them as spirals where we define the track width, the track spacing and the number of turns. To have a reliable process, we limited the minimal feature size to 3 µm as the lithography resolution is 1 µm. We tested different parameters for spacing, width, and number of turns to find the optimal parameters. For this, we designed an array of inductors with different parameters (se figure **3.7**) to allow testing as many inductors as possible with the fabrication of a single $1\,\mathrm{cm}^2$ die. Due to the lag of appropriate testing equipment we relied on testing individual inductors in a dilution fridge which reduced the throughput of inductors to approximately one inductor per day. At this rate we were not able to test enough inductors to have statistical significance on the effect of the different parameters. We finally used a trial and error approach to find an inductor that worked with our setup. A proper analysis of the inductors might be performed with modern microwave simulation software like Sonnet®. As the field is evolving fast and one might change at some point to even more compact kinetic inductors [Hay14], it might be sufficient for today's experiments to work with suboptimal matching.

4 Radio-frequency reflectometry

> If you want to find the secrets of the universe, think in terms of energy, frequency and vibration.
>
> Nikola Tesla

As we have seen in **1.2.5**, "a qubit-specific measurement capability" is an indispensable requirement for building a quantum computer. The work of this thesis evolves around improving and exploring the capabilities of rf-reflectometry, a strong contender for large scale qubit readout in semiconductor quantum dots. We will see that this technique not only is favorable in terms of physical footprint on a device architecture level, but as well can achieve high fidelity spin readout [Con20; Nie22; Urd19; Zhe19]. In this thesis we will refer to high fidelity as fidelities $> 99\,\%$ as these allow to overcome the fault-tolerant threshold for surface codes [Fow12; Wan11]. Nowadays, the semiconductor quantum dot community focuses on the design of spin based qubits, ranging from single spin qubits [Mil22; Noi22; Xue22], singlet-triplet qubits [Jir21; Joc22] to exchange-only qubits [Ha21]. All these require a spin readout that is typically achieved through spin-to-charge conversion and a subsequent charge readout. Measuring the current through a quantum dot system is often the first step to characterize a QD system. Current measurements can even be used to measure the state of a qubit[Cam22; Mau16]. The problem with current measurements is the incompatibility with error correction protocols as such a measurement is always an

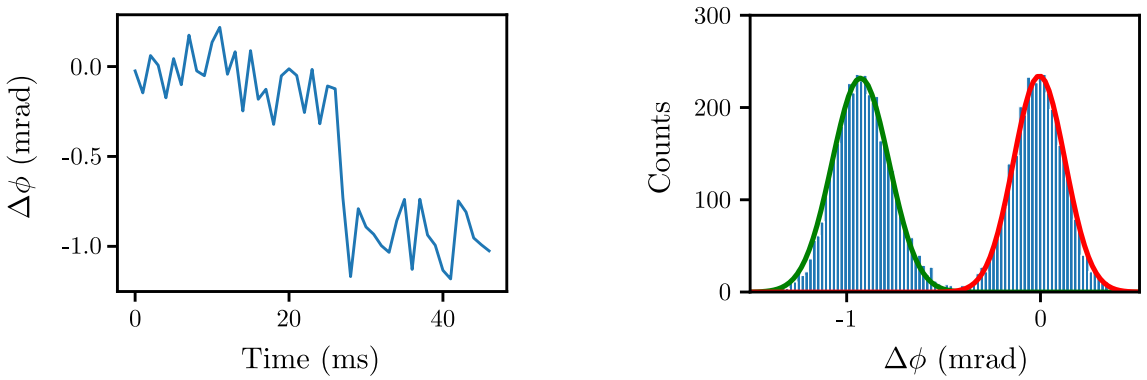

(a) Single shot **(b)** Signal histogram

Figure 4.1: Charge sensing of an electron transition in a quantum dot using rf-reflectometry. **(a)** A single-shot trace where an electron tunneling event is observed. **(b)** Histogram of 8000 single-shot measurements at a readout speed of 1 kHz. Adapted from [Cha20]

average and not single-shot[Fow12]. Nowadays, remote charge sensors are used to perform very sensitive single-shot charge measurements. For QD systems, the most prominent remote sensors are either quantum point contacts (QPCs) (in 2D- heterostructures) or single electron transistors (SETs) [Hou96; Wee88; Wie02]. These systems measure a small current and exploit the small change of conductance as a result of changes in the local electrostatic environment. The figure of merit is the charge sensitivity

$$\delta q = \frac{e}{SNR \cdot \sqrt{BW}}, \tag{4.1}$$

where $e = 1.6022 \times 10^{-19}\,\mathrm{C}$ is the elementary charge, SNR is the signal-to-noise ratio and BW is the measurement bandwidth. The SNR can be extracted from the measurement of the on/off signal of a Coulomb peak at a given bandwidth and calculating the signal separation ΔV with the noise broadening σ. QPCs and SETs suffer from a large resistance ($\sim 100\,\mathrm{k\Omega}$) in combination with stray capacitances ($\sim 1\,\mathrm{nF}$) that pose a bottleneck on the bandwidth of the order of a few kHz [Sch98]. To enhance the bandwidth, rf-techniques were developed that allow to operate sensors at a few 100 MHz. At such frequencies, the 1/f-noise is strongly reduced, allowing much better SNRs than with DC-measurements. While rf-QPCs and rf-SETs became a standard for high fidelity readout, using gate-based readout is a rather new technique for quantum dot devices. An example of a charge detection using gate-based rf-reflectometry is depicted in figure 4.1. Figure 4.1**(a)** shows a single-shot measurement where an electron tunneling event is detected at $\approx 25\,\mathrm{ms}$. Figure 4.1**(b)** shows a histogram from 8000 of such single-shot measurements at a readout speed of 1 kHz. Fitting the two signal levels for the electron in/out of the QD with two normal distributions[1] yields the signal strength ΔV as well as the signal width σ. The SNR for this experiment was 7, giving a charge sensitivity of $5 \times 10^{-3}\,\mathrm{e}/\sqrt{\mathrm{Hz}}$[2] [Cha20]. Before discussing dispersive readout, we want to first present a few basic concepts of rf-electronics that are required to design an rf-circuit.

4.1 Impedance matching and S-parameters

For DC-electric circuits, the most efficient way to transfer power from a source to a load, is to have the same resistance for source and load. In AC-circuits the maximal power transfer is achieved with a load impedance complex conjugate to the source impedance. In other words, the resistance is identical for source and load while the reactances are opposite. A circuit that fulfills this requirement is called impedance matched. Keeping in mind that the reactance of typical components like capacitors and inductors is frequency dependent, it becomes clear that this matching condition is only fulfilled for specific frequencies. A useful concept to understand the reflection of an rf-circuit due to impedance mismatch are

1 The signal noise is mainly due to thermal noise from the low-noise amplifier and can therefore be fitted with a normal distribution.

2 We want to mention here that SNR is sometimes given in terms of voltage and sometimes in terms of power. Here it is given in terms of voltage.

the scattering- or short s-parameters. The scattering parameters assume a linear relation between different ports of a circuit. The relation between input and output port can then be compactly described by an $N \times N$ matrix with N the number of ports. The row corresponds to the input port and the column to the output port. As a result, the diagonal of the matrix describe the reflection coefficients of the ports. The off-diagonal elements describe transmission between ports. A two-port network would thus be described by a 2×2 matrix. The relation between the input signal and output signal can then be written as a matrix multiplication

$$\begin{pmatrix} V_{\text{out}}^1 \\ V_{\text{out}}^2 \end{pmatrix} = \begin{pmatrix} S_{11} & S_{12} \\ S_{21} & S_{22} \end{pmatrix} \begin{pmatrix} V_{\text{in}}^1 \\ V_{\text{in}}^2 \end{pmatrix} \tag{4.2}$$

Nowadays, one uses vector network analyzers (VNAs) to measure these parameters. VNAs have at least two ports which can simultaneously act as input and output of an rf-signal and measure the change of magnitude and phase of the signal over a range of several GHz. The scattering parameters are related to the impedance of a device by

$$\Gamma = \frac{Z - Z_0}{Z + Z_0} \tag{4.3}$$

$$T = \frac{2Z}{Z + Z_0}, \tag{4.4}$$

where Z_0 is the source impedance (typically $50\,\Omega$). As a quick sanity check, one can check the behavior of Γ and T for a matched circuit ($Z = Z_0$ and mismatched circuit $Z \ll Z_0$ or $Z \gg Z_0$) and sees, that in the matched case $\Gamma = 0$ and $T = 1$ meaning that all the power delivered to the port is going through the device (no reflection), whereas in a mismatched circuit $\Gamma \to 1$ and $T \to 0$, indicating nearly perfect reflection.
We now have a method to detect the transmission and reflection of a circuit over a wide bandwidth. Thus, we also know the absorption as transmission, reflection and absorption must sum up to the input signal. Typically, the devices one uses are mismatched to the standard impedance of $50\,\Omega$ and sending a signal directly to the device would result in almost $100\,\%$ reflection. A clever method to match the device better to an impedance of $50\,\Omega$ are so-called matching networks.

4.2 Matching networks

Matching networks are circuits that are used to match the output impedance of a signal source with the input impedance of a load by using reactive elements. One can think of matching networks in two ways. First, the matching network can be considered as a modification of the source impedance, resulting in a source impedance that matches the load impedance. Second, the ensemble of matching network and load build a new load with the impedance of the source. We will use the latter picture to understand what happens in our circuit. Our device can be considered as a very large resistance ($\gtrsim 100\,\text{k}\Omega$) with a parasitic capacitance ($\sim 0.1\,\text{pF}$), which includes the device capacitance, in parallel. The

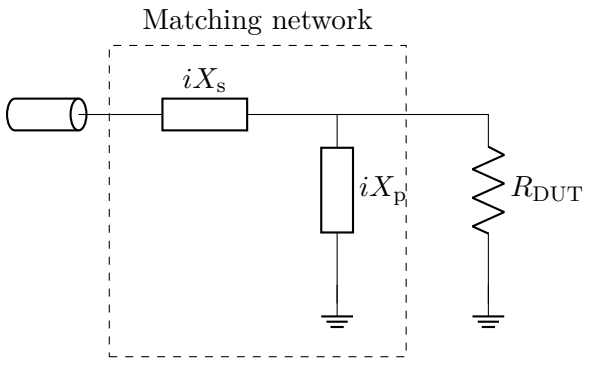

(a) L-matching network

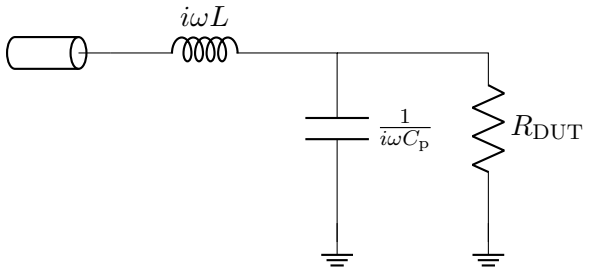

(b) Reflectometry circuit model

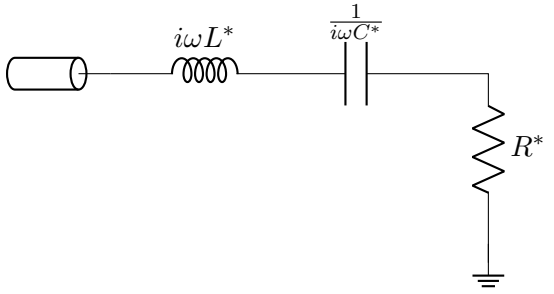

(c) Series RLC equivalent circuit

Figure 4.2: Circuit diagrams of the rf-reflectometry circuit. **(a)** L-matching network with series impedance iX_s and parallel impedance iX_p. **(b)** Circuit model for the rf-reflectometry setup. **(c)** Equivalent series RLC circuit for the rf-reflectometry circuit of **(b)**.

simplest matching networks are the so-called L-networks that consist of two components as depicted in figure **4.2(a)**. Comparing this with our device, it becomes clear that we can consider the parasitic capacitance as the parallel component of our matching network with impedance $Z_\mathrm{p} = iX_\mathrm{p}$ and what we need to do is to add the appropriate series component with impedance $Z_\mathrm{s} = iX_\mathrm{s}$ to match to our device impedance $Z_\mathrm{DUT} = R_\mathrm{DUT}$.

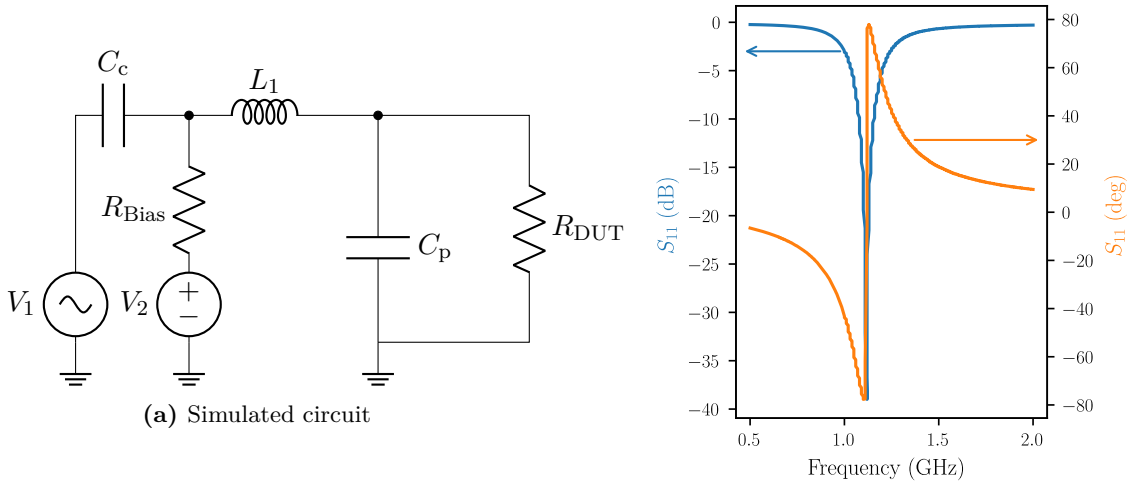

(a) Simulated circuit

(b) S_{11} spice simulation

Figure 4.3: The equivalent circuit used for the simulation is depicted in figure **(a)**. The source V_1 is coupled to the resonance circuit through a capacitor C_1 to block any DC component. C_c forms with R_{Bias} a bias-T that allows to apply a DC bias V_2. The inductance L_1, the capacitances C_p (parasitic capacitance) and the resistance R_{DUT} build an RLC circuit. **(b)** A simulation, using the free SPICE software *LTSPICE XVII*, of the circuit was used to predict system parameters. Reproducing our S_{11} measurements, we can use the simulation software to determine parameters like the parasitic capacitance.

The impedance of the network is then given by

$$Z = Z_s + (1/Z_{DUT} + 1/Z_p)^{-1} = Z_i + \frac{Z_{DUT}Z_p}{Z_{DUT} + Z_p} \stackrel{!}{=} Z_0 \tag{4.5}$$

$$\begin{aligned} \Leftrightarrow Z_0 &= Z_s + \frac{Z_{DUT} + Z_p}{Z_{DUT} + Z_p} = iX_s + \frac{R_{DUT}(iX_p)}{R_{DUT} + iX_p} \\ &= iX_s + \frac{R_{DUT}X_p^2}{R_{DUT}^2 + X_p^2} + j\frac{R_{DUT}^2 X_p}{R_{DUT}^2 + X_p^2} \\ \Rightarrow Z_0 &= \frac{R_{DUT}X_p^2}{R_{DUT}^2 + X_p^2} \\ \Rightarrow X_s &= -\frac{R_{DUT}^2 X_p}{R_{DUT}^2 + X_p^2} \xrightarrow{X_p = -(\omega C_p)^{-1}} -\frac{R_{DUT}^2 \omega C_p}{1 + R_{DUT}^2 \omega^2 C_p^2} \end{aligned} \tag{4.6}$$

We see that for an L-network, the resistive matching is defined by the parallel component and the series reactive component must be of opposite sign to the parallel reactive component. Thus, we need to add an inductance with the impedance given by equation 4.6. Another point to consider are the series and parallel quality factors $Q_s = |X_s/R_0|$ and $Q_p = |R_{DUT}/X_p|$ respectively. These quality factors need to be equal for perfect

matching, resulting in $Q_\mathrm{s} = Q_\mathrm{p} = \sqrt{R_\mathrm{DUT}/R_0 - 1}$ [Poz11]. As the impedance of the reactive components depends on the frequency, the operation frequency will be defined by the parasitic capacitance

$$\begin{aligned} R_0 &= \frac{R_\mathrm{DUT} X_\mathrm{p}^2}{R_\mathrm{DUT}^2 + X_\mathrm{p}^2} \\ \Rightarrow R_0 &= \frac{R_\mathrm{DUT} \frac{1}{\omega^2 C_\mathrm{p}^2}}{R_\mathrm{DUT}^2 + \frac{1}{\omega^2 C_\mathrm{p}^2}} \\ \Leftrightarrow \omega_\mathrm{match} &= \pm \frac{\sqrt{R_\mathrm{DUT} - R_0}}{C_\mathrm{p} R_\mathrm{DUT} \sqrt{R_0}}. \end{aligned} \tag{4.7}$$

With typical values of $R_0 = 50\,\Omega$, $R_\mathrm{DUT} = 200\,\mathrm{k}\Omega$ and $C_\mathrm{p} = 0.3\,\mathrm{pF}$ we find a frequency of $f_0 = \omega_0/(2\pi) \sim 170\,\mathrm{MHz}$. Now that we know that we need an inductance as a third component, it becomes clear that our circuit is an RLC-circuit. As it is neither a pure series RLC- nor a pure parallel RLC-circuit, we can use an equivalent circuit to describe it as a pure series RLC-circuit. We simply identify the resistive and reactive part of our circuit with the resistive and reactive part of a series RLC-circuit, yielding

$$\begin{aligned} Z_\mathrm{s} + (\frac{1}{Z_\mathrm{DUT}} + \frac{1}{Z_\mathrm{p}})^{-1} &= Z_\mathrm{s}^* + Z_\mathrm{DUT}^* + Z_\mathrm{p}^* \\ \Leftrightarrow i\omega L + (\frac{1}{R_\mathrm{DUT}} + i\omega C_\mathrm{p})^{-1} &= i\omega L^* + R_\mathrm{DUT}^* + \frac{1}{i\omega C_\mathrm{p}^*} \\ \Rightarrow R_\mathrm{DUT}^* &= \frac{R_\mathrm{DUT}}{1 + \omega^2 R_\mathrm{DUT}^2 C_\mathrm{p}} \xrightarrow{\omega=\omega_\mathrm{match}} R_0 \\ \Rightarrow L^* &= L \\ \Rightarrow C^* &= C_\mathrm{p} + \frac{1}{R_\mathrm{DUT}^2 \omega^2 C_\mathrm{p}} \xrightarrow{\omega=\omega_\mathrm{match}} C_\mathrm{p}(1 + \frac{R_0}{R_\mathrm{DUT} - R_0}) \xrightarrow{R_\mathrm{DUT} \gg R_0} C_\mathrm{p}. \end{aligned} \tag{4.8}$$

We see that the matched circuit can be treated like a series RLC-circuit with a resistance identical to the source resistance. Thus, operating at the resonance frequency of this circuit would yield perfect matching. Why does the device suddenly "absorb" more energy by adding an inductance? The reason is that the network that we have build is actually a resonator. The signal from the source is absorbed in the resonator. The resonator increases the power of the input signal by its Q-factor and the resistance of our device sees a much larger voltage. Of course, this is a very simple model that assumes perfectly linear components and no other loss channels. Nevertheless, we can use it to get an idea of the parameter ranges for our setup. One could now ask what happens if we are not working at the resonance frequency f_0. Looking at the circuit differently, the inductance acts as a low-pass while the parasitic capacitance acts as a high-pass. In other words, the matching network acts like a band pass. Changing the frequency reduces the matching and the signal reflection is increased. For the experimentalist this means that using the

VNA, one can easily detect the best matching by finding the resonance frequency of the circuit. Knowing that we can send a signal to a matched circuit even though the device impedance is not $50\,\Omega$ is the first step. We have seen as well that we are operating at a resonance frequency f_{res} and a small change of the frequency can considerably change the reflected signal. How large this change is depends on how sharp the LC-resonance is. A way to measure this is the quality factor. One distinguishes the unloaded quality factor Q_0, the loaded quality factor Q_{L} and the external quality factor Q_{e}. For a series RLC-circuit, these are defined as

$$Q_0 = \omega_0 \frac{L}{R} = \frac{1}{\omega_0 RC} = \frac{1}{R}\sqrt{\frac{L}{C}} \tag{4.9}$$

$$Q_e = \frac{\omega_0 L}{R_{\mathrm{L}}} = \frac{1}{R_{\mathrm{L}}}\sqrt{\frac{L}{C}} \tag{4.10}$$

$$\frac{1}{Q_{\mathrm{L}}} = \frac{1}{Q_0} + \frac{1}{Q_{\mathrm{e}}}, \tag{4.11}$$

where R_{L} is the resistance of an external load. The unloaded quality factor is considering the resonator without any external losses. The external quality factor considers the losses through connected loads [Poz11]. The loaded quality factor takes the total of the losses into account. Typically, one measures the loaded quality factor using a VNA. It can be shown that $Q_{\mathrm{L}} = \frac{f_0}{\Delta f_{3\mathrm{db}}}$, where $\Delta f_{3\mathrm{db}}$ is the full-width at half-maximum (FWHM) of the resonance. The take home message for us is that $Q \propto \sqrt{L/C}$, meaning that we can increase the quality factor by decreasing the parasitic capacitance in our circuit. With the quality factor we can define the so-called coupling coefficient $g \coloneqq Q_0/Q_{\mathrm{e}}$. For values of $g < 1$ ($R > R_{\mathrm{L}}$), we say that the resonator is undercoupled and for $g > 1$ ($R < R_{\mathrm{L}}$), we say that the resonator is overcoupled. If the resonator is impedance matched ($g = 1$), the resonator is critically coupled. The coupling coefficient can be measured with a VNA using $g = \frac{S_{21}(\omega_0)}{1-S_{21}(\omega_0)}$ [Poz11].
For a better understanding of our system without too many approximations we used the Spice software *LTSPICE XVII* to simulate our system, using the circuit depicted in figure **4.3**. It allowed us to simulate the circuit together with the bias-T we used. Moreover, using a spice software allows to modify the circuit freely and explore other circuit architectures without tedious calculations and approximations. For the circuit depicted in figure **4.3(a)** we know all the circuit parameters except the parasitic capacitance. We can estimate the parasitic capacitance by tuning the simulated circuit parameters to make the resonance match with the measured resonance of our setup. As depicted in figure **4.3(b)**, we find a resonance at $\sim 1.1\,\mathrm{GHz}$ for $C_{\mathrm{p}} = 0.3\,\mathrm{pF}$, close to the resonance we find for our setup. We want to mention here that the spice software always assumes lumped element circuits and thus might not agree with measurements when working with very small inductors.
Before discussing rf-reflectometry measurements, we want to briefly present alternative matching circuits.

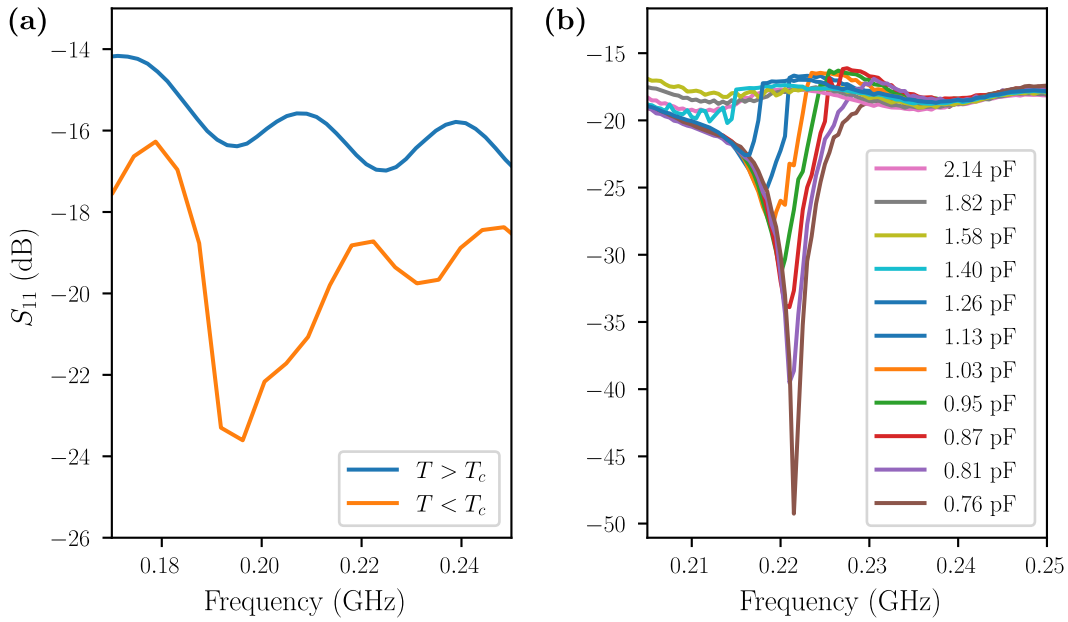

Figure 4.4: S_{11} signal of a reflectometry circuit with a varactor in parallel with the parasitic capacitance C_p. **(a)** S_{11} signal for $T > T_\mathrm{c}$ and $T < T_\mathrm{c}$, where T_c is the critical temperature of the Nb inductor. The S_{11} signal for $T < T_\mathrm{c}$ clearly shows a dip between 190 MHz and 200 MHz with respect to S_{11} for $T > T_\mathrm{c}$, indicating the resonance of the circuit. **(b)** S_{11} signal for different varactor capacitance values, showing an improved quality factor with decreasing capacitance.

4.2.1 Reflectometry circuits for improved impedance matching

Different alternative circuits have been tested to improve the reflectometry setup with a focus on better impedance matching. They range from alternative coupling schemes [Ibb21], alternative matching circuits [Ahm18; Sch20] to the use of varactors [Ibb19]. During this thesis, all of these methods were tested, but did not show a significant improvement compared to the circuit discussed in section 4.1. For instance, using an inductively and capacitively coupled inductor to a stripline as it was used in [Ibb21], instead of a galvanic connection, did not show a strong enough reflectometry signal such that we were not able to use this circuit for reflectometry. We assume that the parameters for such a setup must be carefully chosen to achieve sufficiently strong coupling between stripline and inductor. However, this technique allows to reduce the parasitic capacitance significantly and thus may need further study to determine the design parameters. The alternative matching circuit proposed by Ahmed et al. [Ahm18] replaces the series inductance with a coupling capacitance and sets the inductor in parallel with the parasitic capacitance and the device. Such a circuit adds another tuning knob to adjust the matching. As depicted in figure **4.5**, the coupling interdigited (IDT) capacitor can be integrated on-chip, making it a very

(a) On-chip inductors with coupling capacitor

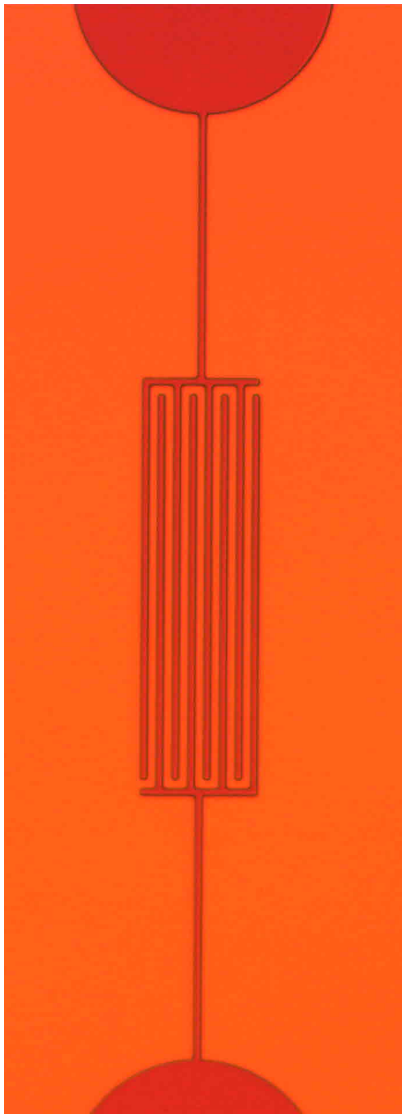

(b) Coupling IDT capacitor

Figure 4.5: **(a)** On-chip inductors with a coupling capacitance IDT. **(b)** On-chip coupling capacitance IDT for rf-reflectometry.

compact circuit. We found that it is very difficult to find the right coupling capacitance as it has to be very small and a good knowledge about the circuit parameters is needed to select the right capacitance and inductance. Lastly, a varactor in parallel with the parasitic capacitance allows to tune the capacitance of the circuit. It is a very attractive method if the system parameters are not known. As depicted in figure **4.4**, the varactor allows to tune the matching significantly. We use a Macom® MA46H202 varactor. The varactor capacitance can be ranged between $\sim 1\,\mathrm{pF}$ - $10\,\mathrm{pF}$ and is GaAs based, allowing operation at cryogenic temperatures without freeze out. If using a varactor is useful is a trade off between improved matching and increase in capacitance. Increasing the total capacitance C_{tot} reduces the reflectometry signal as $SNR \propto \frac{\Delta C}{C_{\mathrm{tot}}}$ and thus should be avoided. In our case, the plot in figure **4.4(b)** reveals that reducing the varactor capacitance continuously improved the matching. We therefore assumed that our circuit rather needs a lower C_{tot} than a larger. Hence, we did not pursue using a varactor in our setup.

4.2.2 Improving the sensor sensitivity

While the demonstration of the superior scalability of gate-based radio-frequency reflectometry compared to multi-terminal sensors like SETs comes for free with the demonstration of a simple proof of principle, demonstration of state-of-the-art charge sensitivity is harder to achieve. So far, many researchers used non-optimized circuits to test this novel sensing approach, resulting in often subpar performance compared to SET measurements [Wes19]. As we have seen, the measured phase shift due to the capacitance change is given by $\Delta\phi = Q\frac{\Delta C}{C_{\mathrm{tot}}}$. Being limited by the Johnson-Nyquist noise of the low-noise amplifier at the 4K-stage, we assume for the noise power $\bar{V}_{\mathrm{n}}^2 = 4k_{\mathrm{B}}TR\big[V^2/Hz\big]$. We see that if we want to increase the SNR, we have two options. First, we can increase $\Delta\phi$ by improving the quality factor Q, reducing the total capacitance C_{tot} or increase the capacitive shift. The latter one depends on the tunneling regime such that the resonance frequency of the circuit should be chosen to maximize ΔC. Second, decreasing the noise affecting the measurement by reducing the dominant noise source (e.g. reducing the thermal noise by using a superconducting amplifier (see section **7.1.1**)). For most setups, the probably easiest way to improve SNR is by improving the LC-circuit. Improving the quality factor Q often goes along with a better matching of the device impedance. The total capacitance C_{tot} can often be considerably improved by using on-chip inductors instead of SMD inductors. SMD inductors have themselves rather large soldering pads, these metallic plates result in a large parasitic capacitance. Additionally, the circuit board, where these are mounted, often adds parasitic capacitances due to bond pads and metal tracks.

4.3 RF-QPCs, RF-SETs and gate-based reflectometry

The first reflectometry measurements were done using charge sensors like quantum point contacts (QPCs) and single electron transistors (SETs) [Sch98]. These devices measure a current that depends on the electrostatic environment. To be more specific, in a typical measurement, the QPC or SET is tuned to a point where a conductance step occurs,

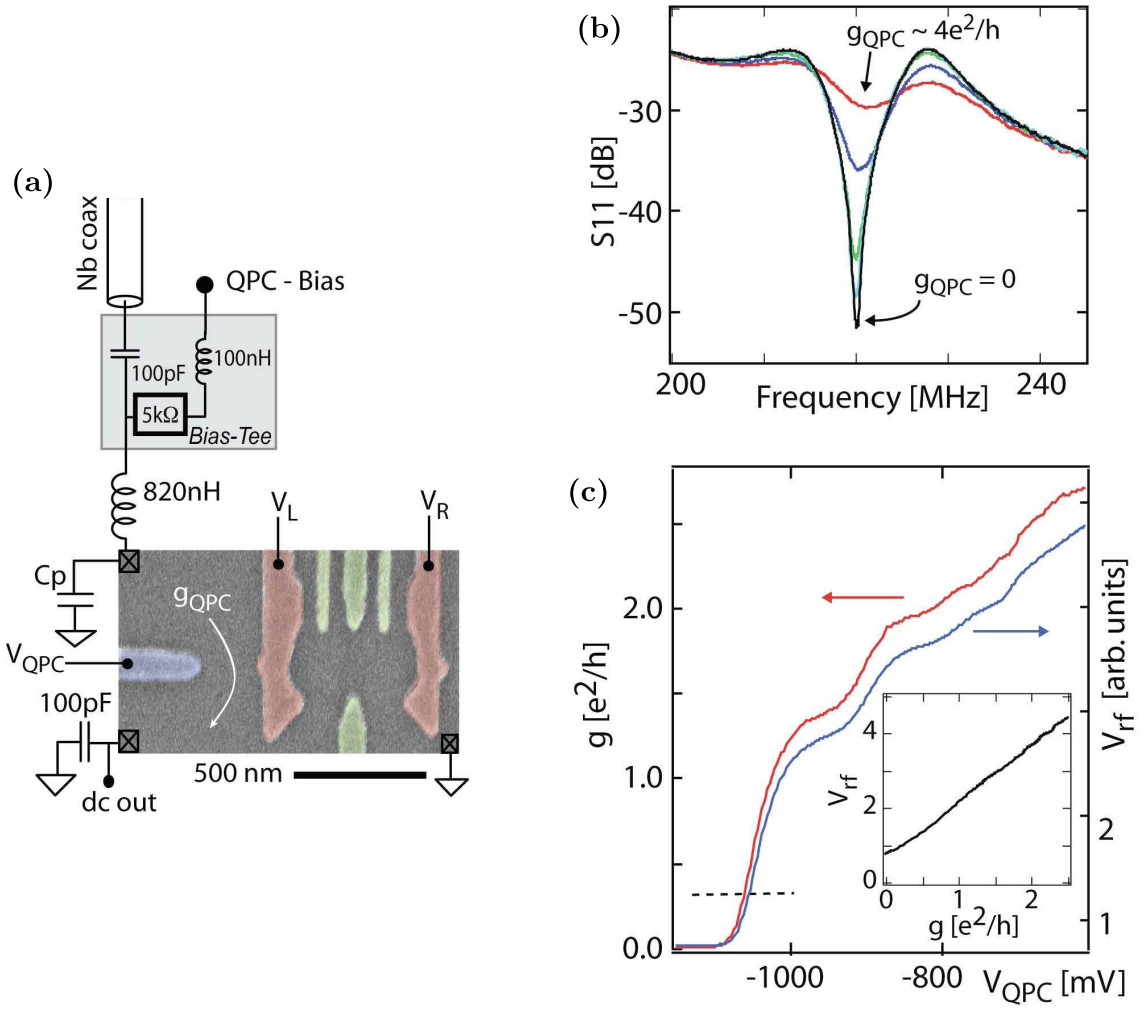

Figure 4.6: RF-quantum point contact for remote sensing of quantum dots. **(a)** RF-circuit with QPC used for readout. **(b)** RF-QPC circuit resonance for a set of QPC conductance. **(c)** Conductance as a function of QPC bias voltage. Adapted from [Rei07]

yielding to a steep slope of current with changing gate voltage. The conductance depends on the gate voltages and the electrostatic environment. When charges are loaded or unloaded to quantum dots nearby, the local electrostatics change, resulting in a change of measured current. In an rf-measurement, the same situation applies, but this time one measures an ac-current. The inductor is connected to source or drain, forming a resonance circuit. A frequency close to resonance probes the rf-circuit by measuring the reflected signal. The QPC or SET is tuned to optimize the impedance matching and maximize the signal change (e.g. at a conductance step) due to changes of the electrostatic environment. An example of such an rf-QPC setup and the related measurements are depicted in figure **4.6**. A bias-T allows to modulate the QPC-bias with an rf-tone (see figure **4.6(a)**). The change of conductance can be tuned with the gate voltage V_{QPC} (see figure **4.6(c)**),

resulting in a different signal reflection of the rf-tone (see figure **4.6(b)**).
In this thesis we used gate-based reflectometry that can be used as a charge sensor similar to QPCs and SETs as well as a dispersive sensor. Dispersive readout works differently as it is not based on a current measurement. Inspired by the superconducting qubit community, a dispersive readout is to couple the readout directly to the qubit. The coupling is off-resonance such that the readout does not drive the qubit. However, the state of the qubit affects the readout mechanism, allowing to readout the qubit state without driving it [Dev04]. For spin qubits that do not use electric fields to drive the qubit, one is free to choose the frequency for dispersive readout[1]. As our QDs are controlled by accumulation gates, we can use these for dispersive readout. The gate resistance is very large ($\gtrsim 100\,\mathrm{k}\Omega$) and can just be estimated since at rf-frequencies the dissipation varies due to resonances in the circuit, dielectric losses, etc.. We will see as well that the impedance of the device can be state dependent. Due to the experimental setup, we will have capacitive contributions which we model with a parasitic capacitance C_p in parallel with the device resistance. The crucial property of dispersive readout for QDs is that there is not only a static capacitance C_p, but a state dependent capacitance C_QD. This state dependent capacitance causes a dispersive shift of the resonance frequency and thus can be detected using a homodyne detection method like gate-based rf-reflectometry.

In order to measure small capacitive changes of the device, we connect the device to an LC-circuit. We probe the LC-circuit by measuring the reflection of an rf-tone close to resonance. To understand the complete measurement circuit depicted in figure **4.7**, we want to give in the following an overview of the setup components and the role they play in the measurement. A hopefully didactic way of describing the measurement setup is to follow the signal from it's generation to the final acquisition. We used a Windfreak Technologies® SynthNV signal generator, allowing us to generate an rf-signal between 34.4 MHz to 4.4 GHz of up to 10 dBm. We typically used 3 dBm as output power of the rf-source. The signal was then split with one channel going in the local oscillator input of a Polyphase microwave® AD0460B demodulator and the other channel going through a Renesas® F2932 rf-switch. After, the signal from the rf-switch is passed through a Renesas® IDT F225x voltage controlled attenuator to control the rf-power of this channel. Next, the signal is passed through two XMA® 20 dB attenuators, one at room temperature and one at 4 K, reducing the noise on the rf-signal to the 4 K level. After, the signal is coupled into a directional coupler with an integrated attenuation of 20 dB, reducing the thermal noise on the signal further to $\sim 100\,\mathrm{mK}$. The directional coupler sends the signal to the LC-circuit, consisting of a Nb on-chip inductor and the sample. The reflected signal in then passed through the directional coupler into a low-temperature low-noise amplifier (add type), where the signal is amplified by 25 dB. After, the signal is amplified at room temperature by $\sim 40\,\mathrm{dB}$ using two Minicircuits® ZX60-33LN-S+ amplifiers. The rf-input of the demodulator receives the signal and demodulates it into I- and Q-signal using the local oscillator signal that was split off after signal generation. I- and Q-signals are the

1 EDSR uses electrical fields to drive the qubit and thus would need to obey the same limitations as superconducting qubits

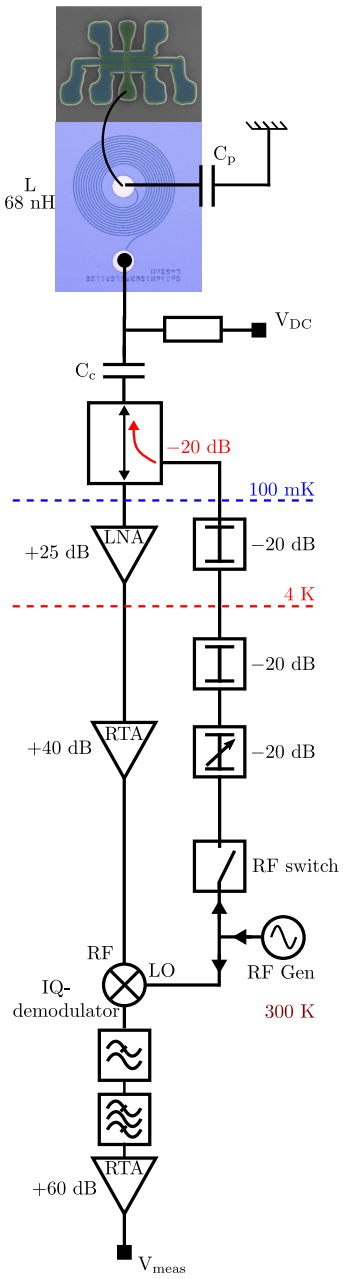

Figure 4.7: RF-setup as it was used in the presented experiments. An RF generator sends an rf-tone that is split into an LO- and an RF-signal. The RF-signal is sent to the device where it is partially reflected. The reflected signal is amplified and demodulated in an IQ-modulator using the LO-signal. The IQ quadratures are filtered, amplified and finally measured.

product of the two input signals where I is the in-phase signal and Q is the signal product with a 90° phase shift applied to the local oscillator. The I- and Q-signals are then filtered using a Minicircuits® VLFX-80 and a Minicircuits® SLP-1.9+ low-pass filter. In a final step, a band pass filter with DC−30 kHz and a 10^3 amplification is applied before the signal is sent to the input of the NI® USB-6229 ADC. Now that we know how the measurement circuit works, we want to present the physical origin of the capacitive change and after, discuss the possible improvements to the measurement circuit.

4.4 Quantum and tunneling capacitance

The state dependent capacitance that is exploited in dispersive readout arises from different physical effects. The origins of the observed dispersive shift are discussed in several articles [Cot11; GZ15; Hou15; Miz17], and we want to focus on the key takeaways from these studies. We can distinguish two contributions to the state dependent capacitance. First, there is a contribution from the tunneling dynamics of the system, yielding to different charge susceptibility for different states. We will refer to this contribution as tunnel capacitance. Second, the so-called quantum capacitance arises from adiabatic charge transitions and the curvature of the eigenstates of the system.
We will first consider a single quantum dot tunnel coupled to a reservoir[1] before discussing a double quantum dot system. We can model the single quantum dot-reservoir system as a two-level quantum system. The two states under consideration are $n_0 = N$ and $n_1 = N+1$ with energy E_0 and E_1 respectively, where n_i is the number of electrons in the quantum dot. While the density of states (DOS) for the QD consists of discrete levels, and we consider just one in our model, the DOS of the reservoir is metallic and 3D and thus can be described as a continuum with a population following the Fermi-Dirac statistic. By applying a bias voltage V_g to the gate that controls the quantum dot, we can tune it to the degeneracy point $n_\mathrm{g}^0 = C_\mathrm{g} V_\mathrm{g}/e = N + 0.5$, where the energy level of the QD is aligned with the electrochemical potential μ of the reservoir. Applying an ac-voltage $V_\mathrm{g}^{rf} \sin \omega_0 t$ to the gate allows to drive the system between the two states with

$$n_\mathrm{g} = C_\mathrm{g} \frac{V_\mathrm{g} + V_\mathrm{g}^{rf}}{e} = n_\mathrm{g}^0 + \delta n_\mathrm{g}. \tag{4.12}$$

We want to distinguish two regimes that depend on the tunnel coupling between reservoir and QD. First, the low tunneling rate regime $k_\mathrm{B}T \gg \hbar\Gamma_0$, where Γ_0 is the tunneling rate between reservoir and QD, and T is the electron temperature of the reservoir. Second, the high tunneling rate regime $k_\mathrm{B}T \ll \hbar\Gamma_0$. In the low tunneling regime, the tunnel

1 Such systems are known as single lead quantum dots or single-electron boxes in the literature[Per10].

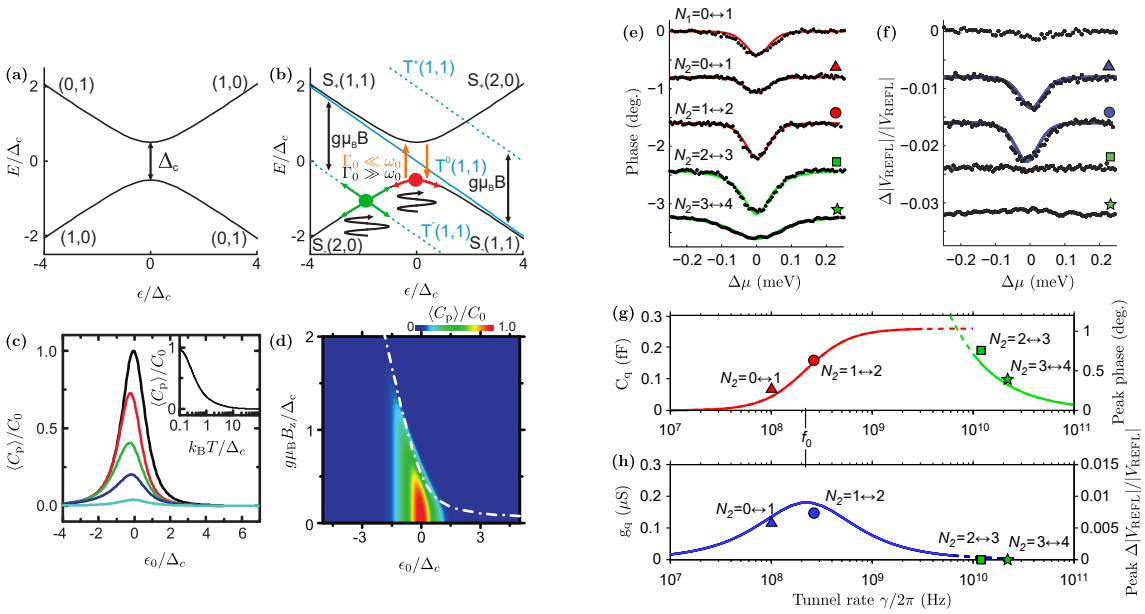

Figure 4.8: **(a)** Energy level diagram of a single electron in a DQD at the interdot transition with a tunnel coupling Δ_c. **(b)** Energy level diagram of a two electron system in a double quantum dot at the (1,1) - (2,0) transition. The Zeeman energy $E_z = g\mu_B B_z$ lifts the triplet degeneracy and an rf-drive applied to the detuning results in an oscillation along the energy levels. If the drive frequency ω_0 is much slower (faster) than the charge relaxation (spin relaxation for singlet-triplet anti-crossing), avoided level crossings are passed adiabatically (non-adiabatically). In the case of non-adiabatic transitions, Sisyphus resistance can occur (orange arrows). **(c)** Parametric capacitance line shape as a function of detuning for different temperatures $k_BT/\Delta_c = 0.1, 0.25, 0.5, 1.0, 5.0$ (black, red, green, dark blue, light blue). The maximal parametric capacitance as a function of k_BT/Δ_c is depicted in the inset. **(d)** Parametric capacitance as a function of detuning ε_0/Δ_c and Zeeman energy $g\mu_B B_z/\Delta_c$, where the dot-dashed white line indicates the position of the S_0-T_- crossing. **(e)** Phase response for different charge transition detected using gate reflectometry with fits using equation 4.13. **(f)** Amplitude response for each of the charge transitions from **(e)** identifiable by the triangle, circle, square and star. The fits use equation **4.14**. **(g)** Parametric capacitance as a function of tunnel rate γ (Γ_0 in the main text) with a plot of the $\hbar\gamma \gg k_BT$ regime (green) using equation **4.15** and $\hbar\gamma \ll k_BT$ (red) using equation **4.13**. **(h)** Conductance g_q as a function of tunnel rate using equation **4.14**. Figures **(a)-(d)** are adapted from [Miz17] and figures **(e)-(h)** are adapted from [Hou15].

capacitance and conductance are given as

$$C_\mathrm{t} = \frac{\alpha^2 e^2}{4k_\mathrm{B}T} \frac{1}{1+\omega_0^2/\Gamma_0^2} \frac{1}{\cosh^2(\Delta\varepsilon/2k_\mathrm{B}T)} \tag{4.13}$$

$$g_{sis} = \frac{\alpha^2 e^2}{4k_\mathrm{B}T} \frac{\Gamma_0}{1+\Gamma_0^2/\omega_0^2} \frac{1}{\cosh^2(\Delta\varepsilon/2k_\mathrm{B}T)}, \tag{4.14}$$

where $\Delta\varepsilon$ is the detuning of the QD energy level with respect to the electrochemical potential μ of the reservoir [Cot11; GZ15; Hou15]. Using these equations allows to fit the reflectometry response (see figure **4.8(e)/(f)**) and identify the tunnel rate with respect to the temperature as depicted in figure **4.8(g)** and figure **4.8(h)**. In the low tunnel rate regime the electron can follow the electrical drive and performs Landau-Zener transitions when passing through the degeneracy point. For a non-adiabatic transition, this can lead to inelastic tunneling after passing the degeneracy point. The energy dissipation during this process is known as Sisyphus resistance [Per10]. The line shape depends on the temperature as the reservoir cut-off smears out with increasing temperature, broadening the tunneling range with increasing temperature. This allows to use the signal response for measuring the electron temperature (see figure **4.8(d)**) [Ahm18]. As this regime shows a change in the resistance as well as capacitance of the circuit, signal amplitude as well as phase change when working in this regime. Using an IQ demodulator allows to measure the signal amplitude as well as phase. However, it as well allows to "rotate" the signal in the IQ-plane and shift all information (phase + amplitude) into on quadrature. Measuring a single channel instead of two to retrieve the full information, allows to measure at a higher rate for many data acquisition systems.
For $k_\mathrm{B}T \ll \hbar\Gamma_0$ the electron relaxation is too slow to allow Sisyphus resistance and only a capacitive response can be found with

$$C_\mathrm{t} = \frac{\alpha^2 e^2}{\pi} \frac{\hbar\Gamma_0}{(\hbar\Gamma_0)^2 + \Delta\varepsilon^2}. \tag{4.15}$$

In this regime, the signal shape is a Lorentzian with a width defined by the tunnel coupling Γ_0.
Importantly, both regimes require that Γ_0 is of the same order of magnitude as ω[Hou15]. Hence, the experimental design must take into account the readout circuit frequency ω_0 and the expected tunnel coupling Γ_0. When working in the right regime, rf-reflectometry can be used in three ways. First, as a direct sensor of the quantum dot state, where the signal indicates a charge transition in the QD [Urd19]. Second as a charge sensor, where the QD is tuned to a degeneracy point and a shift of the sensor signal can be interpreted as a shift in the electrostatic environment nearby the QD [Nie22]. Third, as a sensor of the quantum capacitance of a interdot transition, which we will discuss in the following.
The reflectometry signal arising from transitions in a double quantum dot system are extensible discussed in [Cot11; Est19; Miz17] and the results presented here are taken from these articles. In contrast to the former case, we assume here an isolated system of two quantum dots. Both quantum dots have a 0-D DOS with discrete energy levels.

If we restrict ourself to the two states of (N+1|M) or (N|M+1), where the first (second) number stands for the number of electrons in the QD, we can describe the system with the Hamiltonian of a simple charge qubit given in equation 2.20. The energy diagram of this Hamiltonian is depicted in **4.8(a)**. In contrast to the former case, in the DQD system we find that the parametric capacitance has two contributions

$$C_{\mathrm{p}}(t) = \underbrace{\frac{(e\alpha')^2}{2\Delta_{\mathrm{c}}}}_{C_0}(\underbrace{\frac{\Delta_{\mathrm{c}}^3}{\Delta E^3}\chi_{\mathrm{c}}}_{\text{quantum}} + \underbrace{\frac{\varepsilon\Delta_{\mathrm{c}}}{\Delta E}\frac{\partial\chi_{\mathrm{c}}}{\partial t}\frac{\partial t}{\partial\varepsilon}}_{\text{tunneling}}), \tag{4.16}$$

where $\chi_{\mathrm{c}} = P_- + P_+$ is the population probability difference between ground and excited state, $\Delta E = E_+ - E_- = \sqrt{\varepsilon^2 + \Delta_{\mathrm{c}}^2}$ is the energy difference at the avoided crossing, and $\alpha' = \alpha_2 - \alpha_1$ is the difference in the lever arm on the sensing gate to the two quantum dots. The first term of the parametric capacitance can be attributed to adiabatic transitions in the double QD. The quantum capacitance is similar to the effective mass for reactive behavior as it is proportional to the curvature of the energy levels [Sil05]. The second term arises from the formerly explained Sisyphus effect of non-adiabatic transitions and relaxation. The relaxation results again in Sisyphus resistance

$$R_{\mathrm{Sis}} = \frac{4R_{\mathrm{Q}}}{\alpha'^2}\frac{k_{\mathrm{B}}T}{h\Gamma_0}(\frac{\Delta E_0}{\varepsilon_0})^2\frac{\omega^2 + \Gamma_0^2}{\omega^2}, \tag{4.17}$$

with R_{Q} the resistance quantum [Est19]. While both capacitive contributions show identical signal width $FWHM = 1.53\Delta_{\mathrm{c}}$ at low temperature ($k_{\mathrm{B}}T/\Delta_{\mathrm{c}} \ll 1$), the broadening of the tunneling term increases linearly with temperature, whereas the quantum term saturates. This allows to distinguish the two contributions using temperature dependent measurements of the FWHM. As the maximal signal strength decreases with temperature, there is a limit to the temperature range one can test [Miz17].
In the case of an even number of electrons in the two quantum dots, we need to take into account the spin physics involved in the electron exchange. A scheme of the energy levels at the interdot transition (1|1)-(2|0) is depicted in **4.8(b)**. We have already seen that for the triplet states, the transition (1|1) → (2|0) is blocked due to Pauli spin blockade. This is equivalent to a shift of the avoided crossing of the triplet states to higher detuning (deeper in (2|0)). Hence, for a triplet state the quantum capacitance is zero when for singlet the quantum capacitance can be maximal. Such an effect was observed in different studies [Urd15; Zhe19] and a simulation of this is depicted in **4.8(c)**. The spin state dependent capacitive response allows performing magneto-spectroscopy of multi-spin systems [Lun20]. We want to discuss this in more detail in the final section of this chapter.

4.5 Quantum capacitance sensing - A magneto spectroscopy study

Sensing quantum capacitance directly is probably the most scalable charge sensing technique available for quantum dots. Requiring only two quantum dots and no reservoir would allow easy integration of this readout in an array of quantum dots. So far, the use

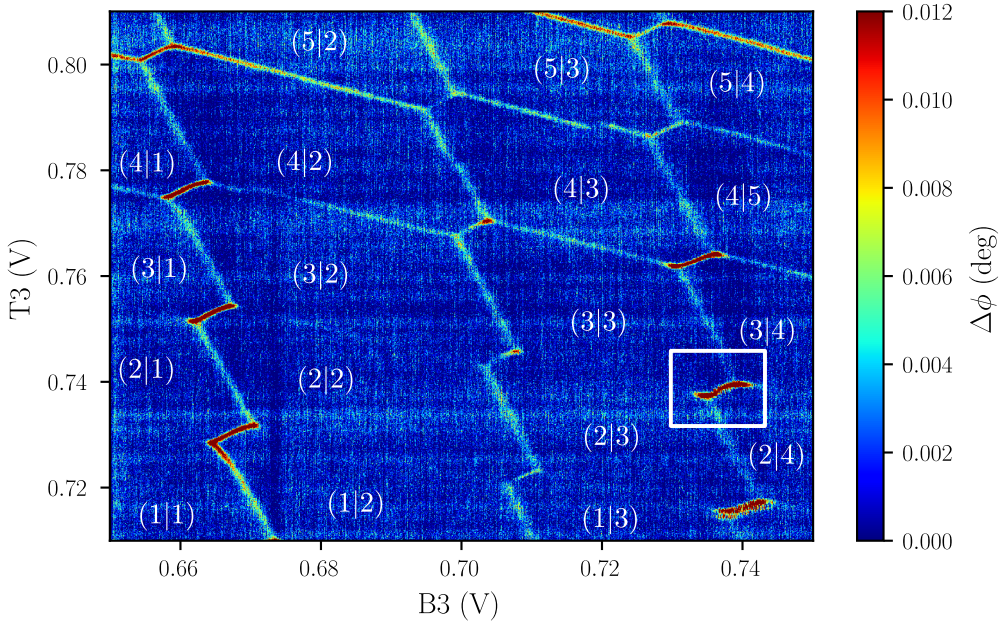

Figure 4.9: The stability diagram shows the honeycomb pattern of a double quantum dot, formed with the two gates close to a reservoir. The reflectometry setup is connected to gate T3. The labels $(i|j)$ in the honeycomb pattern are indicating the number of electrons in the QD formed by T3 and B3 respectively. It is possible that there are electron pairs occupying lower energy levels in the quantum dots that do not interact. The true number of electrons is therefore $2N + i$ (T3) and $2M + j$ (B3). The white rectangle indicates the interdot transition we used for magneto spectroscopy.

of this readout technique is rather rare and only a few publications exist that show spin detection[Wes19; Zhe19]. The dispersive shift resulting from the parametric capacitance of a double quantum dot system is often to small to yield a strong signal response necessary for single-shot readout. Especially in devices, where the tunnel coupling between QDs can not easily be controlled, the chances for a device with the right interdot coupling in the right charging regime are practically zero. An alternative use case for quantum capacitance sensing is the detection of different spin states. As we have seen in section **2.3**, tunneling can be prohibited by Pauli spin blockade in multi-electron systems. Using magneto-spectroscopy of the parametric capacitance allows mapping out the ground state of a spin system with respect to the Zeeman energy.
The results presented here have been published in [Lun20]. We use a device with 3×2 accumulation gates on top of the nanowire similar to the one depicted in figure **1.3(e)**, allowing us to form in total six QDs. The nanowire has a width $w = 80\,\mathrm{nm}$, a gate separation along the nanowire of $S_\mathrm{h} = 40\,\mathrm{nm}$ and vertical spacing of $S_\mathrm{g} = 40\,\mathrm{nm}$. The gate width is 40 nm. We use a pair of split gates (T3 and B3) close to the drain reservoir to form a double quantum dot (DQD) system. The gate reflectometry setup is connected to gate

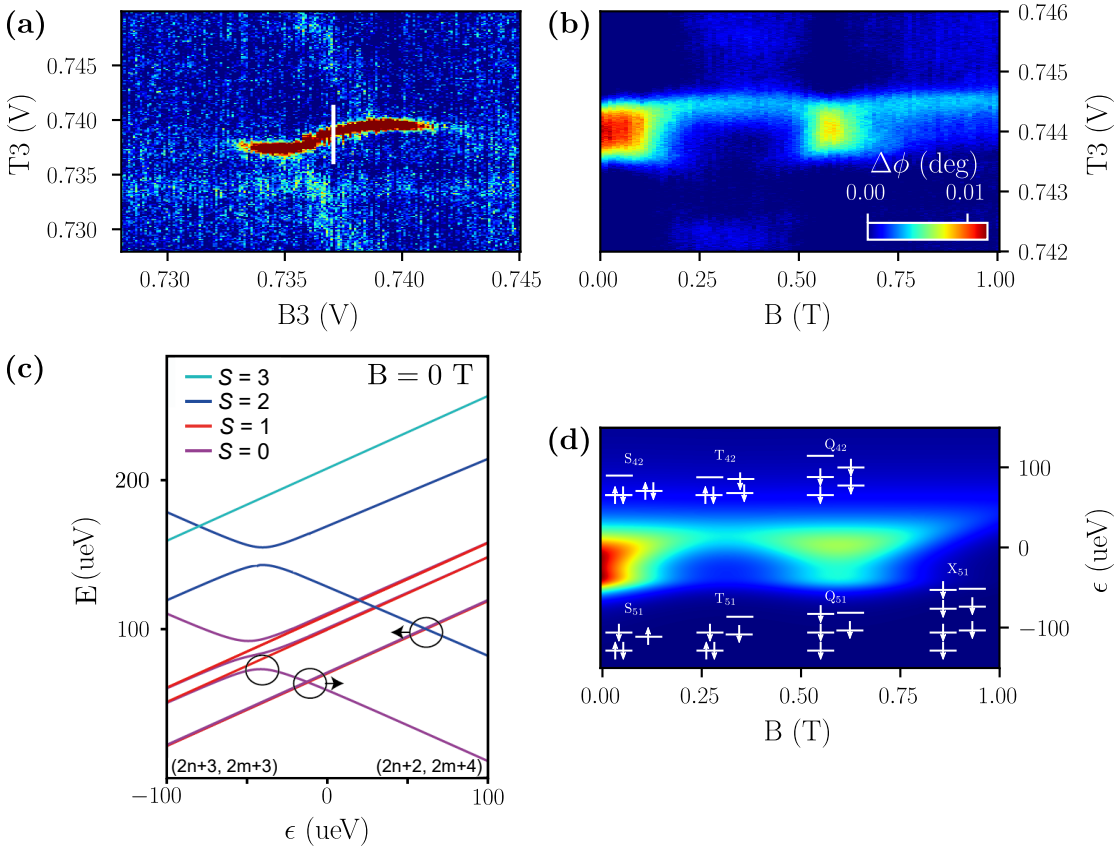

Figure 4.10: Magneto-spectroscopy and simulation of an interdot transition highlighted with a white rectangle in figure **4.9**. **(a)** Stability diagram of the interdot transition that was used for the magneto-spectroscopy. **(b)** Magneto-spectroscopy of the interdot transition, keeping the voltage on B3 constant, while sweeping the T3 gate voltage. **(c)** Energy diagram of the model used to simulate the magneto-spectroscopy. **(d)** Simulation of the magneto-spectroscopy experiment using the model depicted in **(c)**.

T3. The gate reflectometry allows us to detect a phase shift $\Delta\phi$ of the resonant circuit and detect electron tunneling between the QDs as well as between QD and reservoir. In the multi-electron regime with $(2N + i|2M + j)$ electrons we find the honeycomb pattern depicted in figure **4.9**. From our magneto-spectroscopy measurement we can infer the minimum number of electrons in the quantum dots. The respective minimal number is used to label each hexagon in the stability diagram where the first (second) number refers to the number of electrons in the QD defined by T3 (B3).

We perform magneto spectroscopy for the interdot transition highlighted in a white rectangle in the stability diagram in figure **4.9** and depicted in figure **4.10 (a)**. We keep the voltage of gate B3 constant while scanning over the interdot transition with gate T3 for a magnetic field ranging from 0 to 1 T. Additionally, we depict the magneto-spectroscopy

signal in figure **4.10 (b)**. The initial phase response at $B = 0\,\mathrm{T}$ of the interdot decreases as we increase the magnetic field up to $B = 0.12\,\mathrm{T}$. Increasing the magnetic field further to $B = 0.2\,\mathrm{T}$ results in a splitting of the signal into two separate peaks. At a magnetic field of $B \approx 0.25\,\mathrm{T}$, the peak at lower detuning vanishes whereas the peak for higher detuning does not show a significant change of signal strength. At $B \approx 0.5\,\mathrm{T}$, we can observe a revival of the signal, similar in width to the one observed at $B = 0\,\mathrm{T}$. The maximum of the resurged signal is reached at $B = 0.6\,\mathrm{T}$ from which the signal strength declines and the signal for negative detuning vanishes again for $B > 0.8\,\mathrm{T}$.
Our model to describe the magneto spectroscopy measurement consists of a six electron system with either $(2N + 3|2M + 3)$ (negative detuning) or $(2N + 2|2M + 4)$ (positive detuning) electrons. The six electrons are found in four different spin manifolds that can be identified in our measurement. With increasing magnetic field the ground state changes from a spin singlet (S) to a spin triplet (T) to a spin quintet (Q) and finally to a spin septet (X). Due to the valley degree of freedom, different singlet states are present in the system as depicted in figure **4.10 (c)**. The arrows in the energy diagram depict the shift of the crossing with increasing magnetic field. We find an avoided crossing of singlet states at $\varepsilon = -50\,\mu\mathrm{eV}$ (purple) whereas at $\varepsilon = 0$ the singlet states do not couple due to their different valleys. The model uses three different triplet states (red) and a single quintet (dark blue) that hybridizes around $\varepsilon = 50\,\mu\mathrm{eV}$. The last state to consider is a septet state (light blue). To model the measured phase response $\Delta\phi$, we calculate the quantum capacitance change according to our energy spectrum and find the simulated spectroscopy data depicted in figure **4.10 (d)**. It reproduces all the significant features of the data in figure **4.10 (b)**. In particular, the revival seen at around $B = 0.6\,\mathrm{T}$ can be explained by the hybridized quintet states that become the ground state at this field strength due to the larger Zeeman energy. Finally, at magnetic fields $B > 0.8\,\mathrm{T}$ a septet state becomes the ground state and quintet-septet blockade results in a vanishing signal for the hybridized quintet state. The different spin configurations of the ground states at different magnetic fields and detuning are shown as sketches in figure **4.10 (d)**.
Even though the results for large spin systems provide important information, the interpretation of these measurements require a lot of information about the system. The acuracy of the spin model is crucial to understand the system, but it is difficult to find such a model if one has to guess the number of spins as one has just a relative charge sensor. Additionally, the data reveals that the physics of systems with many electrons can become very complex as the ground states vary a lot within a few 100 mT. This makes such spin configurations difficult to use for qubit applications.
These measurements demonstrate the potential and the challenges of measuring the phase response as a result of changing quantum capacitance in a multi spin system. The clear potential is the rich information one can obtain from such measurements and the minimal footprint of the sensor which does not require a reservoir to perform this measurement. Requiring only two quantum dots to measure the spin state is so far the most scalable readout technique demonstrated. We will see that for large scale architectures the use of a readout quantum dot layer would allow scaling. So far, single spin sensing using gate reflectometry is still not very common [Bor21; Zhe19] and single-shot measurements are often not of sufficient fidelity to use for reliable spin sensing [Wes19]. So far, most

reflectometry applications use an ancillar quantum dot as a charge sensor to sense nearby quantum dots [Nie22; Oak22; Urd19]. In the following chapters we will demonstrate the capabilities of this approach using an ancillar QD to sense a DQD in the few-electron regime and perform high fidelity spin readout.

5 Charge sensing in a multi-dot system using source reflectometry

> We never experiment with just one electron or atom or (small) molecule. In thought-experiments we sometimes assume that we do.
>
> Erwin Schrödinger

In this chapter, we want to discuss our approach to measure multiple quantum dots using an ancillary QD nearby. First, we will discuss the procedure we used to tune the source reflectometry and build an electrometer using an ancillary QD. This will enable us to remotely sense the nearby QD charge state, yielding the addition energy spectrum for the QDs in this device for the first few electrons. Second, we will discuss the tuning procedure of the device in order to achieve appropriate capacitive and tunnel coupling between the QDs. Third, we will show the tuning of the device in the few-electron regime of a double quantum dot.

5.1 Preliminary device tests

The devices used in this work are essentially FinFET transistors and thus can be operated as such at room temperature. This makes it easy to screen the devices already before cooling them down to cryogenic temperatures. A good rule of thumb is: "If the device doesn't work at room temperature, it won't work when it is cold.". Following this rule, devices are already tested for current characteristics at a wafer level by CEA-LETI using fully automated probe stations. Moreover, wafers will be tested at temperatures $\sim 1\,\mathrm{K}$ using a newly installed Bluefors® cryo-probe station, that will allow fast feedback on the fabrication thanks to the large number of devices that can be tested.
After tests at the wafer level, the wafers are cut into dies. These dies are glued to a sample holder and finally connected to bond pads using wire bonding. Since devices can be damaged during cutting of the wafer and the bonding process, one tests the device at room temperature after installing it in the cryostat. A typical current test consists of applying a bias ($1\,\mathrm{mV} - 50\,\mathrm{mV}$), opening all gates (for the split gate devices all gates on one side) except one and sweeping this gate from $-1.0\,\mathrm{V}$ to $+1.0\,\mathrm{V}$. Such a current measurement for two bias voltages is plotted in figure **5.1**. This measurement informs about a few properties of the device. First, the device is functioning as one finds characteristic transistor I-V curves and there is no leakage current, which would result in a non-zero current for negative voltage. Second, the gates are probably slightly misaligned as the maximal current and the current onset for the T gate is higher and earlier than for the B gate. The misalignment must be small as the onset difference is $< 10\,\mathrm{mV}$ and the

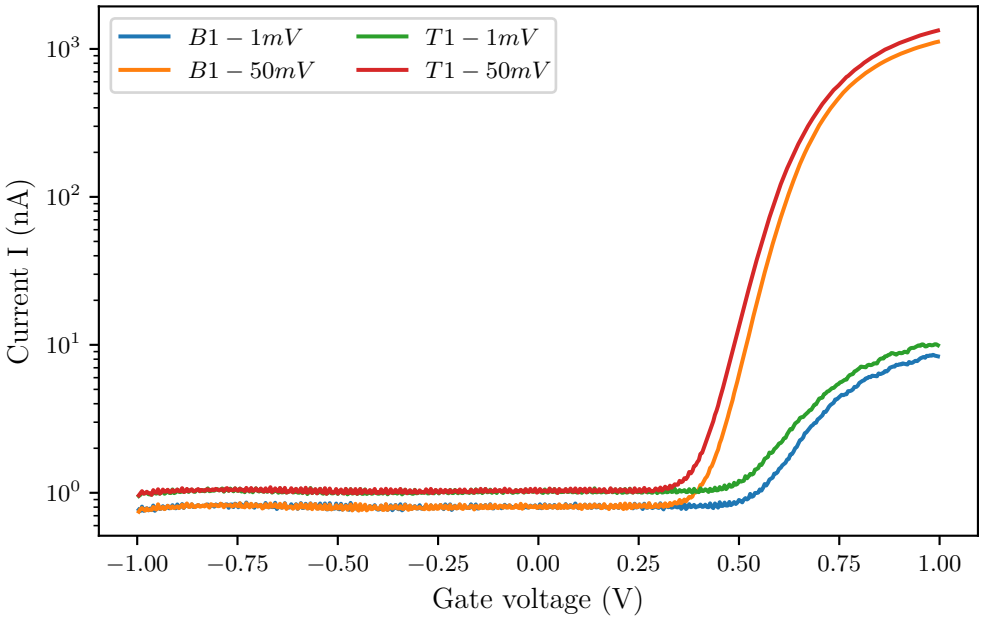

Figure 5.1: Measurement of I-V characteristics at room temperature of a 3-face-to-face device using two bias voltages (1 mV and 50 mV). Each I-V curve represents the sweep of one gate from −1 V to +1 V with the other gates on that side open (+1 V) and the opposite gate side closed (0 V).

maximal current is of the same order of magnitude. With this information, we can cool down the device to cryogenic temperatures. At this temperature the device stops showing characteristic transistor behavior as the state quantization in the quantum dots results in Coulomb blockade for low gate voltages. Moreover, small differences between the gates become much more evident as small potential differences start to matter in the quantum dot formation. How exactly the quantum dots are formed in these devices is presented in the following section.

5.2 Electrostatics of accumulation gates in FDSOI quantum dot devices

Simulations of nanowire devices reveal that the quantum dots are mainly formed in the corners of the nanowire as depicted in figure **5.2**. The electric field of the gate electrodes is strongest in the corners of the nanowire, resulting in a high probability of localization of electrons in the corners. Moreover, surface disorder yields to strong localization effects which are of particular importance in the few-electron regime where the screening potential of the quantum dot is relatively small. These results make it reasonable to refer to the quantum dots in these devices as “corner dots”. The large effective mass of electrons in silicon results in very small quantum dots in the order of $r \sim 10\,\text{nm}$. The pump devices

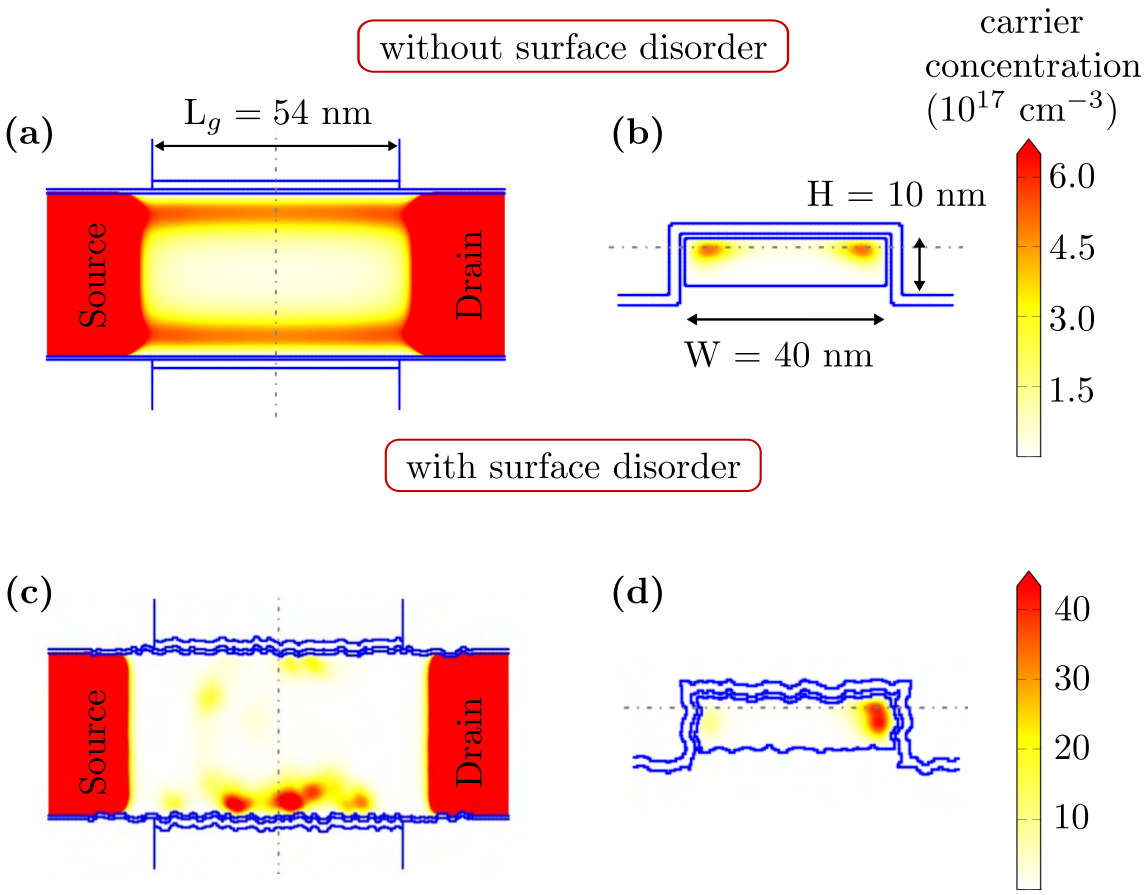

Figure 5.2: Simulation of the electron density in a Fin-FET device similar to the ones that were used in this work. The simulation of the density is performed for a temperature of 77 K (liquid nitrogen) and for the case of one electron in the nanowire channel. Figures **(a)** and **(b)** show the density along the nanowire and the cross-section respectively for the case of no surface disorder. Figures **(c)** and **(d)** depict the case of a nanowire with surface disorder. Adapted from [Voi14].

presented in section **1.3.3** are particularly affected by this as their gates span two edges and thus can control two quantum dots (one in each corner) with a single gate. For most experiments, this is not desired and one tries to have just a single quantum dot in the few-electron regime, which is often the case due to a single dominating impurity. The small extend of the quantum dot results in a very short coupling range and one can usually neglect coupling to non-nearest neighbors. The quantum dots which are not nearest neighbors with a reservoir can therefore be seen as isolated and the exchange of electrons with these is done through neighboring quantum dots. As the quantum dots form mostly at random localized potential minima caused by inhomogenities, the localization of the quantum dots is not easily controlled. This results in challenging tuning of these devices and testing of different geometries. Moreover, the gates serve a double purpose as they not only control the quantum dot's electrochemical potential, but as they are larger

than the quantum dot itself, they control as well the coupling to other quantum dots. We will make use of this in the tuning of the device.

5.3 Building an electrometer using rf-reflectometry

We discussed the principles of rf-reflectometry in section 4.3. Here we want to give an example of the application of this technique and the procedure we use to set the measurement parameters. Considering the physical origin of the rf-reflectometry signal, namely the tunneling of an electron between two locations (e.g. two QDs or a QD and a reservoir), it makes no difference from which side the tunneling is driven. For a reservoir - QD system, we can therefore choose if we want to use the reservoir or the QD gate electrode to connect to the rf-setup. There are different arguments for and against one choice. We made the case for gate reflectometry in section **4.5**. In this work we connected the source to the rf-setup for four reasons and a study, where a similar device was used with the rf-setup connected to one of the gates, can be found in [Cha20]. First, using the source doubles the chances to have a strong coupling at low electron number. The small variations in fabrication of these devices cause small differences in the gate overlap with the nanowire. More overlap results in a higher potential bump in the electrostatic landscape of this gate, making a stronger tunnel coupling to the nearby QDs and reservoirs more likely. Having two gates which barely overlap with the nanowire, a small misalignment will lead to a great difference in relative effectiveness (α-factor) of the gates. Choosing the source allows to ensure that one can use the QD of the gate that has greater overlap with the nanowire and therefore couples stronger to the reservoir. Second, the impedance match with the source electrode is better than with a gate electrode. The reasons for this better matching are not clear as both have a very high resistance, but the observed loaded quality factor seemed to be slightly improved in devices where we used source reflectometry. Third, the center quantum dots are more isolated from cross talk as the rf-modulation is not applied to a next neighbor electrode. Fourth, all gates can be operated at full speed. The inductance, used to build the LC-circuit, acts as a low-pass and the higher the inductance, the longer the rise time of the gate. We now come to the process of tuning the sensor.

5.3.1 Tuning the sensor quantum dot

Without a tool to measure changes in an experiment, we are basically blind and cannot retrieve any information from an experiment. Thus, there is no other way than starting with building a sensor. This task consists in tuning the reflectometry parameters to a position with an SNR > 1. The two parameters, one has to determine, are the rf-power and the frequency of the rf-tone, one sends to drive the rf-circuit. First, the resonance frequency of the circuit is determined by the inductance and capacitance of the circuit. While we can safely assume that the inductance is set by the inductor (neglecting small contributions from bond wires and other metal tracks), the capacitance is more difficult to estimate. Considering just the self-capacitance of a metallic disc of radius R is given by $C_0 = 4\pi\varepsilon_0 R$, it becomes clear that determine the capacitance of the LC-circuit correctly with ground planes and other metal surfaces surrounding the components is not practical.

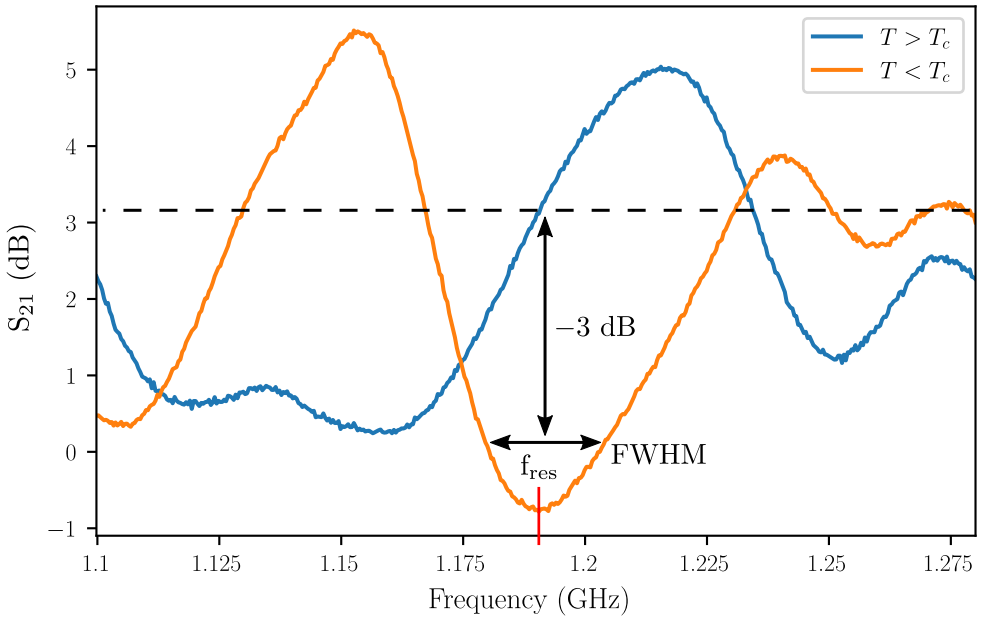

Figure 5.3: S_{21} of the measurement LC-circuit above and below the critical temperature T_c. The S_{21} for $T < T_c$ changes significantly compared to the S_{21} for $T > T_c$. We identify the resonance of the LC-circuit at f_{res} and find the FWHM using an estimated baseline (dashed black line).

In our case it is much easier to measure the parasitic capacitance C_p of the circuit. We can determine C_p by finding the resonance frequency of the LC-circuit it builds with an inductor. In our system, bond pads and ground planes are probably the main contributors, resulting in a parasitic capacitance of a few 100 fF. With an inductance of 64 nH the resonance frequency can range from a few 100 MHz up to a bit more than 1 GHz. To find the resonance frequency, one typically uses a vector network analyzer (VNA). We can use the VNA to measure the scattering parameters of a two port network as described in section **4.1**. Measuring the S_{21} parameter in the given frequency range allows us to detect the resonance frequency f_{res}, indicated by a resonance dip due to the absorption of the rf-tone by the LC-circuit at this frequency. In practice, imperfect impedance matching often causes fluctuations of the S_{21} signal due to standing waves and absorptions. These can be misidentified as resonances. Working with superconducting inductors, a useful trick to find the resonance frequency is to measure S_{21} at a temperature just above the critical temperature of the superconducting inductor and one below the critical temperature as depicted in figure **5.3**. Taking the difference of these traces should just give the resonance

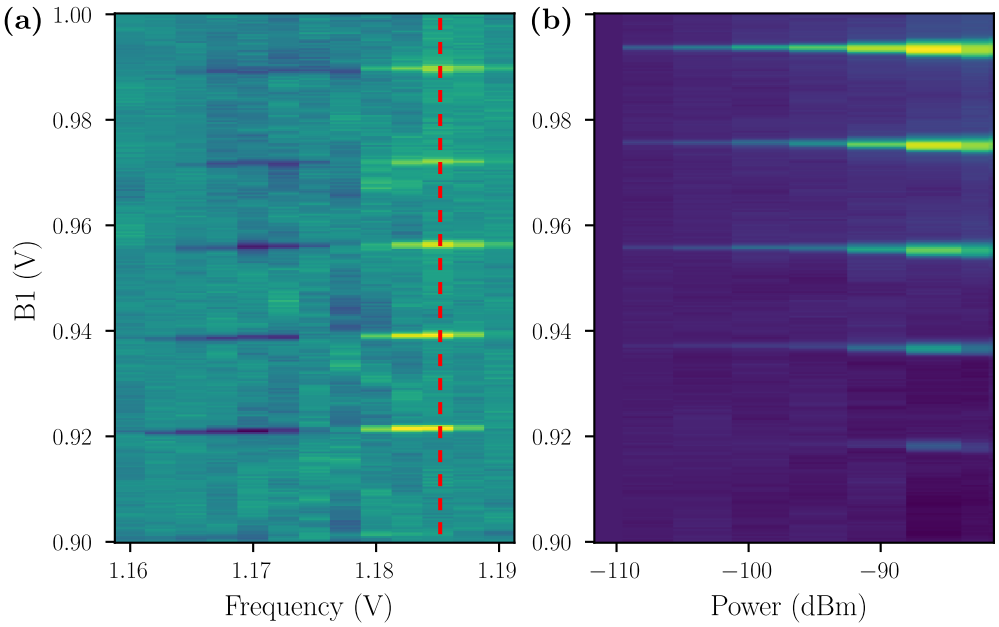

Figure 5.4: Reflectometry response as a function of frequency and power. **(a)** I-quadrature of the source reflectometry signal as a function of frequency and gate T1 voltage. The frequency range is chosen such that it includes the LC-resonance. Bright stripes indicate energy levels of QD_{T1} that result in either a shift to negative (positive) signal (blue (yellow)) for the lower (higher) frequency side of the resonance. **(b)** I-quadrature as a function of rf-power at the device level and gate T1 voltage at a fixed frequency (red dashed line in **(a)**). The I-quadrature signal narrows with decreasing power, indicating power broadening of the tunneling line shape.

dip due to the LC-circuit at the device level [1]. Apart from the resonance frequency, we can as well extract the loaded quality factor from such a measurement by calculating $Q = \frac{f_{\text{res}}}{\Delta f} = \frac{1190\,\text{MHz}}{30\,\text{MHz}} \approx 40$, where $\Delta f \approx 30\,\text{MHz}$ is the full width at half maximum (FWHM), equivalent to the bandwidth between the two 3 dB compression points, indicated in figure **5.3**.

As the reflectometry circuit is connected to the source electrode, we can use QD_{T1} and QD_{B1} as a sensor. We choose freely one of the potential gates since the optimal parameters are likely to be similar for both QDs. We set the power to a relatively high value of $-85\,\text{dBm}$ corresponding to a voltage modulation of $V_{\text{RMS}} = 40\,\mu\text{V}$. With quality factors < 100, the modulation is on the order of $\lesssim$ mV, still smaller than the addition energy for the first few electron transitions as can be seen in figure **5.5(a)**. The high power allows for stronger signal even though power broadening can negatively affect the transition

1 The change from non-superconducting to superconducting results in an effective extension of the circuit of a few millimeters. This can cause a shift of the frequency of standing waves and thus the difference between the two signals results in a non-zero background.

sharpness. Next, we measure the reflectometry signal as a function of B1 voltage (we could as well use T1) vs. rf-frequency. We start with the frequency instead of the power as we need to find the maximal slope of the resonance first before optimizing the power. The power stored in the resonator depends on how close the rf-frequency is to the resonance frequency of the circuit, changing the frequency afterwards would require a retuning of the power.
An example of such a measurement for a device, similar to the devices presented in the rest of this chapter, is depicted in figure **5.4**. We sweep B1 from a few hundred mV below the current onset value, that we found in the current measurement, to a value a few hundred mV above the current onset value. The frequency is varied in a range that covers the complete resonance. Figure **5.4(a)** depicts such a measurement, where the B1 range was reduced to the first visible transitions. A measurement bandwidth of 1 kHz ensures a relatively high SNR that allows to detect a signal even with not optimized parameters. We set the rf-frequency to $f \approx 1185\,\mathrm{MHz}$ (indicated with a red dashed line in figure **5.4(a)**) as the SNR at this frequency is highest. Next, we optimize the power by doing a similar scan as before, changing the attenuation of the rf-power in place of the frequency. From the map in figure **5.4(b)**, we can extract the power with optimal SNR, which is for this device around $-90\,\mathrm{dBm}$. At this point we have finished sensor tuning and can continue with measuring stability diagrams of the sensor and nearby quantum dots.

5.3.2 Stability diagram of the sensor QDs

We begin with a stability diagram of the two sensing QDs controlled by B1 and T1. We set the two gates for the center QDs, V_{B2} and V_{T2}, to 0.5 V, as we have seen that the first energy levels of the quantum dots in this device are around this value and hence, we expect that the range, we will operate these gates in, will be around this value. An exemplary stability diagram of B1-T1 is depicted in figure **5.5(c)**. The colored rectangles colorcode the enlarged voltage ranges that are depicted in figures **5.5(a)**, **(b)** and **(d)**. We identify charging of an electron in $\mathrm{QD_{T1}}$ ($\mathrm{QD_{B1}}$) as discontinuous shifts of the signal of the other QD and highlight these as orange (red) dashed lines in **5.5(a)** (**(d)**). We see that we can use one QD as a charge sensor for the other QD. Next, we determine how many electrons are in each QD, and we find that for $\mathrm{QD_{B1}}$ the rf-reflectometry signal strength is already above the noise level for the third electron, whereas $\mathrm{QD_{T1}}$ requires > 10 electrons to show a significant reflectometry signal. It is for our purposes desirable to work with a sensing QD that is as small as possible as it reduces the tunnel coupling to the sensed dots and is more sensitive due to less screening. Therefore, we use the first transition of $\mathrm{QD_{B1}}$ that shows a strong reflectometry signal. To use the transition of $\mathrm{QD_{B1}}$ as a detector, we must restrict the gate voltages of B1 and T1 to the values along the first charge transition of $\mathrm{QD_{B1}}$. The reason we might want to vary the two gate voltages V_{T1} and V_{B1} is that we can tune the double quantum dot $\mathrm{QD_{B2}}$ and $\mathrm{QD_{T2}}$ by varying the sensing dot configuration. We want to discuss how to tune the double quantum dot system $\mathrm{QD_{B2}}$ and $\mathrm{QD_{T2}}$ in the following.

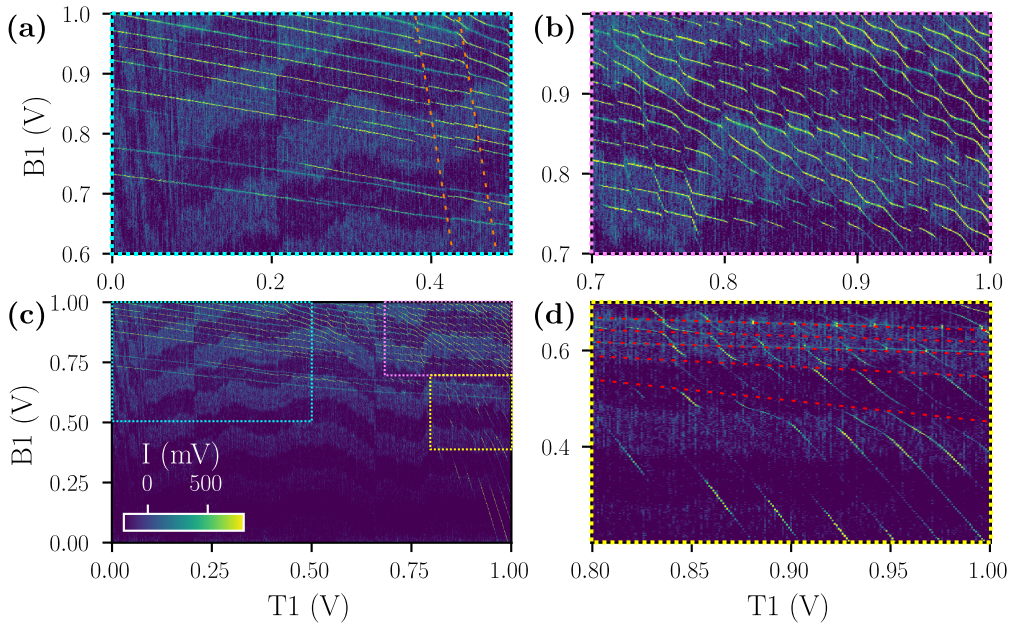

Figure 5.5: Stability diagrams of the two quantum dots closest to the source reservoir. **(a)** Stability diagram showing charge transitions of QD_{B1}. The dashed lines indicate transitions of QD_{T1}. **(b)** Stability diagram of the regime of strong coupling between QD_{B1} and QD_{T1}. **(c)** Stability diagram of QD_{B1} and QD_{T1}. The dotted squared indicate the different voltage windows depicted in figures **(a)**, **(b)** and **(d)**. **(d)** Charge transitions of QD_{T1}. The dashed lines indicate charge transitions of QD_{B1}.

5.4 Tuning of a three quantum dot system without coupling gates

The challenge of the device architecture is the limited amount of gates to control the system. While for instance a typical GaAs/AlGaAs quantum dot is defined by two barrier gates and a plunger gate, our device has a single accumulation gate to define a quantum dot. While this allows to tune the QD's electrochemical potential and by that the equilibrium charge state, there is to gate dedicated to control the potential barrier to nearby quantum dots or reservoirs. Here, we discuss two approaches that have been used to address this challenge.

5.4.1 Quantum dot coupling by means of device geometry

One approach to get the desired capacitive and tunnel coupling between two QDs or QD and reservoir is to have a device geometry that results in the correct positioning of the QDs and coupling between them. This approach makes two assumptions that are not generally true. First, the coupling between the dots and dot-reservoir would not vary a lot, at least in a considerable voltage range in which the QDs are operated. This is usually not the case. In some situations the control of the tunnel coupling over many

orders of magnitude between QDs is desired as it allows qubit control for some qubit implementations. However, single spin qubits do not require such a control and one could work with a constant tunnel coupling for such qubits. Second, the fabrication process is that deterministic that the tunnel coupling between QDs and QD-reservoir can be controlled to very high accuracy. This is partially true as for instance the most advanced industrial silicon manufacturing process today allows structures of a minimal feature size 2 nm [res21]. However, typical gate pitches are more in the range of tens of nm and silicon quantum dots that host just one or two electrons are often much smaller than the gates. This results in quantum dots that are preferably located at surface impurities at the nanowire-gate interface, instead of the center of the gate electrode (see section **5.2**). The surface roughness cannot be controlled to such a high degree that this effect could be avoided and therefore, the few-electron regime in the devices cannot be deterministically controlled by means of fabrication. Nevertheless, our devices often did not show coupling of the quantum dots in the few-electron regime. To overcome this, an etching process was added after patterning the nanowire, reducing the nominal width by 40 nm. This resulted in nanowires of width around 40 nm, 50 nm, and 60 nm instead of 80 nm, 90 nm, and 100 nm, respectively. We will see in the following that by choosing the smallest spacing of 40 nm between neighboring gates, between facing gates and as gate width, we were able to tune devices with non-negligible interdot tunnel coupling between two face-to-face quantum dots in the few-electron regime.
While this trimming of the nanowire was a crucial step towards sufficient QD interdot tunnel coupling, it was not sufficient to have it in all devices in every gate voltage configuration. In fact, tuning the device voltages to control the capacitive as well as tunnel coupling is a large part of current device characterization. We want to explain our tuning process in the following.

5.4.2 Tuning quantum dot coupling using accumulation gates

The task of device tuning consists in shaping the electrostatic potential of the quantum dots to the right charging and coupling regime using electrostatic gates. Tuning of devices is a challenging task as the available gates span a large parameter space to work with. Nowadays, the tuning is mostly done by human experts, but there are approaches to automatize this task using physics informed algorithms[Zie22] or machine learning algorithms[Are21; Kal19; Len19; Moo20; Tes19]. We will discuss the topic of automatized device tuning in section **7.3**. However, the variability between device architectures makes it hard to generalize these algorithms and the field of device tuning automation is still in its infancies. Here, we describe the process we used to tune a split gate device with the available gate electrodes. We have seen in section **1.3.3** that the device architecture tries to reduce the number of gates to a minimum with no dedicated coupling gates, but only accumulation gates. Even though the intended use of the gates was to control the electrochemical potential of the QDs, they can as well be used to change the electrostatics of the nearby QDs and thus the coupling between QDs, and QDs and reservoirs.
We will first give a qualitative description of the different effects of the gates before we follow up with a quantitative analysis of the cross-capacitances between gates and QDs.

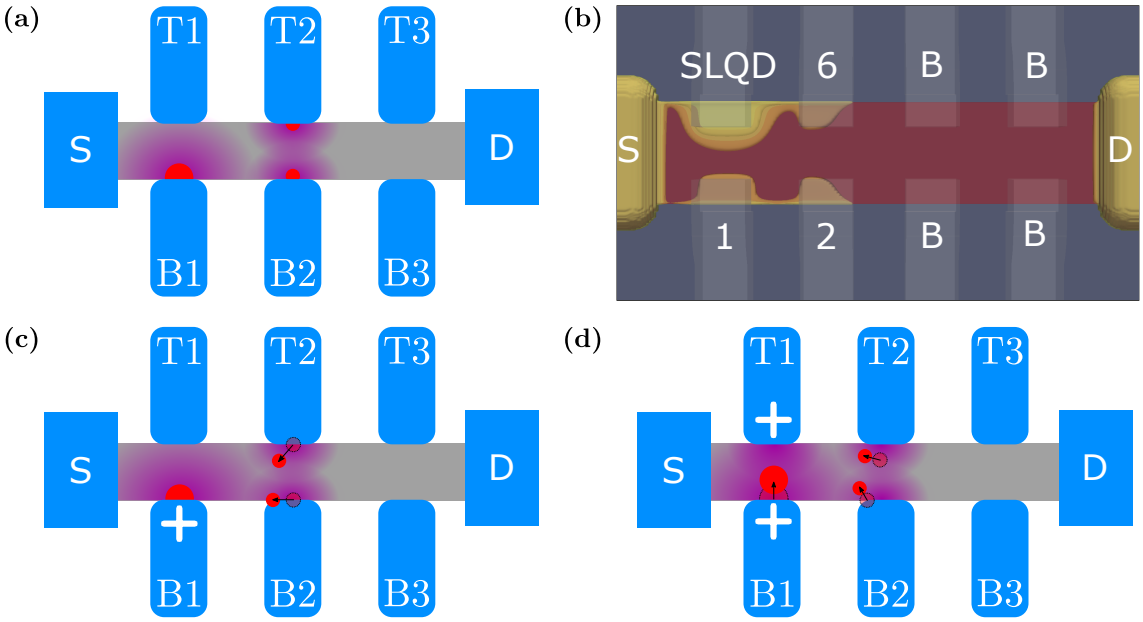

Figure 5.6: Cartoon of the dot position for different gate voltages (**(a)**, **(c)** and **(d)**) and **(b)** a simulation of the electron density inside the channel of a eight gate face-to-face device in a four dot configuration using the Thomas-Fermi approximation. In this work, we used a configuration of three QDs with one large QD controlled by B1 used as a sensing QD and two QD in the few-electron regime controlled by gates B2 and T2. **(a)** Depicts a cartoon of the position of the QDs (red) and a sketch of the electric field (violet) without taking into account cross-capacitances. **(c)** Illustrates the repositioning of the center QDs by applying a high voltage to gate T1, moving the center QDs closer to T1. **(d)** Shows the relocation from **(c)** when raising the voltage on B1, pulling the sensing QD closer to the center of the nanowire and with it the QDs in the center. This relocation effect is probably stronger in the devices used in this work compared to the simulation in **(b)** as the gates do not overlap as strongly and screen less the potential from the environment. Figure **(b)** is a reprint from [Cha20].

We can distinguish two effects. First, the repositioning of the QDs by the push/pull effect of the potential of a gate electrode nearby a QD. With this repositioning, the capacitive coupling can be increased/decreased as the capacitive coupling decays $\sim 1/d^{2.5-3}$ in these devices [Dua20]. Second, the potential barrier between the QDs, and QDs and reservoirs. Essentially, these are both due to the electrostatic deformation of the potential landscape due to the electrostatic gates, but as we are interested in controlling the capacitive coupling and tunnel coupling independently, it makes sense to make the distinction here. Even though the potential of the QDs themselves plays in these trimmed devices a major role, as they are less screened by the gates, it is reasonable to consider the effect on the potential barriers between the dots as rather continuous with the lowering/rising of gate voltages. In contrast, the QDs positions still favor surface impurities and thus the capacitive coupling will show an abrupt change when changing from one impurity to another. This repositioning effect is greatest for small quantum dots with a low number of electrons as the more electrons occupy a quantum dot, the more it smooths out the potential

fluctuations at the surface. A cartoon of the anticipated effects of our four QD gates is depicted in figures **5.6(a)**, **(c)** and **(d)**. Figure **5.6(a)** illustrates the case where we neglect cross-capacitances and the random location of the QDs due to surface roughness etc.. The result are QDs that are located at the center of the respective gates. Taking into account the strong electric field of the sensor QD_{B1}, which has the highest voltage of all gates, QD_{T2} and QD_{B2} are pulled towards the sensor QD_{B1}. The relative effect on QD_{B2} is expected to be larger than on QD_{T2} due to the larger cross-capacitance and closer location. This effect is shown in figure **5.6(c)**, where the opaque red dots indicate the former location of the QDs and the bright red dots the new locations. The cartoon in figure **5.6(d)** goes a step further from figure **5.6(c)** by raising the voltage of gate T1 and by that, not only pull the sensing dot closer to the center of the nanowire, but with it QD_{T2} and QD_{B2}. As these devices usually show a low coupling between the QDs in the few-electron regime, we did not use the gates T3 and B3 to pull the center QDs farther away from the sensor. Moreover, trying to push the center QDs closer to the sensor by applying negative voltages on T3 and B3 had a negligible effect. We assume that QD_{B2} and QD_{T2} are already close to the edge of their respective gate electrodes and strong screening of the electric fields results in a very small potential change. When tuning the device in the DQD regime of QD_{B2} and QD_{T2}, our main tuning knobs are thus the two gates T1 and B1 as the gate voltages of T2 and B2 are given by the charging regime we want to work in. The tuning parameter space reduces further from two to one when we take into account that we operate our sensing QD (QD_{B1} in our case) at a charge transition point. Thus, we can just tune along the charge transitions as depicted in figure **5.5**. We will see that we need to operate the sensing QD at as low voltage as possible to reduce the tunnel coupling to the center QDs as otherwise cotunneling can lift Pauli spin blockade. Having seen that devices with to strong sensor coupling do not show PSB, we assume that PSB can be lifted by tunneling of the electrons through the sensor QD instead of in between the QDs.
After detecting the total number of electrons in each quantum dot, we can identify the regimes of different charge states and in particular the regions where we have a total of two electrons in the double quantum dot system. In the following we want to demonstrate how we can measure the center QDs using QD_{B1} as a sensor.

5.4.3 Stability diagram of the center QDs - Taking the sensor out of the picture

So far we have seen that we can detect charges of QDs using rf-reflectometry when we measure a stability diagram with at least one of the dimensions being a sensor gate, allowing us to detect charge transitions of other QDs as voltage shifts of the sensor charge transitions. While this is in principle a valid technique and in particular for quantum capacitance sensing, one would always use a sensor QD - qubit QD couple, in our configuration we can use the sensor QD as a charge sensor similar to an SET or QPC [Ans20; Cha20]. What makes the QD approach attractive is the high integration level, the small gate overhead (a single gate electrode for the sensor QD) and the very close location to the QDs that are sensed, resulting in a high sensitivity.
To use the sensing QD as a charge sensor, we first validate that it is sufficiently sensitive

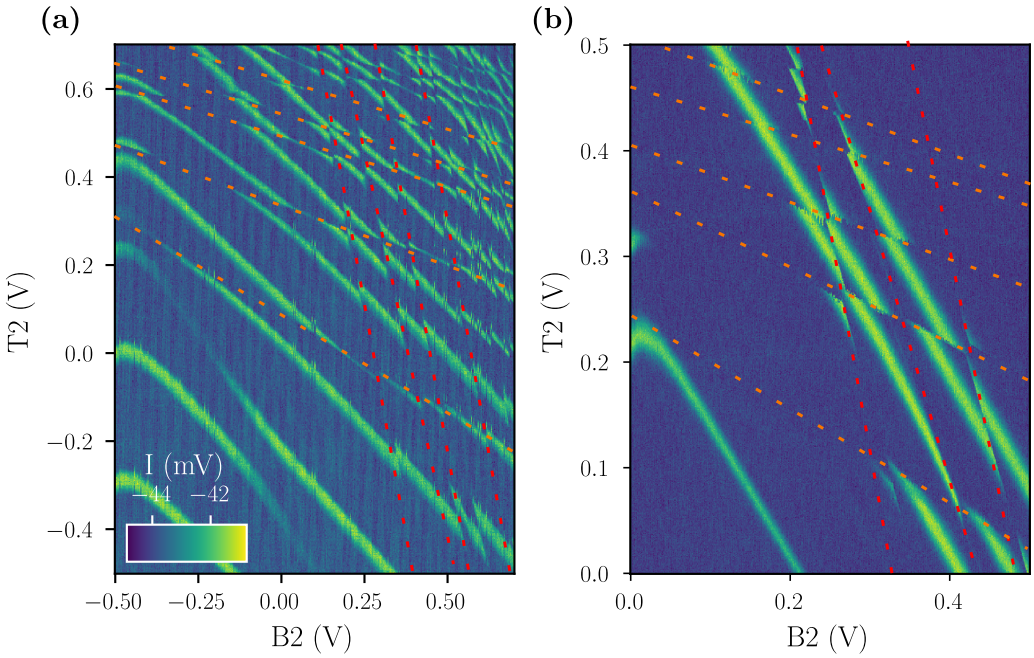

Figure 5.7: Stability diagrams of the two quantum dots in the center of the nanowire. **(a)** shows a stability diagram with the sensor tuned in the multi-electron regime where the sensor QD is defined by T1 and B1 (see figure **5.5(b)**). The small energy spacing between subsequent sensor transitions results in moving through multiple sensor transitions when changing the nearby gates T2 and B2 over a large range. **(b)** shows a stability diagram with the sensor tuned in the multi-electron regime with the sensor QD defined by B1 (see figure **5.5(a)**). Using these stability diagrams with a large range of T2 and B2 voltage, we can identify charge transitions of $\mathrm{QD}_{\mathrm{T2}}$ and $\mathrm{QD}_{\mathrm{B2}}$. The orange (red) dashed lines indicate transitions of $\mathrm{QD}_{\mathrm{T2}}$ ($\mathrm{QD}_{\mathrm{B2}}$).

to the individual QDs, it is supposed to detect, by measuring stability diagrams of the sensor gate (B1) and the QD gates of interest (either B2 or T2) (see appendix section B.1). We can identify the charge transitions of the nearby quantum dots as discontinuous changes of the degeneracy points of the sensor QD with respect to the gate voltage of the nearby quantum dot. Thus, the sensing QD is sensitive enough to the charge state of the nearby QDs to be used as a charge sensor.
Even though we know that we are sensitive to all QDs nearby, we are blind apart from the charge degeneracy lines of the sensor. At first sight, one could conclude that it is not possible to measure the charge state of two QDs at the same time if not one of them is acting as a reflectometry sensor. This is fortunately not the case. Taking for instance the case of the sensor QD defined by gate $B1$, tuned to the maximum value of a Coulomb peak. A slight change of the electrostatics due to a voltage change on another gate nearby will now shift the electrochemical potential of the sensor QD. The result is a sensor signal shift off of the Coulomb peak. In fact, sweeping $B2$ has a similar effect as sweeping

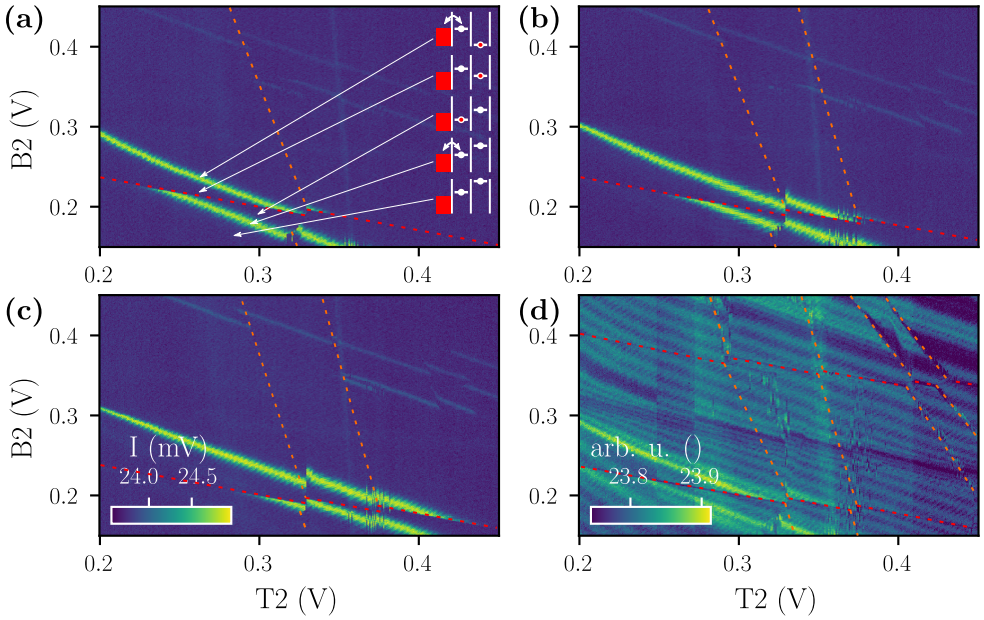

Figure 5.8: Stability diagrams of the two quantum dots in the center of the nanowire. **(a)**, **(b)** and **(c)** depict a remote sensing stability diagram of B2 and T2 for T1 set to 0.387 V, 0.386 V and 0.385 V, respectively. **(d)** Stability diagram reconstructed from taking the average of 21 stability diagrams similar to the ones in **(a)**, **(b)** and **(c)**. The orange (red) dashed lines indicate transitions of QD_{T2} (QD_{B2}).

$B1$ with a smaller lever arm $\alpha_{B2,B1}$. Hence, when tuning the two gates controlling the center QDs (QD_{T2} and QD_{B2}), the sensor potential is changed by $\alpha_{B2,B1}V_{B2} + \alpha_{T2,B1}V_{T2}$. Additionally, to this cross-capacitance effect, charge transitions in the QD defined by $B2$ result in discontinuous shifts in the electrochemical potential of the sensor QD. Figure **5.7** show stability diagrams of $T2$ and $B2$. Figure **5.7(a)** shows a stability diagram where the voltage of the two gates is swept between -0.5 V to $+0.7$ V, ensuring that the first electron transition of both quantum dots QD_{T2} and QD_{B2} is in the voltage range. The sensor is tuned to the multi-electron regime depicted in figure **5.5(b)**. In this regime, the energy separation between the sensor charge transitions is so small, that the cross-capacitance of the T2 gate and B2 gate result in passing of multiple sensor charge transitions through the stability diagram. While the diagram looks very similar to a sensor-QD stability diagram, it shows some different features. First, the sensor charge transitions are more tilted, as both gates T2 and B2 have a similar effect on the sensor QD energy. Second, we can detect charge transitions of two different slopes. We assign the more horizontally sloped charge transitions to QD_{T2} and the more vertial ones to QD_{B2}, indicated using dashed orange and dashed red lines respectivelty. Using this stability diagram, we identify the first charge transition for QD_{T2} and QD_{B2}. In this regime the sensor QD is very large and can tunnel couple strongly to the sensed QDs. To avoid this, we can reduce the sensor gate

voltage. We first reduce the T1 gate voltage resulting in the stability diagram such that the sensor is in the multi-electron regime of B1 as depicted in figure **5.5(a)**. Figure **5.7(b)** shows a stability diagram of this gate voltage configuration. Compared to the stability diagram with higher T1 gate voltage, this diagram shows less sensor charge transitions due to the larger energy spacing between the sensor charge transitions. Finally, we can reduce the B1 gate voltage to the first charge transition that shows a sufficiently strong rf-reflectometry signal. Such a stability diagram is depicted in figure **5.8(a)**. We want to use this stability diagram to discuss the different QD charge configurations of the sensor QD and the $\mathrm{QD}_{\mathrm{B2}}$. Notably, following the red dashed line, indicating a charge transition of $\mathrm{QD}_{\mathrm{B2}}$, a splitting of the sensor Coulomb peak can be observed where the $\mathrm{QD}_{\mathrm{B2}}$ charge transition intersects with the sensor charge transition. The cartoon on the right-hand side of the stability diagram illustrates the different charging states of the sensing QD (left) and the sensed QD (right) at the position indicated with the white arrows. The cartoon helps to understand why we find the sensor transition twice, as it is once seen when there is no electron in the sensed QD and once, when there is an electron in the sensed QD. The spacing between the two corresponds to the shift of the electrochemical potential of the sensor QD due to the charging of an additional electron in the sensed QD. Hence, after V_{B2} is increased by $\Delta V_{\mathrm{B2}}^{m} = \Delta V_{\mathrm{B2}} \frac{C_{\mathrm{m}}}{C1}$, the sensor charge transition can be found again. It becomes clear from the stability diagram that the cross-capacitance of $\mathrm{QD}_{\mathrm{B1}}$ is stronger with B2 than with T2, indicated by an almost parallel alignment of the sensor transitions with respect to the transitions of $\mathrm{QD}_{\mathrm{B2}}$, whereas the transitions of $\mathrm{QD}_{\mathrm{T2}}$ are almost vertical with respect to the sensor transitions.

We can already identify charge transitions of the center QDs with the single map, but we might miss some, since we are only able to detect charge transitions that intersect with the sensor charge transitions within our scanning window and especially the $\mathrm{QD}_{\mathrm{B2}}$ transitions are almost parallel with the sensor transitions. To ensure that we detect all transitions, we can step the sensor voltage in the third dimension of the stability diagram. This results in a shift of the sensor charge transitions over the stability diagram similar to moving the scanning head of a Xerox machine over a sheet of paper. The result is a 3D map that we can use to reconstruct a stability diagram with all the transitions. One way is to overlap all the stability diagrams (average over the last dimension which changes the sensor gate voltage). Such an averaged stability diagram of 21 different sensor gate voltages is depicted in figure **5.8(d)**, where figures **5.8(a)**, **(b)**, and **(c)** are examples for B2-T2 stability diagrams of different sensor gate voltages. We indicate the detected charge transitions of $\mathrm{QD}_{\mathrm{B2}}$ ($\mathrm{QD}_{\mathrm{T2}}$) with red (orange) dashed lines. Further investigation of the transitions, shows that not only is the capacitive coupling between sensor and $\mathrm{QD}_{\mathrm{T2}}$ smaller than for $\mathrm{QD}_{\mathrm{B2}}$, but as well the tunnel coupling. Especially the transition of the second electron in $\mathrm{QD}_{\mathrm{T2}}$ is not very sharp, but the sensor transition seems to switch over a range of a few tens of mV, indicating a very small tunnel coupling of $\mathrm{QD}_{\mathrm{T2}}$ to the sensor QD, which acts as an electron reservoir for the center QDs.

In contrast to a typical SET or QPC measurement, our detection window (Coulomb peak) is very small with respect to the gate voltage range, we use for the stability diagram. While one typically tunes an SET or QPC to a conduction step (side of a Coulomb peak for an SET) and measures a small shift of conduction when a charge transition occurs in

the device, the situation for us is different. Due to the strong capacitive coupling, charge transitions of a nearby QD result in a potential shift of the sensor QD, larger than the width of a Coulomb peak. This has the great advantage that the signal strength is limited by the amplitude of the Coulomb peak of the sensor. The drawback of this strong capacitive coupling is that it is difficult to implement a feedback loop to retune the sensor voltage to the Coulomb peak. For SETs and QPCs the small shift of the sensor signal due to a charge transition can be corrected by maximizing the signal gradient after the shift occurred. When there is no signal gradient as in our case when the signal is shifted completely of a Coulomb peak, following the gradient is not an option. A way to enlarge the signal in any case is by power broadening, which can be detrimental to the quantum state of a nearby spin due to sensor back action as we will see in chapter **6**.
Before we turn our attention to the spin physics of a two electron system in a double quantum dot, we want to calculate the lever arms, capacitance matrix and addition energies of the 2×2 QD array we are working with.

5.5 Quantum dot array characterization

In this section we want to characterize the 2×2 quantum dot array quantitatively and interpret the extracted quantities in terms of QD properties. We will start with the lever arms of the center quantum dots and follow up with the addition energy in each QD. Finally, we will calculate the capacitance matrix for the array and interpret the results in terms of QD location with respect to other QDs and gate electrodes.

5.5.1 Measuring of the gate lever arm of the center quantum dots

The gate lever arm is a metric for the effectiveness of the gate voltage on the actual electrochemical potential of the quantum dot. For instance, a gate lever arm $\alpha = 0.1$ would mean that changing the gate voltage by $\Delta V = 1\,\mathrm{V}$ would change the quantum dot potential by $\alpha e \Delta V = 100\,\mathrm{meV}$. While one can extract the lever arm for single quantum dots from a Coulomb diamond measurement, these measurements are not very reliable for more complex architectures, where more than one quantum dot is involved. In the regime, where we were working in, notably $E_\mathrm{C} \gg k_\mathrm{B} T_\mathrm{e} \gtrsim \Delta\varepsilon$, where T_e is the electron temperature and $\Delta\varepsilon$ single-particle level separation, the broadening of the sensor signal at a charge transition of a nearby QD can be approximated by

$$f(E - E_0) = \frac{1}{1 + e^{-(E-E_0)/k_\mathrm{B}T_\mathrm{e}}} = \frac{1}{1 + e^{-\alpha e(V-V_0)/k_\mathrm{B}T_\mathrm{e}}}, \tag{5.1}$$

where we have used $E = \alpha e V$. The only free parameter in this function is the lever arm α. Fitting the function to a charge transition allows to determine the lever arm on the gate that defines the quantum dot. As can be seen in the stability diagram in figure **5.9(a)**, the tunneling rate is very low that a single measurement along the trace does not give a smooth transition. To overcome this, we average over 500 traces along the red (cyan) bar in figure **5.9(a)**. The resulting signals and the respective fits are depicted in figure **5.9(b)**

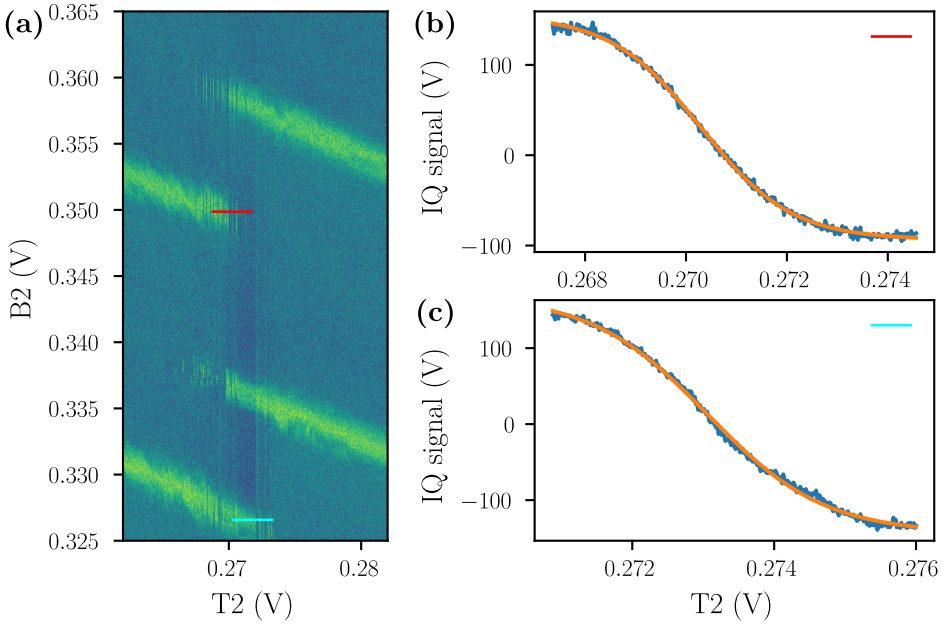

Figure 5.9: Figure (a) depicts a stability diagram with the charge transitions used for measuring the gate lever arm of T2. The red and cyan lines indicate the traces taken for measuring the gate lever arm. Figures **(b)** and **(c)** are the traces depicted in figure **(a)** with the red and cyan bar respectively, averaged 500 times. The fits are used to calculate the lever arm.

and **(c)**. We find a lever arm of $\alpha = 0.05 \pm 0.005$. With this and the interdot transition of B2-T2 in the (1|1) regime, we can calculate the lever arm of B2 to be $\alpha_{\mathrm{B2}} \approx 0.035$ (see appendix **B.2** for derivation).

5.5.2 Addition energy of the different quantum dots

As we know the absolute number of electrons in the QDs, we can calculate the addition energy for the first electrons using $E_{\mathrm{add}} = \alpha e \Delta V$. Where we use the same α-factor for gates on the same side of the nanowire[1]. We can read the voltage spacing ΔV between subsequent charge transitions from the stability diagram given in figure **5.5** for B1 and T1, and from the stability diagrams in figure **B.1** for B2 and T2. We plot the addition energy E_{add} for all QD of the 2×2 array of our experiments up to the 13th electron in figure **5.10**. While all QDs show a monotonous decrease of addition energy, there is not a clear pattern identifiable, that would indicate filling of specific orbitals[Leo20]. We

1 This is a very strong assumption as the small gate overlap in the trimmed devices is likely to result in a strong variation of α factors. Therefore, we advise the reader to not put too much credence into the values given for T1 and B1.

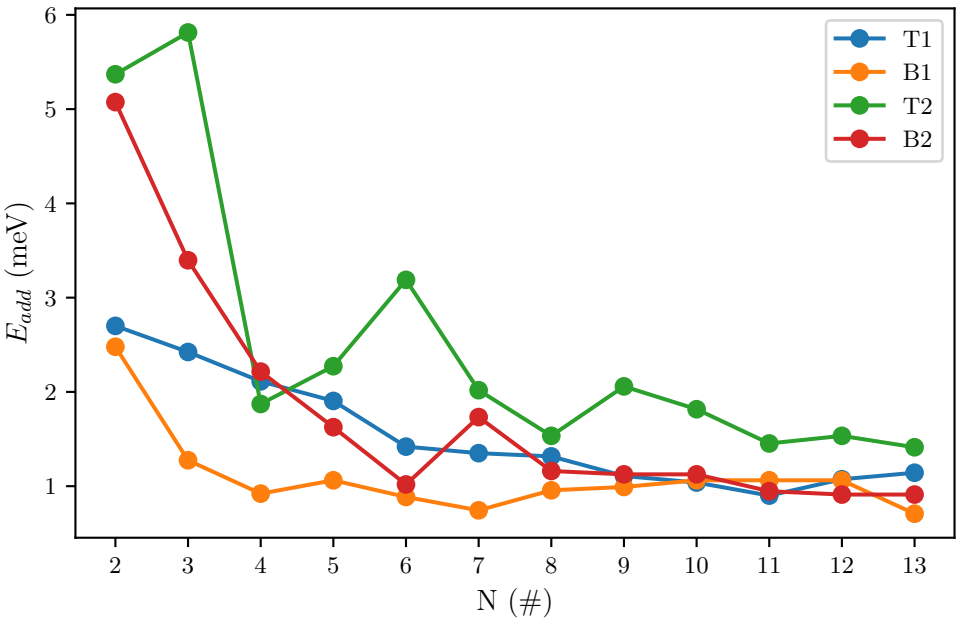

Figure 5.10: Addition energy calculated from the voltage spacing between charge transitions and the gate lever arm $\alpha = 0.05$ for the four QDs defined by T1, B1, T2 and B2. The voltage spacing for T1 and B1 is taken from figure **5.5** and from **B.1** for T2 and B2.

will see in the spin measurements, and it was as well measured in similar devices that the valley energy splitting in these devices is in the order of a few hundred µeV[Spe22]. Thus, valley-orbital states might form the energy levels of the QDs and one could expect a doubling of the regular shell filling (4,12,24,... instead of $2, 6, 12$,... for s-, p-, d-orbitals) due to the two lowest z-valleys. Moreover, the potential relocation and change of shape of the QD in the few-electron regime might change the dot potential after each additional electron. In such a situation the variation of potential is too irregular for the few-electron regime to show orbital spacing like in a harmonic potential.

5.5.3 Capacitance matrix of the quantum dot array

Loading the second electron costs only the charging energy E_C as it occupies the same orbital as the first electron. We can therefore calculate the QD capacitance using

$$\alpha e \Delta V = (2^2 - 1^2)\frac{e^2}{C} \Rightarrow C = 3\frac{e}{\alpha \Delta V}. \tag{5.2}$$

Moreover, we can extract from the stability diagrams the cross-capacitances. The relative effect of the different gates from the slope of the transitions in a stability diagram combined with the absolute capacitance of a QD gate allows us to calculate the capacitance matrix. We find

$$C_{\text{cross}} = \begin{pmatrix} 1.00 & 0.24 & 0.06 & 0.26 \\ 0.20 & 1.00 & 0.06 & 0.72 \\ 0.10 & 0.02 & 1.00 & 0.35 \\ 0.05 & 0.08 & 0.26 & 1.00 \end{pmatrix} \tag{5.3}$$

$$C = \begin{pmatrix} 177 & 41 & 15 & 22 \\ 35 & 172 & 15 & 61 \\ 18 & 3 & 246 & 29 \\ 9 & 14 & 64 & 84 \end{pmatrix} \text{aF}, \tag{5.4}$$

where C_{cross} is the relative cross-capacitance between the gate vector (T1, B1, T2, B2) and the quantum dot vector (QD_{T1}, QD_{B1}, QD_{T2}, QD_{B2}). With the vector of dot capacitances (177 aF, 172 aF, 246 aF, 84 aF), calculated using equation **5.2**, we can calculate the capacitance matrix C. The capacitance matrix clearly shows that the gates to control their respective quantum dots have indeed the strongest capacitance. However, the total capacitance for the different QDs varies significantly. In particular QD_{B2} has a rather small capacitance compared to the other QDs and almost three times smaller than QD_{T2}. We interpret this as a very strong location effect of QD_{B2} with a small and sharp confinement potential, resulting in a small capacitance. In contrast, QD_{T2} probably has a rather shallow potential that gives a large capacitance. Comparing the cross-capacitances, we see again that QD_{B2} sticks out. While in general the QDs show the smallest cross-capacitances to the QDs farthest apart, QD_{B2} shows particularly strong cross-capacitances. This observation supports the strong localization assumption of the QD. An impurity, that pins a QD very strongly, can cause the QD to locate relatively far away from the controlling electrode. This separation results in two effects that augment the relative cross-capacitance for this QD. First, the QD moves closer to the nearby gates (not necessarily closer to T1 and B1, but closer to the center of the nanowire and thus closer to T2) and therefore is more sensitive to these gates. Second, the screening effect of the controlling gate reduces when the QD is farther away, resulting in a stronger electric field of the other gates at the QD location. Especially in the trimmed devices, where the gates are more side gates than wrap around gates, the screening can be considerably reduced. With this and the results from the simulations of the electron density in similar devices, we can safely assume that the center QDs are indeed pulled towards the sensing QD and QD_{B2} is probably not located in a corner, but close to QD_{B1} and QD_{T2}.
Now that we got a better understanding of the QDs in the device, we can go a step further and investigate the spin states in this DQD system.

6 Probing a two-spin system in a double quantum dot

> It is really quite impossible to say anything with absolute precision, unless that thing is so abstracted from the real world as to not represent any real thing.
>
> Richard Feynman

In this chapter we will turn from charge sensing to spin sensing. We will begin with spin sensing, demonstrating two different readout types, required for a full readout of a two spin system. We will explain the optimization of the readout fidelity and demonstrate readout fidelities that exceed 99 %. Using this readout, we will characterize the spin states of a two electron system in a DQD. The majority of the discussed results in this chapter can be found in [Nie22].

6.1 High fidelity spin readout of a double quantum dot

We have seen in section **1.3.4** that a high fidelity spin readout is indispensable for building qubits. Moreover, this readout should be scalable, fast, and not affect the qubit fidelity. Using a double quantum dot system for spin readout has so far achieved the highest fidelities using Pauli spin blockade (PSB)[Bor21; Zhe19]. We will present in the following a PSB readout to perform two different readout types for singlet-triplet states. Optimizing the readout power and integration time results in average readout fidelities $> 99.9\,\%$ at 50 kHz and a temperature of 0.5 K.

6.1.1 Pauli spin blockade detection using an ancillary sensor QD

As discussed in section **2.2.2**, the lowest states of two electrons in a DQD are the three triplet states T_-, T_0, T_+ and the singlet state S_0. As the spin wave function of the singlet is antisymmetric, both electrons can occupy the same orbital state in a quantum dot. In contrast, the triplet spin wave functions are symmetric and thus two electrons that are in a triplet state cannot be in the same orbital, but one of them must be in an excited orbital. In the following, we want to restrict the discussion to the charge regime (2|0)-(1|1) (the same would apply for $(2N+1|2M+1)$-$(2N|2M+2)$, with N and M integers). For the voltage window $\Delta V = \Delta E/(e\alpha)$, where ΔE is the energy splitting between singlet and triplet states in the (2|0) regime, the singlet ground state is (2|0) while the triplet ground state is (1|1). This voltage window is the Pauli spin blockade (PSB) region. The shape of this region is either a triangle or a trapezoid and indicated with dashed lines

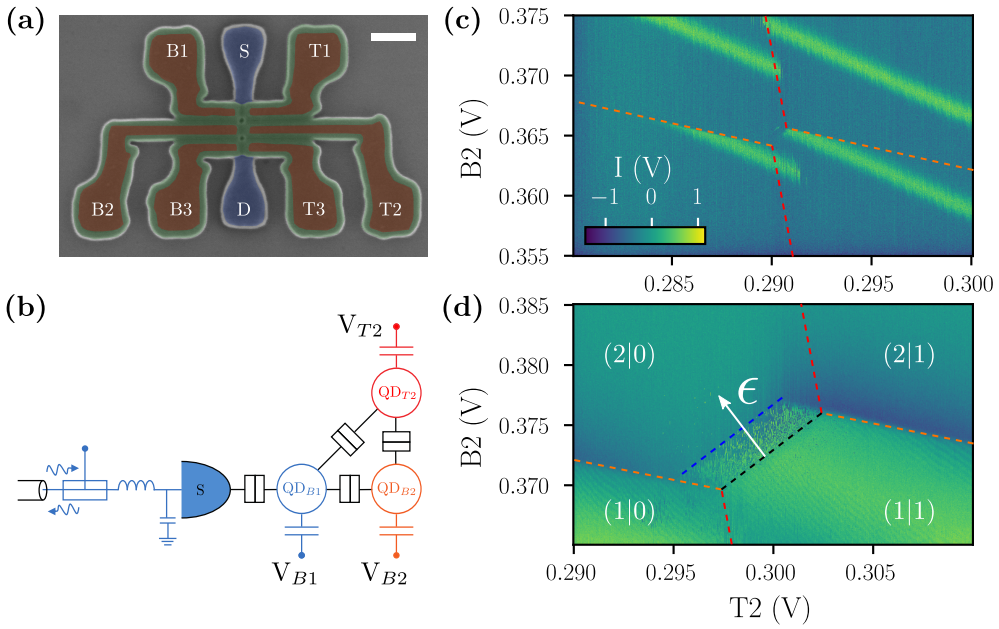

Figure 6.1: **(a)** SEM micrograph of a device similar to the one used in the experiment. The gate electrodes are highlighted in red, the reservoirs and nanowire in blue and the spacers in green. **(b)** Equivalent circuit of the device in the three QD configuration with the rf-reflectometry circuit connected to the source reservoir. **(c)** Stability diagram of the center quantum dots with the sensor tuned such that it detects the interdot transition of the DQD system QD_{B2}-QD_{T2}. **(d)** Two-electron interdot transition of the DQD system QD_{B2}-QD_{T2} at a non-zero magnetic field B_z. The black dashed line highlights the interdot transition, whereas the blue dashed line indicates the lifting of the Pauli Spin blockade regime due to population of a triplet state. The white arrow indicates the detuning axis.

for our device in figure **6.1(d)**. The triangle shape can be understood from removing the interdot transition (the charge transition between the two QDs is blocked) and extending the boundaries to the nearby charge transitions with the reservoir. If the next higher orbital lays within the energy window that is spanned by the triangle, the triangle gets cut off at this point, as the (1|1) charge state becomes the ground state for triplet as well, resulting in a trapezoid shape.
After identifying the (2|0)-(1|1) transition in our stability diagram, we tune the sensor in a position where we have the maximal difference between the signal for (2|0) and (1|1). Applying a sufficiently strong magnetic field B_z, such that $E_z = g\mu B_z > J(\varepsilon)$, results in a lifting of the degeneracy of the triplet states and T_- becomes the ground state of the system in (1|1). If not stated otherwise, the magnetic field we used for the presented experiments was $B_z = 300\,\mathrm{mT}$. We can prepare a T_- state in (1|1) by waiting for relaxation to the ground state. After, pulsing non-adiabatically to a position along the detuning axis in (2|0), indicated as a white arrow in figure **6.1(d)**, allows to measure the extent of the

PSB. If the initial state was triplet T_-, we would measure a (1|1) signal in the PSB, whereas for singlet S_0 we would find a (2|0) signal. As the triplet state is an excited state in the PSB region, it will relax eventually to the ground state with a characteristic time constant T_1. To make this readout work, the tunneling rate for the two singlet states S(1|1) and S(2|0) between the two quantum dots be much faster than the triplet relaxation T_1. In our case, the tunneling rate is higher than our measurement bandwidth of 250 kHz, much faster than typical T_1 times of a few ms. It is also advisable to decouple the QD, from which the electron tunnels, as much as possible from the reservoir. Too strong coupling to the reservoir can result in strong co-tunneling, where QDs of the DQD only exchange electrons with the reservoir instead of in between each other[1]. The co-tunneling process is not subject to PSB and no spin sensitive readout is possible. In fact, we have not achieved PSB spin readout in regimes where the QD showed tunneling faster than our scanning rate of a few kHz. If possible, on can work in the isolated regime to ensure that PSB is not lifted by co-tunneling.
In the regime we were working in, even with a relatively slow scanning rate with 100 µs per point, we observe PSB when scanning from (1|1) to (2|0), as it is shown in figure **6.1(d)** between the black and blue dotted line. As we can see as well in the scan, the PSB has a trapezoid shape, indicating that the next excited state limits the PSB. We can estimate the energy of the excited state using $\Delta E = \alpha e \Delta V \approx 130\,\mu\text{eV}$, a value in good agreement with similar devices[Spe22]. Following the indicated lines of the QD_{T2} transition in figure **6.1(c)**, we can see that the actual charge transition occurs at higher voltage than indicated by the dashed red line. This hysteresis effect indicates that QD_{T2} is weakly coupled to a reservoir, allowing to consider the QD decoupled from the reservoir for all presented spin experiments.

6.1.2 Mapping of the singlet and triplet states - Parity- and ST-readout

To characterize the spin dynamics in the PSB, we start with measuring the characteristic relaxation time T_1. We distinguish here between two different readout schemes. First, the ST-readout that distinguishes the singlet state S_0 from the triplet states. Second, the parity readout that distinguishes polarized spin states T_- and T_+ from the unpolarized spin states T_0 and S_0.
For the ST-readout, we initialize a singlet state by waiting for relaxation to the ground state in (2|0). After, we pulse with the DAC to the position of ST-readout. A Landau-Zener ramp (see section **6.2.2**) combined with S_0-T_0 mixing (see section **6.2.3**) using an AWG pulse into (1|1) is performed. The Landau-Zener ramp allows preparing T_- with a ramp rate dependent probability for $B_z \neq 0$. Allowing mixing of S_0 and T_0 results in a non-zero T_0 population when initialized in S_0, necessary to distinguish between ST-readout and parity readout. When measuring T_1 at the ST measurement position we find a single exponential decay with a $T_1 = 0.9\,\text{ms}$ for $B_z = 0$ as depicted in figure **6.2(c)**. The measurement at the parity readout position results in a flat signal, representing a pure

1 With the reservoir, we refer to the sensing QD in our case as the center QDs are not directly exchanging electrons with the reservoir, but always go through the sensing QD.

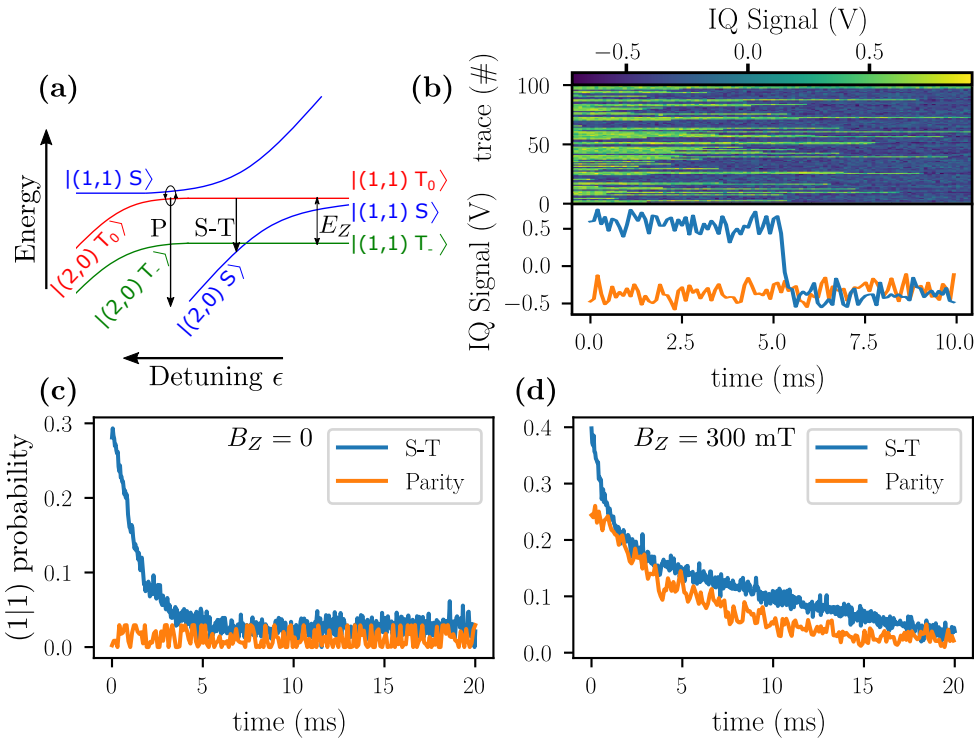

Figure 6.2: The energy diagram in **(a)** shows the lowest states of the two electron system in the double quantum dot around the (2|0)-(1|1) interdot transition for $B_z \neq 0$. The position of parity- (P) and ST-readout (S-T) are indicated with arrows and labels. **(b)** Single shot measurements at the parity-readout position for $B_z = 300\,\mathrm{mT}$. The lower plot shows two exemplary traces. One blocked state that relaxes to the unblocked state (blue) and one unblocked state (orange). **(c)** Relaxation curves for $B_z = 0$ of the mixed state to the unblocked singlet state for ST- (blue) and parity-readout position (orange). While the parity readout does not show any blockade, a single exponential relaxation with $T = 0.9\,\mathrm{ms}$ is observed. **(d)** Relaxation curves for $B_z = 300\,\mathrm{mT}$ of the mixed T_- and T_0 states to the singlet state for the ST- (blue) and parity readout (orange) positions. While the parity readout shows a single exponential decay, the ST-readout shows a double exponential decay consisting of one fast decay similar to the $B_z = 0$ measurement and one slower one, similar to the parity readout decay.

singlet measurement as at $B_z = 0$ the parity readout cannot distinguish S_0 and T_0. For $B_z = 300\,\mathrm{mT}$ the same measurement results in a single exponential decay for the parity readout and a double exponential decay for the ST-readout. The ST-readout shows one fast relaxation, similar to the relaxation at $B_z = 0$, and one slower relaxation, similar to the relaxation of the parity readout. These results can be understood with the help of figure **6.2(a)**. For $B_z \neq 0$, the T_0 and T_- degeneracy is lifted and each of the states relaxes with a different characteristic time to the ground state S_0, resulting in a double exponential decay for ST-readout with $T_1 = 0.9\,\mathrm{ms}$ and $T_1 = 32\,\mathrm{ms}$, respectively. At the parity readout position the T_0 state can mix with the excited $S_0(1|1)$ state that results in a fast relaxation to the $S_0(2|0)$ ground state. The longer relaxation for the T_- state is in good agreement with results in other devices and probably due to the slower relaxation mechanisms that involve a spin flip [See21]. As a preliminary result, we can take away from this experiment that we can distinguish the singlet S_0 state from the triplet states. To distinguish further the different triplet states, one could consider an initial measurement of the state at $t = 0$ and one at $t = 3\,\mathrm{ms}$ when the T_0 state is mostly relaxed to the ground state, whereas the majority of T_- is still blocked. This double measurement would allow distinguishing first, between singlet and triplet, and in a second step, between T_0 and T_- (assuming that the excited T_+ can be neglected). However, the achievable fidelity of such a readout is poor with less than 95 %, due to the relatively fast decay of T_0 with respect to our measurement speed and the small difference between the relaxation rates $T_0 \to S_0$ and $T_- \to S_0$. To increase the fidelity, one could pulse after the initial measurement to a parity readout position. This helps in two ways to improve the readout fidelity. First, the relaxation rate of T_- is longer at this position. Second, the T_0 relaxes quasi instantaneously, which would allow measuring directly after reaching the parity readout position without waiting the previously proposed 3 ms. The limiting factors would be the short T_1 of the T_0 at the ST readout position and the transfer leakage when pulsing from the ST-readout position to the parity readout position.

6.1.3 Fidelity benchmarking of parity readout

We will focus in this section on the parity readout. Everything presented here can be as well applied to characterize the ST-readout. The goal is to present the different parameters that play into the readout fidelity and how we optimized it to reach high fidelity readout. We follow Barthel et al. [Bar09] in measuring the fidelity of our spin readout. While we perform IQ-demodulation of our rf-signal, we shifted all the information into one quadrature (I) as depicted in figure **6.4(a)**. This allows to measure at twice the bandwidth without loosing information. We will refer in the following to the I-quadrature signal as V_{rf}. Moreover, the filtering used in our measurement setup results in a recentering of the IQ-plane, making it impossible to distinguish between phase ϕ and signal amplitude. The main experimental parameters for Barthel are the integration time at the measurement position τ_{m}, the relaxation time constant at this position T_1 and the center of the signal of the blocked (unblocked) state V_{rf}^S (V_{rf}^T). We will refer to the unblocked (blocked) signal with the subscript S (T). Barthel's approach is to measure a sufficient number of blocked and unblocked states, plot these as a histogram and from this, estimate the signal

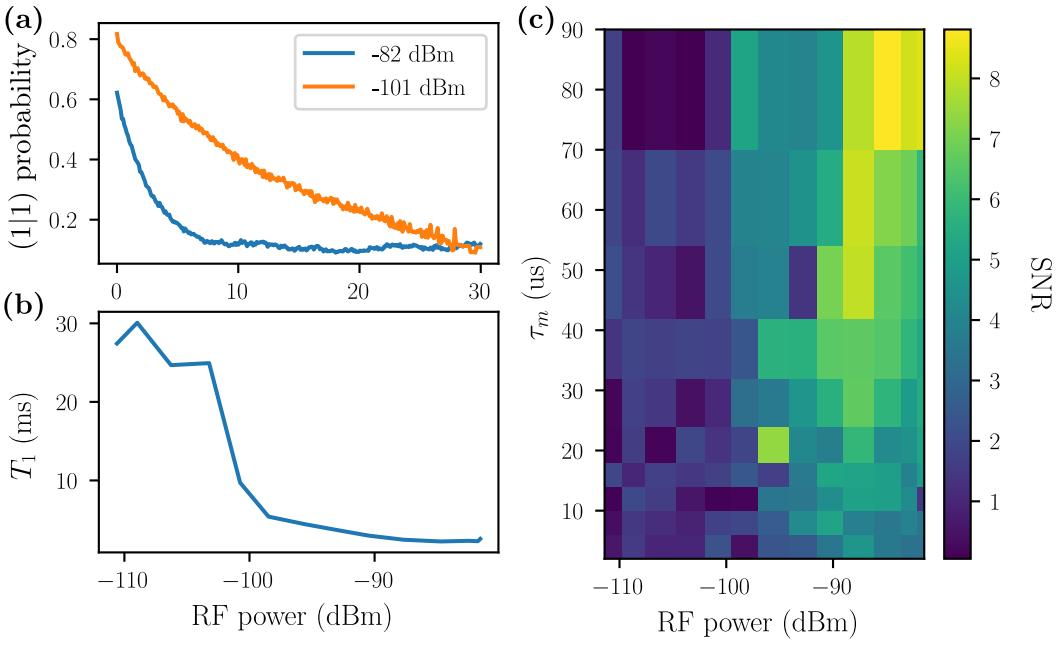

Figure 6.3: **(a)** Relaxation curves at the parity readout position for two different rf-powers. **(b)** Relaxation time at the parity readout as a function of rf-power. **(c)** Map of the SNR as a function of rf-power and integration time τ_m. The data is extracted from histograms from 2000 experiments

distribution. In our experiment the noise broadening is dominated by the thermal noise from our low-noise cryogenic amplifier and thus the signal distribution follows a normal distribution with variance σ^2 and is centered around V_rf^S for blocked and V_rf^T for unblocked states[Urd19]. To account for the relaxation of the blocked to the unblocked state, the distribution of the blocked state $n_{\mathrm{T}(V_\mathrm{rf})}$ is modified with a relaxation term. The three figures of merit for the readout are the fidelity of odd state (S_0 and T_0) $f_\mathrm{S}(V_\mathrm{rf})$, fidelity of even state (T_- and T_+) $f_\mathrm{T}(V_\mathrm{rf})$ and the visibility $V_\mathrm{vis}(V_\mathrm{rf})$, where V_rf is the position of the threshold used to separate even/odd signal. The fidelity of the odd (even) state is defined as the integral of the probability distribution

$$F_\mathrm{S}(V_\mathrm{rf}) := \int_{-\infty}^{V_\mathrm{rf}} dV\, n_{\mathrm{S}(V_\mathrm{rf})} = \int_{-\infty}^{V_\mathrm{rf}} dV \frac{1-\langle P_\mathrm{T}\rangle}{\sqrt{2\pi}\sigma} e^{-\frac{(V-V_\mathrm{rf}^S)^2}{2\sigma^2}} \tag{6.1}$$

$$\begin{aligned} F_\mathrm{T}(V_\mathrm{rf}) :=& \int_{V_\mathrm{rf}}^{\infty} dV\, n_{\mathrm{T}(V_\mathrm{rf})} = \int_{-\infty}^{V_\mathrm{rf}} dV \frac{\langle P_\mathrm{T}\rangle}{\sqrt{2\pi}\sigma} e^{-\frac{\tau_\mathrm{m}}{T_1}} e^{-\frac{(V-V_\mathrm{rf}^S)^2}{2\sigma^2}} \\ &+ \int_{-\infty}^{V_\mathrm{rf}} dV \int_{V_\mathrm{rf}^S}^{V_\mathrm{rf}^T} dV' \frac{\tau_\mathrm{m}}{T_1} \frac{\langle P_\mathrm{T}\rangle}{\Delta V_\mathrm{rf}} e^{-\frac{V'-V_\mathrm{rf}^S}{\Delta V_\mathrm{rf}}\frac{\tau_\mathrm{m}}{T_1}} e^{-\frac{(V-V')^2}{2\sigma^2}} \frac{dV}{\sqrt{2\pi}\sigma}, \end{aligned} \tag{6.2}$$

where $\langle P_\mathrm{T} \rangle$ is the relative population of the blocked state and we assumed that $V_\mathrm{rf}^T > V_\mathrm{rf}^S$. The visibility is defined as

$$V_\mathrm{vis}(V_\mathrm{rf}) := F_\mathrm{S}(V_\mathrm{rf}) + F_\mathrm{T}(V_\mathrm{rf}) - 1 \tag{6.3}$$

and is used to optimize the threshold by searching for the maximum of the visibility with respect to the threshold V_rf. Optimizing the readout consists of finding an optimum in terms of different trade-offs. Here is a non-exhaustive list of optimization parameters.

1. Reduce the noise broadening σ of the signal as much as possible as it results in overlap of the two signal distributions. This can either be achieved by improving the amplification chain or by increasing the integration time as the noise decreases with $\sqrt{t_\mathrm{m}}$.
2. Minimize the ratio τ_m/T_1. A high ratio indicates a high amount of relaxation during the measurement and thus misidentification of formerly blocked states. This is in conflict with increasing the integration time t_m mentioned in 1.
3. Maximize $(V_\mathrm{rf}^T - V_\mathrm{rf}^S)^2/\sigma^2$ or in other words the signal-to-noise ratio. This can be done by optimizing the reflectometry power to sense the charge state. Apart from power broadening at high rf-power, another effect that needs to be taken into account is the back action of the sensor on the system, resulting in a decrease of T_1.

Our approach to optimization is to use a single shot experiment that yields approximately a $1:1$ ratio between blocked/non-blocked state (or even/odd spin state for parity readout) and accumulate 1000 shots to have enough data to fit the two signal distributions for blocked/non-blocked signal. We first measure the T_1 as a function of rf-power, depicted in figures **6.3(a)** and **(b)**. With this, we are able to fit the resulting histograms, since except of τ_m/T_1, all parameters are fit using a least-square fit. Next, we measure the SNR as a proxy for the fidelity as a function of integration time and rf-power. A colormap of the SNR is depicted in figure **6.3(c)**[1]. The colormap reveals that for rf-power below $-100\,\mathrm{dBm}$, the SNR is very poor due to the small separation between V_rf^S and V_rf^T. For rf-power $> -95\,\mathrm{dBm}$, the SNR decreases slightly which we attribute to a constant signal strength and an increased power broadening at higher power. Even though the characteristic relaxation time T_1 is about an order of magnitude longer for rf-power $< -100\,\mathrm{dBm}$ we choose $-91\,\mathrm{dBm}$ as the optimal rf-power due to the better SNR. An exemplary IQ-histogram of 2000 parity measurements with a $\sim 50/50$ preparation at this power is depicted in figure **6.4(a)**. We only used the I-quadrature as shown in the histogram in figure **6.4(b)**. With all parameters set, we then optimize the integration time τ_m. We increase the number of samples to 10000, ensuring enough data to calculate fidelities above $99.9\,\%$. We can use the functions for fidelity and visibility given by equations **6.1** and **6.3**, respectively, to find the optimal voltage threshold (minimum of visibility error) and calculate the optimal fidelities. A plot of the errors of fidelities and visibility as a function of threshold is depicted in figure **6.4(c)**. We plot the minimal errors of fidelities

1 The SNR presented here is in terms of voltage and not power.

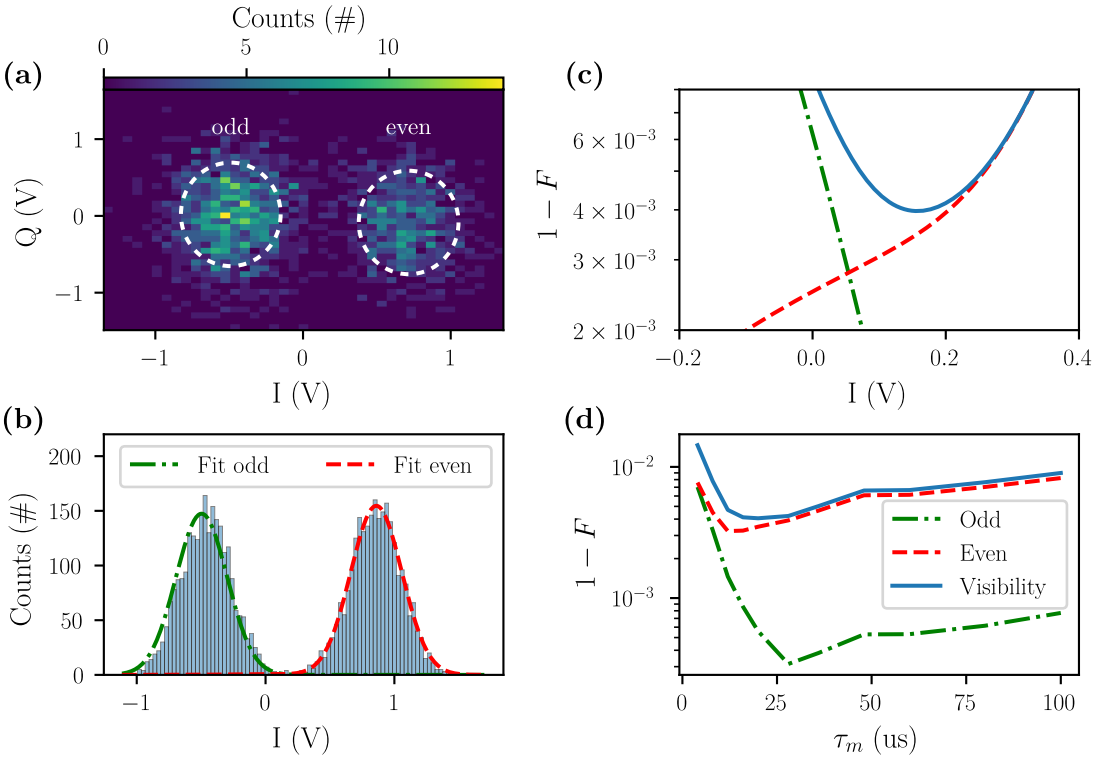

Figure 6.4: The colormap in **(a)**shows the counts of a spin measurement in the IQ plane. The data was acquired at 125 Hz per channel. The signal distribution of the signal for even/odd spin configurations is highlighted with white dashed circles. Figure **(b)** depicts the histogram of the I-quadrature for a readout at 50 kHz with fits to the even and odd population. Using the fits from **(b)**, the misidentification error can be calculated with respect to the voltage threshold as plotted in figure **(c)**. From the optimal fidelities for different measurement speeds we can find the fidelities and visibility as a function of measurement time as shown in **(d)**.

and visibility as a function of integration time τ_m in figure **6.4(d)**. We find an optimal visibility of 99.79 % for $\tau_\mathrm{m} = 20\,\mu\mathrm{s}$ with fidelities of 99.98 % and 99.83 % for non-blocked and blocked state respectively. At a readout speed of 250 kHz $\widehat{=}$ $\tau_\mathrm{m} = 4\,\mu\mathrm{s}$ which is the limit of our measurement bandwidth, we find a fidelity of 99.57 % (99.56 %) for odd (even) and a visibility of 99.13 %. This demonstrates that even at the limit of our readout speed, the fidelity remains above the 99 % threshold. The lower fidelity for shorter integration times is in good agreement with the increased noise $\sigma \propto 1/\sqrt{t_\mathrm{m}}$. For longer integration times, the probability of misidentification of blocked state increases with $e^{-\tau_\mathrm{m}/T_1}$, resulting in a decrease in fidelity for longer integration times.

6.1.4 State preparation and error analysis

The high fidelity of single- and two-qubit gates, demonstrated in spin qubits, has been a very promising result in recent experiments[Noi22; Xue22; Yon20]. On the other hand, qubits require not only high fidelity manipulation, but an overall high fidelity that in-

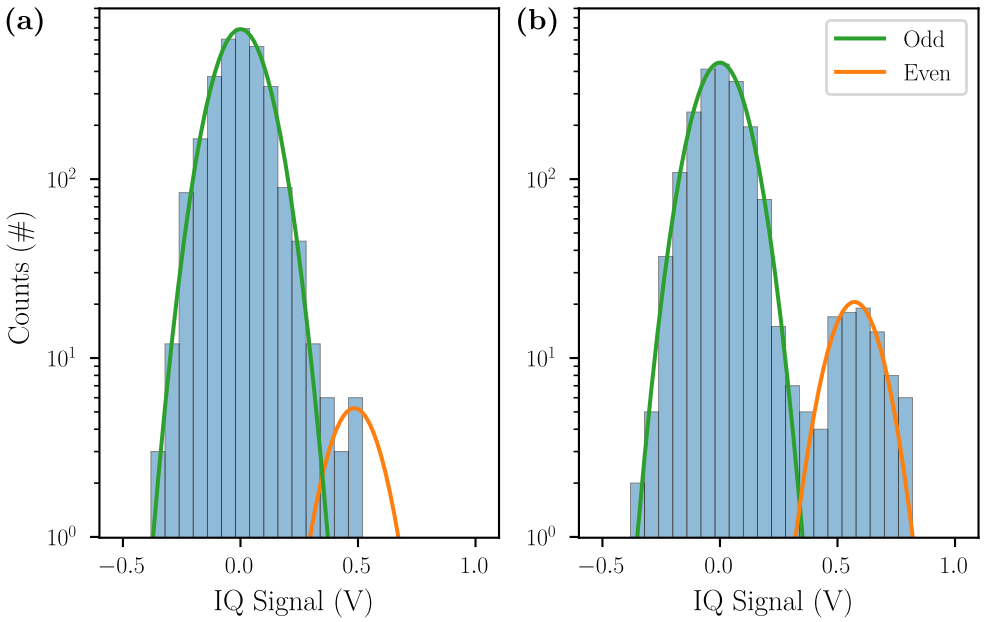

Figure 6.5: **(a)** depicts the signal histogram for the singlet S_0 preparation experiment described in the main text. **b** depicts the signal histogram for the transfer experiment described in the main text.

cludes preparation and readout. The error for the product of the **s**tate **p**reparation **a**nd **m**easurement (SPAM) often ranges around $\sim 10-20\,\%$ being the bottleneck for the overall fidelity[Mil22]. We distinguish three different types of errors, namely initialization, transfer to the regime of single qubit operation (1|1) and readout. We find that the readout is for our experiment of high fidelity as discussed in the previous section. Furthermore, we identify the initialization error for S_0 by an initial wait in (1|0). After, we load a second electron into $\mathrm{QD}_{\mathrm{B2}}$ by pulsing into (2|0), where we remain for 10 ms to allow relaxation to the ground state. A final pulse to the measurement position is followed by the spin readout. From repeating this experiment, we can retrieve the histogram depicted in figure **6.5(a)**. We find a S_0 population of 99.6 %, thus an initialization error of 0.4 % for S_0.
Next, we investigate the transfer errors that occur when we pulse into (1|1), where the two electrons can be decoupled. The pulse sequence is identical to the one described in the previous paragraph except that we transfer to (1|1) after the 10 ms waiting time in (2|0). The transfer from (2|0) to (1|1) is done non-adiabatically for the anti-crossing of $S_0 - T_-$ and adiabatically after the anti-crossing to avoid mixing of $S_0 - T_0$. Without waiting in (1|1) we pulse to the measurement position in (1|1). The total time in (1|1) is $\approx 20\,\mu\mathrm{s}$, accounting for the time per instruction in the pulse sequence. For this experiment we find the histogram depicted in figure **6.5(b)**. From the histogram we calculate a S_0 population of 95.6 %. Thus, the transfer process adds 4 % of error to the SPAM error. The leakage during transfer is therefore the main error source for our SPAM error and a

more carefully designed transfer sequence is required to avoid such errors. To understand where the leakage occurs, we want to discuss in the following a Landau-Zener experiment we performed to better understand the $S_0 - T_-$ anti-crossing.

6.2 Characterization of a two-spin system

In this section, we will present measurements that we used to characterize the two-spin system, using the readout technique that we presented in the previous section. We will begin with a spin funnel experiment. After, we will discuss a Landau-Zener experiment. Next, we will present data from measurements that indicate $S_0 - T_0$ mixing. Finally, we will present indications for Wigner molecularization effects.

6.2.1 Mapping the $S_0 - T_-$ crossing using a spin funnel experiment

A spin funnel experiment can be used to map out the degeneracy point of the S_0T_- anti-crossing. Such an experiment was already performed by Petta et al. [Pet05a] and since, has often been used to estimate the exchange energy J as a function of detuning. When working with an ST-qubit, transfers passing through the avoided-crossing must be non-adiabatic to avoid state leakage, and thus it is important to know the position and strength of this anti-crossing. We will start with our experimental procedure which is following [Fog18].
The spin funnel experiment measures the detuning shift of the anti-crossing of the S_0-T_- transition. For this, we follow the procedure of 1. preparation, 2. manipulation, and 3. measurement.

1. The system is prepared in the S_0 state by pulsing into the (2|0) regime, where S_0 is the ground state. After remaining in this regime much longer than the relaxation time T_1, we can safely assume that the system is in the S_0 state.
2. We pulse closer to the (2|0)-(1|1) transition, while taking care that S_0 is still the ground state at this position. As the tunnel coupling between the two quantum dots is slow compared to the rise time of the DAC voltage, we can use the DAC to perform the measurement. However, DAC channels can only be pulsed sequentially, and we therefore move our gates at a position, where we only need to pulse B_2 to cross the (2|0)-(1|1) transition. Moreover, we use a position within the Pauli spin blockade regime. This avoids additional pulses after the manipulation, reducing state leakage during the transfer to the measurement position. We apply a pulse on gate B_2 with varying amplitude in the direction of the (2|0)-(1|1) transition. We stay at the pulsing position for 10 ms, allowing relaxation to the ground state which is either S_0 or T_0, depending on the pulse amplitude and magnetic field.
3. We return to the position in the Pauli spin blockade region and measure the spin state.

This single measurement is repeated until sufficient statistics are available to calculate the population of even (triplet) or odd (singlet) state. Next, the magnetic field is slightly

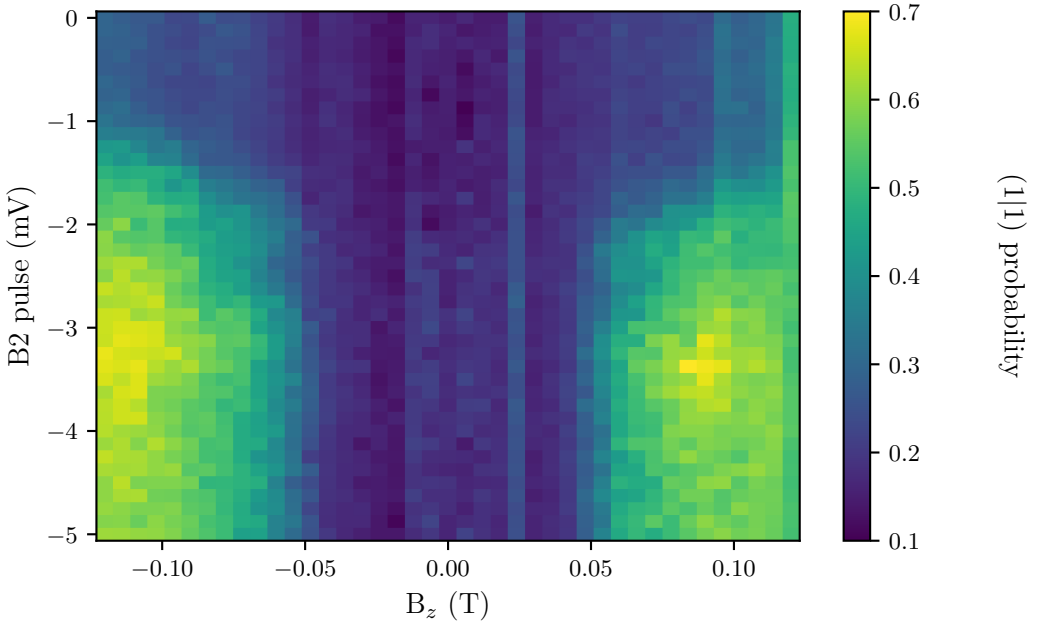

Figure 6.6: Colormap showing the probability of measuring a (1|1) signal (blocked state) after performing a spin funnel experiment. An initial singlet state is pulsed across the interdot transition from (0,2) to (1,1). The experiment varies the B2 pulse amplitude that can be considered as detuning and the magnetic field B_z. The funnel like signature where the signal changes from majority singlet to majority triplet can be interpreted as the avoided-crossing of $S_0 - T_-$.

changed, resulting in a shift of the $S_0 - T_-$ anticrossing. Finally, we can plot a population map of pulsing amplitude vs. magnetic field and find the figure in **6.6**.
While Petta et al.[Pet05a] used short AWG pulses in this experiment, allowing only mixing at the $S_0 - T_-$ avoided crossing, we performed a measurement similar to Fogarty et al. [Fog18]. The longer dwell time compared to the spin funnel experiment performed by Petta et al. has two effects. First, we have a high triplet population for all pulses that surpass the $S_0 - T_-$ anti-crossing due to relaxation to the ground state. Second, close to the anticrossing, we do not have coherent mixing of the two states, but stay long enough to find a population resembling a thermal population, broadening the transition. This broadening is crucial, as the anti-crossing can be very small and difficult to detect.

6.2.2 Characterizing the $S_0 - T_-$ anti-crossing

For $B_z \neq 0$, the T_- state becomes the ground state for (1|1), whereas the S_0 state remains ground state in (2|0). The resulting anti-crossing close to the interdot transition is described by the coupling $\Delta(\theta)$ between the non-polarized singlet state S_0 to the polarized triplet states T_- and T_+. While in GaAs/AlGaAs QDs this coupling mostly originates

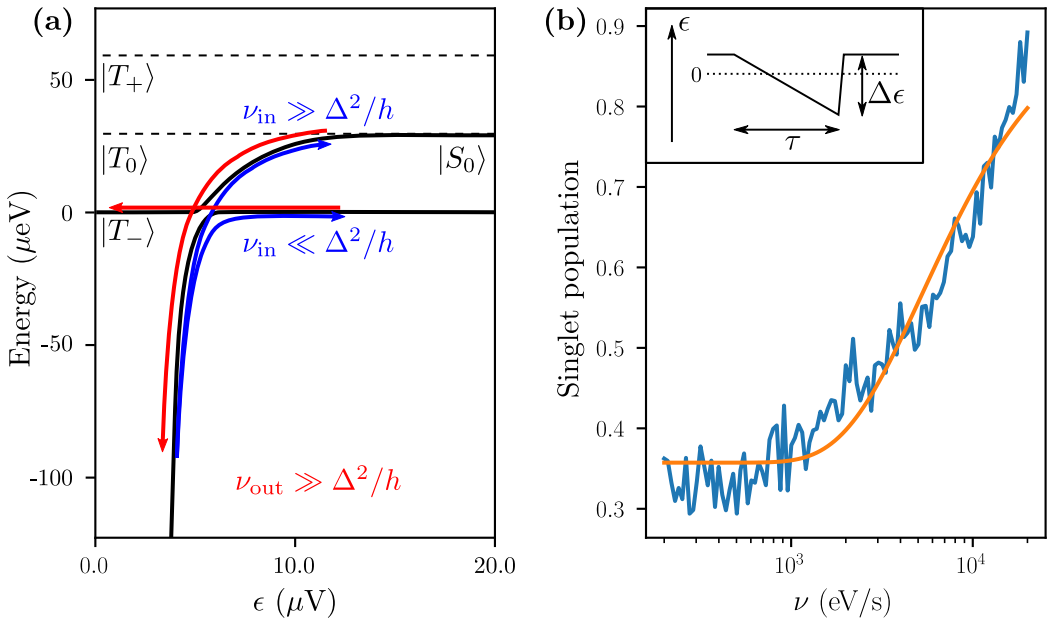

Figure 6.7: **(a)** Scheme of the Landau-Zener experiment in a singlet-triplet system. The blue arrows indicate the path taken for the ramp from the (2|0) to the (1|1) regime. The red arrows indicate the path for the non-adiabatic return pulse. **(b)** Singlet population as a function of ramp speed. The inset depicts the pulse scheme used for the experiment. Figure **(a)** is adapted from [Fog18].

from nuclear spins[Tay07], the isotopically enriched Si of our device can be considered nuclear spin free and spin-orbit coupling is a more likely source for off-diagonal elements in the electronic g-factor[Joc18].

We perform the following experiment to characterize the S_0-T_- anti-crossing. First, we initialize in a S_0 state by waiting for relaxation to the ground state in (2|0). Next, we ramp with amplitude $\Delta\varepsilon$ from (2|0) to (1|1) and pulse non-adiabatically to the parity measurement position. A schematic of the pulse applied to B2, using an AWG, is depicted in the inset in figure **6.7(b)**. We estimate the transfer speed through the avoided crossing using $\nu = \frac{\alpha e \Delta\varepsilon}{\tau}$. The non-adiabatic pulse to the measurement position allows to freeze the state after the ramp (see figure **6.7(a)**). By varying the time τ of the voltage ramp, we can thus map the state probability for different ν. The singlet population as a function of transfer speed ν is plotted in figure **6.7(b)**. We find the expected monotonous increase of singlet population probability with increasing transfer speed. Using the Landau-Zener formula

$$P_{\text{LZ}} = 1 - e^{\frac{-2\pi\left|\Delta_{\text{ST}}^2\right|}{\hbar\nu}} \tag{6.4}$$

to fit the data yields $\Delta_{\mathrm{ST}} = 130\,\mathrm{MHz}$ for $B_{\mathrm{z}} = 120\,\mathrm{mT}$ [Nic15]. A relatively large value compared to other studies of Si [Fog18].
To better understand Δ_{ST}, we use

$$\Delta_{\mathrm{ST}}(\xi) = \left|\cos(\xi)\frac{\delta E_{\mathrm{z}}^{x} + i\delta E_{\mathrm{z}}^{y}}{\sqrt{2}} + \Delta_{\mathrm{SOt}}\sin(\xi)\right|, \tag{6.5}$$

with $\xi = -\arctan(2t_c/E_{\mathrm{z}})$, $\delta E_{\mathrm{z}}^{x}$ and $\delta E_{\mathrm{z}}^{y}$ Zeeman energy differences between the QDs, and Δ_{SOt} the spin mixing due to electron movement induced spin-orbit coupling [Tan19]. We will see in the next section that in this device we can probably assume that $\delta E_{\mathrm{z}}^{x} \approx 0$ and $\delta E_{\mathrm{z}}^{y} \approx 0$. In that case the formula reduces to

$$\Delta_{\mathrm{ST}}(\xi) = \Delta_{\mathrm{SOt}}\sin(\xi). \tag{6.6}$$

We do not find a change of Δ_{ST} with magnetic field for B_{z} between 120 mT and 60 mT. To explain this result we need $t_c > \max(E_{\mathrm{z}})/2 \approx 7\,\mu\mathrm{eV}$. Thus, the lower limit of the tunneling constant t_c is 1.7 GHz.

6.2.3 $S_0 - T_0$ mixing

As already mentioned in section **6.1.2**, we prepared a mixture of S_0-T_0 to prepare the state we used to characterize the ST-readout. We want to present here the details of this state preparation. Following the experiments in [HC18; Mau12], we start by preparing an S_0 state in (2|0) by relaxation to the ground state. After, we transfer to the ST-readout position, followed by an AWG square pulse on gate B2 in the (1|1) regime, separating the two electrons. At this position, the singlet-triplet basis is not the eigenbasis anymore and the spins' evolution is driven by the δE_{z} terms of the Hamiltonian (see equation **2.38**) until pulsing back to (2|0) with considerable $J(\varepsilon)$. On returning to the ST-readout position, an ST-readout can be performed. Figure **6.8** shows the resulting singlet population as a function of pulse duration. We calculate a characteristic time of $18.5 \pm 2.5\,\mu\mathrm{s}$ by fitting an exponential decay to the singlet population. The exponential decay and the convergence towards 50 % singlet population indicate that we indeed observe mixing between $S_0(1|1)$ and $T_0(1|1)$. The often observed spin-orbit induced oscillations are not observed in our device. One explanation for this could be a suppression of the g-factor difference for magnetic fields perpendicular to the nanowire orientation. Studies in planar MOS silicon double quantum dots showed that for a magnetic field perpendicular to the plane, the g-factor difference Δg can be zero [Tan19]. On the other hand, even though when Δg is zero, the spin flipping term Δ_{ST} in the device studied by Tanttu et al. [Tan19] can be in the order of tens of MHz. Performing the same experiment in a similar device showed oscillations in the MHz range, but a much shorter relaxation time of 0.7 µs (see appendix **B.4**).

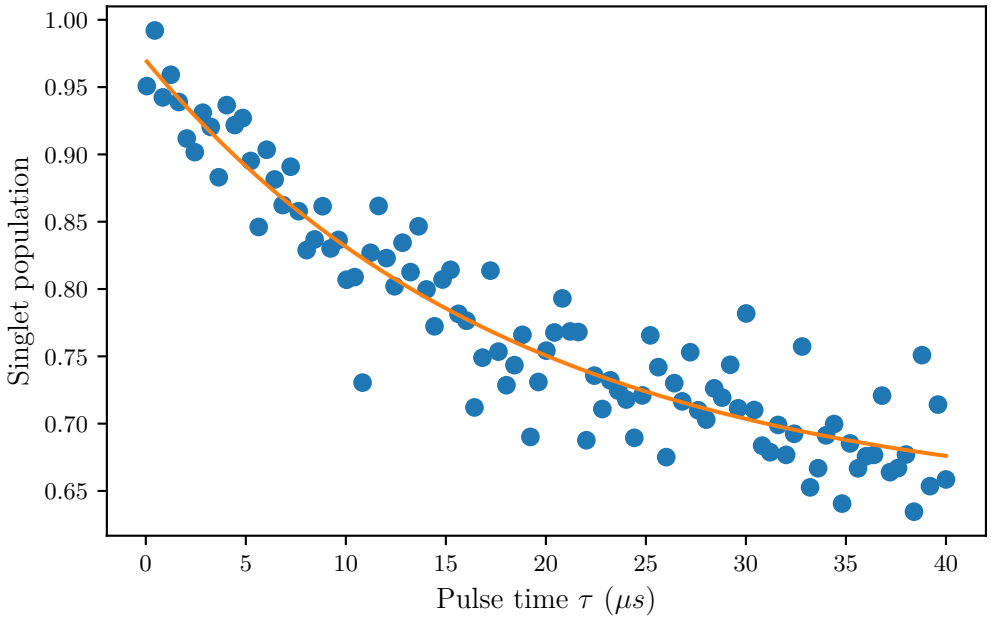

Figure 6.8: Singlet population as a function of AWG pulse duration τ. The population is fit with an exponential decay with a characteristic time of $18.5 \pm 2.5\,\mu s$. The full experiment is described in the main text.

6.2.4 Valley- and orbital effects in nanowire devices

We have already mentioned in several sections that the quantum dot states in silicon quantum dots consist of orbital states as well as valley states. Additionally, the tunnel coupling between QDs is strongly affected by the sharp potentials in the nanowire devices, defining the QD shape and the wave function overlap. Performing Pauli spin blockade measurements in the presented device as well as in another device, with identical geometry and from the same wafer, resulted in a PSB signal that, to our knowledge, has not been observed in another device yet. In this section we want to discuss the observed effect and present a model that can explain these results.

We perform Pauli spin blockade measurements in two devices. One is the device, used for the results presented in the previous sections, and the other is a device with the same geometric parameters and from the same wafer. In both devices we tune the system to an interdot transition of the two electron regime depicted in figure **6.10(a)** and **(c)**, where the charge transitions of QD_{B2} (QD_{T2}) are indicated with orange (black) dashed lines. The interdot transitions are indicated using a white dashed line and the detuning axis with a white arrow. The stability diagram in figure **6.10(c)** shows Pauli spin blockade (stochastic lines) in the (2|0) regime, where the red line indicates a detuning value where no PSB is found. We prepare a singlet S_0 (triplet T_-) state by relaxation to the ground state in (2|0) ((1|1)) and measure the signal along the detuning axis. We take 300 traces

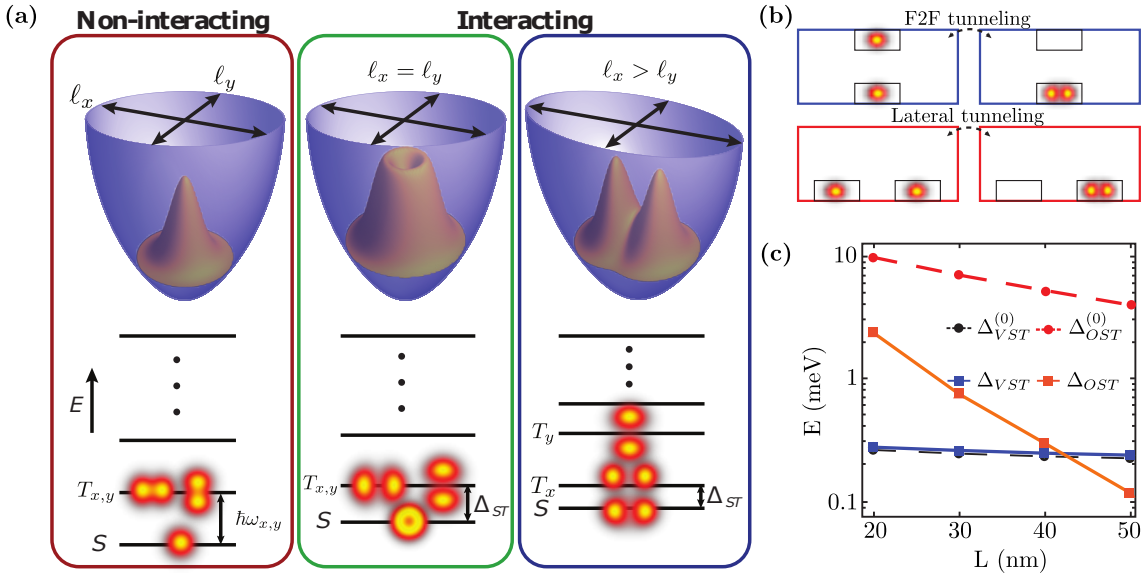

Figure 6.9: **(a)** Panels showing the ground state density for two particles confined in a 2D harmonic potential (top) for non-interacting (red panel) and interacting (green and blue panel) particles. The green panel shows the case for a symmetric potential ($l_x = l_y$) and the blue panel the case for an asymmetric potential. The gap between singlet and triplet states Δ_{ST} reduces for interacting particles and is smallest in the asymmetric case. In the asymmetric case the particles can separate along the weak confinement direction, resulting in an energy renormalization. **(b)** Tunneling types in a face to face device. The upper frame shows the tunneling of face-to-face gates and the lower frame transversal tunneling along the nanowire. **(c)** Orbital splitting Δ_{OST} ($\Delta^{(0)}_{\mathrm{OST}}$) and valley splitting Δ_{VST} ($\Delta^{(0)}_{\mathrm{VST}}$) between the singlet and first triplet state for interacting (non-interacting) particles as a function of gate width. Adapted from [AU21].

and extract from the signal distributions the triplet population, plotted in figure **6.10(d)**. The signal of the singlet preparation (blue) shows no triplet population after surpassing the interdot transition. In contrast, the signal from the triplet preparation (orange) shows a constantly high triplet population (due to PSB) except of a dip between a detuning of 3.5 mV and 4.0 mV. This sharp dip is as well observable in the other device, depicted in the colormap in figure **6.10(b)** and highlighted with a red dashed line. We interpret this dip as a detuning value where the PSB is lifted.

The origin of this PSB lifting is apparently an effect of the detuning, and we are not aware of other systems where such an effect was observed. We thank Biel Martinez Diaz and Yann-Michel Niquet for helping us to develop a model that can describe the observed effect. This model is based on five states and uses assumptions justified by the Wigner molecularization in these devices discussed in [AU21]. In the following, we want to discuss the physics of the PSB lifting according to this model. The states we consider in our model are $\{S_0(1|1), S_0(2|0), T_-(1|1), T_-(2|0), E2(2|0)\}$, with the singlet $S_0(2|0)$ state being the ground state in $(2|0)$, where the triplet state $T_-(2|0)$ is the first excited state. The state $E2$ is another excited state in the $(2|0)$ regime. In our model we assume that $\tau_{T_-} \ll \tau_{S_0}$

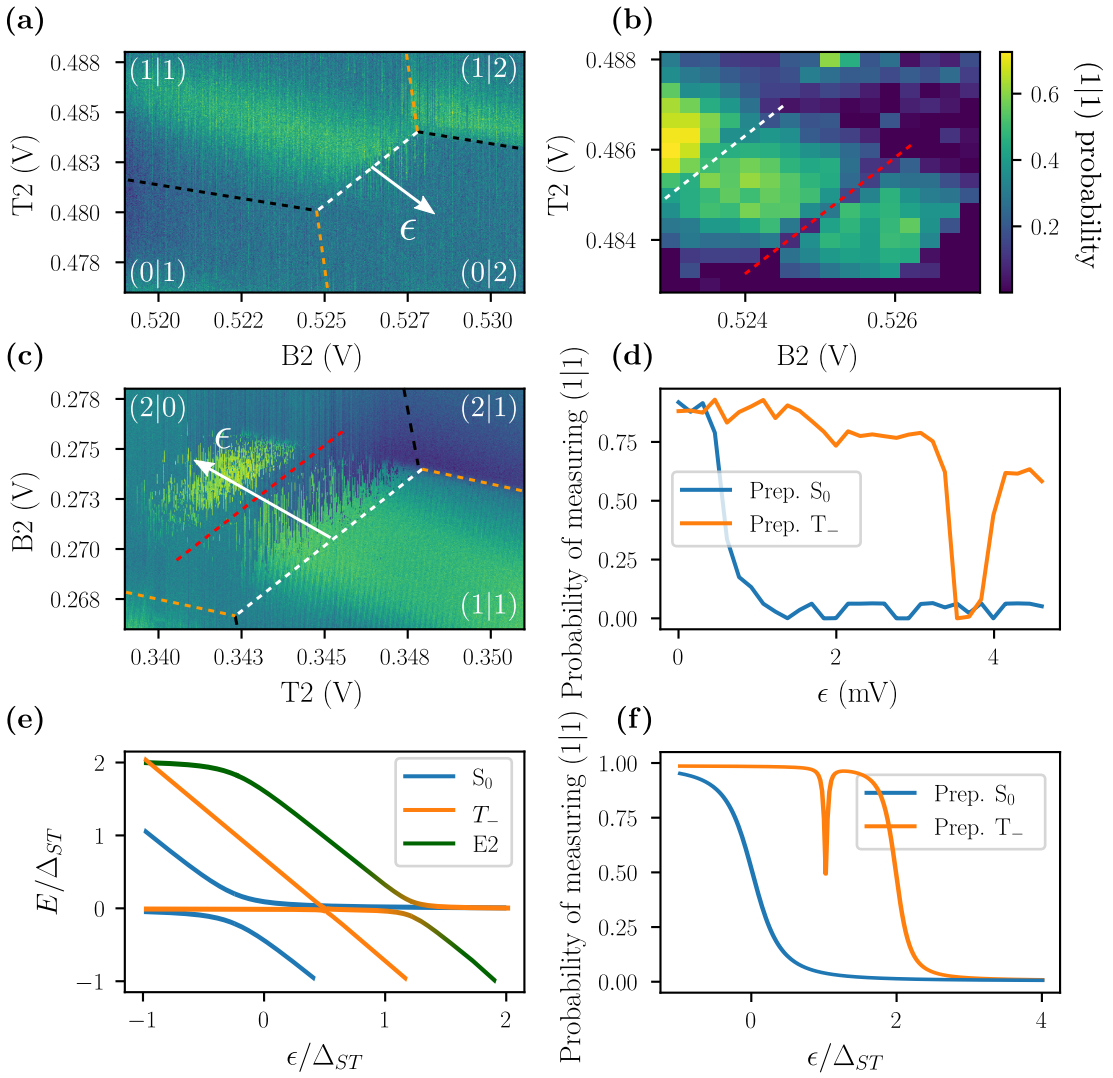

Figure 6.10: Figures **(a)** and **(c)** show stability diagrams of two different devices at a two electron interdot transition with $B_z \neq 0$. The black (orange) dashed lines indicate the transitions of QD_{T2} (QD_{B2}) and the white dashed line the position of the interdot transition. The white arrows indicate the detuning axis and the red dashed line a position where the PSB is lifted. The colormap in figure **(b)** shows the triplet population of a formerly prepared triplet T_- state as a function of measurement position. The dashed white line indicate the interdot transition and the dashed red line indicate a position where the PSB is lifted. Figure **(d)** depicts the triplet population as a function of detuning for an initial singlet S_0 (blue) and initial triplet T_- (orange) state. In our model we use three energy levels, plotted in figure **(e)** for a detuning range that covers the PSB regime that are used by our theoretical model. Using the model, we can simulate the probability of measuring a (1|1) state (blocked) as a function of detuning ε for an initial singlet (blue) and an initial triplet state (orange), plotted in figure **(f)**.

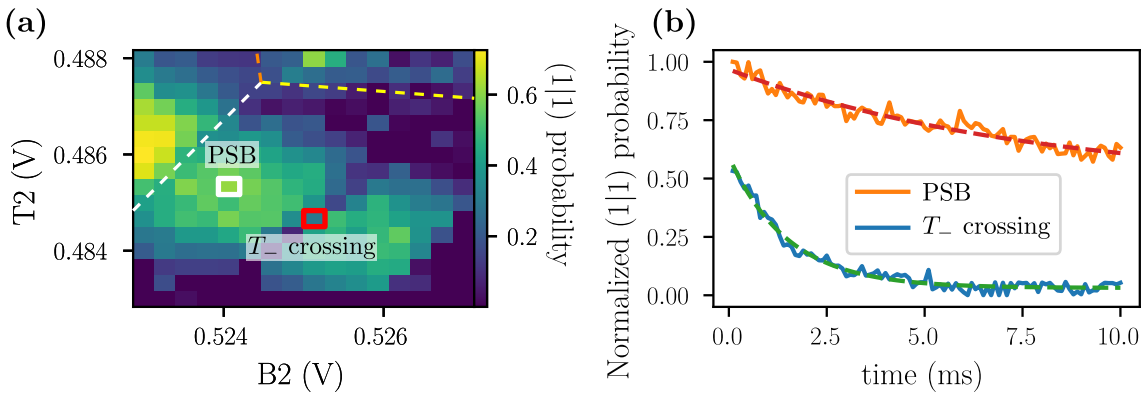

Figure 6.11: Figure **(a)** depicts the probability of measuring a (1|1) for an initial T_- state for gate voltages that cover the PSB regime. The charge transitions are indicated with white, orange, and yellow dashed lines for the interdot, QD_{B2}-reservoir, and QD_{T2}-reservoir transitions respectively. Figure **(b)** depicts the relaxation at the two measurement positions highlighted with a white and red frame in figure **(a)** and labeled PSB and T_- crossing, respectively. The triplet population is calculated from histograms of the signal distribution and normalized to the maximal triplet population measured in the PSB regime. The relaxation time at the PSB (T_- crossing) position is 7.8 ± 1.5 ms (1.51 ± 0.06 ms).

and $\tau_{T_-} \ll \tau_{E2}$, where τ_{T_-}, τ_{S_0}, and τ_{E2} are the tunnel couplings between the two triplet states $T_-(1|1) - T_-(2|0)$, the two singlet states $S_0(1|1) - S_0(2|0)$ and $T_-(1|1) - E2(2|0)$, respectively. Further, we require that the avoided level crossing of $T_-(1|1) - T_-(2|0)$ is so small, due to the small tunnel coupling τ_{T_-}, that the pulse speed of our gates pass the avoided crossing non-adiabatically. In contrast, the other anti-crossings are large enough, such that the pulses on the gates result in adiabatic transitions. The reason we make this choice for the tunnel couplings is the following. First, in a face-to-face device with one quantum dot on each side of the nanowire, the spherically shaped s-orbitals show a rather strong overlap compared to the rather elongated p-orbitals. The p-orbitals are preferably aligned along the nanowire which results in a much smaller wave function overlap and therefore, smaller tunnel coupling [AU21]. This effect is depicted in figure **6.9(a)**, where the density for different potential shapes and for interacting and non-interacting particles is shown. In our case, where the particles interact and the potential is asymmetric with a weak confinement along the nanowire, the particles align along the nanowire rather than face-to-face (blue panel). While the singlet states occupy s-orbitals, the triplet states occupy p-orbitals, resulting in a low tunneling rate for the triplet states between the two quantum dots. In other words, the avoided level crossing of the charge states $S_0(1|1) - S_0(2|0)$ is much stronger than for $T_-(1|1)$-$T_-(2|0)$. Additionally, due to the molecularization effect it can happen that $\Delta_{O,ST} < \Delta_{V,ST}$ such that the triplet populates an orbital state (a p-orbital) and not a valley state (see figure **6.9(c)**). The small tunnel coupling means that even with slow pulses a non-adiabatic transition is likely. If the excited state E2 is valley like, the overlap can be larger than for p-orbitals, resulting in a stronger tunnel coupling. The Hamiltonian in the basis $\{S_0(1|1), S_0(2|0), T_-(1|1), T_-(2|0), E2(2|0)\}$

is then given by

$$\hat{H} = \begin{pmatrix} 0 & \tau_{\mathrm{S}} & 0 & 0 & 0 \\ \tau_{\mathrm{S}} & -\varepsilon & 0 & 0 & 0 \\ 0 & 0 & 0 & \tau_{\mathrm{T}_-} & \tau_{\mathrm{T}_-\mathrm{E2}} \\ 0 & 0 & \tau_{\mathrm{T}_-} & -\varepsilon + \Delta_{\mathrm{ST}_-} & 0 \\ 0 & 0 & \tau_{\mathrm{T}_-\mathrm{E2}} & 0 & -\varepsilon + \Delta_{\mathrm{SE2}} \end{pmatrix}, \tag{6.7}$$

where Δ_{ST_-} (Δ_{SE2}) is the energy splitting between the $S_0(2|0)$ and the $T_-(2|0)$ ($E2(2|0)$) state. Using this Hamiltonian we can plot the energy diagram, depicted in figure **6.10(e)**. The singlet state $\mathrm{S}_0(2|0)$ forms the ground state in (2|0) (green) and the triplet state $T_-(1|1)$ (blue) is the ground state in the (1|1) regime. The excited state $E2$ (orange) that crosses the triplet $\mathrm{T}_-(1|1)$ state at higher detuning is never the ground state. Using this model we simulate the probability of measuring the $\mathrm{T}_-(1|1)$ state as a function of detuning for an initial singlet $S_0(1|1)$ (blue) and initial triplet $T_-(1|1)$ (orange) and plot it in figure **6.10(f)**. For this simulation we assumed that the $S_0(1|1)-S_0(2|0)$ anti-crossing is passed adiabatically, while the $T_-(1|1)-T_-(2|0)$ anti-crossing is passed non-adiabatically. We find that the initial singlet S_0 results in a zero probability to find a (1|1) signal (no PSB observed) after passing the $S_0(1|1) - S_0(2|0)$ anti-crossing, in good agreement with our measurements. For the initial triplet T_-, we find that the state remains in (1|1) (PSB) when passing the $S_0(1|1) - S_0(2|0)$ anti-crossing. When the $T_-(1|1) - T_-(2|0)$ is matched with the measurement position, the probability to measure a blocked state goes to 50 % (mixing of states). For even higher detuning the initial triplet state remains again (1|1) until passing the $T_-(1|1) - E2(2|0)$ anti-crossing, where the non-adiabatic passing results in a zero probability to measure (1|1). In this simulation we do not consider relaxation. That indeed mixing followed by relaxation might be the observed effect is supported by measuring the relaxation in the PSB regime between the $S_0(1|1) - S_0(2|0)$ and the $T_-(1|1) - T_-(2|0)$ anti-crossings and at the $T_-(1|1) - T_-(2|0)$ anti-crossing as depicted in figure **6.11**. We find that, after renormalization of the population to account for the preparation and transfer error, the observed T_- signal is initially $\approx 50\,\%$ at the $T_-(1|1)-T_-(2|0)$, in good agreement with the proposed mixing explanation. Additionally, the relaxation at the $T_-(1|1) - T_-(2|0)$ anti-crossing is faster than in the rest of the PSB regime. This may explain why we do not find 50 % in the other device (see figure **6.10(d)**) as the relaxation at the anti-crossing in this device might be faster than our measurement bandwidth [Wan10; Xia10]. The good agreement between simulation and measurement are indicating that indeed the tunnel coupling of the triplet states is likely to be very small. However, this is not a smoking gun argument, and we cannot rule out that the system is better described by a different Hamiltonian. The next step would be to perform the same measurement using a DQD system along the nanowire, where the tunnel coupling of triplet states should be much stronger (see figure **6.9(b)**). In this case, the PSB should be completely lifted for detuning higher than the $\mathrm{T}_-(1|1)$-$\mathrm{T}_-(2|0)$ crossing. If this could be observed, it would strengthen our interpretation that the main driver for the effect is the orbital overlap of the different states.

6.3 Conclusion

In this chapter we have demonstrated the potential of rf-reflectometry based spin readout. Using a single ancillary QD as sensor, we use a DQD to control a two spin system and achieve high fidelity ST- and parity readout at 50 kHz. The high fidelity readout is achieved by reducing the parasitic capacitance, increasing the readout frequency and using a trimmed FDSOI device. Combining these two readout schemes is of importance to achieve full spin readout of a 2-qubit system. The readout technique proposed in [Nur22], starts with an ST-readout to distinguish S_0 from the triplet states. Next, a parity readout allows differentiating between the unpolarized T_0 state from the polarized triplet states T_- and T_+. Lastly, an adiabatic transfer through the S_0-T_- anti-crossing allows transferring T_- to S_0 and a final parity or ST-readout distinguishes T_- and T_+. The readout requires careful tuning of the three QD system to the correct capacitive and tunnel coupling. We analyzed the different SPAM errors and found that the major error can be attributed to state leakage when pulsing through the S_0-T_- avoided crossing.
Furthermore, we analyzed the spin system in our device using Landau-Zener and spin funnel experiments for the $S_0 - T_-$ anti-crossing and a mixing experiment for the $S_0 - T_0$ interaction. Additionally, we found evidence for Wigner molecularization effects in these devices that prohibit tunneling of triplet states for face-to-face QDs.

7 Outlook

> The future cannot be predicted, but futures can be invented.
>
> Dennis Gabor

In this chapter we want to take a look at the challenges ahead for the different topics we have dealt with in this thesis. We will give some ideas how to improve rf-reflectometry and how to use it in a large scale architecture. This will then lead us to the design of large scale architectures. Additionally, we want to give an idea of the environment that has to be built around the qubit processor, ranging from control electronics, over cryostats to software.

7.1 RF-reflectometry for large scale high fidelity readout

The goal of this section is to discuss a few perspectives for future research in rf-reflectometry for QDs. We will present the required properties for using the readout for large scale architectures and a potential path to further improve the SNR by using a novel kind of amplifier.

7.1.1 Towards high fidelity readout at GHz frequencies

In this thesis we demonstrated high fidelity spin readout approaching MHz speed. Even though the three orders of magnitude faster readout time compared to the relaxation time are sufficient to achieve high fidelity readout, it is desirable to perform a readout even faster. It comes down to the question of how fast one wants to run the quantum processor. If qubit gates can be performed in the 100 MHz range or even faster, a readout at 1 MHz would limit the number of calculations the processor can perform per second significantly. Thus, the readout should be always at least as fast as the slowest step of a quantum algorithm (initialization or qubit gates). Moreover, we will see that it might be necessary to readout qubits sequentially, making a fast readout even more important.
We have seen in section **4.1** that to improve the SNR, which is a good proxy for the readout fidelity, we need a high quality factor, a parasitic capacitance as small as possible and a resonance frequency close to the tunnel rate of the sensed transition. In our work, the devices were fabricated in a separate process from the inductors. This results in the need for bond pads and a still rather large footprint of the readout circuit. Cointegration of readout circuit and qubit chip can be very compact [Bor21; Zhe19] and reduce the parasitic capacitance significantly. Indeed, using a not fully processes wafer from CEA LETI without bond pads allowed to pattern an inductor like it was used in the presented

work on top of the device die and directly connect one of the gates to one end of the spiral inductor. The resulting parasitic capacitance was $\approx 0.23\,\mathrm{pF}$, a 10x reduction. The small parasitic capacitance is not only an advantage in terms of reflectometry signal, but it also allows working at higher frequencies. Higher frequencies allow to improve the SNR even further by using superconducting amplifiers with a very low noise level.

7.1.2 Josephson traveling wave parametric amplifiers for reflectometry readout

For sufficiently strong amplification, the SNR of the measurement is defined by the signal strength, the intrinsic signal noise and the noise of the first amplifier. So far, the noise of the first amplifier was the dominant noise source, such that other noise could be ignored. Following Friis [Fri44], the SNR is then given by signal strength and thermal noise from the first amplifier. In typical dilution fridge setups the first amplifier stage is placed at the 4 K stage to provide sufficient cooling power. The resulting noise temperature of state-of-the-art low-noise amplifiers is around 2.5 K. Thus, the best noise temperature one can achieve with such a setup is in the range of a few Kelvin. A rather new technology are amplifiers using Josephson junctions. These amplifiers operate at base temperature of dilution fridges ($< 100\,\mathrm{mK}$) and their intrinsic noise can be quantum noise limited [Pla20]. Such amplifiers are still not commercialized and pose challenges at every stage, starting with a reliable fabrication process to their final tuning to be compatible with the conceived experiment. Thanks to the group of Nicolas Roch at the Néel Institute, our group is currently working on rf-reflectometry using a superconducting amplifier. While such amplifiers were mostly used with superconducting qubit systems, the similarity of rf-reflectometry for QDs to dispersive readout used for superconducting qubits [Mac15], allows to transfer the technology. For spin qubits, the strong susceptibility to magnetic fields makes the use of these amplifiers particularly challenging and techniques to mitigate this effect have to be explored. Either a passive approach like mounting the amplifier far away from the magnetic field and using μ-metals to shield it or an active approach using small electromagnets to compensate the magnetic field.
The simplest type are so-called Josephson parametric amplifiers (JPAs) which consist of a single Josephson junction. A more elaborate amplifier is the Josephson traveling wave parametric amplifier (TWPA) [Mac15] which is made of a chain of Josephson junctions. Such a chain of Josephson junctions has two main advantages over the JPA. First, it is a broadband amplifier with a bandwidth of around 2 GHz in contrast to a few MHz for a JPA. Second, the saturation point of a TWPA is approximately at around $-100\,\mathrm{dBm}$, around 10 dB higher than for JPAs, which allows higher rf-power, often necessary to drive the QD device sufficiently strong. The working principle of a TWPA is similar to the one of a non-linear crystal in optics. While light traveling through a non-linear crystal shows effects like photon mixing, the same thing happens in a TWPA for microwave photons. In fact, the working principle of a TWPA is four wave-mixing, which is a well known effect from non-linear optics. Two photons of a certain frequency are transformed into two new photons with the same sum frequency, but with different individual frequencies. This effect can be exploited using a so-called pump frequency f_p to provide two photons that are combined to a photon of the frequency of the reflectometry signal f_rf and a photon

at the so-called idler frequency $f_\mathrm{i} = 2f_\mathrm{p} - f_\mathrm{rf}$. This process has limited efficiency and requires a pump signal much stronger than the rf-signal. The art of fabricating a TWPA is to make this conversion very efficient, requiring a matching of the wave numbers k of the different frequencies such that no destructive interference occurs. TWPAs typically reach amplifications of up to 20 dB and the broad bandwidth allows to amplify a large number of rf-tones in parallel.
Apart from the reduced noise level of rf-readout, a technical advantage is the option of parallel readout. Using multiplexing reduces the requirement for multiple readouts to a single rf-cable to transmit a large number of rf-tones only limited to its bandwidth and the frequency separation of the rf-tones. Multiplexed readout was already demonstrated for superconducting qubits [Hei18] and there is no obvious reason it could not be used as well for QDs.
So far, the operation frequencies for TWPAs were around 5 GHz to 7 GHz, matching well the requirements for superconducting qubits that typically show resonances around 6 GHz. This is about an order of magnitude higher than most reflectometry readouts using macroscopic inductors. So far, a TWPA operating below 4 GHz has not been demonstrated, and it might be easier to design reflectometry circuits that work at higher frequencies. Highly integrated rf-reflectometry for QDs operate in the correct frequency range [Bor21; Zhe19], allowing the use of a TWPA for improving the SNR. In how far superconducting amplifiers will play a role for large scale quantum dot based qubits will be seen. We will see in the next section, that it is likely that large scale architectures operate at temperatures > 1 K, rendering superconducting amplifiers useless.

7.2 Towards large-scale architectures

The tasks, a quantum computer could be used for, vary a lot in terms of hardware demands. While small quantum systems and quantum circuits can be already simulated with < 100 qubits [Aru19; Cao21; Kir22], millions of qubits will be required to decrypt modern 2048 bit RSA integers [Gid21]. The susceptibility to different errors makes qubits not only hard to build and scale while still controlling them, but as well requires operations to account for this imperfect behavior. A way to deal with errors in quantum processors are so-called quantum error correction protocols. Error correction protocols are working on specific topologies. The so-called surface code topology is based on a planar 2D qubit array and is one of the most researched in recent years [Bra18]. Error correction protocols allow to transform the error-prone *physical qubits* into a smaller amount of so-called *logical qubits*. Logical qubits can be considered error free when used in a quantum algorithm, but they come at a cost. To build a logical qubit requires different amounts of physical qubits, depending on the error correction protocol and the fidelities of the physical qubits, but estimates are around 10^3 to 10^4 physical qubits per logical qubit [Fow12]. Not considering topological qubits that are out of scope of this thesis [Fre02], the goal is to build a quantum processor with $> 10^6$ qubits. Such a large system will not only require a reliable and scalable qubit unit cell, but comes with a lot of additional challenges. Here, we want to give a brief overview of proposed quantum dot based large scale qubit architectures and a

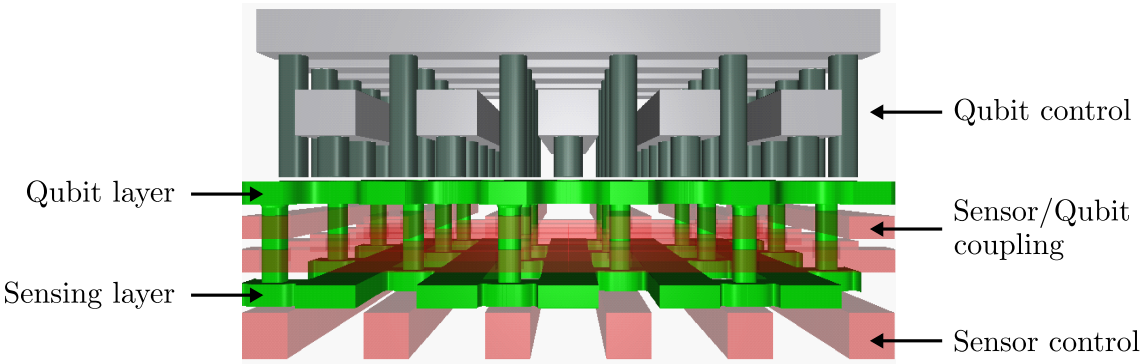

(a) CoolCube architecture

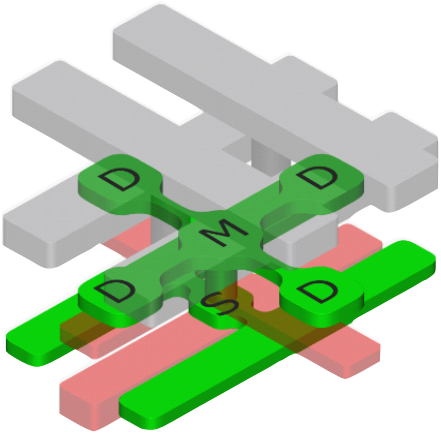

(b) CoolCube unit cell

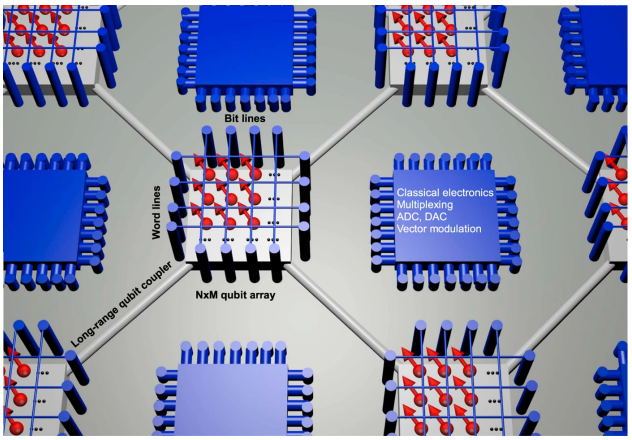

(c) Processor architecture

Figure 7.1: Large scale device architectures for quantum dot based processors. **(a)** CoolCube architecture consisting of a 3D architecture with two quantum dot layers. The upper layer acts as a 2D-array of qubits and the second layer as a sensor array which also provides electrons to the Qubit layer. The control as well as the coupling is controlled with gates on top, between and below the layers. These control layers are structured in a crossbar geometry to minimize the number of gates. **(b)** Unit cell of the CoolCube architecture compatible with surface code error correction. A sensor quantum dot (S) is located below the quantum dot layer hosting quantum dots that host qubits. A central quantum dot (M) is connected through a via with the sensing dot and can be readout via the sensor. The measurement QD is surrounded by four data quantum dots (D). **(c)** Qubit processor architecture proposed by Vandersypen et al. [Van17]. Small qubit arrays are interconnected with long-range qubit couplers. The control of the qubit arrays and couplers is done using integrated control electronics between the qubit arrays. Figure **(c)** is a reprint from [Van17].

few of the challenges that will go along with increasing the system size.

7.2.1 Highly integrated CMOS quantum dots for scalable qubit arrays

Many research groups have published proposals for highly integrated quantum dot arrays [Fog22; Lee20; Li18; Vel17; Vin18] to build quantum processors. An exemplary architecture that was proposed by Vinet et al. [Vin18] is depicted in figure **7.1(a)**. The 3D-architecture consists of different layers that serve a specific purpose. The qubit layer is controlled by an upper layer of control gates. Underneath the qubit layer, another quantum dot array is used as a sensing layer. The sensing layer and the qubit layer are tunnel coupled through vias. The coupling through the vias can be controlled with a grid of electrical gates surrounding the vias. Underneath the sensing layer, a gate layer allows to control the sensing QDs. Similar to classical microprocessors, the quantum dots are addressed using word and bit lines, building a crossbar architecture. Choosing this technique to address QDs in the array allows to scale the number of gates favorably with $\mathcal{O}(\sqrt{N})$. However, such an architecture means that each gate addresses $\sqrt{N}$ QDs and one would need to compensate for this cross-talk using nearby gates. Thanks to the symmetry of the problem, this might be feasible, but would require a very high similarity of each QD, and we have seen that this is rather unlikely to be achieved. A more complex solution is to use local memory that saves the QD potential in a capacitor [Sch18]. We will discuss in the following section how classical electronics could be integrated, but for now continue with the qubit processor architecture.
The unit cell of this architecture is depicted in figure **7.1(b)**. The architecture of the unit cell is not by accident resembling the architecture of unit cells for surface code [Fow12]. The unit cell consists of five quantum dots in the qubit layer with a center quantum dot (M) (representing **m**easure qubits in surface codes) surrounded by four quantum dots (D) (representing **d**ata qubit positions in surface codes). Below M, a sensing QD (S) is located that could be used to sense the qubit state of M. This sensing QD is controlled using a gate electrode underneath which could be connected to a rf-reflectometry setup, enabling gate-reflectometry. Each gate electrode would need to be multiplexed to allow readout of all QDs. This multiplexing will require good control over the resonance of each QD, such that the resonances can be separated from each other while still remaining in the measurement bandwidth of the rf-setup. If this is not possible, a staggered readout could be envisioned where the QDs are all except one decoupled from their measurement QD. This would allow reading out a square array in $t_m = \sqrt{N} \times t'_{\mathrm{m}}$, with t'_{m} the measurement time per qubit and assuming that the rows of sensing QDs can be readout in parallel (e.g. by building an rf-readout for each or multiplexing each line). Even if one can considerably reduce the number of gates per QD, it is unlikely that one can build a quantum processor chip that connects every gate to an external instrument. Cointegrated classical electronics would allow to reduce the amount of wires and heat load going along with these. In the following section, we want to discuss current research on cryo-CMOS used for qubit control.

7.2.2 Cryo-CMOS - Integration of customized control electronics

Following modern microprocessor chips, the periphery used to send or receive information from the processor can be very close or even on the same chip. Following Rent's rule, the amount of processor connections nowadays is by many orders of magnitude smaller than the actual number of transistors of the processor [Chr00; Lan05]. For quantum devices at cryogenic temperatures, the design rules change a bit due to the different constraints in such an environment, but the goal remains to follow the approach for classical processors. We want to briefly discuss three aspects of designing cryo-CMOS for quantum hardware and advise the reader to consult the review by Vandersypen et al. for a more detailed discussion [Van17].
First, even though in terms of physical size and time delay to communicate with the qubit chip, bringing the control electronics as close as physically possible might not be the optimal approach. As the classical control electronics will dissipate considerable amounts of heat, this heat could interfere with the qubits and be detrimental to their fidelity. To thermally decouple the qubits from the control hardware, one can use superconducting vias for the connections and make these sufficiently long to evacuate the heat of the control electronics through a heat sink.
Second, the control electronics should be as energy efficient as possible to allow operation of the qubits at a temperature as low as possible. This means that the accuracy and number of features typical instruments provide nowadays are not necessarily provided, but the functionality is reduced to the minimal requirements to operate the qubit chip [Bar19; Van17].
Third, the amount of data that is produced when operating a processor of millions of qubits can easily be $>$ Ts. Such an amount of data must be processed efficiently and fast such that local processing units will be highly desirable.
Building and interfacing this for a single large array might be more challenging than for smaller systems, especially considering that some features do not show an advantage when scaling up, e.g. the readout speed in an array as discussed in the previous section. Therefore, smaller interconnected arrays should be considered. A cartoon of such a structure is depicted in figure **7.1(c)**. Such long-range qubit couplers are currently researched, ranging from a chain of quantum dots that use a bucket brigade like shuttling of electrons [Sei22], over surface-accoustic waves that carry an electron [Jad21], to photonic coupling [Sam18; Yu22]. The small interconnected arrays will probably be more protected against crosstalk, but as the interconnectivity would be reduced in such a system, the error correction protocols must be adapted to such a system.
To conclude, while it is desirable to adapt as much as possible from classical processor integration, working with qubit processors poses additional challenges. The main challenges are the limited amount of heat load that is allowed, the qubit sensitivity to any noise source and the considerable amount of data that needs to be dealt with. In general, the higher the operation temperature of the qubits, the easier it will be to realize a fully integrated quantum processor. State-of-the-art dilution fridges can provide cooling powers of around $1\,\mathrm{W} - 2\,\mathrm{W}$ at $4\,\mathrm{K}$, a thousand times more than at $100\,\mathrm{mK}$ [Van17]. Such high temperatures require large separation of the relevant energy levels of the qubit system and

this can be challenging. For instance, increasing the Zeeman energy, separating the two states of a single spin qubit, results in an increase of the driving frequency and temperatures above 1 K would require frequencies above 30 GHz to operate the qubit. Circuits compatible with such high frequencies are much more difficult to design than circuits for < 10 GHz. Moreover, the noise and relaxation times typically increase with increasing temperature and make it harder to build high fidelity qubits. This brings us to another topic, namely the control of an array of qubits.

7.2.3 Scalable qubit control

Silicon hole spin qubits have an intrinsic advantage in terms of control as their large spin-orbit coupling allows to operate them using rf-pulses on the QD defining gates and perform electric dipole spin resonance (EDSR). Such a control would in principle be possible for large scale systems, making hole spin qubits easier to interface than electron qubits. In order to achieve the same with electron spins, a magnetic field gradient is required that can be produced by micro-magnets. These micro-magnets are large compared to the size of a QD, and it is unlikely that this technique can be scaled up to operate on large QD arrays. Alternatively, rf-antennas could be integrated as proposed by Li et al. [Li18], going along with a more complex gate architecture. ESR spin control can as well achieved using a global microwave field as it was demonstrated by Vahapoglu et al. [Vah21]. This would allow manipulation with a single microwave source, but require a fast control of the g-factor of the qubits. Last but not least, singlet-triplet qubits or exchange-only qubits could also be used but would go along with more QDs per qubit.

7.2.4 Conclusion

We have seen that many challenges come up when scaling up a qubit system based on quantum dots, ranging from the design of unit cells to the integration of control electronics to the management of higher heat loads and finally a scalable qubit control. What we have not discussed so far is the actual tuning of such a system. At the time of writing, most quantum devices are tuned by human experts. This tuning task is becoming more and more difficult with the increase in device complexity and cross-talk between QDs. It is very unlikely that humans can tune devices of millions of QDs, making automated device tuning indispensable for large scale devices. The research on automated device tuning is the topic of the following section.

7.3 Automated device tuning

We have already seen in chapter **5** that the task of device tuning can be difficult due to cross-capacitances, non-ideal device behavior or lag of control gates. As the number of QDs in a device increases and the number of gates per QD decreases, the task of device tuning becomes increasingly challenging and even for experts it can take days to find the right parameter set. In the largest 2D arrays of QDs conceived so far, the task of controlling the charges and shuffling these in the array has been achieved for nine quantum dots in GaAs

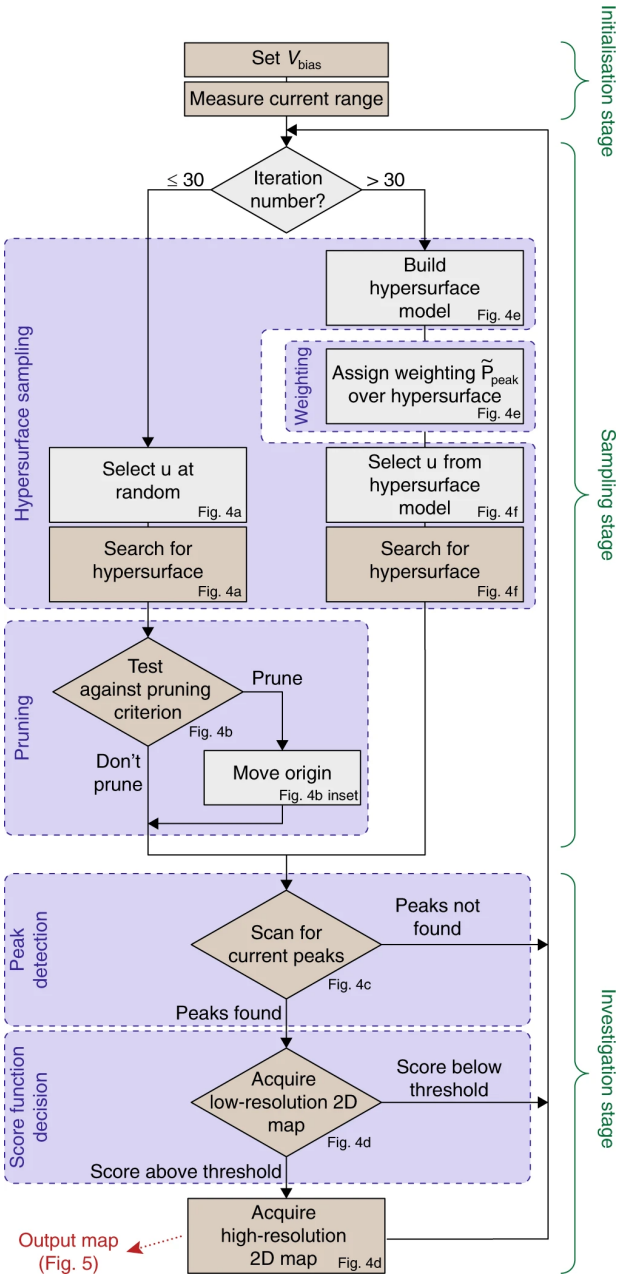

Figure 7.2: Device tuning algorithm used to find optimal parameters for a QD device. Brown boxes are steps that require interaction with the device whereas gray boxes are fully computational. The algorithm consists of an initialization step, followed by a tuning loop going from a sampling stage to an investigation stage. Reprint from [Moo20].

and 16 QDs in SiGe [Bor22; Mor20]. Tuning every QD into the desired charge state and exploiting the hosted spin as a qubit has not yet been demonstrated in these large arrays. The growing parameter space will make it necessary to either build quantum dots that are that predictable that tuning is not necessary or have algorithms to take over the tuning task to replace the human expert. Right now, the first solution seems unlikely. The latter one is an approach that is actively researched [Are21], and we want to discuss a bit these tuning algorithms in the following.
As part of my PhD thesis, I had the chance to visit the group of Natalia Ares at the University of Oxford and learn how machine learning techniques can be used to automatize device tuning. One typically distinguishes between different stages of tuning, ranging from coarse tuning, focusing on the charge configuration in a device [Moo20], to optimization of a qubit [Wis21]. While qubit optimization will probably play a big role in final large scale devices, an algorithm that takes over tuning of the charge configuration is probably more important to make the leap from single digit quantum dot arrays to > 100 QDs. There are different approaches, one can envision, to solve the tuning problem, all based on a tuning loop. The tuning consists of an initialization step, followed by a loop that alternates between a sampling stage and an investigation stage where the decision is made to exit the loop or return to the sampling stage. An exemplary tuning algorithm is depicted in figure **7.2**, used by Moon et al. [Moo20]. The initialization step is used to calibrate the expected signal range and sets the starting point of the algorithm to explore the hypersurface of the parameter space. In the investigation stage, the algorithm selects a set of parameters. The choice of parameters can be random if there is no information about the structure of the hypersurface. On the other hand, if the algorithm already explored a certain set of points of the parameter space, the algorithm can make an "educated guess" using a hypersurface model. In other words, the sampled data provides enough information to exclude certain voltage ranges which reduces the sampling space. When the parameters are set, the investigation step is used to perform a measurement (e.g. a stability diagram using two predefined gates or single traces to detect Coulomb peaks) and evaluates the data according to a predefined metric (e.g. signature of triple point found or last Coulomb peak found). Depending on the score using such a metric, the loop is repeated in order to improve or exited with the given parameters.
The usefulness of such an algorithm depends on the effectiveness to evaluate the measured data and the correct adjustment of parameters. Different aspects of an algorithm need to be carefully designed to allow convergence to the optimal parameters with a minimum of steps. Typically, all the steps that require interaction with the device are costly in terms of time. Thus, an algorithm should focus on processing the acquired data in each loop as efficiently as possible. In the sampling stage, the focus should be on an efficient model for the hypersurface. While random sampling can be a first step, the information from these samples should be evaluated and used for a more sophisticated sampling method. For instance, a model using a Gaussian process can use the tested parameters to restrict further sampling to locations in parameter space that are close to the parameters that showed the best results[Moo20]. The investigation stage must be optimized in terms of detection method and evaluation metric. The detection method can be challenging as it is often difficult to formalize the features that are supposed to be detected. During my time

in Oxford, I mostly worked on developing a feature detection method to detect interdot transitions in a stability diagram. We want to discuss two methods for the detection. Using image recognition for the detection of predefined features can be used if these are easily separated from the rest of the image. Modern image processing software/libraries like scikit-image allow processing data and detect specific features like edges or lines. The best results, we achieved, were using image processing followed by feature detection. Preprocessing consisted of binarization of the signal and an edge detection transformation (e.g. Canny, Sobel, Laplacian). For the feature detection we used the Hough transform. The Hough transform outputs very strong signals for straight lines, allowing to extract the sensor lines from a stability diagram and if the sensor lines are broad enough the charge transitions of a sensed QD can be detected as well. However, the charge sensor lines in our stability diagrams are typically very narrow. This results in either not detecting transitions at all due to a to high threshold to identify something as a line or many misidentifications of small features due to a too low threshold. An alternative was to use a corner detection method (e.g. Harris Corner Detection). While this method is very sensitive to charge transitions, we found that signal switches or noise can yield considerable misidentification. We mitigated these by using clustering, only taking into account those positions where multiple corners were found. We found that while this approach reaches acceptable accuracy, the thresholds had to be adjusted for each device, making it very tedious to use. A solution to explore is to use a version of two-factor authentication, requiring an additional technique to detect the feature that is not sensitive to the errors of the other mechanism. This of course requires that such a technique exists. An alternative approach of detection, that requires less understanding of the exact feature, is to train a neural network (NN) to classify the data, we were not able to use this technique due to a lack of data. We want to outline the idea anyways to complete the discussion. While classification (measurement does (does not) show feature) is a standard task for NNs and many pretrained image recognition NNs exist (e.g. VGG16, VGG19 or ResNet50), these networks are mostly trained on photographs of the real world. Thus, they are well suited for the detection of real world objects, but not necessarily appropriate for measurement data. The way to use these networks for measurement data is to process the data such that it matches the network input (e.g. 256×256 pixels in RGB) and train the network with a set of preclassified data. This training step is not fundamentally changing the network's parameters rather than adjusting the output weighting to classify the input correctly[Den09]. However, the training dataset must cover the range of possible inputs and thus requires data from different device states and different devices. This makes the approach difficult to implement in today's tuning algorithms. Such datasets require the labeling of hundreds of measurements which can take weeks or months. Workarounds for this step exist like simulating data with a model of the device, but the data is just as good as it can reproduce the data a real device would provide[Zie22]. Focusing the research on more industrially made devices might change this. Testing devices fully automatized on a wafer scale at cryogenic temperatures (see section **5.1**), this data scarcity would end and fully automatized characterization could become a standard, using NN for feature detection. Future algorithms will probably still require some physics-informed tuning to be efficient. Considering the increasing complexity of device architectures and reducing

number of control gates per QD (see section **7.2**), these algorithms are likely to be of high research interest in the future.

7.4 Conclusion

In this thesis, we focused on a small aspect of spin qubit readout, which is itself a small part of spin qubit research, which is itself one of a few highly researched qubit platforms, which is just one part of the second quantum revolution. This is why the presentation of future research topics related to the presented material can never be exhaustive. We hope that we were able to give an idea of the challenges looming at the horizon and the great opportunities for finding solutions to these problems. Apart from the commercial use of qubits, quantum dots and in particular spins in quantum dots offer an outstanding platform for fundamental quantum physics research. No matter what quantum dots will be used for, a fast high fidelity sensor for charge and spin will be of high interest.

Bibliography

[Aas01] A. Aassime, G. Johansson, G. Wendin, R. J. Schoelkopf, and P. Delsing: 'Radio-Frequency Single-Electron Transistor as Readout Device for Qubits: Charge Sensitivity and Backaction', *Physical Review Letters* **86** (2001), 3376–3379, DOI: 10.1103/physrevlett.86.3376 (see p. 19).

[AU21] José C. Abadillo-Uriel, Biel Martinez, Michele Filippone, and Yann-Michel Niquet: 'Two-body Wigner molecularization in asymmetric quantum dot spin qubits', *Physical Review B* **104** (2021), 195305, DOI: 10.1103/physrevb.104.195305 (see pp. 111, 113).

[Abr17] N V Abrosimov et al.: 'A new generation of 99.999% enriched ^{28}Si single crystals for the determination of Avogadro's constant', *Metrologia* **54** (2017), 599–609, DOI: 10.1088/1681-7575/aa7a62 (see pp. 9, 22).

[Aha03] Dorit Aharonov: 'A Simple Proof that Toffoli and Hadamard are Quantum Universal', (9, 2003) (see p. 10).

[Ahm18] Imtiaz Ahmed, James A. Haigh, Simon Schaal, Sylvain Barraud, Yi Zhu, Chang min Lee, Mario Amado, Jason W. A. Robinson, Alessandro Rossi, John J. L. Morton, and M. Fernando Gonzalez-Zalba: 'Radio-Frequency Capacitive Gate-Based Sensing', *Physical Review Applied* **10** (2018), 014018, DOI: 10.1103/physrevapplied.10.014018 (see pp. 64, 72).

[Ans20] Fabio Ansaloni, Anasua Chatterjee, Heorhii Bohuslavskyi, Benoit Bertrand, Louis Hutin, Maud Vinet, and Ferdinand Kuemmeth: 'Single-electron operations in a foundry-fabricated array of quantum dots', *Nature Communications* **11** (2020), DOI: 10.1038/s41467-020-20280-3 (see p. 89).

[Are21] Natalia Ares: 'Machine learning as an enabler of qubit scalability', *Nature Reviews Materials* **6** (2021), 870–871, DOI: 10.1038/s41578-021-00321-z (see pp. 87, 125).

[Aru19] Frank Arute et al.: 'Quantum supremacy using a programmable superconducting processor', *Nature* **574** (2019), 505–510, DOI: 10.1038/s41586-019-1666-5 (see pp. 10, 119).

[Asf20] Abraham Asfaw et al.: *Learn Quantum Computation Using Qiskit*, 2020, URL: http://community.qiskit.org/textbook (see pp. 1, 7).

[Asf22] Abraham Asfaw et al.: *Qiskit tutorials*, 2022, URL: https://qiskit.org/documentation/experiments/tutorials/index.html (see p. 6).

[Ash96] R. C. Ashoori: 'Electrons in artificial atoms', *Nature* **379** (1996), 413–419, DOI: 10.1038/379413a0 (see p. 22).

[Bar19] Joseph C. Bardin et al.: 'Design and Characterization of a 28-nm Bulk-CMOS Cryogenic Quantum Controller Dissipating Less Than 2 mW at 3 K', *IEEE Journal of Solid-State Circuits* **54** (2019), 3043–3060, DOI: 10.1109/jssc.2019.2937234 (see p. 122).

[Bar09] C. Barthel, D. J. Reilly, C. M. Marcus, M. P. Hanson, and A. C. Gossard: 'Rapid Single-Shot Measurement of a Singlet-Triplet Qubit', *Physical Review Letters* **103** (2009), DOI: 10.1103/physrevlett.103.160503 (see p. 101).

[Bee91] C. W. J. Beenakker: 'Theory of Coulomb-blockade oscillations in the conductance of a quantum dot', *Physical Review B* **44** (1991), 1646–1656, DOI: 10.1103/physrevb.44.1646 (see pp. 26, 28).

[Ber15] Benoit Bertrand: 'Transport d'information de spin à l'échelle de l'électron unique', Theses, Université Grenoble Alpes, 2015, URL: https://tel.archives-ouvertes.fr/tel-01212493 (see p. 34).

[Boh22] Heorhii Bohuslavskyi, Alberto Ronzani, Joel Hätinen, Arto Rantala, Andrey Shchepetov, Panu Koppinen, Mika Prunnila, and Janne S. Lehtinen: *Scalable on-chip multiplexing of low-noise silicon electron and hole quantum dots*, 2022, DOI: 10.48550/ARXIV.2208.12131 (see p. 16).

[Bor21] F. Borjans, X. Mi, and J.R. Petta: 'Spin Digitizer for High-Fidelity Readout of a Cavity-Coupled Silicon Triple Quantum Dot', *Physical Review Applied* **15** (2021), 044052, DOI: 10.1103/physrevapplied.15.044052 (see pp. 11, 12, 18, 19, 76, 97, 117, 119).

[Bor22] Francesco Borsoi, Nico W. Hendrickx, Valentin John, Sayr Motz, Floor van Riggelen, Amir Sammak, Sander L. de Snoo, Giordano Scappucci, and Menno Veldhorst: *Shared control of a 16 semiconductor quantum dot crossbar array*, 2022, DOI: 10.48550/ARXIV.2209.06609 (see pp. 19, 125).

[Bou18] Léo Bourdet and Yann-Michel Niquet: 'All-electrical manipulation of silicon spin qubits with tunable spin-valley mixing', *Physical Review B* **97** (2018), 155433, DOI: 10.1103/physrevb.97.155433 (see p. 26).

[Bra18] Sergey Bravyi, Matthias Englbrecht, Robert König, and Nolan Peard: 'Correcting coherent errors with surface codes', *npj Quantum Information* **4** (2018), DOI: 10.1038/s41534-018-0106-y (see p. 119).

[Bre06] Henrik Brenning, Sergey Kafanov, Tim Duty, Sergey Kubatkin, and Per Delsing: 'An ultrasensitive radio-frequency single-electron transistor working up to 4.2 K', *Journal of Applied Physics* **100** (2006), 114321, DOI: 10.1063/1.2388134 (see p. 19).

[Bro17] M. A. Broome, T. F. Watson, D. Keith, S. K. Gorman, M. G. House, J. G. Keizer, S. J. Hile, W. Baker, and M. Y. Simmons: 'High-Fidelity Single-Shot Singlet-Triplet Readout of Precision-Placed Donors in Silicon', *Physical Review Letters* **119** (2017), 046802, DOI: 10.1103/physrevlett.119.046802 (see p. 18).

[Buc18] M. Buchner, K. Höfler, B. Henne, V. Ney, and A. Ney: 'Tutorial: Basic principles, limits of detection, and pitfalls of highly sensitive SQUID magnetometry for nanomagnetism and spintronics', *Journal of Applied Physics* **124** (2018), 161101, DOI: 10.1063/1.5045299 (see p. 38).

[Bur21] Guido Burkard, Thaddeus D. Ladd, John M. Nichol, Andrew Pan, and Jason R. Petta: *Semiconductor Spin Qubits*, 2021, DOI: 10.48550/ARXIV.2112.08863 (see pp. 12, 13, 41).

[Cam22] Leon C. Camenzind, Simon Geyer, Andreas Fuhrer, Richard J. Warburton, Dominik M. Zumbühl, and Andreas V. Kuhlmann: 'A hole spin qubit in a fin field-effect transistor above 4 kelvin', *Nature Electronics* **5** (2022), 178–183, DOI: 10.1038/s41928-022-00722-0 (see pp. 11, 19, 57).

[Cao21] Changsu Cao, Jiaqi Hu, Wengang Zhang, Xusheng Xu, Dechin Chen, Fan Yu, Jun Li, Hanshi Hu, Dingshun Lv, and Man-Hong Yung: *Towards a Larger Molecular Simulation on the Quantum Computer: Up to 28 Qubits Systems Accelerated by Point Group Symmetry*, 2021, DOI: 10.48550/ARXIV.2109.02110 (see p. 119).

[Cha20] Emmanuel Chanrion et al.: 'Charge Detection in an Array of CMOS Quantum Dots', *Physical Review Applied* **14** (2020), 024066, DOI: 10.1103/physrevapplied.14.024066 (see pp. 57, 58, 82, 88, 89).

[Che74] James R. Chelikowsky and Marvin L. Cohen: 'Electronic structure of silicon', *Physical Review B* **10** (1974), 5095–5107, DOI: 10.1103/physrevb.10.5095 (see p. 25).

[Chr00] P. Christie and D. Stroobandt: 'The interpretation and application of Rent's rule', *IEEE Transactions on Very Large Scale Integration (VLSI) Systems* **8** (2000), 639–648, DOI: 10.1109/92.902258 (see p. 122).

[Con20] Elliot J. Connors, JJ Nelson, and John M. Nichol: 'Rapid High-Fidelity Spin-State Readout in Si/Si-Ge Quantum Dots via rf ReflectometryRapid High-Fidelity Spin-State Readout in Si/Si-Ge Quantum Dots via rf Reflectometry', *Physical Review Applied* **13** (2020), 024019, DOI: 10.1103/physrevapplied.13.024019 (see p. 57).

[Coo22] Peter Cooper, Philipp Ernst, Dieter Kiewell, and Dickon Pinner: *Quantum computing just might save the planet*, https://www.mckinsey.com/business-functions/mckinsey-digital/our-insights/quantum-computing-just-might-save-the-planet, Accessed: 2022-09-03, 2022 (see p. 16).

[Cot11] Audrey Cottet, Christophe Mora, and Takis Kontos: 'Mesoscopic admittance of a double quantum dot', *Physical Review B* **83** (2011), 121311, DOI: 10.1103/physrevb.83.121311 (see pp. 70, 72).

[Den09] J. Deng, W. Dong, R. Socher, L.-J. Li, K. Li, and L. Fei-Fei: 'ImageNet: A Large-Scale Hierarchical Image Database', *CVPR09*, 2009 (see p. 126).

[Deu92] David Deutsch and Richard Jozsa: 'Rapid solution of problems by quantum computation', *Proceedings of the Royal Society of London. Series A: Mathematical and Physical Sciences* **439** (1992), 553–558, DOI: 10.1098/rspa.1992.0167 (see p. 1).

[Dev04] M. H. Devoret, A. Wallraff, and J. M. Martinis: 'Superconducting Qubits: A Short Review', (2004) (see p. 68).

[Die21] Cornelis J. van Diepen, Tzu-Kan Hsiao, Uditendu Mukhopadhyay, Christian Reichl, Werner Wegscheider, and Lieven M. K. Vandersypen: 'Electron cascade for distant spin readout', *Nature Communications* **12** (2021), DOI: 10.1038/s41467-020-20388-6 (see p. 12).

[DiV00a] D. P. DiVincenzo, D. Bacon, J. Kempe, G. Burkard, and K. B. Whaley: 'Universal quantum computation with the exchange interaction', *Nature* **408** (2000), 339–342, DOI: 10.1038/35042541 (see p. 11).

[DiV00b] David P. DiVincenzo: 'The Physical Implementation of Quantum Computation', *Fortschritte der Physik* **48** (2000), 771–783, DOI: 10.1002/1521-3978(200009)48:9/11<771::aid-prop771>3.0.co;2-e (see p. 8).

[Dua20] Jingyu Duan, Michael A. Fogarty, James Williams, Louis Hutin, Maud Vinet, and John J. L. Morton: 'Remote Capacitive Sensing in Two-Dimensional Quantum-Dot Arrays', *Nano Letters* **20** (2020), 7123–7128, DOI: 10.1021/acs.nanolett.0c02393 (see p. 88).

[Ega21] Laird Egan, Dripto M. Debroy, Crystal Noel, Andrew Risinger, Daiwei Zhu, Debopriyo Biswas, Michael Newman, Muyuan Li, Kenneth R. Brown, Marko Cetina, and Christopher Monroe: 'Fault-tolerant control of an error-corrected qubit', *Nature* **598** (2021), 281–286, DOI: 10.1038/s41586-021-03928-y (see p. 11).

[Elz04] J. M. Elzerman, R. Hanson, L. H. Willems van Beveren, B. Witkamp, L. M. K. Vandersypen, and L. P. Kouwenhoven: 'Single-shot read-out of an individual electron spin in a quantum dot', *Nature* **430** (2004), 431–435, DOI: 10.1038/nature02693 (see pp. 11, 18, 39).

[Est19] M. Esterli, R. M. Otxoa, and M. F. Gonzalez-Zalba: 'Small-signal equivalent circuit for double quantum dots at low-frequencies', *Applied Physics Letters* **114** (2019), 253505, DOI: 10.1063/1.5098889 (see pp. 72, 73).

[Fog18] M. A. Fogarty, K. W. Chan, B. Hensen, W. Huang, T. Tanttu, C. H. Yang, A. Laucht, M. Veldhorst, F. E. Hudson, K. M. Itoh, D. Culcer, T. D. Ladd, A. Morello, and A. S. Dzurak: 'Integrated silicon qubit platform with single-spin addressability, exchange control and single-shot singlet-triplet readout', *Nature Communications* **9** (2018), DOI: 10.1038/s41467-018-06039-x (see pp. 19, 35, 37, 106–109).

[Fog22] Michael A. Fogarty: *Silicon edge-dot architecture for quantum computing with global control and integrated trimming*, 2022, DOI: 10.48550/ARXIV.2208.09172 (see p. 121).

[Fow12] Austin G. Fowler, Matteo Mariantoni, John M. Martinis, and Andrew N. Cleland: 'Surface codes: Towards practical large-scale quantum computation', *Physical Review A* **86** (2012), DOI: 10.1103/physreva.86.032324 (see pp. 16, 17, 19, 57, 58, 119, 121).

[Fre02] Michael Freedman, Alexei Kitaev, Michael Larsen, and Zhenghan Wang: 'Topological quantum computation', *Bulletin of the American Mathematical Society* **40** (2002), 31–38, DOI: 10.1090/s0273-0979-02-00964-3 (see p. 119).

[Fre95] M. M. Freund, T. Hirao, V. Hristov, S. Chegwidden, T. Matsumoto, and A. E. Lange: 'Compact low-pass electrical filters for cryogenic detectors', *Review of Scientific Instruments* **66** (1995), 2638–2640, DOI: 10.1063/1.1145601 (see p. 47).

[Fri10] Mark Friesen and S. N. Coppersmith: 'Theory of valley-orbit coupling in a Si/SiGe quantum dot', *Physical Review B* **81** (2010), 115324, DOI: 10.1103/physrevb.81.115324 (see p. 26).

[Fri03] Mark Friesen, Paul Rugheimer, Donald E. Savage, Max G. Lagally, Daniel W. van der Weide, Robert Joynt, and Mark A. Eriksson: 'Practical design and simulation of silicon-based quantum-dot qubits', *Physical Review B* **67** (2003), 121301, DOI: 10.1103/physrevb.67.121301 (see p. 12).

[Fri44] H.T. Friis: 'Noise Figures of Radio Receivers', *Proceedings of the IRE* **32** (1944), 419–422, DOI: 10.1109/jrproc.1944.232049 (see p. 118).

[Fri18] Nicolai Friis, Oliver Marty, Christine Maier, Cornelius Hempel, Milan Holzäpfel, Petar Jurcevic, Martin B. Plenio, Marcus Huber, Christian Roos, Rainer Blatt, and Ben Lanyon: 'Observation of Entangled States of a Fully Controlled 20-Qubit System', *Physical Review X* **8** (2018), 021012, DOI: 10.1103/physrevx.8.021012 (see p. 11).

[Gid21] Craig Gidney and Martin Ekerå: 'How to factor 2048 bit RSA integers in 8 hours using 20 million noisy qubits', *Quantum* **5** (2021), 433, DOI: 10.22331/q-2021-04-15-433 (see p. 119).

[Gla97] D. C. Glattli, P. Jacques, A. Kumar, P. Pari, and L. Saminadayar: 'A noise detection scheme with 10 mK noise temperature resolution for semiconductor single electron tunneling devices', *Journal of Applied Physics* **81** (1997), 7350–7356, DOI: 10.1063/1.365332 (see p. 47).

[GZ15] M. F. Gonzalez-Zalba, S. Barraud, A. J. Ferguson, and A. C. Betz: 'Probing the limits of gate-based charge sensing', *Nature Communications* **6** (2015), DOI: 10.1038/ncomms7084 (see pp. 17, 19, 70, 72).

[Ha21] Wonill Ha et al.: 'A Flexible Design Platform for Si/SiGe Exchange-Only Qubits with Low Disorder', *Nano Letters* **22** (2021), 1443–1448, DOI: 10.1021/acs.nanolett.1c03026 (see pp. 14, 57).

[Had03] Yoko Hada and Mikio Eto: 'Size and shape dependence of electronic states in silicon quantum dots', *physica status solidi (c)* (2003), 1153–1156, DOI: 10.1002/pssc.200303025 (see p. 26).

[Hah50] E. L. Hahn: 'Spin Echoes', *Physical Review* **80** (1950), 580–594, DOI: 10.1103/physrev.80.580 (see p. 6).

[Han05] R. Hanson, L. H. Willems van Beveren, I. T. Vink, J. M. Elzerman, W. J. M. Naber, F. H. L. Koppens, L. P. Kouwenhoven, and L. M. K. Vandersypen: 'Single-Shot Readout of Electron Spin States in a Quantum Dot Using Spin-Dependent Tunnel Rates', *Physical Review Letters* **94** (2005), 196802, DOI: 10.1103/physrevlett.94.196802 (see pp. 18, 39, 40).

[Han07] R. Hanson, L. P. Kouwenhoven, J. R. Petta, S. Tarucha, and L. M. K. Vandersypen: 'Spins in few-electron quantum dots', *Reviews of Modern Physics* **79** (2007), 1217–1265, DOI: 10.1103/revmodphys.79.1217 (see pp. 11, 29).

[HC18] Patrick Harvey-Collard, Benjamin D'Anjou, Martin Rudolph, N. Tobias Jacobson, Jason Dominguez, Gregory A. Ten Eyck, Joel R. Wendt, Tammy Pluym, Michael P. Lilly, William A. Coish, Michel Pioro-Ladrière, and Malcolm S. Carroll: 'High-Fidelity Single-Shot Readout for a Spin Qubit via an Enhanced Latching Mechanism', *Physical Review X* **8** (2018), DOI: 10.1103/physrevx.8.021046 (see p. 109).

[Hay14] K Hayashi, A Saito, Y Ogawa, M Murata, T Sawada, K Nakajima, H Yamada, S Ariyoshi, T Taino, H Tanoue, C Otani, and S Ohshima: 'Design and Fabrication of Microwave Kinetic Inductance Detectors using NbN Symmetric Spiral Resonator Array', *Journal of Physics: Conference Series* **507** (2014), 042015, DOI: 10.1088/1742-6596/507/4/042015 (see p. 55).

[Hay03] T. Hayashi, T. Fujisawa, H. D. Cheong, Y. H. Jeong, and Y. Hirayama: 'Coherent Manipulation of Electronic States in a Double Quantum Dot', *Physical Review Letters* **91** (2003), 226804, DOI: 10.1103/physrevlett.91.226804 (see p. 32).

[Hei18] Johannes Heinsoo, Christian Kraglund Andersen, Ants Remm, Sebastian Krinner, Theodore Walter, Yves Salathé, Simone Gasparinetti, Jean-Claude Besse, Anton Potočnik, Andreas Wallraff, and Christopher Eichler: 'Rapid High-fidelity Multiplexed Readout of Superconducting Qubits', *Physical Review Applied* **10** (2018), 034040, DOI: 10.1103/physrevapplied.10.034040 (see p. 119).

[Hen20] N. W. Hendrickx, W. I. L. Lawrie, L. Petit, A. Sammak, G. Scappucci, and M. Veldhorst: 'A single-hole spin qubit', *Nature Communications* **11** (2020), DOI: 10.1038/s41467-020-17211-7 (see p. 33).

[Hil05] C. D. Hill, L. C. L. Hollenberg, A. G. Fowler, C. J. Wellard, A. D. Greentree, and H.-S. Goan: 'Global control and fast solid-state donor electron spin quantum computing', *Physical Review B* **72** (2005), 045350, DOI: 10.1103/physrevb.72.045350 (see p. 12).

[Hou15] M. G. House, T. Kobayashi, B. Weber, S. J. Hile, T. F. Watson, J. van der Heijden, S. Rogge, and M. Y. Simmons: 'Radio frequency measurements of tunnel couplings and singlet-triplet spin states in Si:P quantum dots', *Nature Communications* **6** (2015), DOI: 10.1038/ncomms9848 (see pp. 70–72).

[Hou92] H. Van Houten, C. W. J. Beenakker, and A. A. M. Staring: 'Coulomb-Blockade Oscillations in Semiconductor Nanostructures', *NATO ASI Series*, 1992, 167–216, DOI: 10.1007/978-1-4757-2166-9_5 (see p. 26).

[Hou96] Henk van Houten and Carlo Beenakker: 'Quantum Point Contacts', *Physics Today* **49** (1996), 22–27, DOI: 10.1063/1.881503 (see p. 58).

[Hua19] W. Huang, C. H. Yang, K. W. Chan, T. Tanttu, B. Hensen, R. C. C. Leon, M. A. Fogarty, J. C. C. Hwang, F. E. Hudson, K. M. Itoh, A. Morello, A. Laucht, and A. S. Dzurak: 'Fidelity benchmarks for two-qubit gates in silicon', *Nature* **569** (2019), 532–536, DOI: 10.1038/s41586-019-1197-0 (see p. 14).

[Ibb18] D. J. Ibberson, L. Bourdet, J. C. Abadillo-Uriel, I. Ahmed, S. Barraud, M. J. Calderón, Y.-M. Niquet, and M. F. Gonzalez-Zalba: 'Electric-field tuning of the valley splitting in silicon corner dots', *Applied Physics Letters* **113** (2018), 053104, DOI: 10.1063/1.5040474 (see p. 26).

[Ibb19] David J. Ibberson, Lisa A. Ibberson, Geoff Smithson, James A. Haigh, Sylvain Barraud, and M. Fernando Gonzalez-Zalba: 'Low-temperature tunable radio-frequency resonator for sensitive dispersive readout of nanoelectronic devices', *Applied Physics Letters* **114** (2019), 123501, DOI: 10.1063/1.5082894 (see p. 64).

[Ibb21] David J. Ibberson, Theodor Lundberg, James A. Haigh, Louis Hutin, Benoit Bertrand, Sylvain Barraud, Chang-Min Lee, Nadia A. Stelmashenko, Giovanni A. Oakes, Laurence Cochrane, Jason W.A. Robinson, Maud Vinet, M. Fernando Gonzalez-Zalba, and Lisa A. Ibberson: 'Large Dispersive Interaction between a CMOS Double Quantum Dot and Microwave Photons', *PRX Quantum* **2** (2021), 020315, DOI: 10.1103/prxquantum.2.020315 (see p. 64).

[Ibm] *IBM Quantum Blogpost Eagle Processor*, https://research.ibm.com/blog/127-qubit-quantum-processor-eagle, Accessed: 2022-08-23 (see p. 10).

[Ihn10] Thomas Ihn: *Semiconductor nanostructures : quantum states and electronic transport*, Oxford University Press, 2010 (see pp. 1, 2, 26, 28, 32, 152).

[Isb12] J. Isberg, M. Gabrysch, S. Majdi, and D. J. Twitchen: 'Negative electron mobility in diamond', *Applied Physics Letters* **100** (2012), 172103, DOI: 10.1063/1.4705434 (see p. 25).

[Jad21] Baptiste Jadot, Pierre-André Mortemousque, Emmanuel Chanrion, Vivien Thiney, Arne Ludwig, Andreas D. Wieck, Matias Urdampilleta, Christopher Bäuerle, and Tristan Meunier: 'Distant spin entanglement via fast and coherent electron shuttling', *Nature Nanotechnology* **16** (2021), 570–575, DOI: 10.1038/s41565-021-00846-y (see p. 122).

[Jeh06] X. Jehl, M. Hofheinz, M. Boehm, M. Sanquer, G. Molas, M. Vinet, and S. Deleonibus: 'Peak spacing statistics in silicon single-electron transistors: Size and gate oxide thickness dependence', *Physica E: Low-dimensional Systems and Nanostructures* **34** (2006), 620–623, DOI: 10.1016/j.physe.2006.03.043 (see p. 23).

[Jir21] Daniel Jirovec et al.: 'A singlet-triplet hole spin qubit in planar Ge', *Nature Materials* **20** (2021), 1106–1112, DOI: 10.1038/s41563-021-01022-2 (see p. 57).

[Joc18] Ryan M. Jock, N. Tobias Jacobson, Patrick Harvey-Collard, Andrew M. Mounce, Vanita Srinivasa, Dan R. Ward, John Anderson, Ron Manginell, Joel R. Wendt, Martin Rudolph, Tammy Pluym, John King Gamble, Andrew D. Baczewski, Wayne M. Witzel, and Malcolm S. Carroll: 'A silicon metal-oxide-semiconductor electron spin-orbit qubit', *Nature Communications* **9** (2018), DOI: 10.1038/s41467-018-04200-0 (see p. 108).

[Joc22] Ryan M. Jock, N. Tobias Jacobson, Martin Rudolph, Daniel R. Ward, Malcolm S. Carroll, and Dwight R. Luhman: 'A silicon singlet–triplet qubit driven by spin-valley coupling', *Nature Communications* **13** (2022), DOI: 10.1038/s41467-022-28302-y (see p. 57).

[Joh05a] A. C. Johnson, J. R. Petta, C. M. Marcus, M. P. Hanson, and A. C. Gossard: 'Singlet-triplet spin blockade and charge sensing in a few-electron double quantum dot', *Physical Review B* **72** (2005), DOI: 10.1103/physrevb.72.165308 (see p. 40).

[Joh05b] A. C. Johnson, J. R. Petta, J. M. Taylor, A. Yacoby, M. D. Lukin, C. M. Marcus, M. P. Hanson, and A. C. Gossard: 'Triplet–singlet spin relaxation via nuclei in a double quantum dot', *Nature* **435** (2005), 925–928, DOI: 10.1038/nature03815 (see p. 40).

[Kal19] Sandesh S. Kalantre, Justyna P. Zwolak, Stephen Ragole, Xingyao Wu, Neil M. Zimmerman, M. D. Stewart, and Jacob M. Taylor: 'Machine learning techniques for state recognition and auto-tuning in quantum dots', *npj Quantum Information* **5** (2019), DOI: 10.1038/s41534-018-0118-7 (see p. 87).

[Kam22] Kamal Y. Kamal: 'The Silicon Age: Trends in Semiconductor Devices Industry', *Journal of Engineering Science and Technology Review* **15** (2022), 110–115, DOI: 10.25103/jestr.151.14 (see p. 14).

[Kan98] B. E. Kane: 'A silicon-based nuclear spin quantum computer', *Nature* **393** (1998), 133–137, DOI: 10.1038/30156 (see p. 12).

[Kaw16] Erika Kawakami, Thibaut Jullien, Pasquale Scarlino, Daniel R. Ward, Donald E. Savage, Max G. Lagally, Viatcheslav V. Dobrovitski, Mark Friesen, Susan N. Coppersmith, Mark A. Eriksson, and Lieven M. K. Vandersypen: 'Gate fidelity and coherence of an electron spin in an Si/SiGe quantum dot with micromagnet', *Proceedings of the National Academy of Sciences* **113** (2016), 11738–11743, DOI: 10.1073/pnas.1603251113 (see pp. 11, 33).

[Kei19] D Keith, S K Gorman, L Kranz, Y He, J G Keizer, M A Broome, and M Y Simmons: 'Benchmarking high fidelity single-shot readout of semiconductor qubits', *New Journal of Physics* **21** (2019), 063011, DOI: 10.1088/1367-2630/ab242c (see p. 18).

[Kir22] Josh J. M. Kirsopp, Cono Di Paola, David Zsolt Manrique, Michal Krompiec, Gabriel Greene-Diniz, Wolfgang Guba, Agnes Meyder, Detlef Wolf, Martin Strahm, and David Muñoz Ramo: 'Quantum computational quantification of protein–ligand interactions', *International Journal of Quantum Chemistry* (2022), DOI: 10.1002/qua.26975 (see p. 119).

[Kit97] A Yu Kitaev: 'Quantum computations: algorithms and error correction', *Russian Mathematical Surveys* **52** (1997), 1191–1249, DOI: 10.1070/rm1997v052n06abeh002155 (see p. 10).

[Kop06] F. H. L. Koppens, C. Buizert, K. J. Tielrooij, I. T. Vink, K. C. Nowack, T. Meunier, L. P. Kouwenhoven, and L. M. K. Vandersypen: 'Driven coherent oscillations of a single electron spin in a quantum dot', *Nature* **442** (2006), 766–771, DOI: 10.1038/nature05065 (see p. 12).

[Kou97] Leo P. Kouwenhoven, Charles M. Marcus, Paul L. McEuen, Seigo Tarucha, Robert M. Westervelt, and Ned S. Wingreen: 'Electron Transport in Quantum Dots', *Mesoscopic Electron Transport*, 1997, 105–214, DOI: 10.1007/978-94-015-8839-3_4 (see pp. 11, 26, 27).

[Lan05] M. Y. Lanzerotti, G. Fiorenza, and R. A. Rand: 'Microminiature packaging and integrated circuitry: The work of E. F. Rent, with an application to on-chip interconnection requirements', *IBM Journal of Research and Development* **49** (2005), 777–803, DOI: 10.1147/rd.494.0777 (see p. 122).

[Lau15] Arne Laucht, Juha T. Muhonen, Fahd A. Mohiyaddin, Rachpon Kalra, Juan P. Dehollain, Solomon Freer, Fay E. Hudson, Menno Veldhorst, Rajib Rahman, Gerhard Klimeck, Kohei M. Itoh, David N. Jamieson, Jeffrey C. McCallum, Andrew S. Dzurak, and Andrea Morello: 'Electrically controlling single-spin qubits in a continuous microwave field', *Science Advances* **1** (2015), DOI: 10.1126/sciadv.1500022 (see p. 33).

[Lee20] N. Lee, R. Tsuchiya, G. Shinkai, Y. Kanno, T. Mine, T. Takahama, R. Mizokuchi, T. Kodera, D. Hisamoto, and H. Mizuno: 'Enhancing electrostatic coupling in silicon quantum dot array by dual gate oxide thickness for large-scale integration', *Applied Physics Letters* **116** (2020), 162106, DOI: 10.1063/1.5141522 (see p. 121).

[Len19] D. T. Lennon, H. Moon, L. C. Camenzind, Liuqi Yu, D. M. Zumbühl, G. A .D. Briggs, M. A. Osborne, E. A. Laird, and N. Ares: 'Efficiently measuring a quantum device using machine learning', *npj Quantum Information* **5** (2019), DOI: 10.1038/s41534-019-0193-4 (see p. 87).

[Leo20] R. C. C. Leon, C. H. Yang, J. C. C. Hwang, J. Camirand Lemyre, T. Tanttu, W. Huang, K. W. Chan, K. Y. Tan, F. E. Hudson, K. M. Itoh, A. Morello, A. Laucht, M. Pioro-Ladrière, A. Saraiva, and A. S. Dzurak: 'Coherent spin control of s-, p-, d- and f-electrons in a silicon quantum dot', *Nature Communications* **11** (2020), DOI: 10.1038/s41467-019-14053-w (see pp. 25, 94).

[Lev02] Jeremy Levy: 'Universal Quantum Computation with Spin-1/2 Pairs and Heisenberg Exchange', *Physical Review Letters* **89** (2002), 147902, DOI: 10.1103/physrevlett.89.147902 (see p. 11).

[Li18] Ruoyu Li, Luca Petit, David P. Franke, Juan Pablo Dehollain, Jonas Helsen, Mark Steudtner, Nicole K. Thomas, Zachary R. Yoscovits, Kanwal J. Singh, Stephanie Wehner, Lieven M. K. Vandersypen, James S. Clarke, and Menno Veldhorst: 'A crossbar network for silicon quantum dot qubits', *Science Advances* **4** (2018), DOI: 10.1126/sciadv.aar3960 (see pp. 121, 123).

[Lil21] S. D. Liles, F. Martins, D. S. Miserev, A. A. Kiselev, I. D. Thorvaldson, M. J. Rendell, I. K. Jin, F. E. Hudson, M. Veldhorst, K. M. Itoh, O. P. Sushkov, T. D. Ladd, A. S. Dzurak, and A. R. Hamilton: 'Electrical control of the g tensor of the first hole in a silicon MOS quantum dot', *Physical Review B* **104** (2021), 235303, DOI: 10.1103/physrevb.104.235303 (see p. 33).

[Lim09] W. H. Lim, F. A. Zwanenburg, H. Huebl, M. Möttönen, K. W. Chan, A. Morello, and A. S. Dzurak: 'Observation of the single-electron regime in a highly tunable silicon quantum dot', *Applied Physics Letters* **95** (2009), 242102, DOI: 10.1063/1.3272858 (see p. 12).

[Los98] Daniel Loss and David P. DiVincenzo: 'Quantum computation with quantum dots', *Physical Review A* **57** (1998), 120–126, DOI: 10.1103/physreva.57.120 (see p. 9).

[Lun20] Theodor Lundberg, Jing Li, Louis Hutin, Benoit Bertrand, David J. Ibberson, Chang-Min Lee, David J. Niegemann, Matias Urdampilleta, Nadia Stelmashenko, Tristan Meunier, Jason W. A. Robinson, Lisa Ibberson, Maud Vinet, Yann-Michel Niquet, and M. Fernando Gonzalez-Zalba: 'Spin Quintet in a Silicon Double Quantum Dot: Spin Blockade and Relaxation', *Physical Review X* **10** (2020), 041010, DOI: 10.1103/physrevx.10.041010 (see pp. 73, 74).

[Mac15] C. Macklin, K. O'Brien, D. Hover, M. E. Schwartz, V. Bolkhovsky, X. Zhang, W. D. Oliver, and I. Siddiqi: 'A near–quantum-limited Josephson traveling-wave parametric amplifier', *Science* **350** (2015), 307–310, DOI: 10.1126/science.aaa8525 (see p. 118).

[Mac93] M. Macucci, Karl Hess, and G. J. Iafrate: 'Electronic energy spectrum and the concept of capacitance in quantum dots', *Physical Review B* **48** (1993), 17354–17363, DOI: 10.1103/physrevb.48.17354 (see p. 22).

[Mąd22] Mateusz T. Mądzik et al.: 'Precision tomography of a three-qubit donor quantum processor in silicon', *Nature* **601** (2022), 348–353, DOI: 10.1038/s41586-021-04292-7 (see pp. 11, 12).

[Man11] Soumen Mandal, Tobias Bautze, Rémi Blinder, Tristan Meunier, Laurent Saminadayar, and Christopher Bäuerle: 'Efficient radio frequency filters for space constrained cryogenic setups', *Review of Scientific Instruments* **82** (2011), 024704, DOI: 10.1063/1.3543736 (see p. 47).

[Mas10] J.D. Mason, L. Gaudreau, S.A. Studenikin, A. Kam, B. Djurkovic, A.S. Sachrajda, and J.B. Kycia: 'A high speed radio-frequency quantum point contact charge detector for time resolved readout applications of spin qubits', *Physica E: Low-dimensional Systems and Nanostructures* **42** (2010), 813–816, DOI: 10.1016/j.physe.2009.11.108 (see p. 19).

[Mau12] B. M. Maune, M. G. Borselli, B. Huang, T. D. Ladd, P. W. Deelman, K. S. Holabird, A. A. Kiselev, I. Alvarado-Rodriguez, R. S. Ross, A. E. Schmitz, M. Sokolich, C. A. Watson, M. F. Gyure, and A. T. Hunter: 'Coherent singlet-triplet oscillations in a silicon-based double quantum dot', *Nature* **481** (2012), 344–347, DOI: 10.1038/nature10707 (see pp. 12, 19, 109, 156).

[Mau16] R. Maurand, X. Jehl, D. Kotekar-Patil, A. Corna, H. Bohuslavskyi, R. Laviéville, L. Hutin, S. Barraud, M. Vinet, M. Sanquer, and S. De Franceschi: 'A CMOS silicon spin qubit', *Nature Communications* **7** (2016), 13575, DOI: 10.1038/ncomms13575 (see pp. 12, 17, 19, 33, 57).

[Mei03] Florian Meier, Jeremy Levy, and Daniel Loss: 'Quantum Computing with Spin Cluster Qubits', *Physical Review Letters* **90** (2003), 047901, DOI: 10.1103/physrevlett.90.047901 (see p. 11).

[Met13] Rodney Van Meter and Dominic Horsman: 'A blueprint for building a quantum computer', *Communications of the ACM* **56** (2013), 84–93, DOI: 10.1145/2494568 (see pp. 10, 16).

[Mi21] Xiao Mi et al.: 'Time-crystalline eigenstate order on a quantum processor', *Nature* **601** (2021), 531–536, DOI: 10.1038/s41586-021-04257-w (see p. 10).

[Mic00] P. Michler, A. Kiraz, C. Becher, W. V. Schoenfeld, P. M. Petroff, Lidong Zhang, E. Hu, and A. Imamoglu: 'A Quantum Dot Single-Photon Turnstile Device', *Science* **290** (2000), 2282–2285, DOI: 10.1126/science.290.5500.2282 (see p. 21).

[Mil22] Adam R. Mills, Charles R. Guinn, Michael J. Gullans, Anthony J. Sigillito, Mayer M. Feldman, Erik Nielsen, and Jason R. Petta: 'Two-qubit silicon quantum processor with operation fidelity exceeding 99%', *Science Advances* **8** (2022), DOI: 10.1126/sciadv.abn5130 (see pp. 14, 17, 57, 105).

[Miz17] R. Mizuta, R. M. Otxoa, A. C. Betz, and M. F. Gonzalez-Zalba: 'Quantum and tunneling capacitance in charge and spin qubits', *Physical Review B* **95** (2017), 045414, DOI: 10.1103/physrevb.95.045414 (see pp. 70–73).

[Moh99] Sunderarajan S. Mohan, Maria Del Mar Hershenson, Stephen P. Boyd, and Thomas H. Lee: 'Simple accurate expressions for planar spiral inductances', *IEEE Journal of Solid-State Circuits* **34** (1999), 1419–1424 (see p. 55).

[Moh21] F.A. Mohiyaddin et al.: 'Large-Scale 2D Spin-Based Quantum Processor with a Bi-Linear Architecture', *2021 IEEE International Electron Devices Meeting (IEDM)*, 2021, DOI: 10.1109/iedm19574.2021.9720606 (see p. 16).

[Moo20] H. Moon, D. T. Lennon, J. Kirkpatrick, N. M. van Esbroeck, L. C. Camenzind, Liuqi Yu, F. Vigneau, D. M. Zumbühl, G. A. D. Briggs, M. A. Osborne, D. Sejdinovic, E. A. Laird, and N. Ares: 'Machine learning enables completely automatic tuning of a quantum device faster than human experts', *Nature Communications* **11** (2020), DOI: 10.1038/s41467-020-17835-9 (see pp. 87, 124, 125).

[Mor10] Andrea Morello et al.: 'Single-shot readout of an electron spin in silicon', *Nature* **467** (2010), 687–691, DOI: 10.1038/nature09392 (see pp. 12, 18).

[Mor20] Pierre-André Mortemousque, Emmanuel Chanrion, Baptiste Jadot, Hanno Flentje, Arne Ludwig, Andreas D. Wieck, Matias Urdampilleta, Christopher Bäuerle, and Tristan Meunier: 'Coherent control of individual electron spins in a two-dimensional quantum dot array', *Nature Nanotechnology* **16** (2020), 296–301, DOI: 10.1038/s41565-020-00816-w (see pp. 17, 19, 125).

[Nak19] Takashi Nakajima, Akito Noiri, Jun Yoneda, Matthieu R. Delbecq, Peter Stano, Tomohiro Otsuka, Kenta Takeda, Shinichi Amaha, Giles Allison, Kento Kawasaki, Arne Ludwig, Andreas D. Wieck, Daniel Loss, and Seigo Tarucha: 'Quantum non-demolition measurement of an electron spin qubit', *Nature Nanotechnology* **14** (2019), 555–560, DOI: 10.1038/s41565-019-0426-x (see pp. 19, 42).

[Nic15] John M. Nichol, Shannon P. Harvey, Michael D. Shulman, Arijeet Pal, Vladimir Umansky, Emmanuel I. Rashba, Bertrand I. Halperin, and Amir Yacoby: 'Quenching of dynamic nuclear polarization by spin–orbit coupling in GaAs quantum dots', *Nature Communications* **6** (2015), DOI: 10.1038/ncomms8682 (see p. 109).

[Nie22] David J. Niegemann et al.: *Parity and singlet-triplet high fidelity readout in a silicon double quantum dot at 0.5 K*, 2022, DOI: 10.48550/ARXIV.2207.10523 (see pp. 11, 57, 72, 77, 97).

[Nie19] David Josef Niegemann: 'High fidelity spin readout in a siliconMOS device', MA thesis, Karlsruhe Institute of Technology, 2019 (see p. 49).

[Nie09] Michael A. Nielsen and Isaac L. Chuang: *Quantum computation and quantum information*, Cambridge University Press, 2009, DOI: 10.1017/cbo9780511976667 (see pp. 1, 10).

[Noi22] Akito Noiri, Kenta Takeda, Takashi Nakajima, Takashi Kobayashi, Amir Sammak, Giordano Scappucci, and Seigo Tarucha: 'Fast universal quantum gate above the fault-tolerance threshold in silicon', *Nature* **601** (2022), 338–342, DOI: 10.1038/s41586-021-04182-y (see pp. 11, 12, 14, 17, 57, 104).

[Nur22] Martin Nurizzo, Baptiste Jadot, Pierre-André Mortemousque, Vivien Thiney, Emmanuel Chanrion, David Niegemann, Matthieu Dartiailh, Arne Ludwig, Andreas D. Wieck, Christopher Bäuerle, Matias Urdampilleta, and Tristan Meunier: *Complete readout of two-electron spin states in a double quantum dot*, 2022, DOI: 10.48550/ARXIV.2209.00535 (see p. 115).

[Oak22] G. A. Oakes et al.: *Fast high-fidelity single-shot readout of spins in silicon using a single-electron box*, 2022, DOI: 10.48550/ARXIV.2203.06608 (see p. 77).

[Ono02] K. Ono, D.G. Austing, Y. Tokura, and S. Tarucha: 'Current Rectification by Pauli Exclusion in a Weakly Coupled Double Quantum Dot System', *Science* **297** (2002), 1313–1317, DOI: 10.1126/science.1070958 (see pp. 18, 40).

[Pak18] P. Pakkiam, A. V. Timofeev, M. G. House, M. R. Hogg, T. Kobayashi, M. Koch, S. Rogge, and M. Y. Simmons: 'Single-Shot Single-Gate rf Spin Readout in Silicon', *Physical Review X* **8** (2018), 041032, DOI: 10.1103/physrevx.8.041032 (see p. 19).

[Pau21] S. J. Pauka, K. Das, R. Kalra, A. Moini, Y. Yang, M. Trainer, A. Bousquet, C. Cantaloube, N. Dick, G. C. Gardner, M. J. Manfra, and D. J. Reilly: 'A cryogenic CMOS chip for generating control signals for multiple qubits', *Nature Electronics* **4** (2021), 64–70, DOI: 10.1038/s41928-020-00528-y (see p. 11).

[Per10] F. Persson, C. M. Wilson, M. Sandberg, G. Johansson, and P. Delsing: 'Excess Dissipation in a Single-Electron Box: The Sisyphus Resistance', *Nano Letters* **10** (2010), 953–957, DOI: 10.1021/nl903887x (see pp. 70, 72).

[Pet05a] J. R. Petta, Johnson AC, Taylor JM, Laird EA, Yacoby A, Lukin MD, Marcus CM, Hanson MP, and Gossard AC.: 'Coherent Manipulation of Coupled Electron Spins in Semiconductor Quantum Dots', *Science* **309** (2005), 2180–2184, DOI: 10.1126/science.1116955 (see pp. 12, 19, 36, 37, 106, 107).

[Pet05b] J. R. Petta, A. C. Johnson, A. Yacoby, C. M. Marcus, M. P. Hanson, and A. C. Gossard: 'Pulsed-gate measurements of the singlet-triplet relaxation time in a two-electron double quantum dot', *Physical Review B* **72** (2005), 161301, DOI: 10.1103/physrevb.72.161301 (see p. 40).

[PL08] M. Pioro-Ladrière, T. Obata, Y. Tokura, Y.-S. Shin, T. Kubo, K. Yoshida, T. Taniyama, and S. Tarucha: 'Electrically driven single-electron spin resonance in a slanting Zeeman field', *Nature Physics* **4** (2008), 776–779, DOI: 10.1038/nphys1053 (see pp. 12, 33).

[Pio22] N. Piot et al.: 'A single hole spin with enhanced coherence in natural silicon', *Nature Nanotechnology* (2022), DOI: 10.1038/s41565-022-01196-z (see p. 17).

[Pla12] Jarryd J. Pla, Kuan Y. Tan, Juan P. Dehollain, Wee H. Lim, John J. L. Morton, David N. Jamieson, Andrew S. Dzurak, and Andrea Morello: 'A single-atom electron spin qubit in silicon', *Nature* **489** (2012), 541–545, DOI: 10.1038/nature11449 (see p. 12).

[Pla20] Luca Planat, Arpit Ranadive, Rémy Dassonneville, Javier Puertas Martínez, Sébastien Léger, Cécile Naud, Olivier Buisson, Wiebke Hasch-Guichard, Denis M. Basko, and Nicolas Roch: 'Photonic-Crystal Josephson Traveling-Wave Parametric Amplifier', *Physical Review X* **10** (2020), 021021, DOI: 10.1103/physrevx.10.021021 (see p. 118).

[Poz11] David M. Pozar: *Microwave Engineering*, ed. by 1990 Addison-Wesley, WILEY, 1, 2011, 732 pp., URL: https://www.ebook.de/de/product/14948033/david_m_pozar_microwave_engineering.html (see pp. 62, 63).

[Rei07] D. J. Reilly, C. M. Marcus, M. P. Hanson, and A. C. Gossard: 'Fast single-charge sensing with a rf quantum point contact', *Applied Physics Letters* **91** (2007), 162101, DOI: 10.1063/1.2794995 (see p. 67).

[Rei15] Joachim Reinhold: *Quantentheorie der Molekule Eine Einfuhrung*, Springer Spektrum, Wiesbaden, 2015 (see p. 36).

[res21] IBM research: *Introducing the world's first 2 nm node chip*, https://research.ibm.com/blog/2-nm-chip, Accessed: 2022-09-22, 2021 (see p. 87).

[Sak93] J. J. Sakurai: *Modern Quantum Mechanics (Revised Edition)*, Addison Wesley, 1993 (see pp. 5, 6).

[Sam18] N. Samkharadze, G. Zheng, N. Kalhor, D. Brousse, A. Sammak, U. C. Mendes, A. Blais, G. Scappucci, and L. M. K. Vandersypen: 'Strong spin-photon coupling in silicon', *Science* **359** (2018), 1123–1127, DOI: 10.1126/science.aar4054 (see p. 122).

[Sar09] A. L. Saraiva, M. J. Calderón, Xuedong Hu, S. Das Sarma, and Belita Koiller: 'Physical mechanisms of interface-mediated intervalley coupling in Si', *Physical Review B* **80** (2009), 081305, DOI: 10.1103/physrevb.80.081305 (see p. 26).

[Sas98] S. Sasaki, D.G. Austing, and S. Tarucha: 'Spin states in circular and elliptical quantum dots', *Physica B: Condensed Matter* **256-258** (1998), 157–160, DOI: 10.1016/s0921-4526(98)00486-4 (see p. 11).

[Sch20] S. Schaal, I. Ahmed, J. A. Haigh, L. Hutin, B. Bertrand, S. Barraud, M. Vinet, C.-M. Lee, N. Stelmashenko, J. W. A. Robinson, J. Y. Qiu, S. Hacohen-Gourgy, I. Siddiqi, M. F. Gonzalez-Zalba, and J. J. L. Morton: 'Fast Gate-Based Readout of Silicon Quantum Dots Using Josephson Parametric Amplification', *Physical Review Letters* **124** (2020), 067701, DOI: 10.1103/physrevlett.124.067701 (see p. 64).

[Sch18] S. Schaal, S. Barraud, J. J. L. Morton, and M. F. Gonzalez-Zalba: 'Conditional Dispersive Readout of a CMOS Single-Electron Memory Cell', *Physical Review Applied* **9** (2018), 054016, DOI: 10.1103/physrevapplied.9.054016 (see p. 121).

[Sch98] R. J. Schoelkopf: 'The Radio-Frequency Single-Electron Transistor (RF-SET): A Fast and Ultrasensitive Electrometer', *Science* **280** (1998), 1238–1242, DOI: 10.1126/science.280.5367.1238 (see pp. 58, 66).

[Sch14] Lars R. Schreiber and Hendrik Bluhm: 'Silicon comes back', *Nature Nanotechnology* **9** (2014), 966–968, DOI: 10.1038/nnano.2014.249 (see p. 12).

[See21] Amanda E. Seedhouse, Tuomo Tanttu, Ross C.C. Leon, Ruichen Zhao, Kuan Yen Tan, Bas Hensen, Fay E. Hudson, Kohei M. Itoh, Jun Yoneda, Chih Hwan Yang, Andrea Morello, Arne Laucht, Susan N. Coppersmith, Andre Saraiva, and Andrew S. Dzurak: 'Pauli Blockade in Silicon Quantum Dots with Spin-Orbit Control', *PRX Quantum* **2** (2021), 010303, DOI: 10.1103/prxquantum.2.010303 (see p. 101).

[Sei22] Inga Seidler, Tom Struck, Ran Xue, Niels Focke, Stefan Trellenkamp, Hendrik Bluhm, and Lars R. Schreiber: 'Conveyor-mode single-electron shuttling in Si/SiGe for a scalable quantum computing architecture', *npj Quantum Information* **8** (2022), DOI: 10.1038/s41534-022-00615-2 (see p. 122).

[She10] S.N. Shevchenko, S. Ashhab, and Franco Nori: 'Landau–Zener–Stückelberg interferometry', *Physics Reports* **492** (2010), 1–30, DOI: 10.1016/j.physrep.2010.03.002 (see p. 38).

[Sil05] M. A. Sillanpää, T. Lehtinen, A. Paila, Yu. Makhlin, L. Roschier, and P. J. Hakonen: 'Direct Observation of Josephson Capacitance', *Physical Review Letters* **95** (2005), 206806, DOI: 10.1103/physrevlett.95.206806 (see p. 73).

[Sim07] C. B. Simmons, Madhu Thalakulam, Nakul Shaji, Levente J. Klein, Hua Qin, R. H. Blick, D. E. Savage, M. G. Lagally, S. N. Coppersmith, and M. A. Eriksson: 'Single-electron quantum dot in SiSiGe with integrated charge sensing', *Applied Physics Letters* **91** (2007), 213103, DOI: 10.1063/1.2816331 (see p. 12).

[Sou04] Rogerio de Sousa, J. D. Delgado, and S. Das Sarma: 'Silicon quantum computation based on magnetic dipolar coupling', *Physical Review A* **70** (2004), 052304, DOI: 10.1103/physreva.70.052304 (see p. 12).

[Spe22] Cameron Spence et al.: 'Spin-Valley Coupling Anisotropy and Noise in CMOS Quantum Dots', *Physical Review Applied* **17** (2022), 034047, DOI: 10.1103/physrevapplied.17.034047 (see pp. 95, 99).

[Sta22] Peter Stano and Daniel Loss: 'Review of performance metrics of spin qubits in gated semiconducting nanostructures', *Nature Reviews Physics* (2022), DOI: 10.1038/s42254-022-00484-w (see p. 12).

[Tak16] Kenta Takeda, Jun Kamioka, Tomohiro Otsuka, Jun Yoneda, Takashi Nakajima, Matthieu R. Delbecq, Shinichi Amaha, Giles Allison, Tetsuo Kodera, Shunri Oda, and Seigo Tarucha: 'A fault-tolerant addressable spin qubit in a natural silicon quantum dot', *Science Advances* **2** (2016), DOI: 10.1126/sciadv.1600694 (see p. 33).

[Tak21] Kenta Takeda, Akito Noiri, Takashi Nakajima, Jun Yoneda, Takashi Kobayashi, and Seigo Tarucha: 'Quantum tomography of an entangled three-qubit state in silicon', *Nature Nanotechnology* **16** (2021), 965–969, DOI: 10.1038/s41565-021-00925-0 (see p. 12).

[Tan19] Tuomo Tanttu, Bas Hensen, Kok Wai Chan, Chih Hwan Yang, Wister Wei Huang, Michael Fogarty, Fay Hudson, Kohei Itoh, Dimitrie Culcer, Arne Laucht, Andrea Morello, and Andrew Dzurak: 'Controlling Spin-Orbit Interactions in Silicon Quantum Dots Using Magnetic Field Direction', *Physical Review X* **9** (2019), 021028, DOI: 10.1103/physrevx.9.021028 (see p. 109).

[Tay07] J. M. Taylor, J. R. Petta, A. C. Johnson, A. Yacoby, C. M. Marcus, and M. D. Lukin: 'Relaxation, dephasing, and quantum control of electron spins in double quantum dots', *Physical Review B* **76** (2007), DOI: 10.1103/physrevb.76.035315 (see p. 108).

[Ter96] J. Tersoff, C. Teichert, and M. G. Lagally: 'Self-Organization in Growth of Quantum Dot Superlattices', *Phys. Rev. Lett.* **76** (1996), 1675–1678, DOI: 10.1103/PhysRevLett.76.1675, URL: https://link.aps.org/doi/10.1103/PhysRevLett.76.1675 (see p. 21).

[Tes19] Julian D. Teske, Simon Sebastian Humpohl, René Otten, Patrick Bethke, Pascal Cerfontaine, Jonas Dedden, Arne Ludwig, Andreas D. Wieck, and Hendrik Bluhm: 'A machine learning approach for automated fine-tuning of semiconductor spin qubits', *Applied Physics Letters* **114** (2019), 133102, DOI: 10.1063/1.5088412 (see p. 87).

[Thi14] Stefan Thiele: 'Read-out and coherent manipulation of an isolated nuclear spin using a single molecule magnet spin transistor', PhD thesis, Institut Néel (Grenoble) - École doctorale physique (Grenoble), 2014, URL: https://tel.archives-ouvertes.fr/tel-00984973 (see pp. 44, 47).

[Urd15] Matias Urdampilleta, Anasua Chatterjee, Cheuk Chi Lo, Takashi Kobayashi, John Mansir, Sylvain Barraud, Andreas C. Betz, Sven Rogge, M. Fernando Gonzalez-Zalba, and John J. L. Morton: 'Charge Dynamics and Spin Blockade in a Hybrid Double Quantum Dot in Silicon', *Physical Review X* **5** (2015), 031024, DOI: 10.1103/physrevx.5.031024 (see p. 73).

[Urd19] Matias Urdampilleta et al.: 'Gate-based high fidelity spin readout in a CMOS device', *Nature Nanotechnology* **14** (2019), 737–741, DOI: 10.1038/s41565-019-0443-9 (see pp. 17, 19, 57, 72, 77, 102).

[Vah21] Ensar Vahapoglu, James P. Slack-Smith, Ross C. C. Leon, Wee Han Lim, Fay E. Hudson, Tom Day, Tuomo Tanttu, Chih Hwan Yang, Arne Laucht, Andrew S. Dzurak, and Jarryd J. Pla: 'Single-electron spin resonance in a nanoelectronic device using a global field', *Science Advances* **7** (2021), DOI: 10.1126/sciadv.abg9158 (see pp. 33, 123).

[Van17] L. M. K. Vandersypen, H. Bluhm, J. S. Clarke, A. S. Dzurak, R. Ishihara, A. Morello, D. J. Reilly, L. R. Schreiber, and M. Veldhorst: 'Interfacing spin qubits in quantum dots and donors—hot, dense, and coherent', *npj Quantum Information* **3** (2017), DOI: 10.1038/s41534-017-0038-y (see pp. 11, 120, 122).

[Van19] Lieven M. K. Vandersypen and Mark A. Eriksson: 'Quantum computing with semiconductor spins', *Physics Today* **72** (2019), 38–45, DOI: 10.1063/pt.3.4270 (see p. 9).

[Vel17] M. Veldhorst, H. G. J. Eenink, C. H. Yang, and A. S. Dzurak: 'Silicon CMOS architecture for a spin-based quantum computer', *Nature Communications* **8** (2017), DOI: 10.1038/s41467-017-01905-6 (see p. 121).

[Vel14] M. Veldhorst, J. C. C. Hwang, C. H. Yang, A. W. Leenstra, B. de Ronde, J. P. Dehollain, J. T. Muhonen, F. E. Hudson, K. M. Itoh, A. Morello, and A. S. Dzurak: 'An addressable quantum dot qubit with fault-tolerant control-fidelity', *Nature Nanotechnology* **9** (2014), 981–985, DOI: 10.1038/nnano.2014.216 (see p. 12).

[Vel15] M. Veldhorst, C. H. Yang, J. C. C. Hwang, W. Huang, J. P. Dehollain, J. T. Muhonen, S. Simmons, A. Laucht, F. E. Hudson, K. M. Itoh, A. Morello, and A. S. Dzurak: 'A two-qubit logic gate in silicon', *Nature* **526** (2015), 410–414, DOI: 10.1038/nature15263 (see pp. 9, 12, 33).

[Vin18] M. Vinet et al.: 'Towards scalable silicon quantum computing', *2018 76th Device Research Conference (DRC)*, 2018, DOI: 10.1109/drc.2018.8442198 (see p. 121).

[Vin16] Maud Vinet et al.: 'Opportunities brought by sequential 3D CoolCube™ integration', *2016 46th European Solid-State Device Research Conference (ESSDERC)*, 2016, DOI: 10.1109/essderc.2016.7599627 (see p. 16).

[Voi15] B. Voisin, R. Maurand, S. Barraud, M. Vinet, X. Jehl, M. Sanquer, J. Renard, and S. De Franceschi: 'Electrical Control of ig/i-Factor in a Few-Hole Silicon Nanowire MOSFET', *Nano Letters* **16** (2015), 88–92, DOI: 10.1021/acs.nanolett.5b02920 (see p. 33).

[Voi14] Benoit Voisin, Viet-Hung Nguyen, Julien Renard, Xavier Jehl, Sylvain Barraud, François Triozon, Maud Vinet, Ivan Duchemin, Yann-Michel Niquet, Silvano de Franceschi, and Marc Sanquer: 'Few-Electron Edge-State Quantum Dots in a Silicon Nanowire Field-Effect Transistor', *Nano Letters* **14** (2014), 2094–2098, DOI: 10.1021/nl500299h (see p. 81).

[Wan11] David S. Wang, Austin G. Fowler, and Lloyd C. L. Hollenberg: 'Surface code quantum computing with error rates over 1%', *Physical Review A* **83** (2011), DOI: 10.1103/physreva.83.020302 (see p. 57).

[Wan10] L. Wang, K. Shen, B. Y. Sun, and M. W. Wu: 'Singlet-triplet relaxation in multivalley silicon single quantum dots', *Physical Review B* **81** (2010), 235326, DOI: 10.1103/physrevb.81.235326 (see p. 114).

[Wat18] T. F. Watson, S. G. J. Philips, E. Kawakami, D. R. Ward, P. Scarlino, M. Veldhorst, D. E. Savage, M. G. Lagally, Mark Friesen, S. N. Coppersmith, M. A. Eriksson, and L. M. K. Vandersypen: 'A programmable two-qubit quantum processor in silicon', *Nature* **555** (2018), 633–637, DOI: 10.1038/nature25766 (see p. 12).

[Wec14] Dave Wecker, Bela Bauer, Bryan K. Clark, Matthew B. Hastings, and Matthias Troyer: 'Gate-count estimates for performing quantum chemistry on small quantum computers', *Physical Review A* **90** (2014), 022305, DOI: 10.1103/physreva.90.022305 (see pp. 10, 16).

[Wee88] B. J. van Wees, H. van Houten, C. W. J. Beenakker, J. G. Williamson, L. P. Kouwenhoven, D. van der Marel, and C. T. Foxon: 'Quantized conductance of point contacts in a two-dimensional electron gas', *Physical Review Letters* **60** (1988), 848–850, DOI: 10.1103/physrevlett.60.848 (see p. 58).

[Wes19] Anderson West, Bas Hensen, Alexis Jouan, Tuomo Tanttu, Chih-Hwan Yang, Alessandro Rossi, M. Fernando Gonzalez-Zalba, Fay Hudson, Andrea Morello, David J. Reilly, and Andrew S. Dzurak: 'Gate-based single-shot readout of spins in silicon', *Nature Nanotechnology* **14** (2019), 437–441, DOI: 10.1038/s41565-019-0400-7 (see pp. 19, 66, 74, 76).

[Wie02] W. G. van der Wiel, S. De Franceschi, J. M. Elzerman, T. Fujisawa, S. Tarucha, and L. P. Kouwenhoven: 'Electron transport through double quantum dots', *Reviews of Modern Physics* **75** (2002), 1–22, DOI: 10.1103/revmodphys.75.1 (see pp. 24, 30, 31, 58).

[Wis21] David F. Wise, John J.L. Morton, and Siddharth Dhomkar: 'Using Deep Learning to Understand and Mitigate the Qubit Noise Environment', *PRX Quantum* **2** (2021), 010316, DOI: 10.1103/prxquantum.2.010316 (see p. 125).

[Wit10] Wayne M. Witzel, Malcolm S. Carroll, Andrea Morello, Łukasz Cywiński, and S. Das Sarma: 'Electron Spin Decoherence in Isotope-Enriched Silicon', *Physical Review Letters* **105** (2010), 187602, DOI: 10.1103/physrevlett.105.187602 (see p. 9).

[Xia10] M. Xiao, M. G. House, and H. W. Jiang: 'Measurement of the Spin Relaxation Time of Single Electrons in a Silicon Metal-Oxide-Semiconductor-Based Quantum Dot', *Physical Review Letters* **104** (2010), 096801, DOI: 10.1103/physrevlett.104.096801 (see p. 114).

[Xue20] Xiao Xue, Benjamin D'Anjou, Thomas F. Watson, Daniel R. Ward, Donald E. Savage, Max G. Lagally, Mark Friesen, Susan N. Coppersmith, Mark A. Eriksson, William A. Coish, and Lieven M. K. Vandersypen: 'Repetitive Quantum Nondemolition Measurement and Soft Decoding of a Silicon Spin Qubit', *Physical Review X* **10** (2020), 021006, DOI: 10.1103/physrevx.10.021006 (see p. 19).

[Xue22] Xiao Xue, Maximilian Russ, Nodar Samkharadze, Brennan Undseth, Amir Sammak, Giordano Scappucci, and Lieven M. K. Vandersypen: 'Quantum logic with spin qubits crossing the surface code threshold', *Nature* **601** (2022), 343–347, DOI: 10.1038/s41586-021-04273-w (see pp. 11, 12, 14, 17, 18, 57, 104).

[Xue21] Xiao Xue et al.: 'CMOS-based cryogenic control of silicon quantum circuits', *Nature* **593** (2021), 205–210, DOI: 10.1038/s41586-021-03469-4 (see p. 11).

[Yan19] C. H. Yang, K. W. Chan, R. Harper, W. Huang, T. Evans, J. C. C. Hwang, B. Hensen, A. Laucht, T. Tanttu, F. E. Hudson, S. T. Flammia, K. M. Itoh, A. Morello, S. D. Bartlett, and A. S. Dzurak: 'Silicon qubit fidelities approaching incoherent noise limits via pulse engineering', *Nature Electronics* **2** (2019), 151–158, DOI: 10.1038/s41928-019-0234-1 (see pp. 11, 19).

[Yan20] C. H. Yang, R. C. C. Leon, J. C. C. Hwang, A. Saraiva, T. Tanttu, W. Huang, J. Camirand Lemyre, K. W. Chan, K. Y. Tan, F. E. Hudson, K. M. Itoh, A. Morello, M. Pioro-Ladrière, A. Laucht, and A. S. Dzurak: 'Operation of a silicon quantum processor unit cell above one kelvin', *Nature* **580** (2020), 350–354, DOI: 10.1038/s41586-020-2171-6 (see pp. 11, 14, 17).

[Yon20] J. Yoneda, K. Takeda, A. Noiri, T. Nakajima, S. Li, J. Kamioka, T. Kodera, and S. Tarucha: 'Quantum non-demolition readout of an electron spin in silicon', *Nature Communications* **11** (2020), DOI: 10.1038/s41467-020-14818-8 (see pp. 19, 42, 104).

[Yon21] Jun Yoneda, Wister Huang, Mengke Feng, Henry Yang, Kok Chan, Tuomo Tanttu, Will Gilbert, R. Leon, Fay Hudson, K. Itoh, A. Morello, S. Bartlett, Arne Laucht, Andre Saraiva, and A. Dzurak: 'Coherent spin qubit transport in silicon', *Nature Communications* **12** (2021), 4114, DOI: 10.1038/s41467-021-24371-7 (see p. 33).

[Yon17] Jun Yoneda, Kenta Takeda, Tomohiro Otsuka, Takashi Nakajima, Matthieu R. Delbecq, Giles Allison, Takumu Honda, Tetsuo Kodera, Shunri Oda, Yusuke Hoshi, Noritaka Usami, Kohei M. Itoh, and Seigo Tarucha: 'A quantum-dot spin qubit with coherence limited by charge noise and fidelity higher than 99.9%', *Nature Nanotechnology* **13** (2017), 102–106, DOI: 10.1038/s41565-017-0014-x (see pp. 11, 18).

[Yu22] Cécile X. Yu, Simon Zihlmann, José C. Abadillo-Uriel, Vincent P. Michal, Nils Rambal, Heimanu Niebojewski, Thomas Bedecarrats, Maud Vinet, Etienne Dumur, Michele Filippone, Benoit Bertrand, Silvano De Franceschi, Yann-Michel Niquet, and Romain Maurand: 'Strong coupling between a photon and a hole spin in silicon', (2022) (see p. 122).

[Zha19] R. Zhao et al.: 'Single-spin qubits in isotopically enriched silicon at low magnetic field', *Nature Communications* **10** (2019), DOI: 10.1038/s41467-019-13416-7 (see p. 33).

[Zhe19] G. Zheng, N. Samkharadze, M. L. Noordam, N. Kalhor, D. Brousse, A. Sammak, G. Scappucci, and L. M. K. Vandersypen: 'Rapid high-fidelity gate-based spin read-out in silicon', *arXiv* (3, 2019) (see pp. 11, 12, 18, 19, 57, 73, 74, 76, 97, 117, 119).

[Zie22] Joshua Ziegler, Florian Luthi, Mick Ramsey, Felix Borjans, Guoji Zheng, and Justyna P. Zwolak: *Tuning arrays with rays: Physics-informed tuning of quantum dot charge states*, 2022, DOI: 10.48550/ARXIV.2209.03837 (see pp. 87, 126).

[Zor95] A. B. Zorin: 'The thermocoax cable as the microwave frequency filter for single electron circuits', *Review of Scientific Instruments* **66** (1995), 4296–4300, DOI: 10.1063/1.1145385 (see p. 47).

[Zu22] H. Zu, W. Dai, and A.T.A.M. de Waele: 'Development of dilution refrigerators—A review', *Cryogenics* **121** (2022), 103390, DOI: 10.1016/j.cryogenics.2021.103390 (see p. 46).

[Zwa13] Floris A. Zwanenburg, Andrew S. Dzurak, Andrea Morello, Michelle Y. Simmons, Lloyd C. L. Hollenberg, Gerhard Klimeck, Sven Rogge, Susan N. Coppersmith, and Mark A. Eriksson: 'Silicon quantum electronics', *Reviews of Modern Physics* **85** (2013), 961–1019, DOI: 10.1103/revmodphys.85.961 (see pp. 12, 22, 25).

[Zwa09] Floris A. Zwanenburg, Cathalijn E. W. M. van Rijmenam, Ying Fang, Charles M. Lieber, and Leo P. Kouwenhoven: 'Spin States of the First Four Holes in a Silicon Nanowire Quantum Dot', *Nano Letters* **9** (2009), 1071–1079, DOI: 10.1021/nl803440s (see p. 12).

[Zwe22] A. M. J. Zwerver et al.: 'Qubits made by advanced semiconductor manufacturing', *Nature Electronics* **5** (2022), 184–190, DOI: 10.1038/s41928-022-00727-9 (see p. 16).

List of Figures

A Theoretical background

A.1 Describing a multi qubit system - The density matrix

While the Bloch sphere is only valid for single qubits, the density matrix is a useful description for multi qubit systems. The density matrix of a single qubit is given by

$$\hat{p} := \begin{pmatrix} |\alpha|^2 & \alpha\beta^* \\ \alpha^*\beta & |\beta|^2 \end{pmatrix} = \begin{pmatrix} \cos^2(\theta/2) & 1/2e^{-i\varphi}\sin\theta \\ 1/2e^{i\varphi}\sin\theta & \sin^2(\theta/2) \end{pmatrix} = \frac{1}{2}\begin{pmatrix} 1+P_z & P_x - iP_y \\ P_x + iP_y & 1-P_z \end{pmatrix}, \quad \text{(A.1)}$$

where the diagonal elements give the probabilities of $|0\rangle$ and $|1\rangle$, and the off-diagonal elements are called interferences. From this it becomes clear, that the trace of the density matrix must be one. In contrast to the Bloch sphere, the density matrix can as well be used for mixed states. These
The density matrix for a multi qubit system is the product of the individual density matrices, for instance the two qubits with the density matrices $\hat{p}_1$ and $\hat{p}_2$ would be described by

$$\hat{p}_{tot} = \hat{p}_1 \otimes \hat{p}_2. \quad \text{(A.2)}$$

An important feature of this is that one can use partial traces.

$$\left\langle \hat{O} \right\rangle = trace(\hat{O}\hat{\rho}) \quad \text{(A.3)}$$

An operator $\hat{O}$ that just acts on a subsystem of the density matrix $\hat{\rho}$ results in a new density matrix with reduced dimension. This reduction of dimension is achieved using a partial trace over the subsystem, the operator acts on (e.g. a single qubit). The new density matrix now reflects the state of the system after the operation that was described by the partial trace over $\hat{O}\hat{\rho}$ (e.g. the measurement of a single qubit). When we will work with two spin systems, we will see that a single measurement is in general not sufficient to determine the quantum state. Using density matrices, this can easily be seen using for instance the two non-entangled states $|\psi_1\rangle = |{\downarrow}{\uparrow}\rangle$ and $|\psi_2\rangle = \frac{1}{\sqrt{2}}(|{\downarrow}{\downarrow}\rangle \pm |{\downarrow}{\uparrow}\rangle) = |{\downarrow}\rangle_{\mathrm{A}} \otimes \frac{1}{\sqrt{2}}(|{\downarrow}\rangle_{\mathrm{B}} \pm |{\uparrow}\rangle_{\mathrm{B}})$. The reduced density matrix for the first qubit is

$$\hat{\rho}_{\mathrm{A}} = \begin{pmatrix} 1 & 0 \\ 0 & 0 \end{pmatrix}. \quad \text{(A.4)}$$

Hence, the two states can not be distinguished by measuring just system A. As the two systems are not entangled, the subsystems remain pure states with $\rho^2 = \rho$. Now that we have the tools to describe the state of a quantum system, we want to go a step further

and see how we can describe the evolution of such a system[Ihn10].

B Additional measurements

B.1 Stability diagrams of a sensor QD and a center QD

We used the stability diagrams depicted in figure **B.1** to calculate the addition energies for the QDs defined by T2 and B2 as presented in section **5.5.2**. The stability diagrams reveal the different cross capacitances between the gates. While the T2 transitions are clearly affected by T1 voltage and thus tilt slightly, the charge transitions for the QD underneath B2 are almost vertical in the diagram, indicating that the cross-capacitance is negligible. This tilting changes with the number of electrons in the QD and is most significant for the first few electrons. We interpret this as a stronger relocation of the QD center when loading the first electrons and the marginal effect per electron is larger. Additionally, the more electrons are in the QD, the stronger the screening potential, allowing to reduce the effect of the nearby gates.

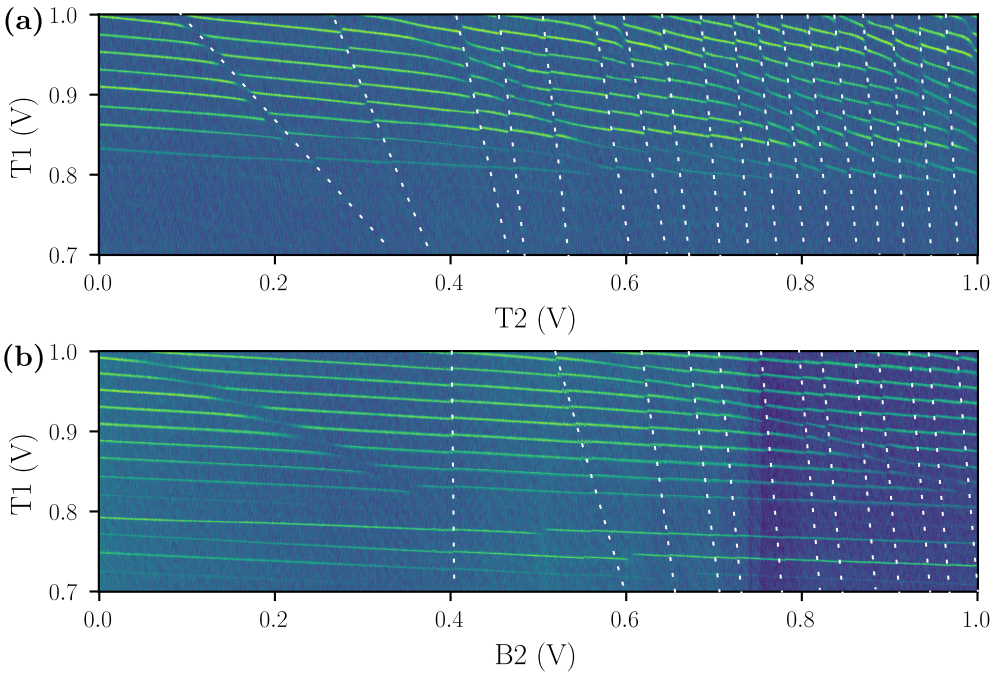

Figure B.1: **(a)** Stability diagrams for the two QDs T1-T2 with charge transitions of T2 indicated with white dashed lines. **(b)** Stability diagrams for the two QDs T1-B2 with charge transitions of B2 indicated with white dashed lines.

B.2 Derivation of the lever arm of gate B2

We have seen that we can use a fit of the charge transition broadening to extract the lever arm of the gate T2 in section (add ref to lever arm section). From this measurement and our knowledge about the charge states of a double quantum dot, we can calculate the lever arm of gate B2 on $\mathrm{QD_{B2}}$. We recall the voltages that define the honeycomb pattern given in equations **2.16**:

$$\Delta V_{\mathrm{G1}} = \frac{|e|}{C_{\mathrm{G1}}}(1 + \frac{\Delta E}{E_{\mathrm{C1}}}) \tag{B.1}$$

$$\Delta V_{\mathrm{G2}} = \frac{|e|}{C_{\mathrm{G2}}}(1 + \frac{\Delta E}{E_{\mathrm{C2}}}) \tag{B.2}$$

$$\Delta V^{m}_{\mathrm{G1}} = \frac{|e|C_{\mathrm{m}}}{C_{\mathrm{G},1}C_2} = \Delta V_{\mathrm{G1}}\frac{C_{\mathrm{m}}}{C_2}(1 + \frac{\Delta E}{E_{\mathrm{Cm}}}) \tag{B.3}$$

$$\Delta V^{m}_{\mathrm{G2}} = \frac{|e|C_{\mathrm{m}}}{C_{\mathrm{G2}}C_1} = \Delta V_{\mathrm{G2}}\frac{C_{\mathrm{m}}}{C_1}(1 + \frac{\Delta E}{E_{\mathrm{Cm}}}). \tag{B.4}$$

We will neglect ΔE terms in the following as we are considering the honeycomb of (1|1) where there is no additional orbital energy. We know that we can use the lever arms to

relate the voltage with the QD capacitance following

$$\alpha_{\mathrm{G1}}|e|\Delta V_{\mathrm{G1}} = \frac{e^2}{C_1} \tag{B.5}$$

$$\alpha_{\mathrm{G2}}|e|\Delta V_{\mathrm{G2}} = \frac{e^2}{C_2}. \tag{B.6}$$

Thus, we have an expression for C_1 and C_2 that we can use for ΔV^m_{G1} and ΔV^m_{G2}, resulting in

$$\Delta V^m_{\mathrm{G1}} = \Delta V_{\mathrm{G1}}\frac{C_{\mathrm{m}}}{C_2} = \alpha_{\mathrm{G2}}\Delta V_{\mathrm{G1}}\Delta V_{\mathrm{G2}}\frac{C_{\mathrm{m}}}{e} \tag{B.7}$$

$$\Delta V^m_{\mathrm{G2}} = \Delta V_{\mathrm{G2}}\frac{C_{\mathrm{m}}}{C_1} = \alpha_{\mathrm{G1}}\Delta V_{\mathrm{G1}}\Delta V_{\mathrm{G2}}\frac{C_{\mathrm{m}}}{e}. \tag{B.8}$$

Multiplying equation **B.7** (**B.8**) with $1/\alpha_{\mathrm{G2}}$ ($1/\alpha_{\mathrm{G1}}$) and subtracting equation **B.7** from **B.8**, gives us:

$$\frac{\Delta V^m_{\mathrm{G1}}}{\alpha_{\mathrm{G2}}} - \frac{\Delta V^m_{\mathrm{G2}}}{\alpha_{\mathrm{G1}}} = 0 \tag{B.9}$$

$$\Leftrightarrow \alpha_{\mathrm{G2}} = \frac{\Delta V^m_{\mathrm{G1}}}{\Delta V^m_{\mathrm{G2}}}\alpha_{\mathrm{G1}} \tag{B.10}$$

Using the stability diagram of B2-T2, we can find the values for $\Delta V^m_{\mathrm{T2}} = 4.8\,\mathrm{mV}$ and $\Delta V^m_{\mathrm{B2}} = 6.8\,\mathrm{mV}$, resulting in an α-factor for B2 of $\alpha_{B2} = \frac{48}{68}\cdot 0.05 \approx 0.035$.

B.3 Landau-Zener experiment

We performed the Landau-Zener experiment described in section **6.2.2** for different magnetic fields B_{z} of 120 mT, 90 mT, and 60 mT. The resulting singlet population as a function of transition speed is plotted in figure **B.2**. From these measurements, we find that Δ_{ST} is for all of these measurements $\sim 130\,\mathrm{MHz}$.

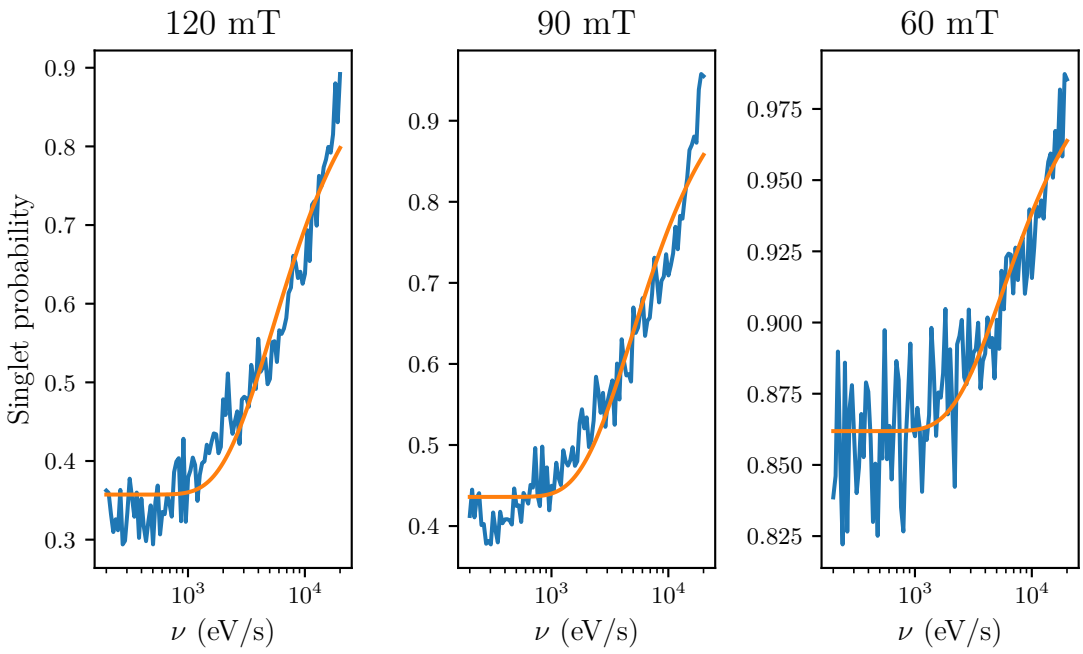

Figure B.2: Landau-Zener experiment at a magnetic field B_z of 120 mT, 90 mT, and 60 mT. From the fits to the data we can extract for all three magnetic fields a value for $\Delta_{ST} \approx 130$ MHz.

B.4 $S_0 - T_0$ mixing

In a similar device to the one presented in the main text, we performed a mixing experiment as it is presented in section **6.2.3**. We were not able to tune this device in a regime where

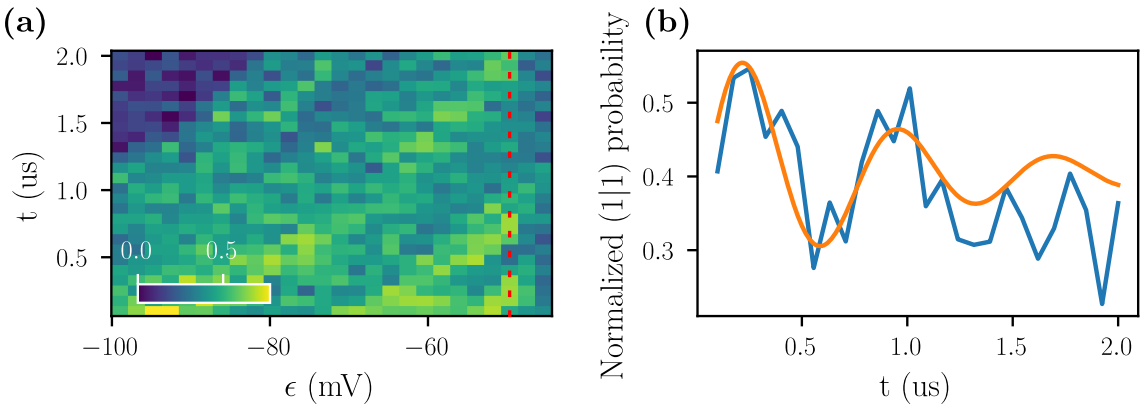

Figure B.3: $S_0 - T_0$ mixing experiment. **(a)** Normalized probability to measure (1|1) as a function of AWG pulse duration and pulse amplitude. The pattern resembles the $S_0 - T_0$ mixing signature presented by Maune et al.[Mau12]. **(b)** Single trace along one pulse amplitude with a fit of a damped oscillation with a frequency of 1.4 MHz.

we could measure an ST-readout, but relied on a parity readout. Thus, the blocked signal corresponds only to states that relaxed to the T_- state during the mixing pulse. We assume that the relaxation $T_0 \rightarrow T_-$ was much faster than $S_0 \rightarrow T_-$ such that we could still measure a difference between these two states. However, this measurement required averaging over vast amounts of data to achieve the low SNR we show in **B.3**. Additionally, the device was rather instable, such that we lost the measurement signal during many experiments, increasing the required number of experiment repetitions further.
In contrast to the other device, we find indications for $S_0 - T_0$ oscillations at 1.4 MHz and a decay of $\approx 0.7\,\mu s$. The oscillations indicate that in this device the δE_z components are non-zero, resulting in a non-zero mixing drive when pulsing in the (1|1) regime. The much shorter relaxation time compared to the other device makes sense as the oscillations indicate that $\Delta g \neq 0$, resulting in stronger sensitivity to charge noise.

Acknowledgments

As this marks the end of my PhD and with that the end of an important chapter of my life, I would like to thank all the people who made this such a formative experience. Even though this time had its highs and lows with a global pandemic overshadowing most of the time, I would not be the same person today without these experiences.
First, I would like to thank my supervisors Franck and Matias for offering me the opportunity to pursue my research at the Néel Institute. The constant support, advise and discussions were of utmost importance for the success of this project. Moreover, Matias already supervised me during my Master thesis, and during these years I have learned more from him than he probably knows. Additionally, I want to thank Tristan for his support and advise during my PhD. His understanding of the device physics is second to none and often helped me interpreting the measurements.
Appart from my supervisors, I need to thank all my colleagues of the QuantECA group and in particular the spin qubit team. In particular, Emmanuel taught me during the first month of my Master thesis how to work with dilution fridges and perform rf-reflectometry readouts. His work ethics and dedication are still very inspiring. Next, Baptiste who always helped me out when I was struggling with the software. Martin for fruitful discussions on rf-reflectometry and spin readout. Of course, I learned a lot and enjoyed the time with the other team members Bernhard, Cameron, Pierre-Andre, Bruna, and Victor and I hope that they keep on making working in the lab such a pleasure. Not directly part of the team, but of tremendous influence during my time in the lab was Jun Liang (Ángel) who was the best co-worker I could have imagined. I am grateful for Biel's theory support and amazing outdoor adventures.
Special thanks goes to the staff at the Néel Institute who make all the research possible. For my research, I need to thank in particular the liquefier team, providing more than 100 L liquid helium per week, and the Nanofab team for helping me to develop a recipe for fabricating on-chip inductors. I also want to thank the electronics workshop who made innumerable PCBs for me. Finally, I am incredibly grateful for the constant support and patience of Eric. He helped me to maintain the cryostat and I enjoyed his presence immensely. Everyone who has the chance to work with him can consider himself lucky.
This thesis would not have been such a great experience without my stay in Natalia Ares group in Oxford. I enjoyed the time tremendously and hold the memories dear to my heart. I cannot thank Natalia enough for inviting me to work in her group. Not only that, but I learned a lot during my stay and working with the whole group was a great experience.
Last but not least, I would like to thank my parents for always being there for me during these years and having taught me the needed attitude to pursue such a long project. I would also like to thank my brothers and sisters who probably had the greatest influence

on who I became.